NORTHWESTERN UNIVERSITY

Excited State Dynamics of Non-Fullerene Acceptors Towards Solar Energy Conversion Applications: Multi-Chromophore Rylenediimide Arrays and Beyond

A DISSERTATION

SUBMITTED TO THE GRADUATE SCHOOL

IN PARTIAL FULFILLMENT OF THE REQUIREMENTS

for the degree

DOCTOR OF PHILOSOPHY

Field of Chemistry

By

Joaquin Miguel Alzola

EVANSTON, ILLINOIS

September 2021

Abstract

Excited State Dynamics of Non-Fullerene Acceptors Towards Solar Energy Conversion Applications: Multi-Chromophore Rylenediimide Arrays and Beyond

Joaquin Miguel Alzola

Recent developments in research concerning organic photovoltaics (OPVs) have overseen massive increases in device performance and the ascension of electron acceptor materials that outclass the preeminent acceptor compounds, buckminsterfullerene (C_{60}) derivatives. New design strategies in the molecular structure of perylenediimides (PDIs) and fused-ring electron acceptors (FREAs) have increased single-junction photovoltaic efficiencies to values greater than 17%.

This dissertation investigates the excited-state dynamics of various molecular electron acceptors and how chemical structure modifications influence these. Recent advances in the design of perylenediimide acceptors has demonstrated high efficiencies in molecular structures incorporating several PDI chromophores with highly twisted geometries and extended π-conjugation. Headland substitution on the PDI core gives consistently higher device performance than does equivalent bay-substitution. Model compounds with this substitution pattern (***o*-PDI$_2$**, ***m*-PDI$_2$**, ***p*-PDI$_2$**) show enhanced intersystem crossing and in the case of ***o*-PDI$_2$**, symmetry-breaking charge separation.

PDIs are also capable of enhanced charge delocalization. In a model triad with two PDIs oriented cofacially to one another, photoinduced electron transfer is increased by a factor of 50% compared to a single PDI unit. This effect is limited to two PDIs, however, as no additional rate increased is observed in the three-PDI compound **ZnTPP$_2$-PDI$_3$**, owing to weak electronic coupling across all three PDIs. Regardless, PDIs can efficiently delocalize electrons in a conjugated motif that exhibits high solar cell performance, as demonstrated by the blending of

Ph(PDI)$_3$ with two donor polymers. The highly fluorinated polymer **PBDTTF-FTTE** paired with this molecule boasts a power conversion efficiency (PCE) of 9.1% through increased phase separation and reduced bimolecular recombination compared to blends using the fluorine-poor polymer **PBDTT-FTTE**.

More recently designed chromophores of the **ITIC** and **Y6** families of molecules exhibit strong photovoltaic responses exceeding 17%. π-extension and fluorination of both sets of molecules enhance their efficiency in devices. **ITN-F4** and **ITzN-F4** undergo efficient charge separation despite the formation of an excimer state, while **BT-BO-L4F** and **BT-LIC** have enhanced charge transport properties that manifest in accelerated recombination when an external bias is not present. The same is true when blends containing **Y6** are thermally annealed, despite this process increasing overall PCE.

Acknowledgements

I would first like to think my advisors, Professor Michael R. Wasielewski and Professor Tobin J. Marks, for giving me the opportunity to conduct research by drawing on the techniques and knowledge of two different research groups. I am very grateful for the mentorship, resources, and collaborative opportunities the two of you have provided, which have shaped my time here in a highly impactful way. Thank you to my committee members, Professor Lin X. Chen and Professor Emily A. Weiss, for your feedback and advice. I would also like to thank Professor Omar K. Farha for serving as the chair of my qualifying exam committee.

I would next like to acknowledge the work of my collaborators and coauthors: **Chapter 2** – Dr. Nikolai A. Tcyrulnikov for running computational experiments, Paige J. Brown for collecting time-resolved fluorescence data, and Prof. Ryan M. Young for guidance and discussion; **Chapter 3** – Dr. Natalia E. Powers-Riggs, and Prof. Nathan T. La Porte for the femtosecond transient visible and mid-infrared measurements, Prof. Yi-Lin Wu for assistance with chemical calculations, Dr. Michelle Chen and Prof. Ryan M. Young for insightful discussions and feedback; **Chapter 4** – Dr. Weigang Zhu for providing guidance and direction in a new field, Dr. Patrick E. Harnett and Dr. Thomas J. Aldrich for providing the materials of interest, Prof. Ryan M. Young for discussions and useful feedback, and others too many to name for their participation and measurements; **Chapter 5** – Dr. Steven M. Swick, Dr. Weigang Zhu, and Guoping Li, for brainstorming interesting project ideas and giving me the opportunity to contribute by conducting transient absorption measurements. I would also like to thank the IMSERC staff, particularly Saman Shafaie for collecting high-resolution mass spectrometry data.

I would next like to acknowledge the many Wasielewski and Marks group members who have helped me along the way. First, I would like to thank Dr. Ryan Young for everything he has

taught me from operating the fsTA experiment to discussions about excited-state dynamics, and all his help in the formulation of my written manuscripts. Next, I would like to give special thanks to Prof. Yi-Lin Wu for teaching me about the synthetic techniques used in the group and helping guide the design of my first synthetic route, and for all his knowledge regarding DFT calculations. I would also like to thank Dr. Matt Krzyaniak and Haochuan Mao for their help regarding EPR experiments. Dr. Ferdinand Melkonyan was a great mentor in all things related to materials for organic photovoltaics. I would like to thank Dr. Jenna Logsdon for training me on how to work with the compounds we study in the group. I would like to further thank Dr. Jinyuan Zhang, Dr. Tomáš Šolomek, Dr. Nikolai Tcyrulnikov, Dr. Jenna Logsdon, Dr. Adam Coleman and Haochuan Mao for useful discussions concerning synthesis over the years. For their assistance with various spectroscopies, I would like to thank Dr. Youn Jue Bae, Haochuan Mao, Chenjian Lin, and Paige J. Brown. I also want to thank Amanda J. Mahoney, Melanie S. Sandberg, Morgan T. Eklund, and Elyse Bento for making sure the Wasielewski and Marks groups run smoothly.

I also want to thank my friends from home for their words of support and encouragement, and for extra necessary socialization during unprecedented times. I would also like to thank my roommates this past year, Daylan T. Sheppard and Suyog Padgaonkar, for a supportive and welcoming home environment during a difficult year. I also want to thank Adam F. Coleman and Natalia E. Powers-Riggs for being friends and resources during the Covid-19 pandemic. A special shoutout to Michelle Chen. Michelle, thank you for a supportive friend during the most difficult parts of this process, always ready to help with any problem. I am very thankful to be able to count you as a friend. Lastly, I want to thank my family: my mother, father, and my sister Carla. Thank you for being a loving and supportive family.

Thank you everyone. I would not be where I am today without everyone's individual contributions.

To my family.

Table of Contents

List of Figures

List of Schemes

List of Tables

Chapter 1 – Introduction

1.1. Background: An Introduction to Organic Photovoltaics

The increasing urgency of the climate crisis and reliance on fossil fuels coupled with increasing energy needs has spurred research and development of alternative energy technologies, that are environmentally friendly and do not rely on limited fuel and natural gas reserves.[1, 2] Alternative energy technologies broadly refers to various energy sources, such as solar, wind, hydrothermal, and nuclear energy. Solar energy generation is of particular interest given the raw energy output from the sun that reaches the Earth's surface, with energy harvesting capabilities increasing by hundreds of gigawatts in the US yearly.[3] Models that incorporate the available land area for energy conversion have demonstrated that energy from solar photovoltaic cells is projected to be instrumental in satisfying future energy demands.[3, 4] Continued research into these technologies paired with development initiatives has sharply reduced the average cost per kWh of energy derived from solar photovoltaics.[5-8] As a result, research into these technologies is poised to drive a revolution into energy dependences on a global scale.

While traditional solar photovoltaic technology employs inorganic semiconductor materials such as silicon or gallium arsenide (GaAs), among others, there has also been significant research into photovoltaic technology employing organic compounds as the charge generation material. Organic solar cells (OSCs) are of significant interest as photovoltaic materials owing to their low cost, solution processability, and mechanical flexibility. OSCs operate through a different mechanism than those based on inorganic semiconductors. In traditional photovoltaic cells, an electron is promoted from the valence band to the conduction band through photoexcitation, forming two charge carriers, one negative (electron) and one positive (hole) (**Figure 1.1A)**. These charge carriers are weakly bound to one another and constitute a Wannier-Mott exciton. The component electron and hole then separate and diffuse to the device electrodes to be collected as

current, driven by the field gradient of the material. In contrast, organic materials have a low inherent dielectric constant (~3-4), which is unfavorable for charge generation.[9] In this environment, the Coulombic interaction between electron and hole is strong, resulting in large exciton binding energies of the electron-hole pair on the order of hundreds of meV, also known as a Frenkel exciton.[10]

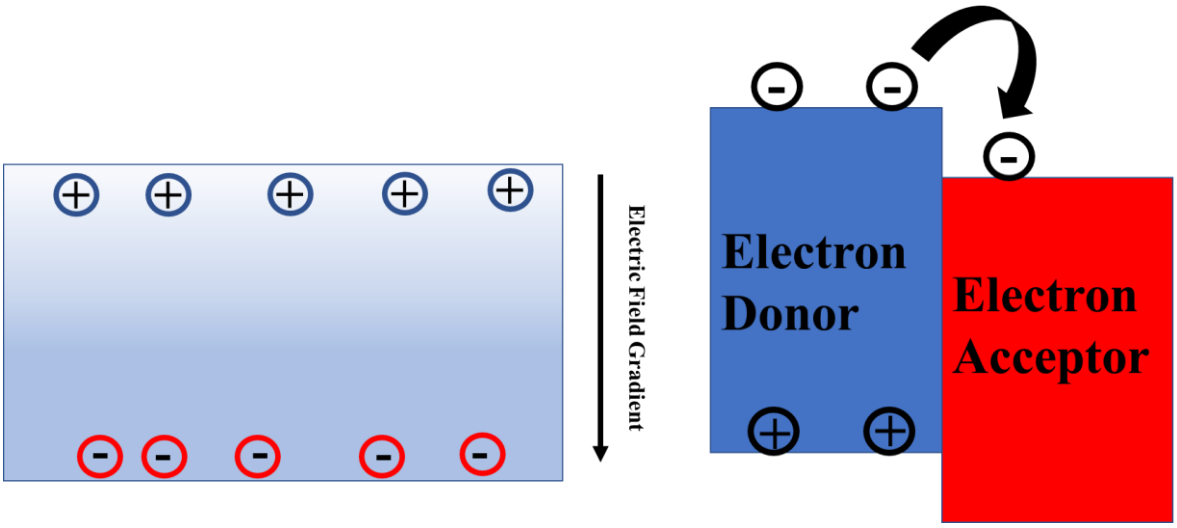

Figure 1.1. A. Schematic of charge generation in an inorganic semiconductor following light absorption. **B.** Schematic of charge generation in an organic heterojunction following light absorption.

To overcome this energetic penalty, OSC active layers are composed of two materials, a p-type electron donor and an n-type electron acceptor, combined to form a heterojunction (**Figure 1.1B**). In this type of system, photoexcited excitons migrate to a contact site of the two materials, at which point the energetic offset between the two materials provides a driving force to permit dissociation of the exciton into its component electron and hole as free charge carriers. Many years of experimentation have consistently determined that the optimal active layer composition is that of a bulk heterojunction (BHJ). In a BHJ, the two materials are blended through a process such as spin-coating to form interpenetrating domains of donor and acceptor materials that are similar in size to the average exciton diffusion distance (~10 nm, **Figure 1.2A**).[11, 12] This blending of

materials permits exciton migration while reducing the probability of two free carriers encountering one another and recombining back to the electronic ground state, a process known as recombination and a persistent issue in the study of other morphologies such as bilayers.

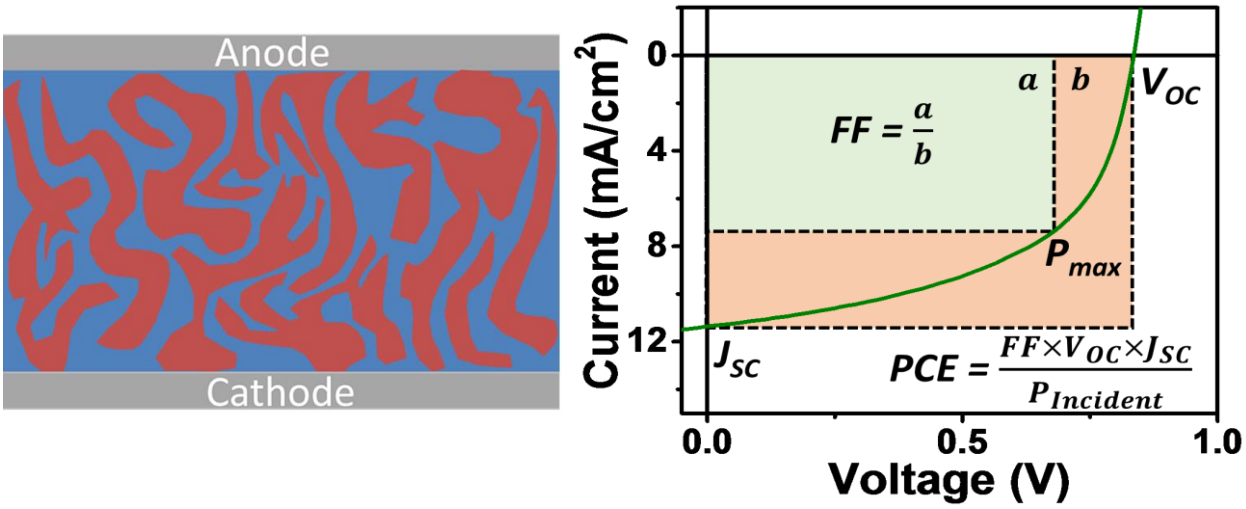

Figure 1.2: A. Schematic of a bulk heterojunction (BHJ) morphology. **B.** The J-V curve used to characterize photovoltaic devices. The power conversion efficiency (PCE) of a device is the power produced at the maximum power point (P_{max}) divided by the incident power on the device ($P_{Incident}$). P_{max} is the product of the open-circuit voltage (V_{OC}), the short-circuit current (J_{SC}), and the fill-factor (*FF*).

Power conversion efficiency (PCE) is defined as the ratio of the maximum amount of power that can be extracted from a solar cell to the incident power on the cell. The incident power on the cell is generally defined as 1 sun or 1.5 AMG. PCE is considered the key metric for evaluating the viability of photovoltaics cells and is dependent on three parameters: the fill factor (FF), open-circuit voltage (V_{oc}) and short-circuit current (J_{sc}) (**Figure 1.2B**). FF is influenced by electrical resistance in the active layer that impedes current flow, and balanced charge mobilities are generally associated with a high FF. V_{oc} is governed by the by the difference in th frontier molecular orbital energies of the two materials, and J_{sc} is strongly dependent on the amount of light absorbed by the active layer. Careful optimization of many variables is essential to balancing these paramters against one another, as V_{oc} can be increased by raising the energy levels of the

materials, but this translates into a larger optical bandgap, implying a smaller range of light absorption and thus a lower J_{sc}. Careful experimentation over decades has resulted in power conversion efficiencies (PCEs) exceeding of over 17%, demonstrating the utility of organic semiconductor molecules as photovoltaic materials.[13]

1.2. Design Strategies for Perylenediimide Nonfullerene Acceptors

For decades, the highest efficiency active layer composition was a BHJ made up of a conjugated polymer as the donor material and a derivative of buckminsterfullerene (C_{60}) as the acceptor material. Despite the initial investigation of a perylenediimide dye as the very first acceptor material in an organic photovoltaic cell, early device efficiencies consistently fell behind those of fullerenes.[14] Employing unsubstituted perylenediimide as an electron accepting material in a solar cell yielded PCEs of < 5%, far less than what fullerenes have been capable of.[15-17] However, perylenediimides are noted for their large molecular extinction coefficients, synthetic versatility, and photochemical stability, all properties that fullerenes lack.[18, 19] Perylenediimides are planar molecules and are electronically coupled in only one dimension whereas the spherical structure of fullerenes enables delocalization of electrons and electronic coupling in three directions.[20] The molecular structure of perylenediimides also makes them susceptible to aggregation through strong π- π interactions which can result in large crystalline domains as well as facilitate the formation of electronic trap states that favor geminate recombination of unbound holes and electrons. Nevertheless, significant research advancements have overcome these limitations and boosted PCE of perylenediimide-derived OSCs to equal and in some cases exceed those of fullerenes.[21, 22]

Research by Hartnett *et al*. showcased a successful design strategy for perylenediimides that strategically suppressed excimer formation and boosted PCEs through formation of a slip-

stacked geometry that favored charge generation over excimer formation.[23] Further research has showed that the most consistently effective strategy to improve PCEs of perylenediimide solar cells is the extension of the conjugated surface of the aromatic core through ring-fusion, which has been shown to enhance electron delocalization and increase donor-acceptor domain purity.[24, 25] This strategy generally incorporates multiple rylene units into one molecule, which also forces each chromophore to adopt an out-of-plane geometry that suppresses the formation of a large crystalline microstructure and disrupts noncovalent interactions between molecules.[25]

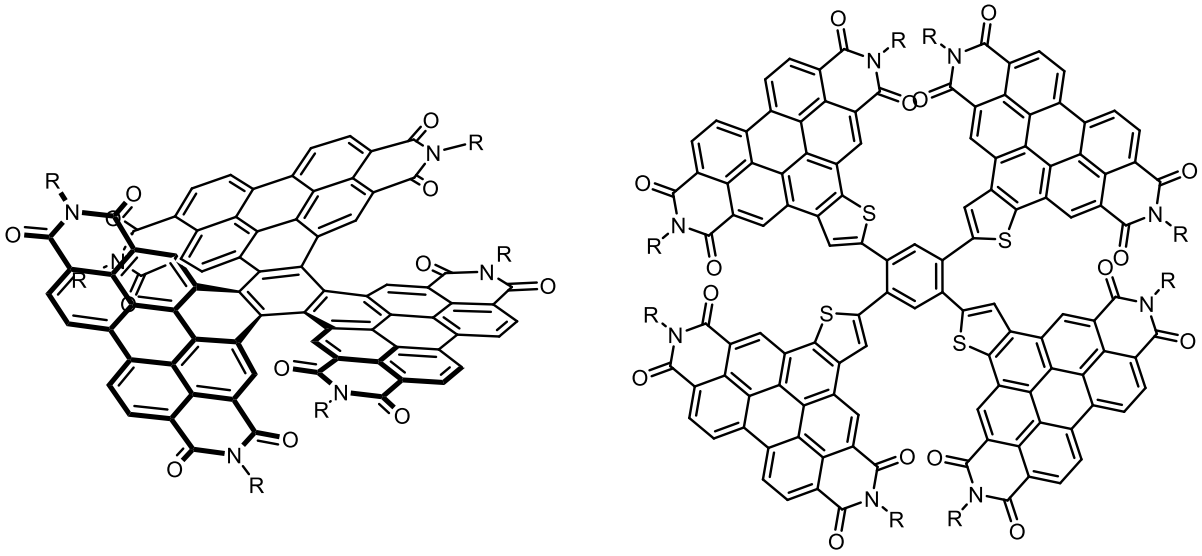

Figure 1.3: Chemical structures of two PDI-based electron acceptor materials employing a ring-fusion motif that demonstrate high PCEs of over 9%.

1.3. Time-Resolved Spectroscopy Applied to Organic BHJs

Evaluating the variables underpinning the PCE of OSCs is a complex undertaking, one that requires a combination of various experimental techniques to acquire a thorough understanding of the organic blend being studied. Reports concerning OSCs generally incorporate optical and electrochemical characterization techniques to examine the energetics of the system, microscopy such as AFM and TEM to examine the microstructure, X-ray techniques to study the morphology, all of which contribute towards a systematic evaluation of device fabrication conditions. However,

the lessons imparted by these studies are very system dependent, and modifications that improve the PCE of one BHJ blend may detract from another. Studies that attempt to understand the charge-transfer processes aim to produce more generally applicable insights and incorporate techniques such as transient photovoltage (TPV) and transient optical spectroscopy techniques.[26-28]

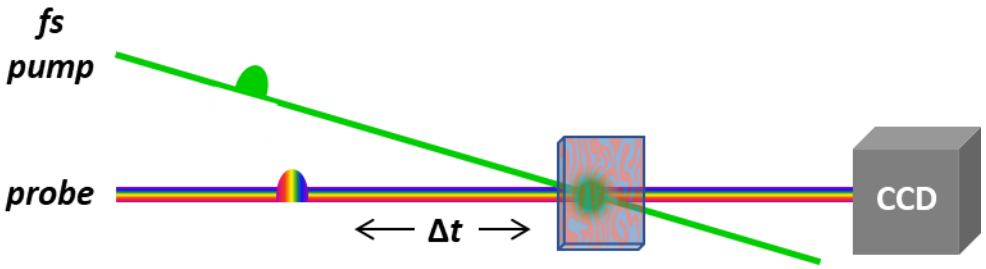

Figure 1.4: General experimental scheme of transient absorption spectroscopy on a thin film BHJ sample.

Time-resolved optical spectroscopy such as femtosecond transient absorption spectroscopy (fsTA) and nanosecond transient absorption spectroscopy (nsTA) can shed light on the timescales of underlying processes through detection of optical signatures of different electronic states. This technique has been used as part of several in-depth studies on the behavior of photogenerated charge carries in thin films of organic semiconductors and in BHJ blends.[29-34] A time resolution on the order of ~300 fs has demonstrated differing rates of charge transfer in high- vs. low-performance blends which informs on how changes in processing conditions and chemical modifications impact photocurrent generation beyond observing increases or decreases in the parameters described above (FF, V_{oc} and J_{sc}).[32] The nsTA experiment provides insight into recombination of the liberated charge carriers, and highly efficient systems have demonstrated persistence of these species into the microsecond regime, a behavior linked to reduced bimolecular recombination and low energy loss.[35, 36]

1.4. Dissertation Outline

Though derivatives of buckminsterfullerene (C_{60}) as the acceptor material dominated research in BHJ OSCs for decades, the field has rapidly shifted in favor of nonfullerene acceptor materials. Perylenediimides retain many advantages as acceptor materials in photovoltaic cells, and so have retained significant interest within the field of organic photovoltaics.[37-39] Years of research on the photovoltaic properties of these materials has determined that incorporation of multiple individual chromophores into a single molecular architecture is essential to improving the photovoltaic response.[21, 40, 41] Most of the following chapters of this thesis (2-4) aim to understand the impact of multiple chromophores on the transient dynamics and charge generation properties of perylene dye organic semiconductors and the resulting implications for the success of these dyes as photovoltaic materials. In addition, fused-ring electron acceptors (FREAs) originally developed in 2015 have decisively demonstrated their utility as acceptor materials and their photophysics will be discussed in chapter 5.

As one of the current top classes of organic electron-acceptors, PDI acceptor materials boast efficiencies of up to 11%.[22] Most of these strategies incorporate several PDIs derivatized at the bay position, all linked together through a central core to promote electron delocalization in a manner akin to fullerenes.[41] There is some evidence that substitution of PDI at the headland position is a promising strategy for increased photovoltaic performance of PDIs.[42, 43] Chapter 2 examines the photophysics of PDI dimers linked to a phenyl group at this position and summarizes the differences in transient dynamics as a function of substitution pattern on the phenyl. The *meta*- and *para*- derivatives demonstrate accelerated singlet decay with a minority population undergoing intersystem crossing (ISC), while the *ortho*-substituted derivative undergoes symmetry-breaking charge separation before recombining to the triplet state through radical-ion pair intersystem

crossing (RP-ISC). Strong electronic coupling in the *ortho* derivative extends the lifetime of the ion pair state relative to the *meta*- and *para*- isomers, a property that is of interest in electron acceptor materials.

One of the factors driving high photovoltaic performance in OSCs based on PDI is the use of highly conjugated architectures that enable electron delocalization across a large aromatic surface.[21, 24] However, this effect is difficult to study in a bulk heterojunction phase as the disorder complicates the isolation of individual charge transfer events. Model systems designed to probe this effect incorporate two PDIs oriented cofacially to one another to observe electron delocalization between two individual PDI units.[44] The electron-transfer process from a porphyrin electron donor is 50% faster in the dimer structure compared to the analogous single PDI system. Chapter 3 explores the consequences of an additional PDI oriented in the same manner and resulting effects on the rate of electron transfer. The third PDI unit is found to have no observable impact on the charge separation process as the observed electron transfer rate is identical to that of the dimer system. Further examination of the individual variables that influence this process are found to be largely unchanged relative to the dimer construct. Given the observed propagation of free charge carries in the solid state of PDI, this system demonstrates the limits of covalent model systems in explaining the trends observed in full photovoltaic devices.

With the lessons of Chapter 3 in mind, approaches to improving the PCE of PDI-based OSCs other than molecular modification of the electron acceptor are important to consider. A ring-fused perylenediimide acceptor material was designed utilizing the previously discussed strategies to enhance electron delocalization and has demonstrated high performance when blended with a donor polymer.[41] The success of this molecular design warranted further investigation into the precise factors that influence device performance in PDI-based devices, such as the carrier

dynamics and microstructure. A systematic study was conducted utilizing two donor polymers with high and low amounts of fluorine incorporation along the polymer backbone to isolate the key factors driving high device performance. Notably, the highly fluorinated polymer-based devices far outperformed the fluorine-deficient pair, demonstrating significant increases in each performance metric (J_{sc}, V_{oc}, FF). The additional fluorination increased device performance by 50% through ideal phase separation that resulted in improved carrier mobility, increased lifetimes of free charges and reduced bimolecular recombination.

Although PDI remains an attractive material for OSCs, their performance is still limited relative to other families of electron acceptor materials. The development and optimization of the fused-ring electron acceptor (FREA) class of materials has yielded PCEs as high as 17% and 18% in tandem cells, values that rapidly approach the industrial standard performance of α-Si panels (~21%).[13, 45, 46] The molecular design structure of FREAs incorporates alternating electron donating and accepting groups flanked by orthogonally positioned solubilizing groups, facilitating electronic coupling interactions between chromophores while retaining solubility in organic solvents and appropriately sized crystalline domains. FREAs absorb light strongly in the redder regions of the visible range of the electromagnetic spectrum and into the near infrared region, increasing the range of photons available for energy conversion and promoting the absorption of lower energy photons that reduces thermalization losses. Chapter 6 utilizes time-resolved spectroscopy techniques to analyze the charge-transfer dynamics of these and discusses these to understand the increasingly high device performance of the FREA family of organic semiconductors. The effects of π-extension and fluorination are examined for ADA-type derivatives derived from the prototypical example **ITIC.** The enlarged π-surfaces of these compounds facilitates an excimer relaxation process, though notably this process appears to occur

away from the donor-acceptor boundary and does not impact device performance. The influence of a thermal annealing process is examined for the A-DAD-A-type **Y6**, demonstrates accelerated bimolecular recombination despite the increase in performance. This is thought to result from the increased hole mobility which facilitates random free carrier movement in the absence of an external bias. Similar behavior is observed in π-extended and fluorinated analogues of **Y6**. Excimer relaxation is also observed in neat films of these acceptors, though this process appears suppressed in the blends, likely contributing to their overall high performance.

Chapter 2 - Intersystem Crossing and Symmetry-Breaking Charge Separation in a Series of Phenyl-Bridged Perylenediimide Dimers

2.1. Introduction

Perylenediimides (PDIs) are versatile strongly visible-light absorbing chromophores that have found widespread application as industrial coatings and have properties suitable for optoelectronic and spintronic applications. PDIs show particular promise in organic electronics as both small molecule electron acceptors in organic solar cells (OSCs) with device efficiencies as high as 11% and as transport-layer materials in both organic and perovskite solar cells.[22, 37, 47, 48] This molecular building block has been researched extensively over many decades and the current state-of-the-art device performance is largely driven by molecular scaffolds incorporating multiple PDI subunits in contorted geometries with long-range ordering that function to enhance light absorption and reduce energy losses from exciton recombination and excimer formation.[23, 40, 49]

An important factor in PDI utility and versatility is the flexibility in tuning electronic properties using diverse rational substitution patterns. Substitution at the imide nitrogen (R_1 in **Figure 3.1**) greatly enhances solubility and modifies solid-state packing, while substitution at the 1,6,7,12 (bay; R_3) positions tunes both its redox properties and electronic absorption. The wide variety of available PDI core modifications has significant implications for the photophysics of these molecules, which are integral to the operation and optimization of OSCs using non-fullerene electron acceptors. In contrast to the imide and bay substitution, the impact of substituents at the 2,5,8,11 (headland; R_2) positions adjacent to their carbonyl groups on PDI photophysics has been less explored, but the existing literature suggests a promising range of properties. PDIs linked at their headland positions offer increased photovoltaic performance when compared to analogous structures joined at the bay position, owing to smaller domain sizes and decreased aggregation of the π-surface.[42, 43, 50] Headland

substitution has also been shown to suppress excimer formation by promoting slip-stacking between chromophores, a key feature in PDIs that exhibit singlet exciton fission, and has also been shown to directly facilitate this processes, whereas analogous bay-substituted PDIs do not.[23, 51, 52]

In some cases, PDIs are known to undergo symmetry-breaking charge separation (SB-CS), which can be observed when two structurally identical chromophores are positioned in close spatial proximity to one another and the ion pair state is energetically accessible.[53, 54] This process is of interest as a mechanism for enhancing photovoltaic efficiency as a means to increase the open-circuit voltage (V_{oc}).[55] This process has been observed in tetrameric PDI scaffolds that exhibit a strong photovoltaic response, raising the possibility that these dynamics may be active in charge generation.[56]

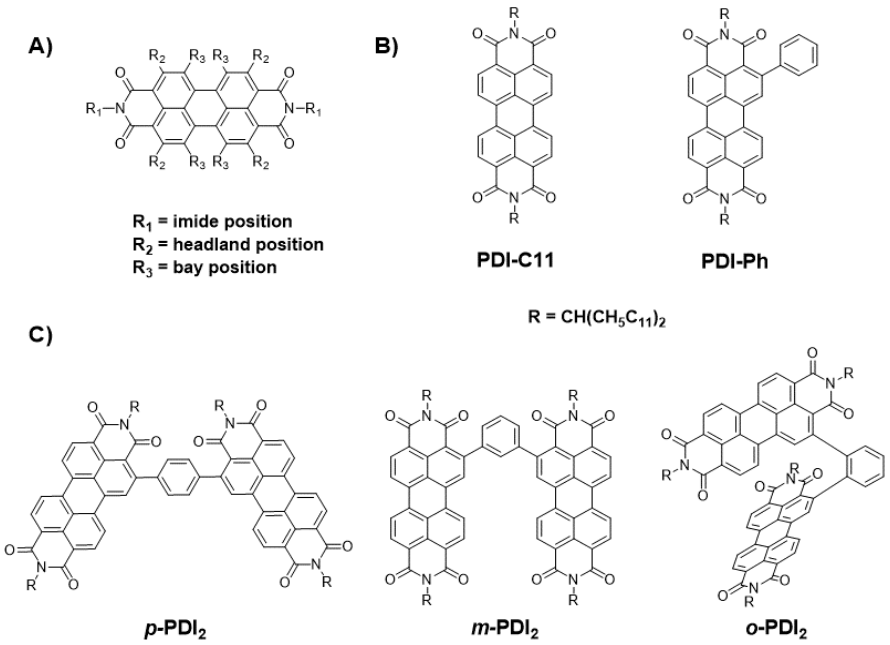

Figure 2.1. A) PDI substituent positions: R_1 = imide, R_2 = ortho/headland, R_3 = bay. B) Molecular structures of PDI and PDI-Ph control compounds. C) Molecular structures of headland-substituted PDI dimers.

Systems in which SB-CS are observed in solution often have significant π-π overlap between chromophores[53, 57-59] controlled by covalent bonding to enforce a face-on configuration of the chromophores and significant *H*-aggregate character observable in their UV-Vis absorption spectra. SB-CS in PDI systems has been observed in architectures with restricted conformations[54] and even in the solid state,[60] though we note that these studies are focused on bay-substituted phenoxy derivatives of PDI, for which this phenomenon is more commonly observed.[53, 54, 57, 61] One notable exception is the observation of SB-CS in a linear PDI dimer observed by Fang, *et al*.[62]

It is important to understand the dynamics of headland-substituted PDI multimers considering their enhanced performance relative to their bay-substituted analogs. In addition, the potential for SB-CS as a charge generation mechanism in photovoltaic cells requires more research to understand this phenomenon. Here we present a comparative study on three PDI dimers linked by a phenyl group at the headland position (**Figure 2.1**). It will be seen that differences in the geometry and electronic coupling of these molecules have a significant impact on their excited-state properties. Sterically encumbered ***o*-PDI$_2$** exhibits SB-CS in a high polarity solvent such as CH_2Cl_2, while the less crowded ***m*-PDI$_2$** and ***p*-PDI$_2$** demonstrate significantly reduced fluorescence quantum yields and long-lived triplet state formation that is accelerated in a polar medium. In non-polar toluene, SB-CS does not occur in ***o*-PDI$_2$**, and the dimer recovers the high fluorescence yield typical of PDI.

2.2. Experimental Section

2.2.1. Materials Synthesis.

PDI-*o*-Ph, ***o*-PDI$_2$**, ***m*-PDI$_2$**, and ***p*-PDI$_2$** were prepared through a synthetic scheme detailed in the Supporting Information (SI).

2.2.2. Electrochemistry.

Reduction potentials for each of the compounds **PDI-*o*-Ph**, ***o*-PDI$_2$**, ***m*-PDI$_2$**, and ***p*-PDI$_2$** were determined by cyclic voltammetry and differential pulse voltammetry, which were performed using a CH Instruments Model 622 electrochemical workstation on 0.5 mM solutions in anhydrous CH_2Cl_2 with 100 mM Bu_4N^+ PF_6^- supporting electrolyte. Measurements were performed using a Pt disc working electrode, Pt wire counter electrode, and Ag wire quasi-reference electrode. Potentials are referenced to ferrocene/ferrocenium as an internal standard and are reported vs. SCE.

2.2.3. Steady-State Optical Characterization.

Absorption spectra were collected on a Shimadzu 1800 spectrophotometer. Steady-state fluorescence spectra were collected on a Horiba Nanolog fluorimeter set to right-angle detection mode. Spectra were collected in 1cm cuvettes with λ_{ex} = 480 nm. Fluorescence quantum yields (Φ_f) were determined by referencing to a rhodamine 6G standard using λ_{ex} = 480 nm.

2.2.4. Computational Details.

All calculations were performed in QChem 5.1 software.[63] Input geometries were constructed in Avogadro software and pre-optimized using MMFF94 force field. DFT optimizations were performed at B3LYP/3-21G level of theory.[64, 65] Due to memory limitations of our hardware and significant increase of computational time we used a 3-21G basis set (memory limitations did not allow us to perform frequency analysis at B3LYP/6-31G(d) level of theory). Absence of imaginary frequencies was used to confirm the ground-state geometries. In the case of ***o*-PDI$_2$**, our numerous attempts to obtain a result free of imaginary frequencies were unsuccessful. We believe that difficulties in reaching the ground-state geometry are associated with the tight packing of the PDI units and alkyl chains in ***o*-PDI$_2$**. Given that the structure of ***o*-PDI$_2$** is very rigid with limited degrees of freedom, we believe that the presence of small imaginary vibrational

frequencies (< 22*i* cm^{-1}) does not significantly alter the structure from the "true" energy minimum and does not significantly affect predictions of electron density distributions over the PDI units in the dimer or indicate the presence of a transition state. To map electron densities, we used single-point calculations at B3LYP/6-31G(d) level. Geometries optimized at B3LYP/3-21G served as starting geometries for single-point calculations. Output files were visualized in IQmol software.

2.2.5. Transient Absorption Spectroscopy.

The experimental femtosecond transient absorption (fsTA) and nanosecond transient absorption (nsTA) apparatus has been previously described.[66, 67] Femtosecond transient absorption spectroscopy (fsTA) was performed using a regeneratively amplified Ti:sapphire laser system operating at 1 kHz to generate 828 nm light. The frequency-doubled 414 nm light was used without further amplification to avoid pump scatter at the spectra regions of interest to excite samples of **PDI-*o*-Ph**, ***o*-PDI$_2$**, ***m*-PDI$_2$**, and ***p*-PDI$_2$** each in toluene and CH_2Cl_2. Solution samples were prepared in 2 mm path length glass cuvettes and degassed with three freeze-pump-thaw cycles. The TA data were subjected to global kinetic analysis to obtain the evolution- and decay-associated spectra and kinetic parameters as described in detail previously.[20] The femtosecond transient infrared (fsIR) absorption spectrometer has also been previously described.[68] Time-resolved IR spectra were acquired following 480 nm excitation generated from the output of a commercial optical parametric amplifier (TOPAS-C, Light-Conversion, LLC). Samples were prepared in variable pathlength cell (Harrick Scientific) with 500 μm spacers to an OD of ~1 at the excitation wavelength and were rastered to reduce the effects of local heating and degradation under visible and mid-infrared irradiation.

2.2.6. Time-Resolved Fluorescence.

Picosecond time-resolved fluorescence (psTRF) data were collected using a Hamamatsu C4780 streak camera described previously.[69] The excitation pulses at 100 kHz were tuned to 530 nm and attenuated to ~1 nJ/pulse to reduce the effects of pump scatter. Data were collected using 1, 20, and 100 ns windows; the instrument response function (IRF) was ~4% of the acquisition window, with the shortest time resolution being 40 ps. The optical density of the samples was ~0.1 at the excitation wavelength in 1 mm cuvettes. All data were acquired in the single-photon counting mode using the Hamamatsu HPD-TA software.

2.3. Results and Discussion

2.3.1. Computational Modeling.

Geometry-minimized structures of the three dimers are given in **Figure 2.2** along with their highest-occupied molecular orbitals (HOMOs). Each structure was computed with the full 5-undecyl tail included to account for the effect of these large groups on the steric crowding surrounding the PDIs. In ***p*-PDI$_2$** and ***m*-PDI$_2$**, there is sufficient space between the PDI units to avoid overcrowding and the individual chromophores maintain their structural rigidity. Additionally, the HOMO is constrained to one PDI and the phenylene spacer unit, and there is negligible electron density on the second PDI unit. Conversely, there is significant electron density located on the second PDI in ***o*-PDI$_2$**, indicating that there is electronic communication between the two PDIs. The energy gaps between the HOMO and lowest unoccupied molecular orbital (LUMO) levels for ***p*-PDI$_2$**, ***m*-PDI$_2$**, and ***o*-PDI$_2$** are 2.50 eV, 2.53 eV, and 2.39, respectively. The LUMO-LUMO+1 gap in ***o*-PDI$_2$**, is 0.11 eV, which corresponds well with the splitting in the reduction potentials observed in the electrochemical experiments described below. This may be a consequence of constructive π-orbital overlap from conjugation through the phenylene spacer that

is maintained by the geometric constraints of the two sterically encumbered PDI units. The dihedral angle between the two planes formed by four oxygen atoms each can serve as a value of core twisting angle. Our calculations indicate that PDI cores in ***o*-PDI$_2$** are twisted by 12° and 23.8°. In contrast, both ***m*-PDI$_2$** and ***p*-PDI$_2$** have significantly smaller values of this angle, as shown in **Figure 2.2**.

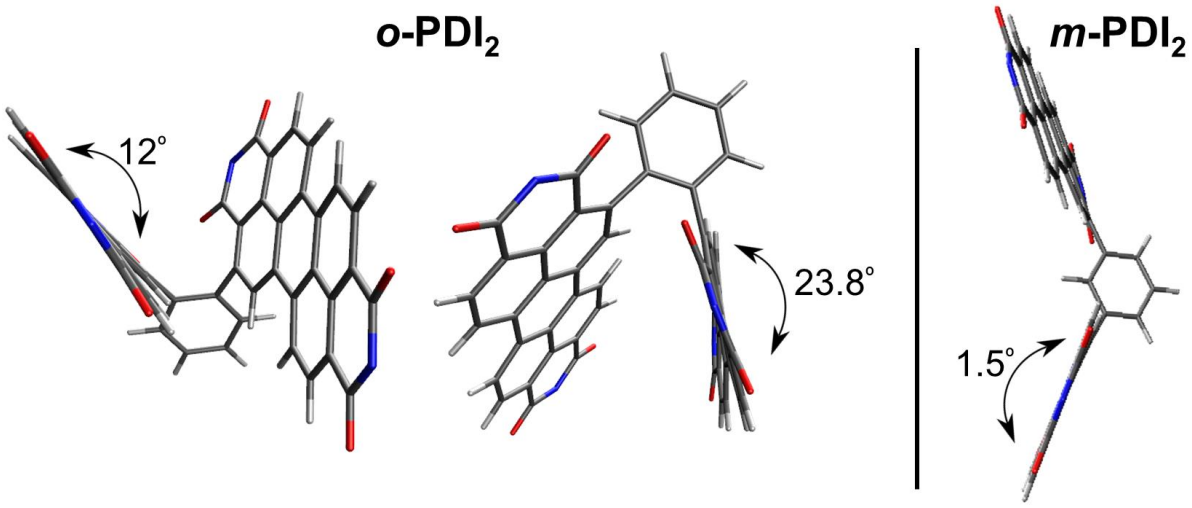

Figure 2.2. Twisting of two PDI cores in ***o*-PDI$_2$** and in ***m*-PDI$_2$** calculated at the B3LYP/3-21G level of theory. Alkyl tails omitted for clarity.

Furthermore, the two PDIs exhibit non-negligible core-twisting from planarity, an unexpected observation in PDIs with no bay-substituents. This twisting likely reflects steric crowding around the two PDI cores, as significant π-π interactions will force the chromophores apart, but their rotational flexibility is very low owing to the 1,2-substitution pattern. Steric repulsions between hydrogens in ***p*-PDI$_2$** are likely to result in minimal orbital overlap as occurs in other flexible aromatic systems with a 1,4-substitution such as biphenyl,[70, 71] while ***m*-PDI$_2$** exhibits the typical weak electronic coupling that occurs in 1,3-disubstituted aromatic systems.[72] In the LUMOs (**Figure 2.47-2.50**), the orbital isolation is maintained in ***p*PDI$_2$** while there is

significant distribution of density across both PDIs in ***m*-PDI$_2$** and ***o*-PDI$_2$**. This has implications for the charge-transfer dynamics, which are discussed below.

2.3.2. Energetics.

2.3.2.1. Steady-State Spectroscopy.

The normalized ground-state absorption spectra of **PDI-*o*-Ph**, ***o*-PDI$_2$**, ***m*-PDI$_2$**, and ***p*-PDI$_2$** provide insight into the influence of headland substitution on the electronic properties of PDI dimers (**Figure 2.3**). Each dimer as well as the **PDI-Ph** reference compound display an absorption spectrum similar to that of *N*,*N*-bis(5-undecyl)-PDI, **PDI-C11**,[73] with ***o*-PDI$_2$**, ***m*-PDI$_2$**, and ***p*-PDI$_2$** maintaining the same 0-0/0-1 vibronic progression. The absorption maxima are separated by only 1-3 nm in all the derivatives and their vibronic ratios are also consistent between these PDIs (**Figure 2.3**, **Table 2.1**).

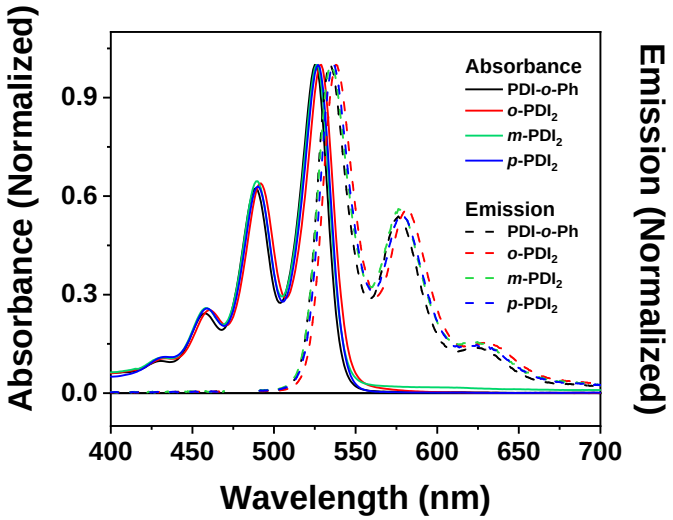

Figure 2.3. Steady-state absorption and emission spectra for all compounds in CH_2Cl_2. Spectra in toluene are provided in the SI.

The invariant nature of the absorption spectra stands in contrast to the bay-substituted analogs of ***p*-PDI$_2$** and ***m*-PDI$_2$** which exhibit decreased vibronic band ratios[74] associated with *H*-aggregates within the Kasha exciton model.[75] Intermolecular aggregation is also disfavored

because the headland-substituted PDI derivatives experience significant twisting between the aromatic core and the substituent aryl group.[76] The absorption spectra in low polarity solvents, such as toluene ($\varepsilon = 2.38$), do not change significantly relative to those in higher polarity CH_2Cl_2 ($\varepsilon = 8.93$), evidence that the ground-state properties of these compounds are relatively insensitive to the polarity of the surrounding solvent bath.

The steady-state emission spectra of **PDI-Ph**, ***p*-PDI$_2$**, ***m*-PDI$_2$**, and ***o*-PDI$_2$** in **Figure 2.3** also confirm the spatial and electronic isolation of the PDIs in these molecules. The emission spectra of each closely mirror the absorption spectra in both toluene and CH_2Cl_2 with the well-defined vibronic band structure suggesting that excimer formation is disfavored.[77] Fluorescence quantum yields (Φ_f) for each PDI in both solvents were determined using rhodamine 6G as a reference[57] and are compiled in **Table 2.1**. Φ_f for **PDI-*o*-Ph** is 0.61 and 0.43 in toluene and CH_2Cl_2, respectively, significantly quenched compared to that of **PDI-C11** ($\Phi_f = 0.99$ in CH_2Cl_2).[78]

The unhindered motion of the phenyl group at the headland position acts as a "loose bolt," which accelerates $S_1 \rightarrow S_0$ internal conversion by coupling nuclear motion to the excited electronic state to kinetically outcompete fluorescence and thus reduce Φ_f.[79] Similarly, Φ_f for ***p*-PDI$_2$** and ***m*-PDI$_2$** in toluene are 0.52 and 0.39, respectively, while in CH_2Cl_2 these values decrease to 0.27 and 0.25, respectively. Indeed, lower Φ_f values are expected in a high polarity solvent due to stabilization of a charge-transfer (CT) contribution to the electronic structure that opens another nonradiative decay pathway, as discussed below, although other solvent effects may also be contributing. The behavior of ***o*-PDI$_2$** is very different, however, with significantly higher quantum yields in both solvents: 1.0 in toluene and 0.85 in CH_2Cl_2. ***o*-PDI$_2$** is therefore likely to exhibit substantially different behavior in the excited state (*vide infra*). The S_1 energy for each compound is listed in **Table 2.1** along with a summary of the steady-state optical data.

Table 2.1. Steady-State Optical Characterization of Headland-Substituted PDIs.

	PDI-*o*-Ph		***o*-PDI$_2$**		***m*-PDI$_2$**		***p*-PDI$_2$**	
	toluene	CH_2Cl_2	toluene	CH_2Cl_2	toluene	CH_2Cl_2	toluene	CH_2Cl_2
$\lambda_{max, abs}$, nm	526	525	531	529	528	526	528	527
$\lambda_{max, em}$, nm	536	534	540	538	537	535	537	536
A_{0-0}/A_{0-1}	1.64	1.61	1.59	1.56	1.65	1.54	1.72	1.59
Φ_f	0.61 ± 0.03	0.43 ± 0.01	1.00 ± 0.03	0.85 ± 0.04	0.39 ± 0.02	0.25 ± 0.05	0.52 ± 0.01	0.27 ± 0.01
E_{00}, eV	2.34	2.34	2.32	2.32	2.33	2.34	2.33	2.33

2.3.2.2 Electrochemistry.

Differential pulse voltammetry (DPV) experiments performed on each derivative reflect the changes in the frontier orbitals of PDI induced by headland substitution. **PDI-*o*-Ph** has a first reduction potential E_{red} = -0.61 V vs. SCE, 60 mV more negative than the parent PDI (E_{red} = -0.55 V vs. SCE),[44] and an oxidation potential of E_{ox} = 1.77 V vs SCE (**Figure 2.8**). The installation of a phenyl group slightly increases the electron density present on the electron-rich perylene core, opposing the electron-withdrawing character of the imide groups which modestly increases the reduction potential. ***m*-PDI$_2$** and ***p*-PDI$_2$** have very similar first reduction potentials of E_{red} = -0.61 V vs. SCE for ***m*-PDI$_2$** and E_{red} = -0.63 V vs. SCE for ***p*-PDI$_2$** (**Figure 2.9-2.11**). The 20 mV difference despite the different substitution patterns is indicative of the electronic isolation between the chromophores. In the case of ***o*-PDI$_2$**, the first and second reduction potentials are split by 90 and 110 mV, respectively, resulting in four peaks at -0.60, -0.70, -0.84, and -0.95 V vs SCE. This splitting agrees with the calculated LUMO-LUMO+1 gap discussed above. Similarly, this splitting is consistent with that of other PDI derivatives and demonstrates significant electronic coupling resulting from spatial overlap;[44, 80] however, the steady-state absorption spectra indicate that there is no *H*-aggregate character that often accompanies such splittings. Changes in the

absorption spectra arise from dipolar coupling of the transition dipole moments, which is a through-space interaction, as well as orbital overlap, which can occur through-space or through-bond. We rule out the possibility of a null-aggregate since the same behavior is observed for each dimer despite the difference in transition dipole distance and orientation. The steric constraints intrinsic to ***o*-PDI$_2$** necessitate that the electronic coupling between PDIs be driven by through-bond interactions, such as charge-transfer coupling.[53, 81, 82] Importantly, the splitting of the ***o*-PDI$_2$** LUMO levels implied by the DPV results can impart additional driving force for symmetry-breaking charge separation (*vide infra*), although from the measured reduction potentials this enhancement would be on the order of only an additional -10 meV.

2.3.3. Excited-State Dynamics.

2.3.3.1. Transient Absorption Spectroscopy.

Femtosecond transient absorption (fsTA) and nanosecond transient absorption (nsTA) spectroscopies were employed to characterize the excited-state dynamics of the present PDI derivatives. TA spectra at several pump-probe delay times are early times are shown for **PDI-Ph**, ***p*-PDI$_2$** and ***m*-PDI$_2$** following photoexcitation at 414 nm in CH_2Cl_2 (**Figure 2.4**). With no additional PDI present, reference compound **PDI-Ph** displays ground-state bleach (GSB) features present at 440-530 nm, while stimulated emission (SE) is observed at 580 and 633 nm. Excited-state (ESA) extends broadly from 630-1030 nm with diminished absorption tailing out to the end of the experimental window at 1500 nm. The weak absorption in the near-infrared can be attributed to a small intermolecular excimer contribution, a relatively common phenomenon in sterically unencumbered PDI derivatives.[83]

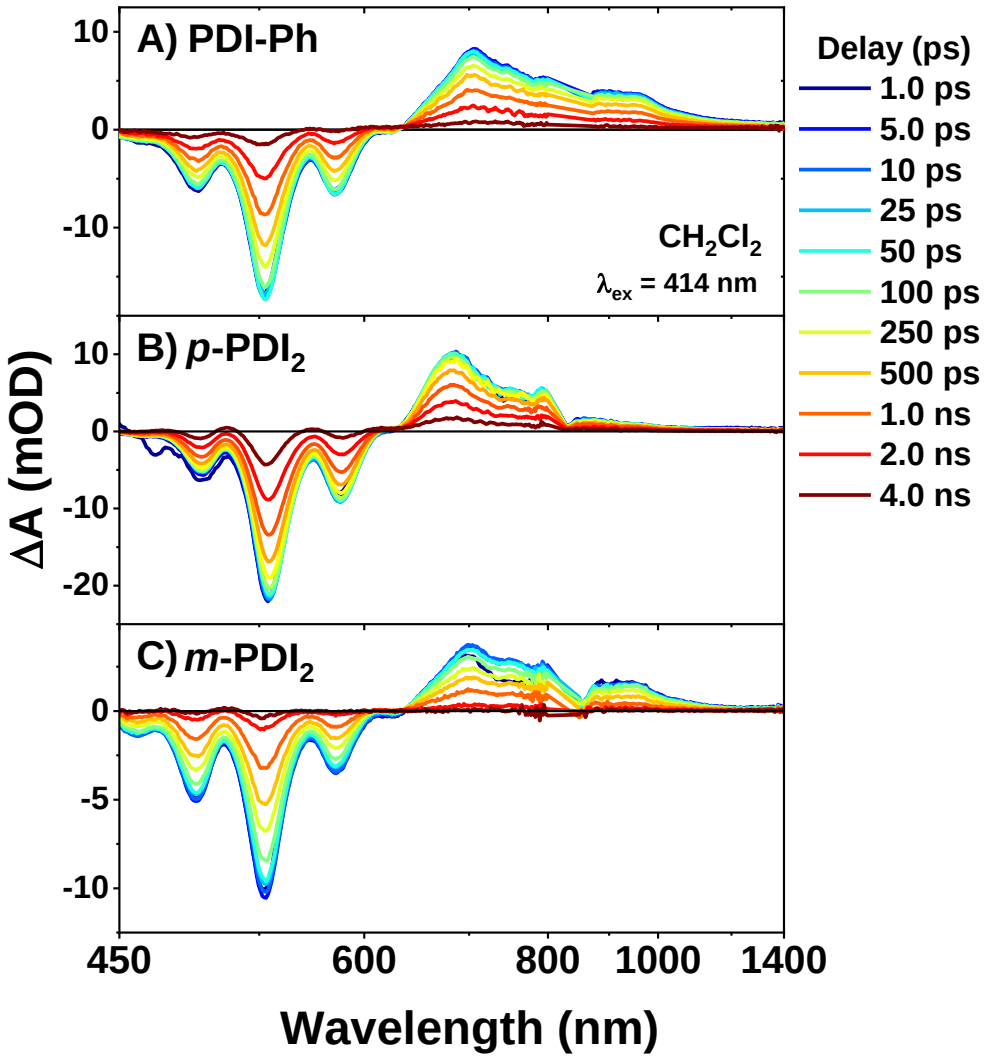

Figure 2.4. fsTA spectra for A) **PDI-Ph** 2, B) ***p*-PDI2**, and C) ***m*-PDI2** in CH_2Cl_2 following λ_{ex} = 414 nm, 1 μJ/pulse, ~100 fs excitation.

In CH_2Cl_2, global analysis of the fsTA data set at selected wavelengths yields a two-state model, A → B → GS. The A → B process is assigned to the decay of the singlet excited state with a lifetime τ_1 = 1.5 ns, a further shortening of the ^{1*}PDI lifetime from what is observed in toluene. A second process B → GS shows a weak spectral profile with bleach features at 484 nm and 523 nm and a broad positive feature spanning 600 nm to 800 nm that exists past the 7 ns experimental time window; these are spectral features generally associated with the triplet state[84] of PDI, ^{3*}PDI.

This assignment is confirmed by the existence of a long-lived species with the same key features at 484, 523 and 600-800 nm following the decay of ^{1*}PDI. The presence of an additional transient species is supported by a change in Φ_f, which is ~20% lower in CH_2Cl_2 than in toluene. The transient absorption data for **PDI-Ph** in toluene are similar (**Figure 2.14)** and the kinetics are well-described by a single exponential decay with τ_1 = 2.4 ns, which is significantly shorter than that of **PDI-C11** (τ_1 = 4.5 ns) owing to the loose bolt effect discussed above.

In ***m*-PDI$_2$** and ***p*-PDI$_2$** the photophysics of the excited state behave somewhat differently. (**Figure 2.4**) The general transient spectral features (GSB, SE and ESA) are all consistent with what is observed for **PDI-Ph**, although notably the near-infrared region past 1000 nm is devoid of the weak positive absorption present for **PDI-Ph**. As noted above, the highly twisted structure and steric bulk of these dimers minimizes the potential for the aggregation required for excimer formation, even at the concentrations used in TA experiments. The lifetime of ^{1*}PDI is shortened relative to that of the reference compound, with τ_1 = 731 ps in CH_2Cl_2 and τ_1 = 1.3 ns in toluene for ***m*-PDI$_2$** and τ_1 = 863 ps in CH_2Cl_2 and τ_1 = 1.9 ns in toluene for ***p*-PDI$_2$**. In contrast to the monomer, the evolution-associated model shows that ***m*-PDI$_2$** and ***p*-PDI$_2$** have two kinetic components in both solvents and the spectra at long times indicate the presence of ^{3*}PDI in both cases (**Figure 2.4, Figure 2.15-2.18**). The fluorescence quantum yields in these compounds (**Table 2.1**) are lower than those of **PDI-*o*-Ph** which is consistent with the formation of ^{3*}PDI in both solvents. Interestingly, the spectral features attributed to ^{3*}PDI are evident in both low polarity toluene and high polarity CH_2Cl_2. This suggests a mechanism that does not directly involve a charge-transfer intermediate, which is disfavored in a low polarity solvent. It is possible that the shorter S_1 lifetimes observed in ***p*-PDI$_2$** and ***m*-PDI$_2$** are the result of SB-CS wherein the charge recombination time is significantly shorter than the separation time. This would result in the

formation of a triplet product state but no observable population of the SB-CS intermediate. However, there is no evidence from the DPV data that the PDI units possess strong enough coupling for rapid and efficient SB-CS in ***p*-PDI$_2$** and ***m*-PDI$_2$**. Without lowering the acceptor energy levels, the free energy for SB-CS is likely also insufficient, especially in a non-polar solvent.

The time-resolved spectra of ***o*-PDI$_2$** are considerably different (**Figure 2.5)**. Following photoexcitation at 430 nm in CH_2Cl_2, the growth of ^{1*}PDI features is accompanied by two additional peaks at 605 nm and at 950 nm. The feature at 950 nm is representative of PDI$^{\bullet-}$, suggesting the formation of an ion pair species. [80] The lack of an obvious electron donor species implies formation of PDI$^{\bullet+}$, which we assign to the peak at 605 nm. While this species is rarely observed in prototypical PDI, a similar feature appears in a tetraphenoxy PDI investigated extensively by Würthner and co-workers.[85-87] These features are prominent in the spectrum obtained in CH_2Cl_2 but not in that obtained in toluene, supporting the formation of a radical ion pair stabilized in the polar solvent. Femtosecond transient infrared absorption experiments also support the assignment of SB-CS (**Figure 2.30**) [44, 57, 68]. Importantly, the splitting of the acceptor levels observed in the DPV experiment shows that the electrochemical bandgap may indeed be lower than the optical energy gap, which is a necessary condition for SB-CS.[53] Global analysis of this dataset identifies τ_1 = 9.3 ps, indicating that charge separation occurs rapidly in this system (**Figure 2.19**). The lifetime of the PDI$^{\bullet+}$-PDI$^{\bullet-}$ ion pair state persists past the experimental window. nsTA measurements in CH_2Cl_2 (**Figure 2.28**) show that this state has an 11 ns lifetime before

recombining primarily to the ground state, although with a small amount of triplet product.

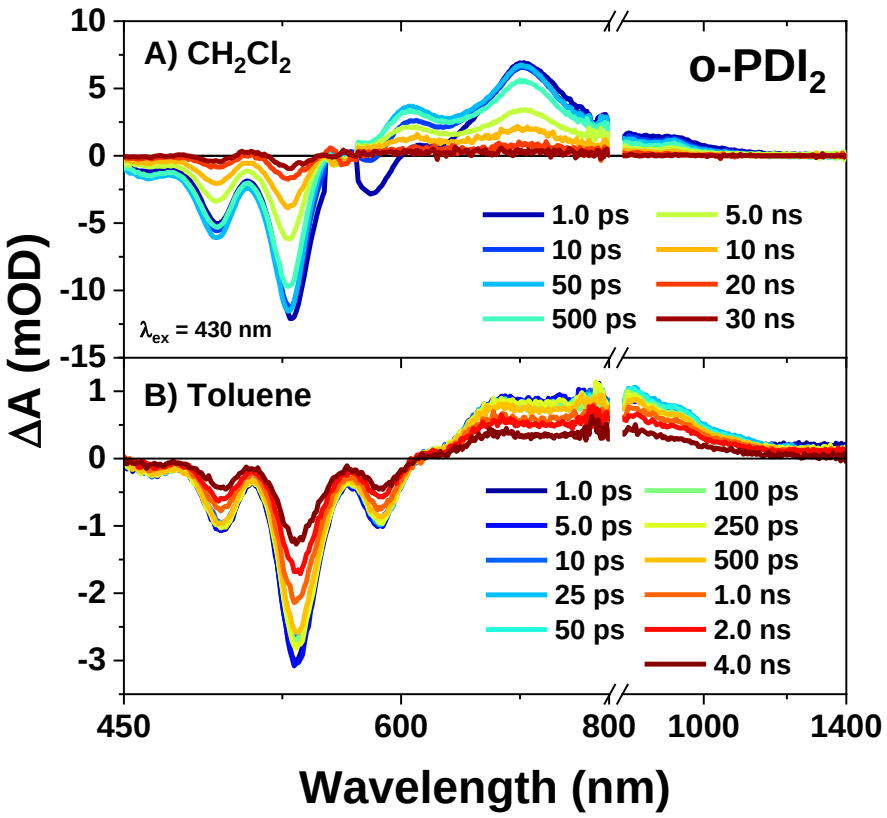

Figure 2.5. fsTA spectra for ***o*-PDI$_2$** in A) CH_2Cl_2 and B) toluene following λ_{ex} = 430 nm, 0.5 μJ/pulse, ~100 fs excitation.

To the best of our knowledge, this is one of the first observations of a transiently formed $PDI^{\bullet+}$- $PDI^{\bullet-}$ species in a headland-substituted PDI derivative. Interestingly, such a fast timescale for singlet excited state deactivation should fully quench the fluorescence; however, Φ_f = 0.85. The similarity in optical and electrochemical bandgaps implies that the singlet excited state and the SB-CS state are nearly isoenergetic in CH_2Cl_2, and that recombination to repopulate the excited state is favorable, leading to delayed emission. This idea is explored in detail below.

In marked contrast, the ***o*-PDI$_2$** excited state in toluene (**Figure 2.12B**) exhibits a simple monoexponential decay from ^{1*}PDI with τ_1 = 4.6 ns, comparable to the excited-state lifetime of

PDI-C11 (τ_1 = 4.5 ns). This correlates well with the high ***o*-PDI$_2$** fluorescence quantum yield in toluene (Φ_f = 1), such that ***o*-PDI$_2$** behaves similarly to **PDI-C11**, underscoring the instability of the ion pair state in a low polarity environment, although note that this is not always the case.[57, 60] The nsTA spectra (**Figure 2.20**) show no evidence of triplet formation in toluene, again in analogy to **PDI-C11**. The TA evolution-associated global analysis results are summarized in **Table 2.2**.

Table 2.2. Time Constants from Evolution-Associated Global Analysis of TA Data.

Evolution-Associated Model							
	τ (ps) in CH_2Cl_2			**τ (ps) in toluene**			
PDI-Ph	1500 ± 10			2400 ± 15			
***p*-PDI$_2$**	860 ± 10			1900 ± 40			
***m*-PDI$_2$**	731 ± 5			1300 ± 40			
***o*-PDI$_2$**	τ_1: 9.3 ± 0.3 τ_2: 10800 ± 20			4600 ± 40			
Species-Associated Model in CH_2Cl_2							
	τ_{CS} (ps)	**τ_{CS} (ps)**	**τ_{CR-S} (ns)†**	**τ_{CR-T} (ns)†**	***K***	**ΔG_{CS} (meV)**	**Φ_T**
***o*-PDI$_2$**	14.5	26	119	78	1.8	-15	0.09

† Constrained to $k_{CR-S} + k_{CR-T} = (47\ ns)^{-1}$

2.3.3.2. Time-Resolved Fluorescence Spectroscopy.

Picosecond time-resolved fluorescence (psTRF) experiments provide additional insight into the behavior of the excited state, and in particular the delayed emission predicted for ***o*-PDI$_2$** in CH_2Cl_2. The emission lifetimes obtained from this experiment for **PDI-Ph**, ***p*-PDI$_2$** and ***m*-PDI$_2$** (**Figure 2.31-2.44**) match those obtained from the transient absorption experiments and spectra are provided in the SI. For ***o*-PDI$_2$** in toluene, a single exponential decay with τ = 5.0 ns is observed (**Figure 2.45**), while in CH_2Cl_2 there are two processes, one instrument-limited (<40 ps) and the other having a lifetime τ = 10 ns (**Figure 2.5**). The first process in CH_2Cl_2 corresponds to the charge transfer event, while the second time constant agrees well with that of charge recombination determined in the nsTA experiment. Importantly, the 10 ns component dominates the emission decay and exhibits the same structured spectrum observed in the steady-state fluorescence

experiment; there is no observable spectral evolution. This implies that the longer emission component also originates from the singlet excited state following recombination from the SB-CS state.

2.3.4. Symmetry-Breaking Charge Separation Mechanism.

Differences in the transient spectra of these compounds are noteworthy given their nearly identical steady-state optical properties. Interchromophore coupling is the principal effect underlying these differences in most cases, although from the molecular structure of these compounds such differences are not readily apparent. Interchromophore coupling may arise either from transition dipole interactions or significant mixing of π orbitals,[84, 88] though neither is readily apparent in ***o*-PDI$_2$** given that the large solubilizing groups at the imide N atoms and significant twist angle should prevent significant intramolecular overlap between the PDI units.

The arrangement of individual molecules necessary for this coupling is similar in both covalently linked dimers as well as in ordered aggregates.[89] The observation of SB-CS in ***o*-PDI$_2$** is additionally intriguing given that the electrochemical measurements indicate a similar propensity for charge separation, i.e., similar electrochemical and optical bandgaps. This implies that the electronic coupling between the PDI units in ***o*-PDI$_2$** is sufficiently strong to promote efficient SB-CS. As discussed above, this coupling is most likely a through-bond interaction utilizing the σ orbitals of the *o*-phenylene spacer given that the spacer π orbitals are nearly orthogonal to those of the two PDIs.

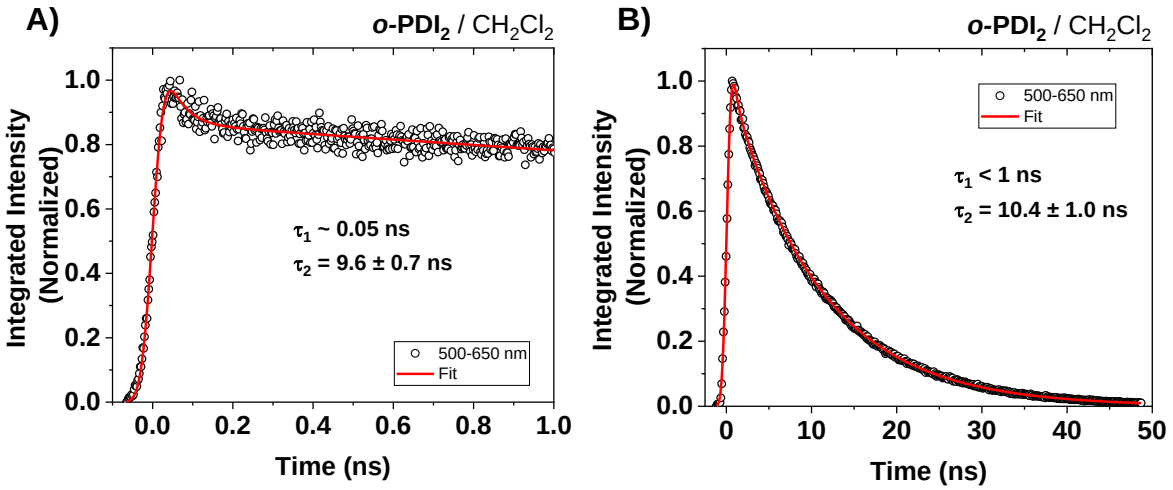

Figure 2.6. A) 1 ns and B) 100 ns picosecond TRF (psTRF) fits for ***o*-PDI$_2$** in CH_2Cl_2 following λ_{ex} = 480 nm, 1 nJ/pulse, ~50 fs excitation.

This is visualized clearly in the orbital maps of **Figures 2.46-2.49**, in which the electron density is shared between PDIs rather than being confined to a single PDI unit in both frontier orbitals. The core distortions may also be a key prerequisite for observing symmetry-breaking charge separation. Such twisting may break the electronic symmetry of the system *in the ground state*, effectively energetically favoring one of the PDI units prior to absorption of the photon.

The energy of the SB-CS state is difficult to accurately estimate using the method proposed by Weller,[44] as the approximations upon which that equation is formulated are not valid for closely interacting π surfaces such as those considered here.[57, 90] We can infer, however, that the SB-CS state is nearly the same energy as the singlet excited state by comparison of the optical and electrochemical bandgaps. This near-degeneracy has important consequences for the dynamics of ***o*-PDI$_2$**, since, as discussed above, the rapid charge separation observed in the fsTA data would suggest a low fluorescence quantum yield. The relatively high yield (Φ_f = 0.85) and agreement with the psTRF data imply that the SB-CS state can repopulate the highly emissive S_1 state, which can subsequently undergo further, repeated reversible charge separation. This situation will result in fluorescence with the same salient features observed in the psTRF data, namely the same

spectrum as the monomer and the same lifetime as the SB-CS state observed by TA spectroscopy. Coleman *et al.*[57] and others[91] have modeled the dynamics of reversible SB-CS. Using the data presented here, we can construct the same model and determine the rates of forward and backward charge transfer (k_{CS} and k_{-CS}, respectively), recombination to the ground state (k_{CR-S}) and to the triplet state (k_{CR-T}). The energy levels and rate processes are shown schematically in **Figure 2.6**.

Importantly, this model predicts that the fluorescence quantum yield of the dimer can be *at most* equal to that of the monomer, which is not satisfied by the **PDI-Ph** control compound. The significantly higher quantum yield of ***o*-PDI$_2$** in toluene and CH_2Cl_2 and the lifetime in toluene suggest that **PDI-Ph** undergoes a fast deactivation process that is not present in ***o*-PDI$_2$**. It is likely that the loose bolt effect of the phenyl substituent in **PDI-Ph** is not present in the *ortho*-linked dimer due to the steric crowding of the closely spaced PDIs. Eliminating this degree of conformational freedom greatly reduces the internal conversion rate ($k_{IC} = k_{eff}(1-\Phi_f)$, where $k_{eff} = 1/\tau_{eff}$ is the effective rate of decay): in toluene $k_{IC} = (2.6\ \text{ns})^{-1}$ in **PDI-Ph**, compared to $k_{IC} \sim 0$ for ***o*-PDI$_2$** due to the unity fluorescence quantum yield. Additionally, the small degree of core twisting in ***o*-PDI$_2$** will slightly alter the energetics and instantaneous symmetry of the PDIs of the dimer compared to the **PDI-Ph** monomer. Conversely, as discussed above, ***o*-PDI$_2$** in toluene behaves almost identically to **PDI-C11**.

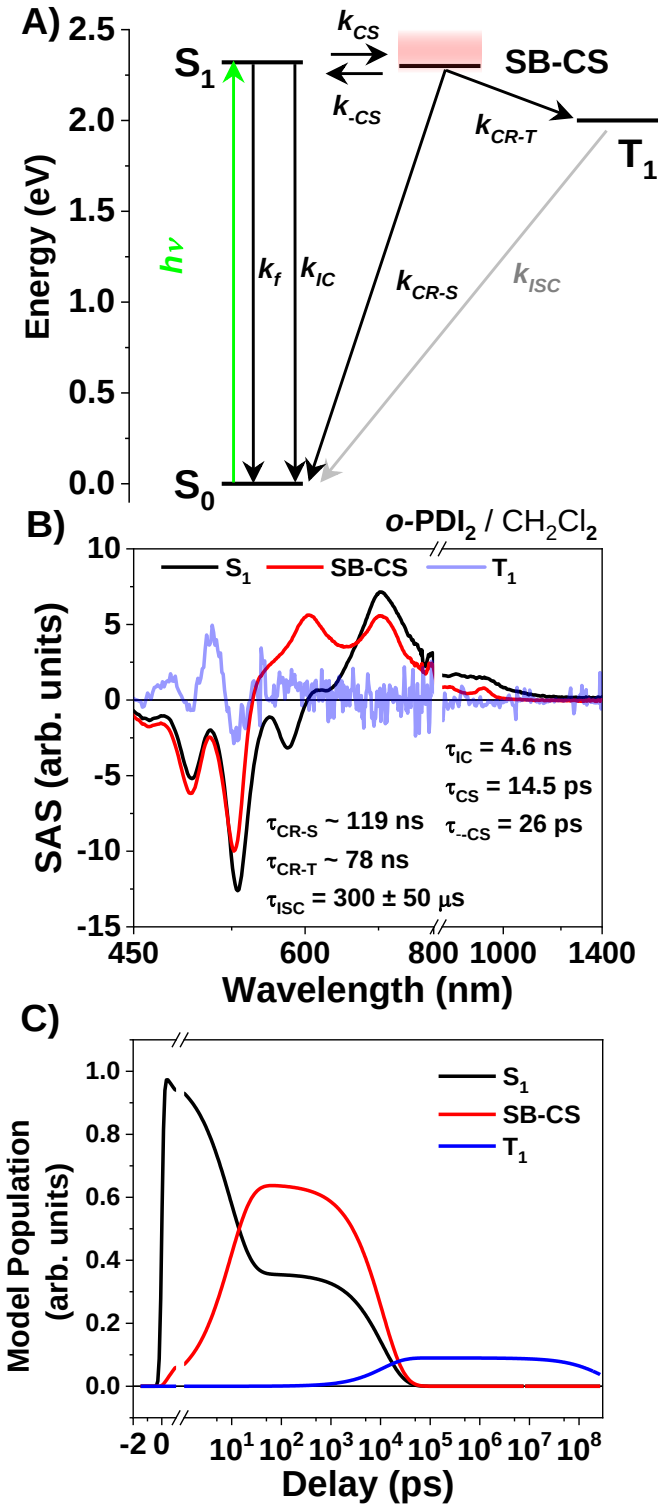

Figure 2.7. A) Jablonski diagram of the pseudoequilibrium dynamics of ***o*-PDI$_2$** in CH_2Cl_2. B) Species-associated spectra. C) Model populations for the pseudoequilibrium kinetic scheme. $\tau = 1/k$ for lifetimes given in **Table 2.2**.

Therefore, to model the reversible SB-CS dynamics in ***o*-PDI$_2$** in CH_2Cl_2, we use ***o*-PDI$_2$** in toluene as an effective monomer, since the emission spectrum, yield, and decay profile all suggest the emission is localized on one PDI unit within the dimer. However, the reference compound does give insight into the dynamics of the other dimers, as detailed below.

Using the ***o*-PDI$_2$** data in toluene as a surrogate for the monomer, we can extract approximate values for the rate constants. As shown in **Table 2.2**, $k_{CS} = (14.5\ ps)^{-1}$ and $k_{-CS} = (26\ ps)^{-1}$, while $k_{CR\text{-}S}+k_{CR\text{-}T} = (47\ ns)^{-1}$. The pseudoequilibrium constant $K = k_{CS}/k_{-CS} = 1.8$ is consistent with the features in the fsTA spectrum, notably the partial coexistence of features of the SB-CS state and the singlet excited state, such as the stimulated emission feature near 580 nm. This implies a free energy change for SB-CS of $\Delta G_{CS} = -15$ meV, which is in good agreement with the ~10 meV shift in the first DPV reduction potential. The fast forward electron transfer rate in the absence of a large free energy change implies a strong, through-bond CT coupling between the two PDI units, as supported by **Figure 2.11**. The observed SB-CS state lifetime, and thus the observed emission lifetime, will be determined by $S_1 \rightarrow S_0$ internal conversion, fluorescence, and charge recombination to the ground and triplet states. The model predicts the sum of the singlet ground- and triplet-state recombination rates to be $k_{CR\text{-}S}+k_{CR\text{-}T} = (47\ ns)^{-1}$. This total rate constant is small likely due to the modest spin-orbit coupling to the triplet state, and the large free energy change for recombination to the ground state (~2.31 eV), which is firmly in the Marcus-inverted regime.[92, 93] As discussed above, the internal conversion rate of the ^{1*}PDI state in the dimer was taken here to be 0. With such a slow recombination to the ground (and triplet) states and without internal conversion, the energy is effectively trapped between the S_1 and SB-CS states, leaving only emission as a viable decay pathway, ultimately giving rise to the high fluorescence quantum yield of ***o*-PDI$_2$** in CH_2Cl_2. The triplet yield can be estimated from the model by using the values above

and constraining $k_{CR\text{-}S}+k_{CR\text{-}T} = (47\ ns)^{-1}$ while freely varying $k_{CR\text{-}T}$.[57] This method gives values of $k_{CR\text{-}S} \sim (119\ ns)^{-1}$ and $k_{CR\text{-}T} \sim (78\ ns)^{-1}$, with a corresponding triplet quantum yield of $\Phi_T = 0.09$. This small yield is in good agreement with the low-amplitude $T_n \leftarrow T_1$ absorption in the nsTA spectra.

These parameters can be used to construct species-associated spectra and populations for the true S_1, SB-CS, and T_1 states of ***o*-PDI$_2$** in CH_2Cl_2 (**Figure 2.8B-2.8C**). These spectra show better separation of the stimulated emission and the $PDI^{\bullet+}$ absorption near 600 nm, as well as providing population kinetics for the S_1 state that accurately reflect the time-resolved emission data. The resultant T_1 species-associated spectrum also shows an amplitude more commensurate with the extinction coefficient of the ^{3*}PDI.[51] The slow reverse electron transfer to S_1 compared to those of SB-CS states in substituted PDI cyclophanes is likely a consequence of the smaller free energy change. For example, in a cyclophane consisting of two cofacial tetraphenoxy-substituted PDIs spaced by 6.4 Å, SB-CS occurs in τ_{CS} = 24 ps, comparable to ***o*-PDI$_2$**, and with a free energy change of -70 meV; however, reverse electron transfer in that system was considerably slower than in ***o*-PDI$_2$**, about 450 ps, because of the larger barrier for charge recombination to the excited state.[57]

Note that the high ***o*-PDI$_2$** fluorescence quantum yield and long lifetime may arise from radiative recombination of the SB-CS state, which will be at nearly the same energy as the direct fluorescence. However, the 10 ns emission spectrum in CH_2Cl_2 strongly resembles monomeric ^{1*}PDI fluorescence, which implies that the emitting state shares a similar geometry with the singlet excited state. Radiative recombination in organic systems is often weak, even from charge-separated states formed in high yield, and changes in the geometry between the S_1 and SB-CS states will alter the Franck-Condon factors and broaden the emission spectrum;[94] both of these

qualities contrast the strong, structured emission spectrum observed in ***o*-PDI$_2$**. Lastly, excited-state behavior of ***o*-PDI$_2$** in toluene in the absence of SB-CS also suggests that the origin of the emission is from a localized PDI excited state and not due to radiative recombination. These considerations argue that the excited-state equilibrium mechanism is the most likely for the dynamics of ***o*-PDI$_2$** in CH_2Cl_2.

2.3.5. Triplet Formation Mechanisms.

Given the inherently low triplet yield from intersystem crossing in PDI (<1%), it is clear from the fsTA data that the interaction of the two PDI units enhance triplet formation in ***p*-PDI$_2$** and ***m*-PDI$_2$**. The relatively slow time constants for the appearance of ^{3*}PDI are sufficient to discount singlet exciton fission as a triplet formation mechanism. Previous studies of rylene dye derivatives have shown intersystem crossing may results from the radical pair (RP-ISC) or spin-orbit charge-transfer (SOCT-ISC) mechanisms.[95-97] However, in ***p*-PDI$_2$** and ***m*-PDI$_2$**, there is no direct evidence for ion pair state formation, so that RP-ISC and SOCT-ISC are not operative here. The PDI chromophores in ***p*-PDI$_2$** and ***m*-PDI$_2$** have far more conformational freedom about the single bonds joining them to their phenylene spacers than does ***o*-PDI$_2$**. Furthermore, the ^{3*}PDI formation rate is faster than those of constrained PDI dimer systems ($\leq$ 1 ns), which are generally observed to occur on the order of 5-20 ns.[44] The acceleration of those rates in the more polar CH_2Cl_2 suggest that solvent polarity plays a role in this process. Previous studies have proposed an SO-ISC mechanism in which the virtual $PDI^{\bullet+}$-$PDI^{\bullet-}$ state mixes with the singlet excited state ^{1*}PDI, providing a pathway for the transfer of spin angular momentum necessary to facilitate ISC.[84] Increasing solvent polarity would then lower the energy of this virtual CT state increasing its degree of mixing with the S_1 state, thereby accelerating the rate of SO-ISC. Such mixing has been proposed in other PDI dimers in which SB-CS has been observed.[53] The core twist imparted

by the headland substitution may also lead to enhanced intersystem crossing.[98] Such "twist-induced" ISC has been reported previously for core-fused PDI derivatives leading to unexpected triplet formation,[99] and may explain the very weak triplet features observed at long times in the **PDI-Ph** transient absorption data. The rate of this enhanced ISC must still be very slow compared to those of both fluorescence and internal conversion, as the observed triplet yield is very low.

2.4. Conclusions.

The photophysics of a series of PDI dimers covalently linked at their headland positions using phenylene linkers has been explored. Time-resolved absorption and fluorescence experiments demonstrate SB-CS in sterically constrained ***o*-PDI$_2$**, while ***m*-PDI$_2$** and ***p*-PDI$_2$** exhibit diminished fluorescence quantum yields due to rapid internal conversion and formation of the triplet state through intersystem crossing. The absence of steric crowding in ***p*-PDI$_2$** and ***m*-PDI$_2$** results in transient dynamics resembling the monomeric reference compound **PDI-Ph**, highlighting the loose bolt effect that drives internal conversion and deactivation of the emissive excited state. The rotational flexibility of the phenyl group in **PDI-Ph** makes this derivative a less than ideal benchmark for the charge-separation dynamics in ***o*-PDI$_2$**. Structural distortion of ***o*-PDI$_2$** indicated by computational modeling and splitting of the reduction potentials accounts for the unusual charge separation behavior in ***o*-PDI$_2$**, which is shown to be in pseudo-equilibrium with the singlet excited state, underlying the high fluorescence quantum yield. This process is inaccessible in low polarity toluene as no ion-pair features are observable. These results highlight the utility of headland substitution in tuning the excited-state properties in PDIs and will inform future molecular designs of non-fullerene electron acceptors for use in OSCs.

2.5. Supplementary Information

2.5.1. Materials Synthesis

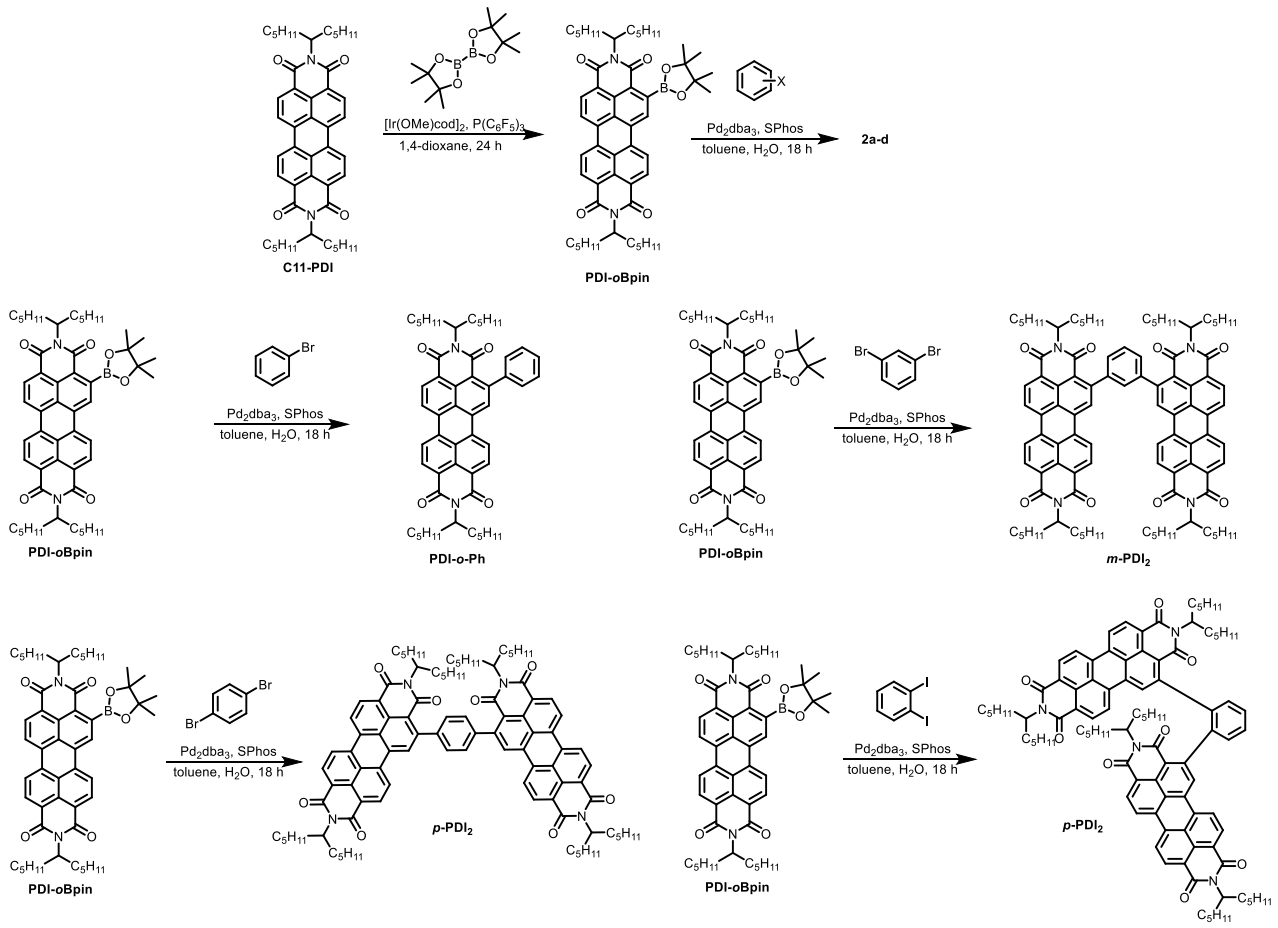

Scheme 2.1. Synthetic scheme of compounds used in this study.

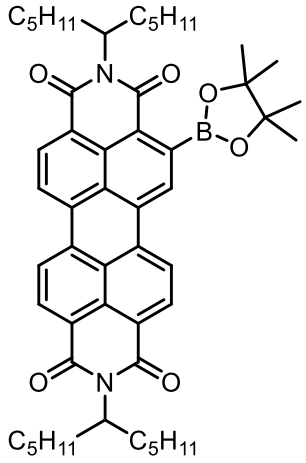

PDI*o*Bpin: PDI*o*Bpin was synthesized according to a modified literature procedure.[100]

To a 300 mL pressure vessel charged with a magnetic stir bar were added **PDI-C11** (2.00 g, 2.86 mmol), bis(pinacolato)diboron (1.25 g, 5.72 mmol), and tris(pentafluorophenyl)phosphine (183 mg, 0.343 mmol). The vessel was then brought into a nitrogen atmosphere glovebox and $[Ir(OMe)cod]_2$ (3 mol %, 57 mg, 0.858 mmol) and dry 1,4-dioxane (72 mL) were added. The vessel was then sealed and removed from nitrogen atmosphere. The reaction was then stirred at 110 ^{o}C for 24 h, after which the reaction mixture was cooled and the solvent was removed *in vacuo*. Column chromatography (silica gel, toluene) afforded **1** as a dark red solid (445 mg, 19%). Spectral data were in agreement with previously reported data.[100]

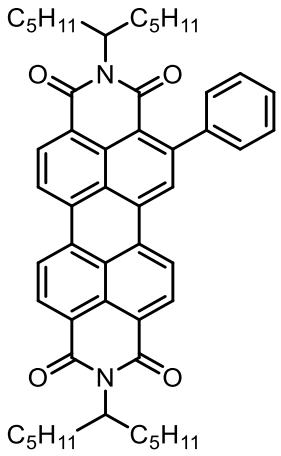

PDI*o*Ph: To a 25 mL round-bottom flask charged with a magnetic stir bar were added bromobenzene (25 mg, 0.159 mmol, 0.017 ml), **PDI*o*Bpin** (138 mg, 0.167 mmol), Na_2CO_3 (169 mg, 1.59 mmol), toluene (19 mL), and H_2O (2 mL). The reaction mixture was stirred and bubbled for 15 min with N_2. Pd_2dba_3 (3 mol%, 4.4 mg, 0.005 mmol) and SPhos (3.4 mg, 0.01 mmol) were added and the reaction mixture was bubbled with N_2 for an additional 5 min. The reaction was then stirred at 85 ^oC for 18 h, cooled to rt, diluted into toluene, and washed with sat. $NaHCO_3$. The organic layer was collected, dried over anhyd. Na_2SO_4, filtered, and the solvent was removed *in* vacuo. Column chromatography (silica gel, 75% CH_2Cl_2 in hexanes) afforded **PDI*o*Ph (**72 mg, 59 %) as a dark red solid. ^1H NMR (500 MHz, $CDCl_3$): δ 8.77-8.57 (m, 6H) 8.44 (s, 1H) 5.23-5.14 (m, 1H) 5.13-4.95 (m, 1H) 2.29-2.05 (m, 4H) 1.90-1.70 (m, 4H) 1.39-1.18 (m, 24H) 0.83 (t, *J* = 6.7 Hz). ^{13}C NMR (125 MHz, $CDCl_3$): δ 164.73, 164.65, 163.6, 163.4, 148.3, 147.9, 146.8, 146.5, 142.1, 142.0, 140.8, 140.6, 134.7, 134.3, 133.2, 131.9, 131.1, 130.6, 129.6, 128.4, 128.0, 127.9, 126.5, 126.0, 124.0, 123.9, 123.13, 123.06, 122.9, 54.8, 32.3, 32.1, 31.8, 29.7, 26.62, 26.57, 22.59, 22.56, 14.06, 14.04. ESI HRMS *m*/*z* calcd. for $C_{52}H_{59}N_2O_4$ $(M + H)^+$ 775.4469, found: 775.4469.

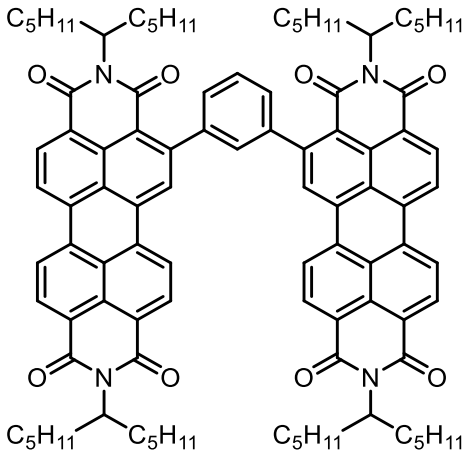

***m*PDI$_2$:** To a 25 mL round-bottom flask charged with a magnetic stir bar were added 1,3-dibromobenzene (20 mg, 0.085 mmol, 0.01 ml), **PDI*o*Bpin** (147 mg, 0.178 mmol), K_2CO_3 (117 mg, 0.848 mmol) toluene (10 mL), and H_2O (1 mL). The reaction mixture was stirred and bubbled for 15 min with N_2. Pd_2dba_3 (6 mol%, 4.7 mg, 0.005 mmol) and SPhos (4.2 mg, 0.01 mmol) were added and the reaction mixture was bubbled with N_2 for an additional 5 min. The reaction was then stirred at 85 ^oC for 18 h, cooled to rt, diluted into toluene, and washed with sat. $NaHCO_3$. The organic layer was collected, dried over anhyd. Na_2SO_4, filtered, and the solvent was removed *in* vacuo. Column chromatography (silica gel, gradient 50-60% CH_2Cl_2 in hexanes) afforded ***m*PDI$_2$ (**70 mg, 56%) as a dark red solid. ^1H NMR (500 MHz, $C_2D_2Cl_4$): δ 8.80-8.59 (m, 14H) 7.82-7.75 (m, 1H) 7.74-7.62 (m, 2H) 7.61-7.55 (s, 1H) 5.20-5.12 (m, 2H) 5.11-5.04 (m, 1H) 5.03-4.89 (m, 1H) 2.27-2.11 (m, 8H) 1.93-1.89 (m, 8H) 1.43-1.10 (m, 48H) 0.85 (t, *J* = 6.3 Hz). ^{13}C NMR (125 MHz, $CDCl_3$): δ 164.7, 164.3, 163.6, 163.3, 147.8, 147.2, 141.9, 141.7, 134.5, 134.4, 134.2, 131.8, 131.2, 130.6, 129.6, 128.4, 128.2, 127.7, 126.5, 126.0, 124.0, 123.3, 123.1, 122.9, 120.9, 120.2, 54.8, 32.3, 31.7, 26.6, 22.5, 14.0. ESI HRMS *m*/*z* calcd. for $C_{94}H_{110}N_4O_8Na$ $(M + Na)^+$ 1472.8249, found: 1494.8206.

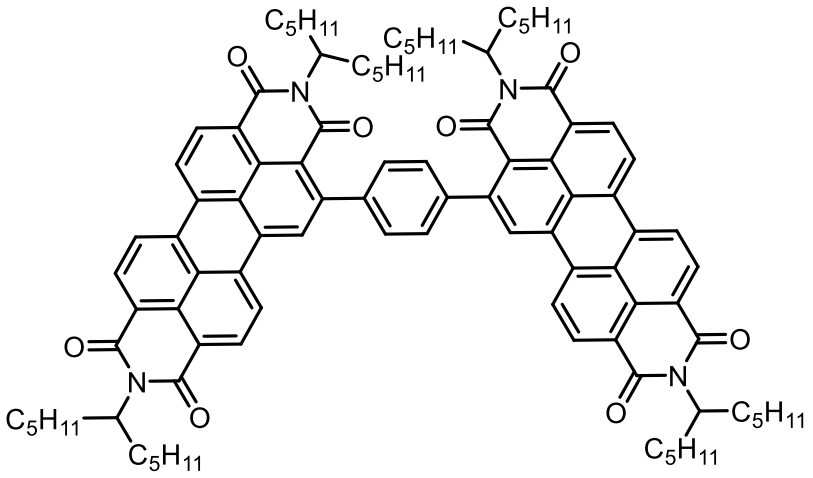

***p*PDI$_2$:** To a 25 mL round-bottom flask charged with a magnetic stir bar were added 1,4-dibromobenzene (36 mg, 0.153 mmol, 0.018 ml), **PDI*o*Bpin** (264 mg, 0.320 mmol), Na_2CO_3 (211 mg, 1.53 mmol) toluene (18 mL), and H_2O (2 mL). The reaction mixture was stirred and bubbled for 15 min with N_2. Pd_2dba_3 (6 mol%, 8.4 mg, 0.009 mmol) and SPhos (7.5 mg, 0.018 mmol) were added and the reaction mixture was bubbled with N_2 for an additional 5 min. The reaction was then stirred at 85 ^oC for 18 h, cooled to rt, diluted into toluene, and washed with sat. $NaHCO_3$. The organic layer was collected, dried over anhyd. Na_2SO_4, filtered, and the solvent was removed *in* vacuo. Column chromatography (silica gel, 50% CH_2Cl_2 in hexanes) followed by further purification via HPLC afforded ***p*PDI$_2$ (**77 mg, 34%) as a dark red solid. ^1H NMR (500 MHz, $CDCl_3$): δ 8.80-8.63 (m, 12H) 7.63 (s, 4H) 5.24-5.04 (m, 4H) 2.32-2.12 (m, 8H) 1.92-1.76 (m, 8H) 1.43-1.20 (m, 48H) 0.84 (t, J = 6.5 Hz). ^{13}C NMR (125 MHz, $CDCl_3$): δ 164.7, 164.2, 163.6, 163.4, 147.8, 147.2, 141.6, 134.7, 134.4, 134.28, 134.25, 133.4, 132.0, 131.7, 131.2, 130.7, 129.6, 128.4, 126.5, 126.0, 124.1, 123.4, 123.1, 122.9, 121.2, 120.3, 54.8, 32.4, 32.2, 31.8, 29.7, 26.6, 22.61, 22.59, 14.09, 14.07. ESI HRMS *m/z* calcd. for $C_{94}H_{110}N_4O_8Na$ $(M + Na)^+$ 1494.8249, found: 1494.8240.

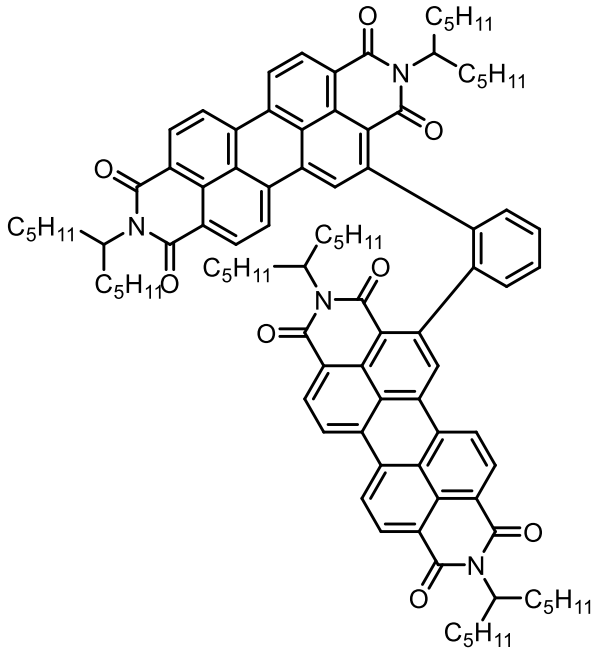

***o*PDI$_2$:** To a 25 mL round-bottom flask charged with a magnetic stir bar were added 1,2-diiodobenzene (36 mg, 0.109 mmol, 0.014 ml), **PDI*o*Bpin** (189 mg, 0.229 mmol), K_2CO_3 (151 mg, 1.09 mmol) toluene (20 mL), and H_2O (102 mL). The reaction mixture was stirred and bubbled for 15 min with N_2. Pd_2dba_3 (6 mol%, 6.0 mg, 0.007 mmol) and SPhos (5.4 mg, 0.013 mmol) were added and the reaction mixture was bubbled with N_2 for an additional 5 min. The reaction was then stirred at 85 ^oC for 18 h, then cooled to rt, diluted into toluene, and washed with sat. $NaHCO_3$. The organic layer was collected, dried over anhyd. Na_2SO_4, filtered, and the solvent was removed *in* vacuo. Column chromatography (silica gel, 75% in CH_2Cl_2 in hexanes) followed by further column chromatography (1% acetone in CH_2Cl_2) afforded ***o*PDI$_2$** (15 mg, 9%) as a dark red solid. ^1H NMR (500 MHz, $CDCl_3$): δ 8.77 (s, 1H) 8.68-8.39 (m, 8H) 8.26 (s, 2H) 7.57 (s, 2H) 7.39 (s, 2H) 5.27-5.17 (m, 2H) 5.16-5.06 (m, 2H) 2.41-2.10 (m, 8H) 1.92-1.70 (m, 8H) 1.53-1.09 (m, 48H) 1.00-0.75 (m, 24H). ^{13}C NMR (125 MHz, $CDCl_3$): δ 164.6, 164.2, 163.5, 163.1, 147.9, 147.5, 145.3, 139.7, 134.4, 134.3, 134.2, 133.3, 131.8, 131.0, 130.3, 129.4, 129.2, 128.1, 126.3, 125.8,

123.9, 123.2, 122.9, 122.7, 121.0, 120.2, 54.9, 54.6, 32.3, 31.7, 29.7, 26.5, 22.8, 22.5, 14.1, 14.0.

ESI HRMS *m*/*z* calcd. for $C_{94}H_{111}N_4O_8$ $(M + H)^+$ 1472.8429, found: 1472.8423.

2.5.2. Differential Pulse Voltammetry

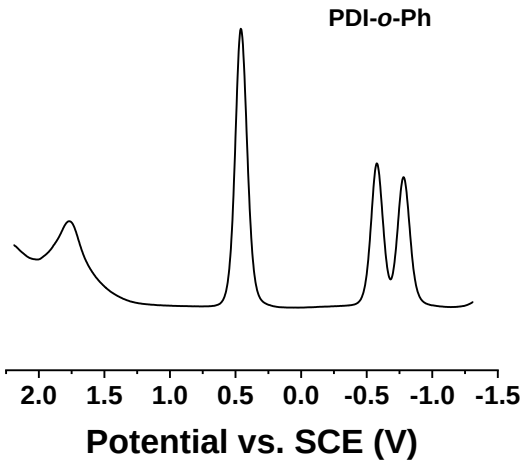

Figure 2.8. Differential pulse voltammogram for **PDI-*o*-Ph** in CH_2Cl_2 referenced to the ferrocene/ferrocenium redox couple.

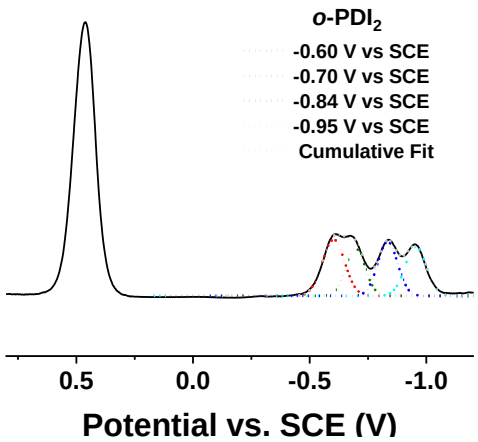

Figure 2.9. Differential pulse voltammogram for ***o*-PDI$_2$** in CH_2Cl_2 referenced to the ferrocene/ferrocenium redox couple. Peaks were determined by Gaussian fits.

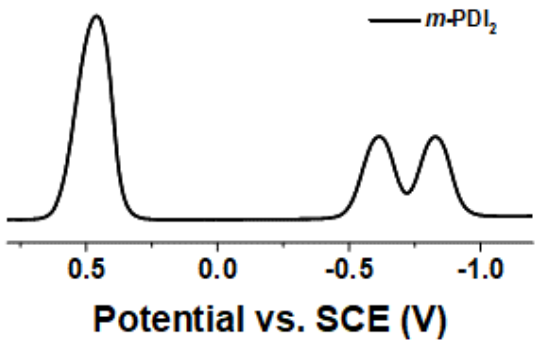

Figure 2.10. Differential pulse voltammogram for ***m*-PDI2** in CH_2Cl_2 referenced to the ferrocene/ferrocenium redox couple.

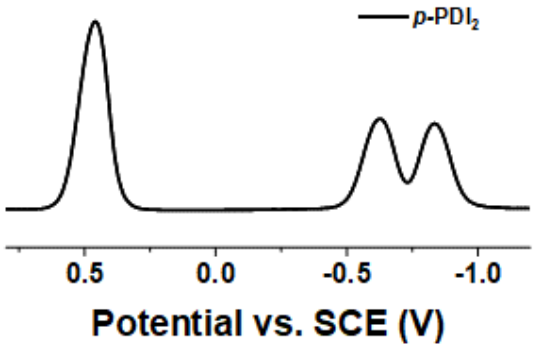

Figure 2.11. Differential pulse voltammogram for ***p*-PDI2** in CH_2Cl_2 referenced to the ferrocene/ferrocenium redox couple.

2.5.3. Additional Optical Characterization

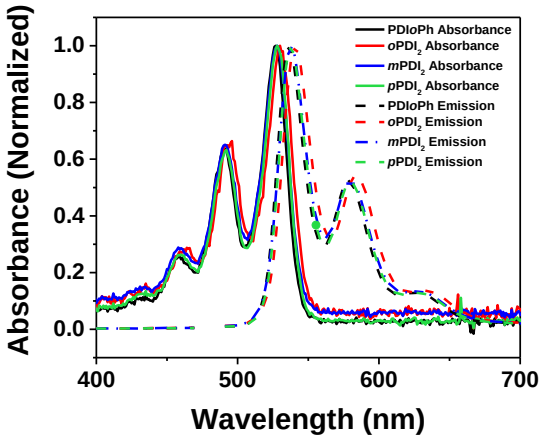

Figure 2.12. Absorbance and emission spectra for the four compounds examined in toluene.

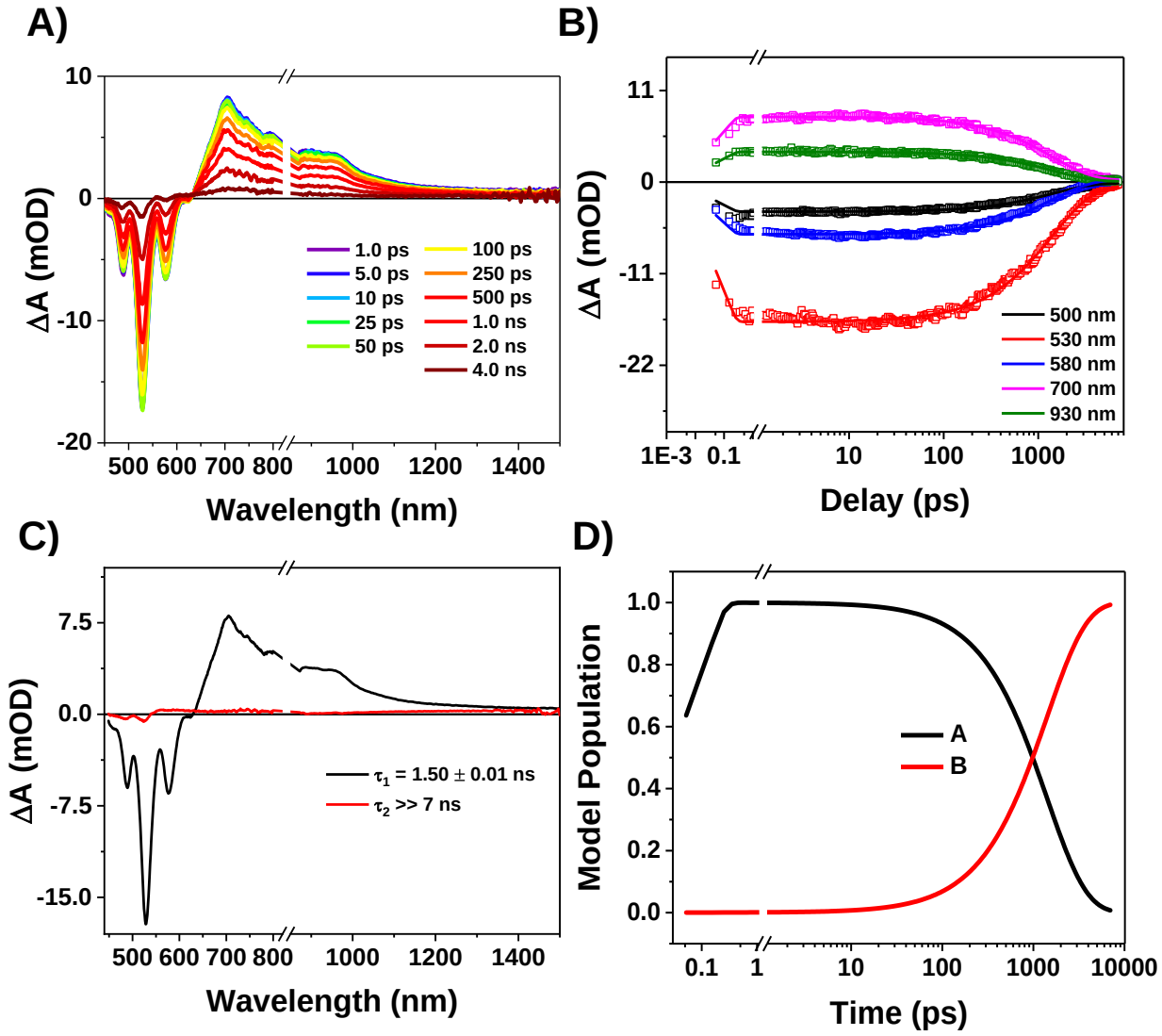

Figure 2.13. A) fsTA spectra of **PDI-Ph** in CH_2Cl_2 following 414 nm excitation. B) Kinetics fits to the raw data at the indicated wavelengths with the kinetic model as described in the text. $\tau = 1/k$. C) Evolution-associated spectra. D) Model population kinetics, distribution of species in time.

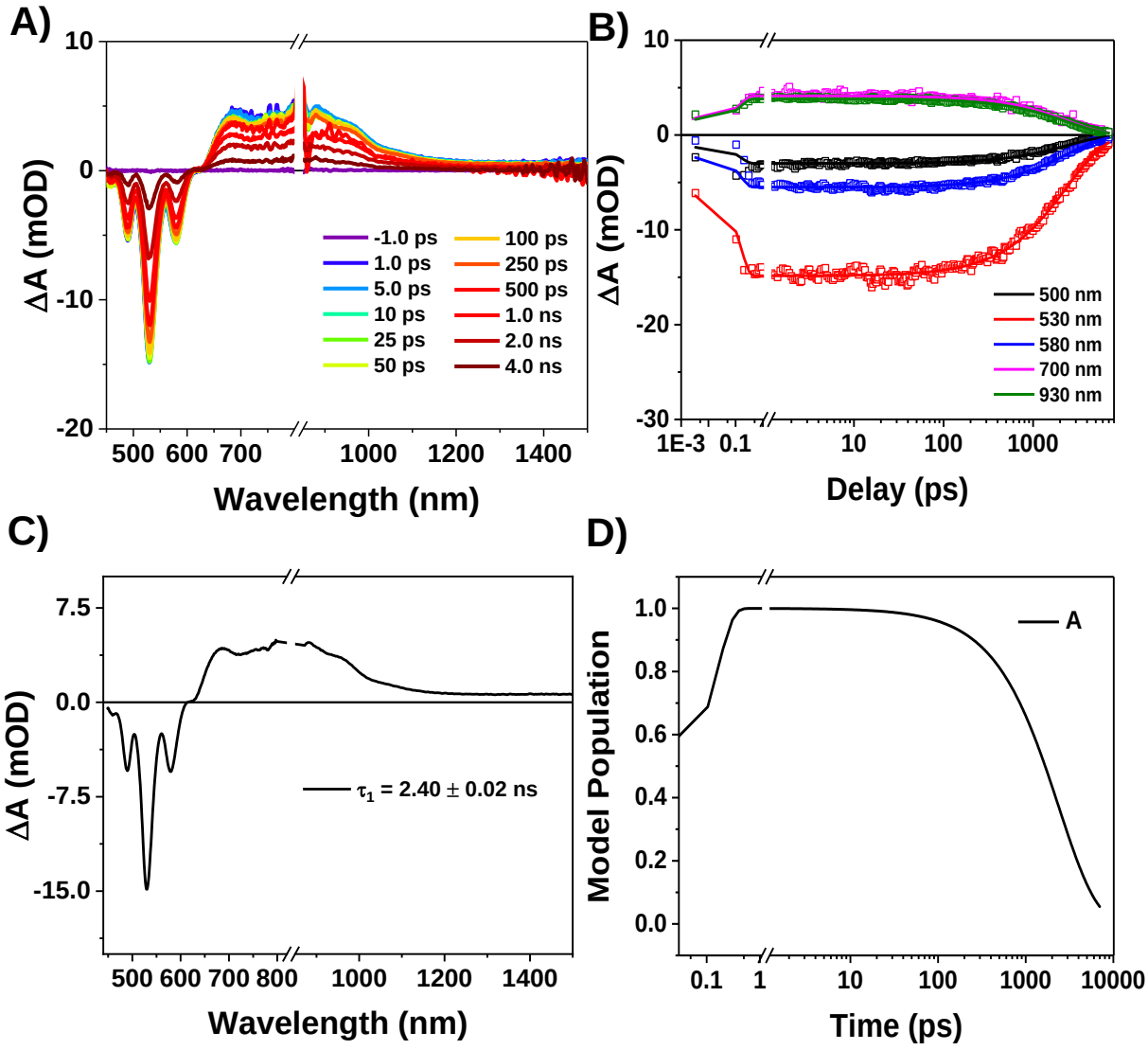

Figure 2.14. A) fsTA spectra of **PDI-Ph** in toluene following 414 nm excitation. B) Kinetics fits to the raw data at the indicated wavelengths with the kinetic model as described in the text. $\tau = 1/k$. C) Evolution-associated spectra. D) Model population kinetics, distribution of species in time.

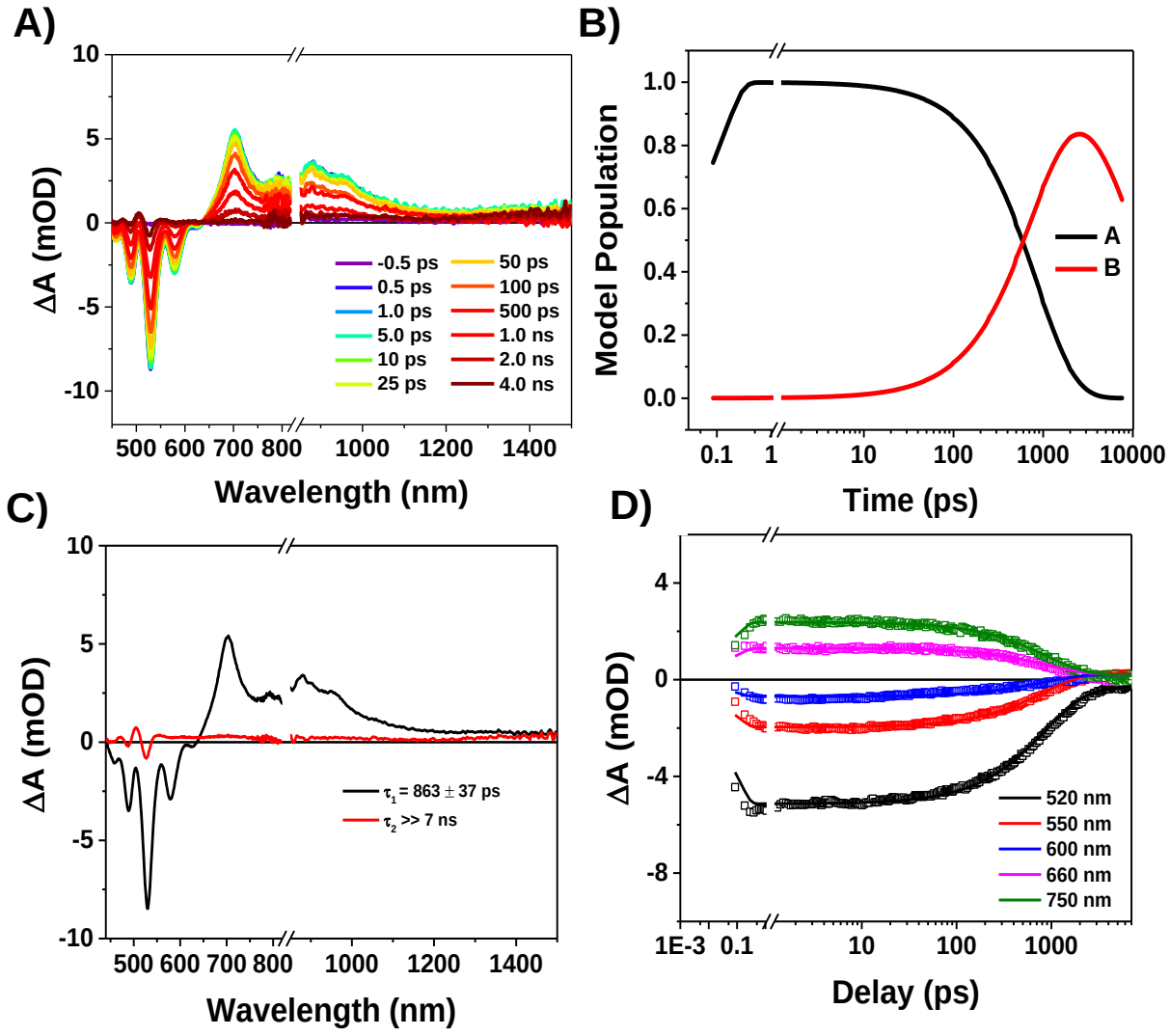

Figure 2.15. A) fsTA spectra of ***p*-PDI$_2$** in CH_2Cl_2 following 414 nm excitation. B) Kinetics fits to the raw data at the indicated wavelengths with the kinetic model as described in the text. $\tau = 1/k$. C) Evolution-associated spectra. D) Model population kinetics, distribution of species in time.

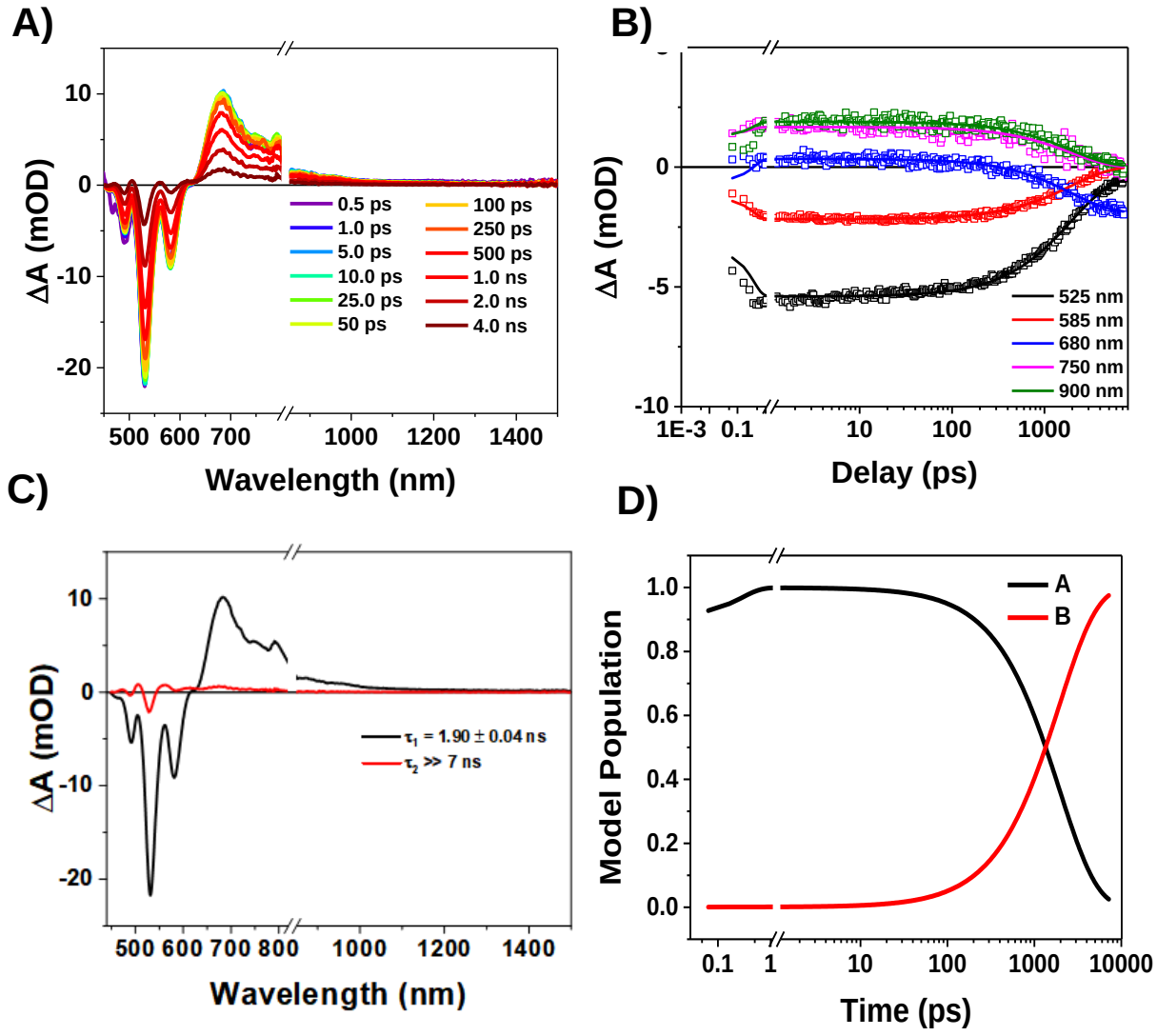

Figure 2.16. A) fsTA spectra of ***p*-PDI$_2$** in toluene following 414 nm excitation. B) Kinetics fits to the raw data at the indicated wavelengths with the kinetic model as described in the text. $\tau = 1/k$. C) Evolution-associated spectra. D) Model population kinetics, distribution of species in time.

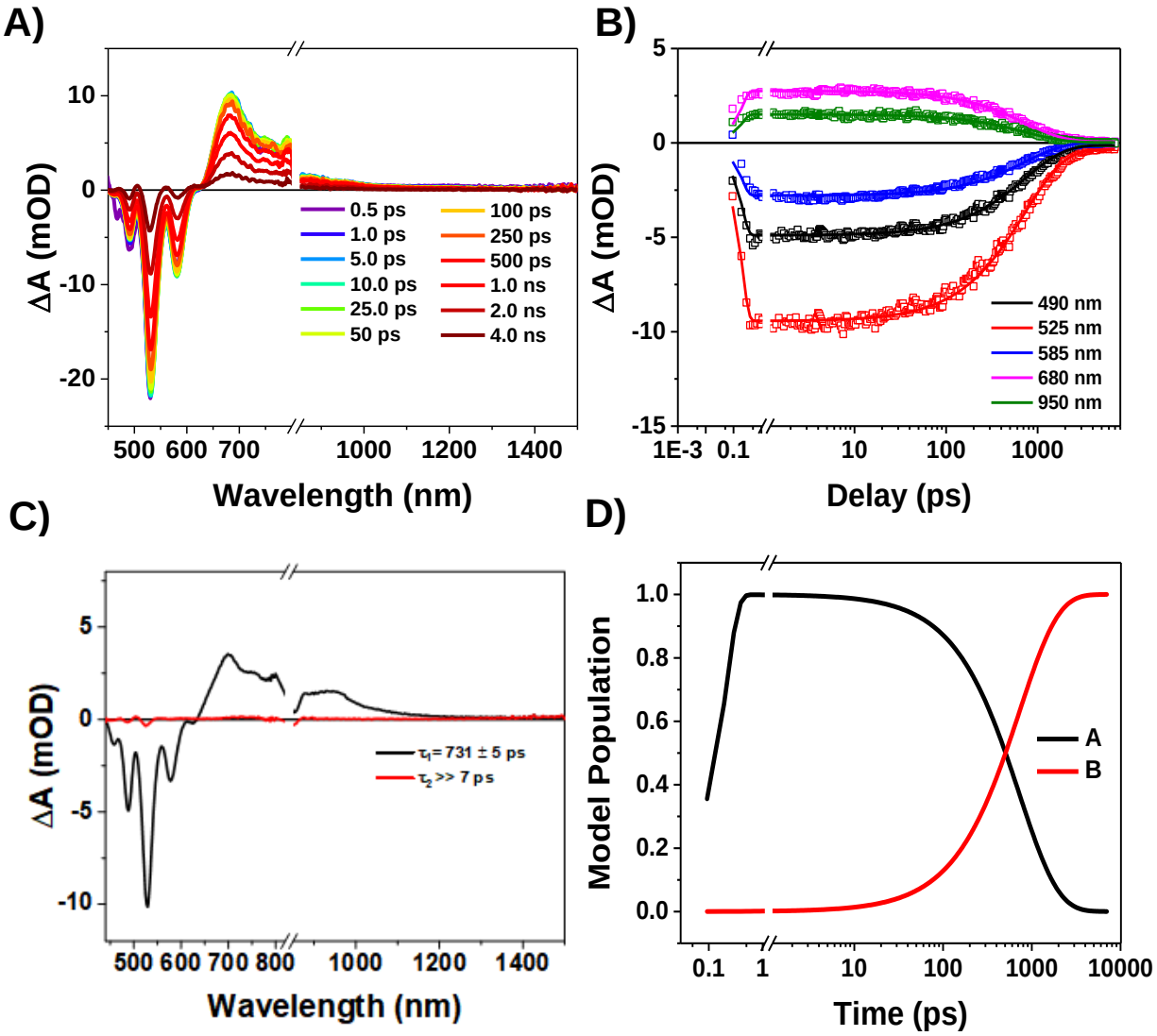

Figure 2.17. A) fsTA spectra of ***m*-PDI$_2$** in CH_2Cl_2 following 414 nm excitation. B) Kinetics fits to the raw data at the indicated wavelengths with the kinetic model as described in the text. $\tau = 1/k$. C) Evolution-associated spectra. D) Model population kinetics, distribution of species in time.

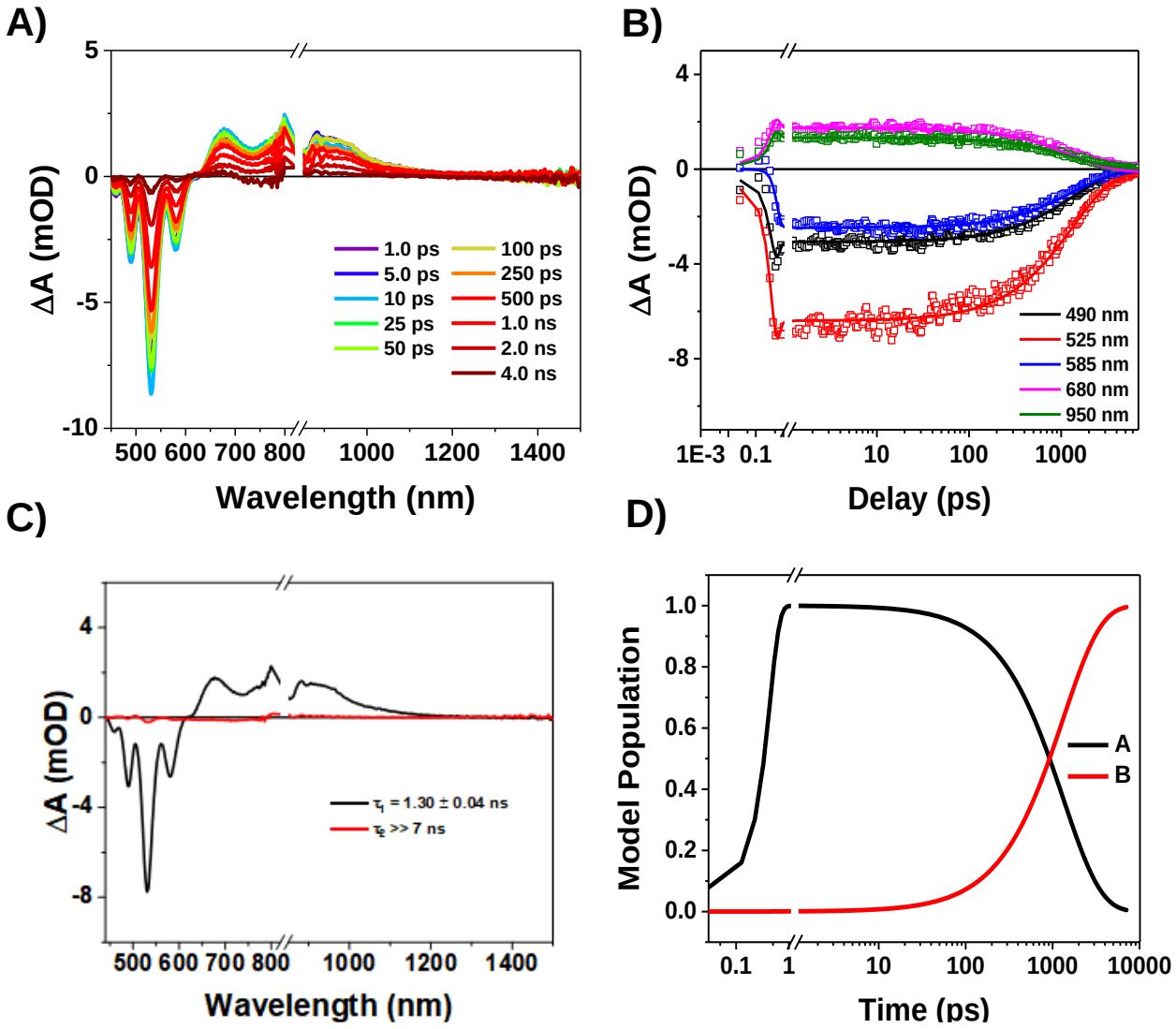

Figure 2.18. A) fsTA spectra of ***m*-PDI$_2$** in toluene following 414 nm excitation. B) Kinetics fits to the raw data at the indicated wavelengths with the kinetic model as described in the text. $\tau = 1/k$. C) Evolution-associated spectra. D) Model population kinetics, distribution of species in time.

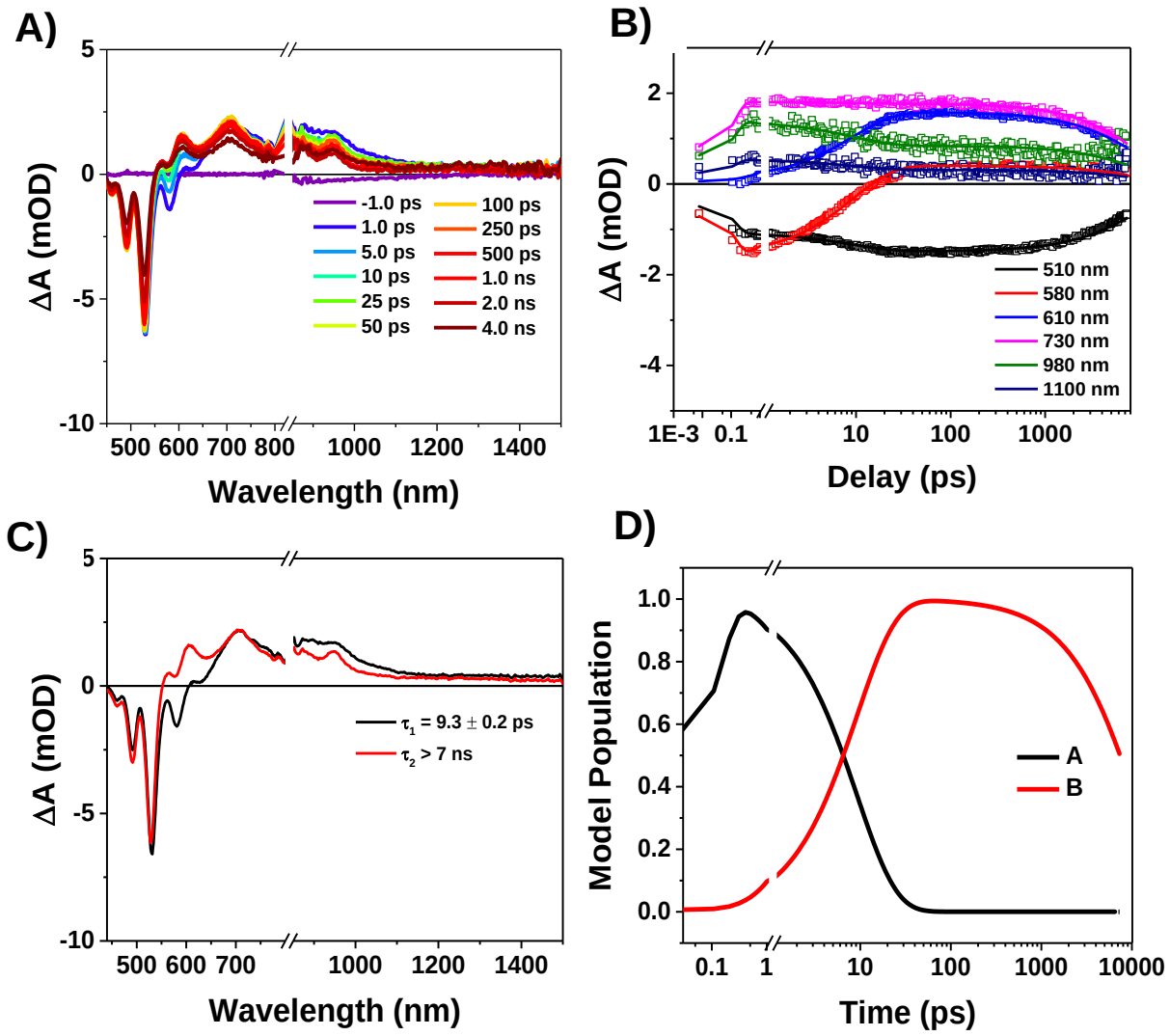

Figure 2.19. A) fsTA spectra of ***o*-PDI$_2$** in CH_2Cl_2 following 430 nm excitation. B) Kinetics fits to the raw data at the indicated wavelengths with the kinetic model as described in the text. $\tau = 1/k$. C) Evolution-associated spectra. D) Model population kinetics, distribution of species in time.

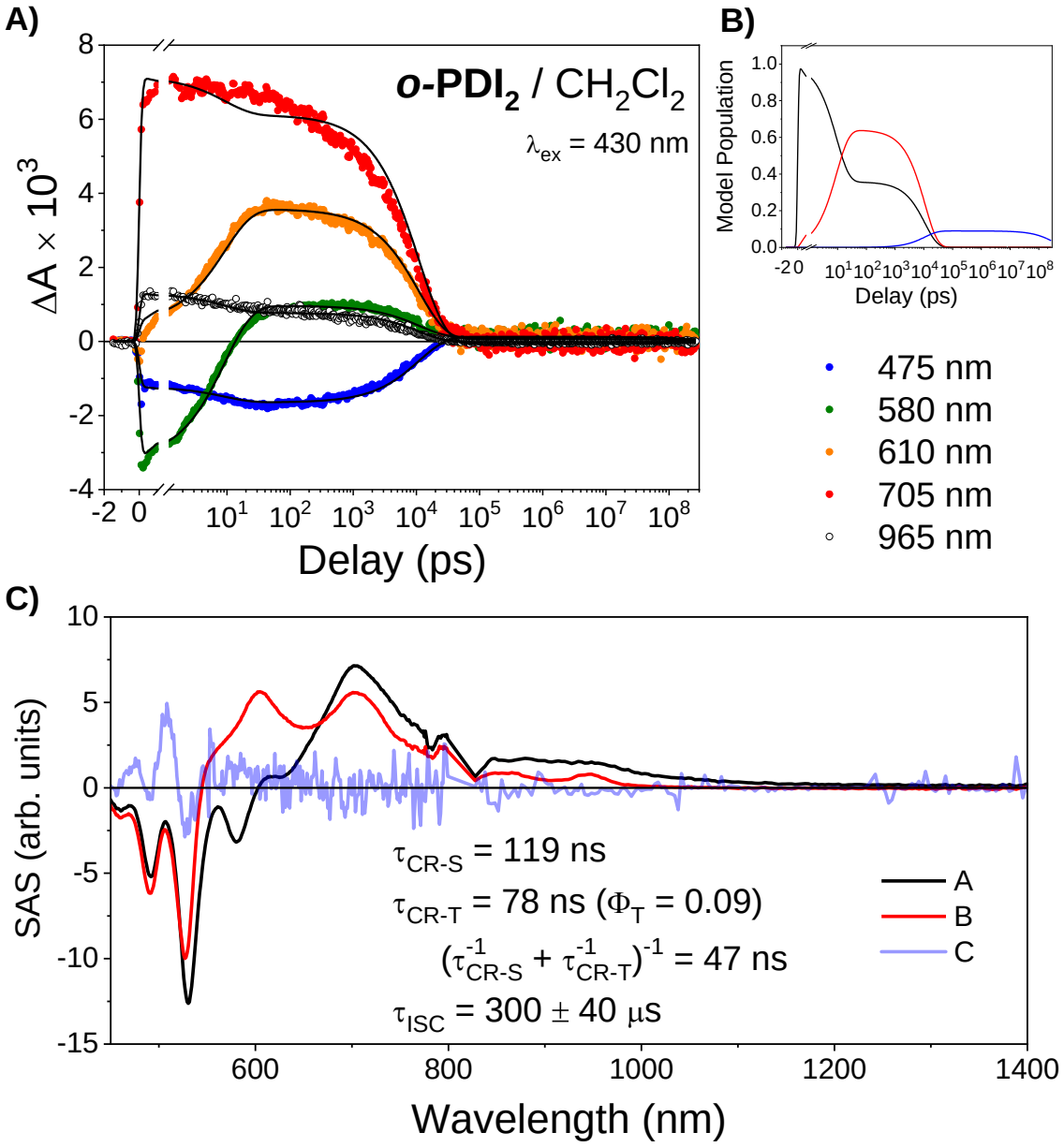

Figure 2.20. A) Kinetic fits of the merged fs/nsTA spectra of ***o*-PDI$_2$** in CH_2Cl_2 following 430 nm excitation to the pseudoequilibrium model in the text. B) Model population kinetics, distribution of species in time. C) Species-associated spectra.

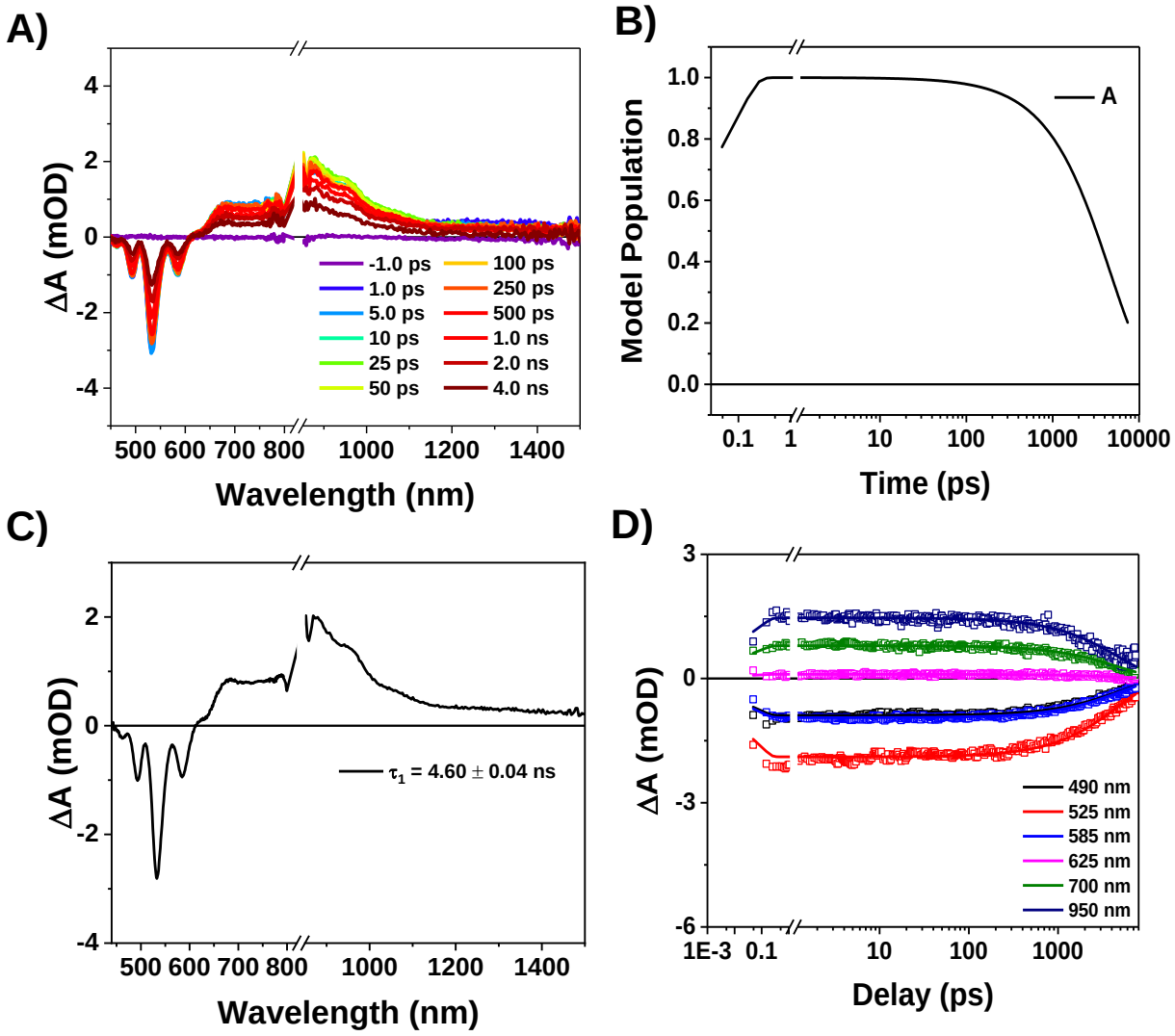

Figure 2.21. A) fsTA spectra of ***o*-PDI$_2$** in toluene following 430 nm excitation. B) Kinetics fits to the raw data at the indicated wavelengths with the kinetic model as described in the text. $\tau = 1/k$. C) Evolution-associated spectra. D) Model population kinetics, distribution of species in time. NIR spectra scaled by a factor of two for emphasis.

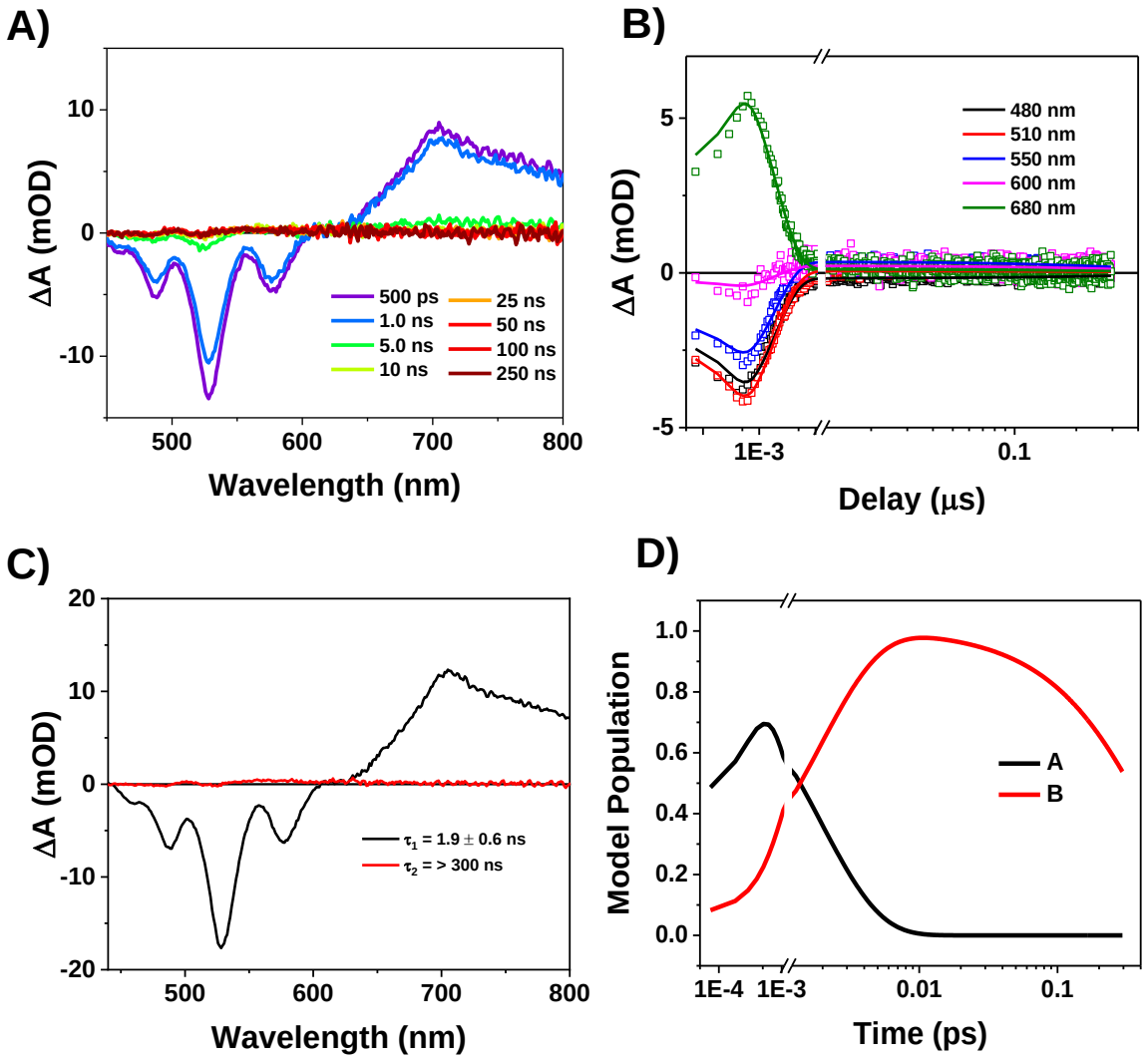

Figure 2.22. A) nsTA spectra of **PDI-Ph** in CH_2Cl_2 following 414 nm excitation. B) Kinetics fits to the raw data at the indicated wavelengths with the kinetic model as described in the text. $\tau = 1/k$. C) Evolution-associated spectra. D) Model population kinetics, distribution of species in time.

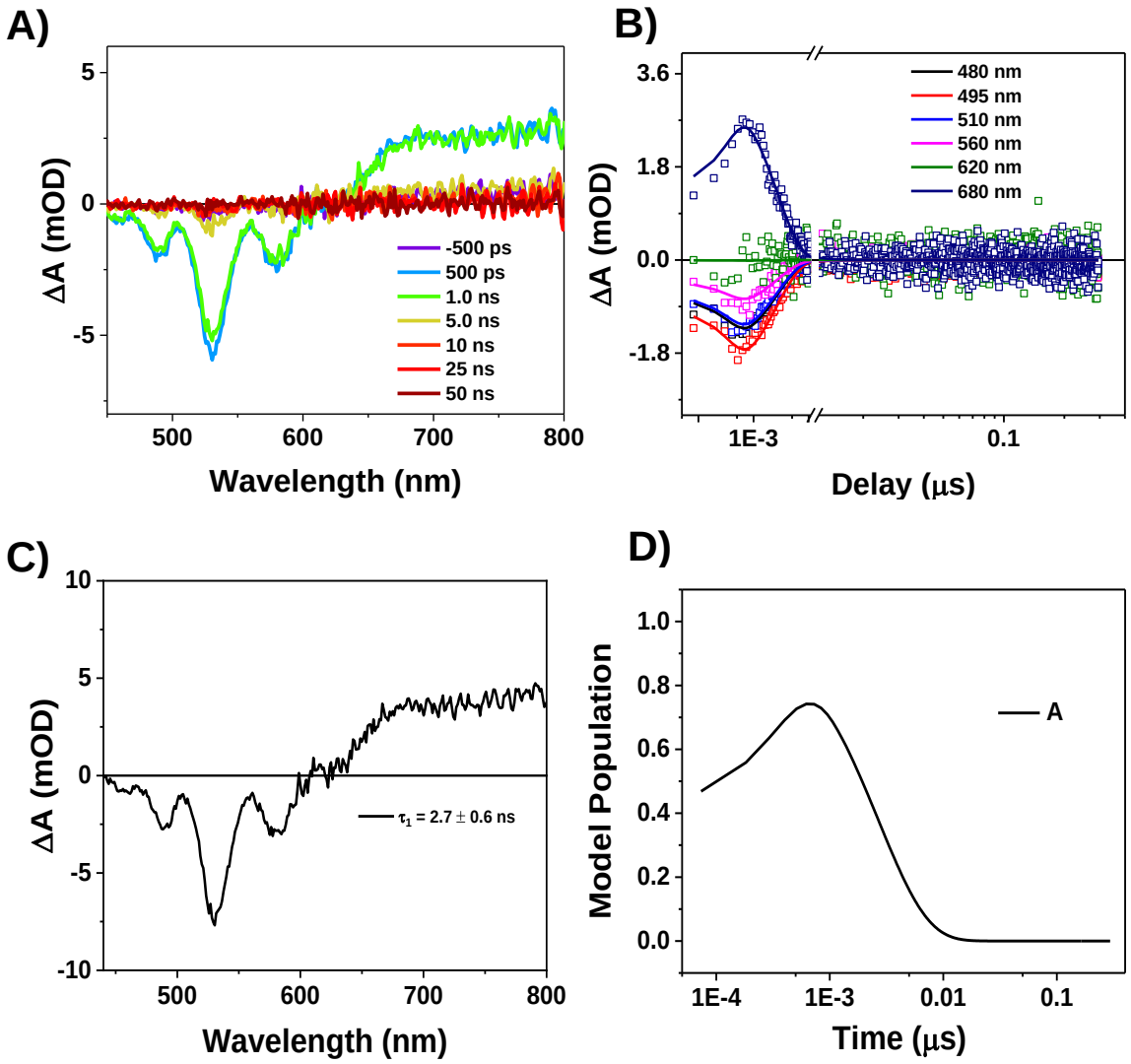

Figure 2.23. A) nsTA spectra of **PDI-Ph** in toluene following 414 nm excitation. B) Kinetics fits to the raw data at the indicated wavelengths with the kinetic model as described in the text. $\tau = 1/k$. C) Evolution-associated spectra. D) Model population kinetics, distribution of species in time.

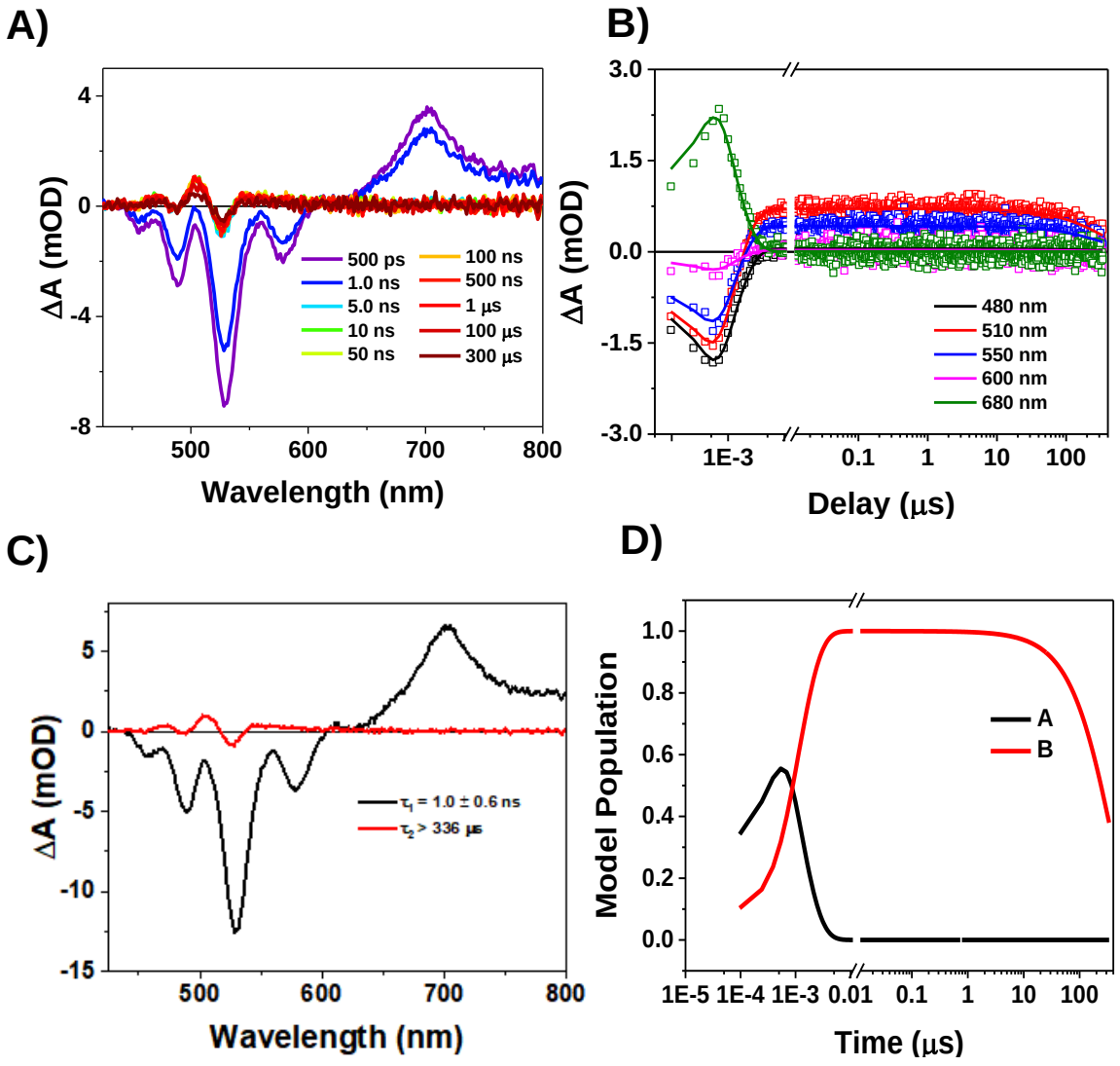

Figure 2.24. A) nsTA spectra of ***p*-PDI$_2$** in CH_2Cl_2 following 414 nm excitation. B) Kinetics fits to the raw data at the indicated wavelengths with the kinetic model as described in the text. $\tau = 1/k$. C) Evolution-associated spectra. D) Model population kinetics, distribution of species in time.

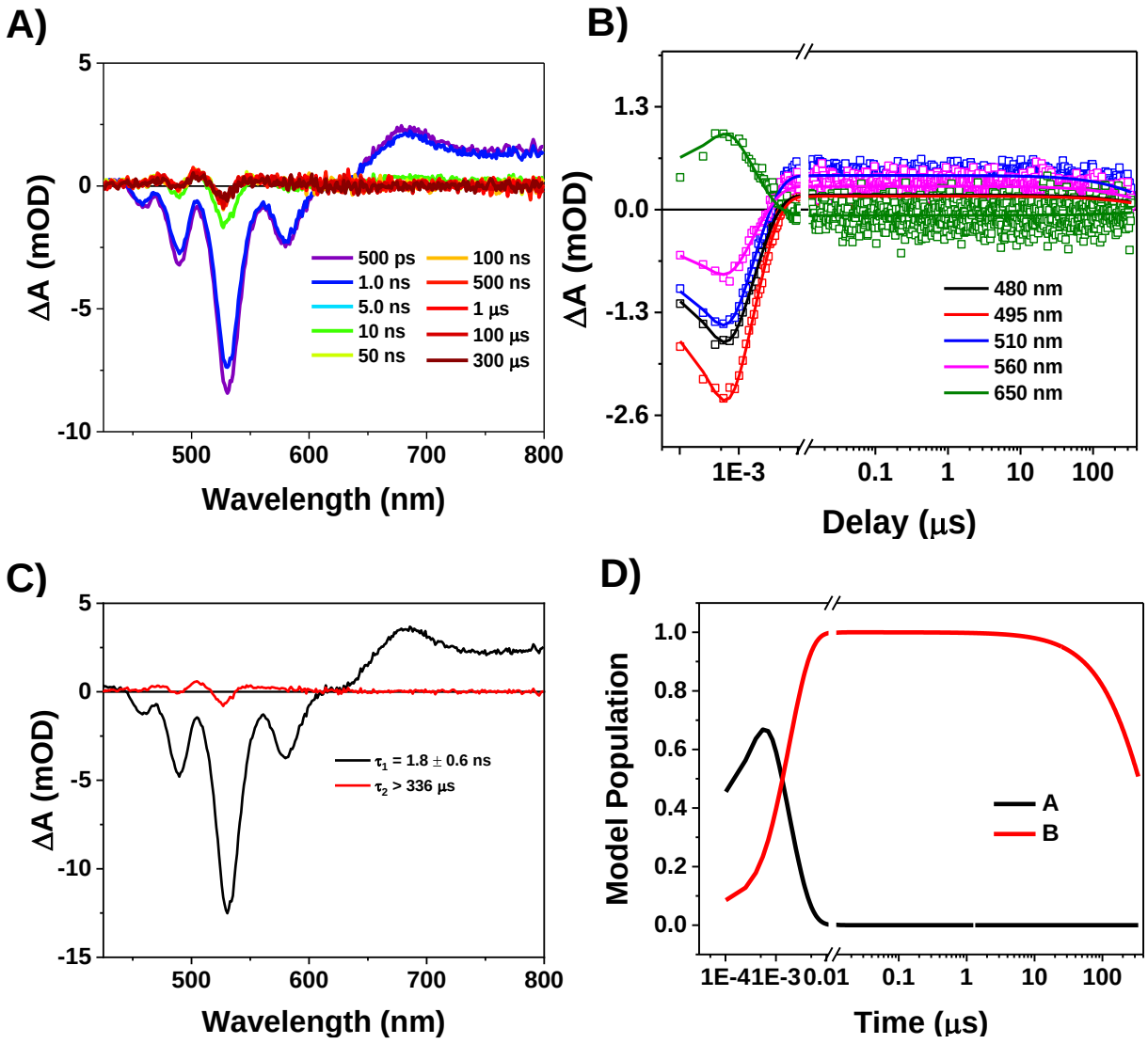

Figure 2.25. A) nsTA spectra of ***p*-PDI$_2$** in toluene following 414 nm excitation. B) Kinetics fits to the raw data at the indicated wavelengths with the kinetic model as described in the text. $\tau = 1/k$. C) Evolution-associated spectra. D) Model population kinetics, distribution of species in time.

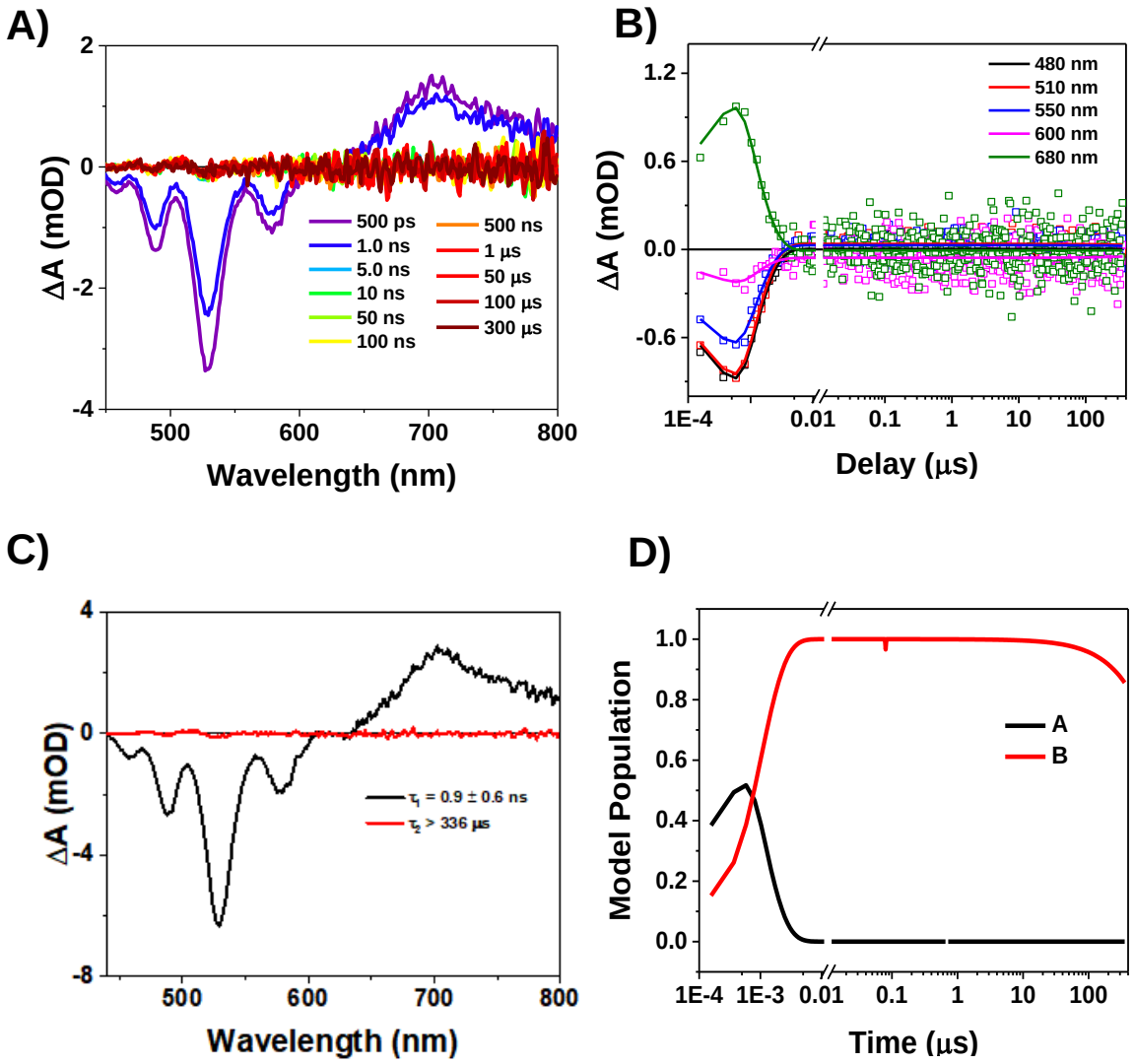

Figure 2.26. A) nsTA spectra of ***m*-PDI$_2$** in CH_2Cl_2 following 414 nm excitation. B) Kinetics fits to the raw data at the indicated wavelengths with the kinetic model as described in the text. $\tau = 1/k$. C) Evolution-associated spectra. D) Model population kinetics, distribution of species in time.

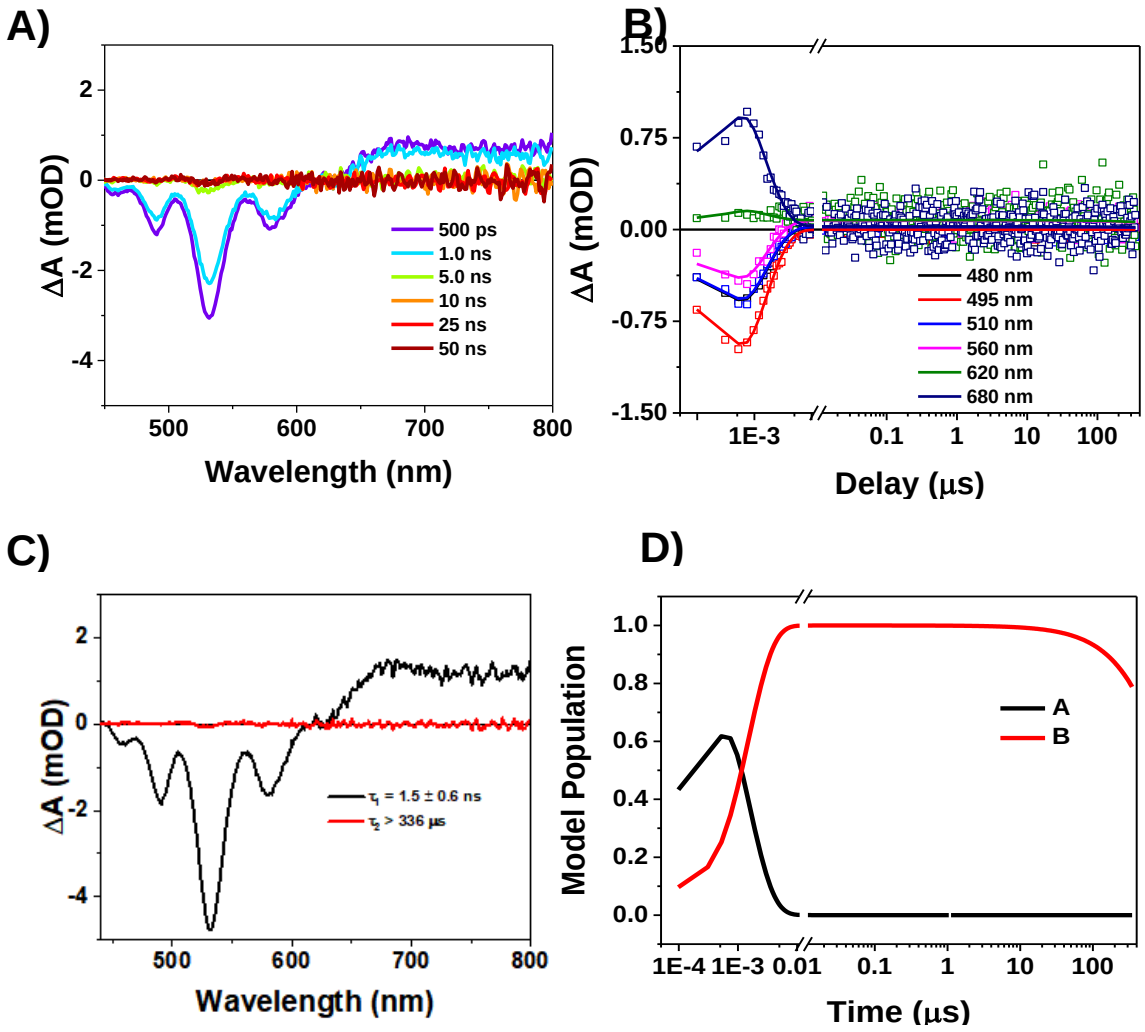

Figure 2.27. A) nsTA spectra of ***m*-PDI$_2$** in toluene following 414 nm excitation. B) Kinetics fits to the raw data at the indicated wavelengths with the kinetic model as described in the text. $\tau = 1/k$. C) Evolution-associated spectra. D) Model population kinetics, distribution of species in time.

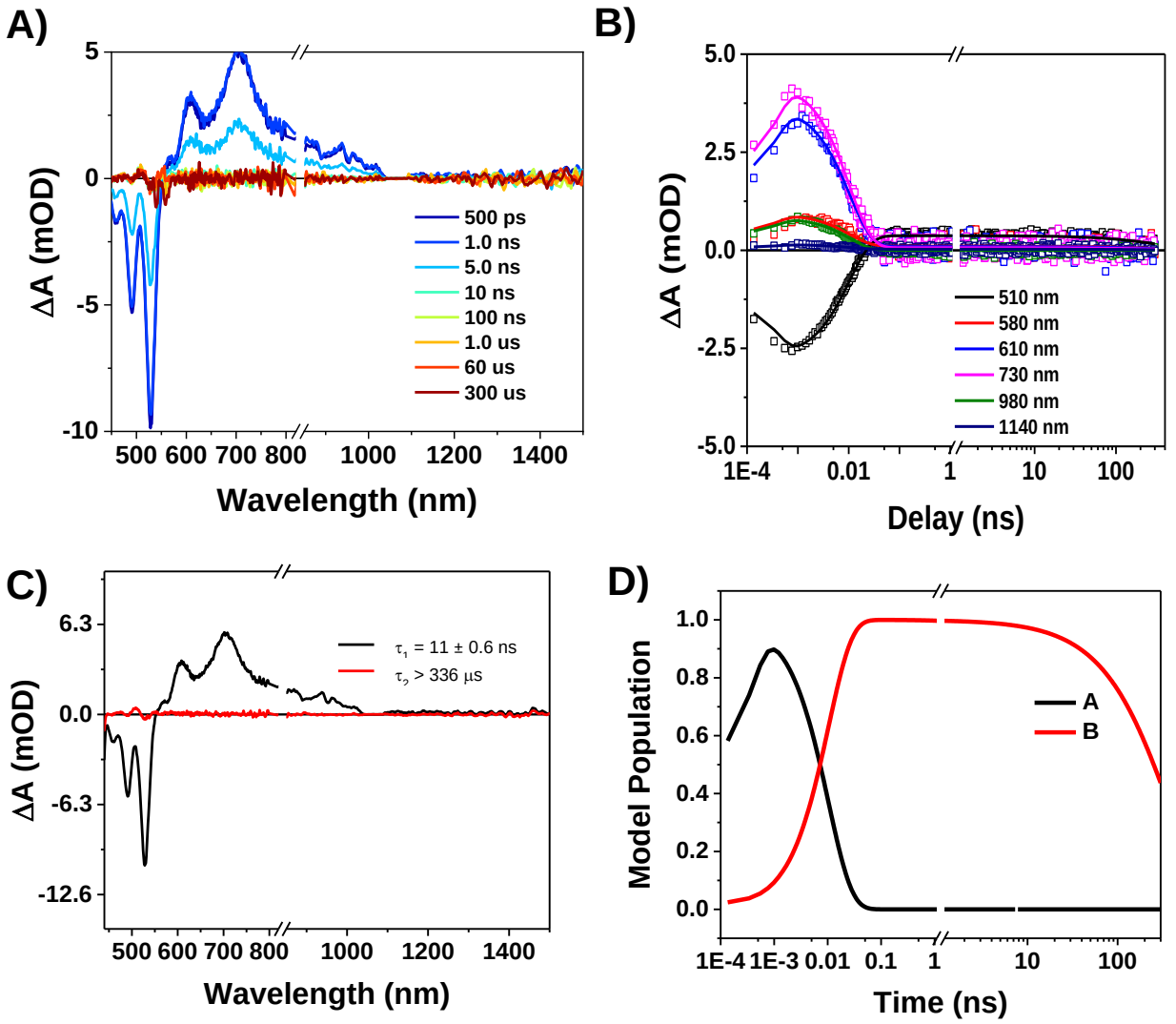

Figure 2.28. A) nsTA spectra of ***o*-PDI$_2$** in CH_2Cl_2 following 430 nm excitation. B) Kinetics fits to the raw data at the indicated wavelengths with the kinetic model as described in the text. $\tau = 1/k$. C) Evolution-associated spectra. D) Model population kinetics, distribution of species in time.

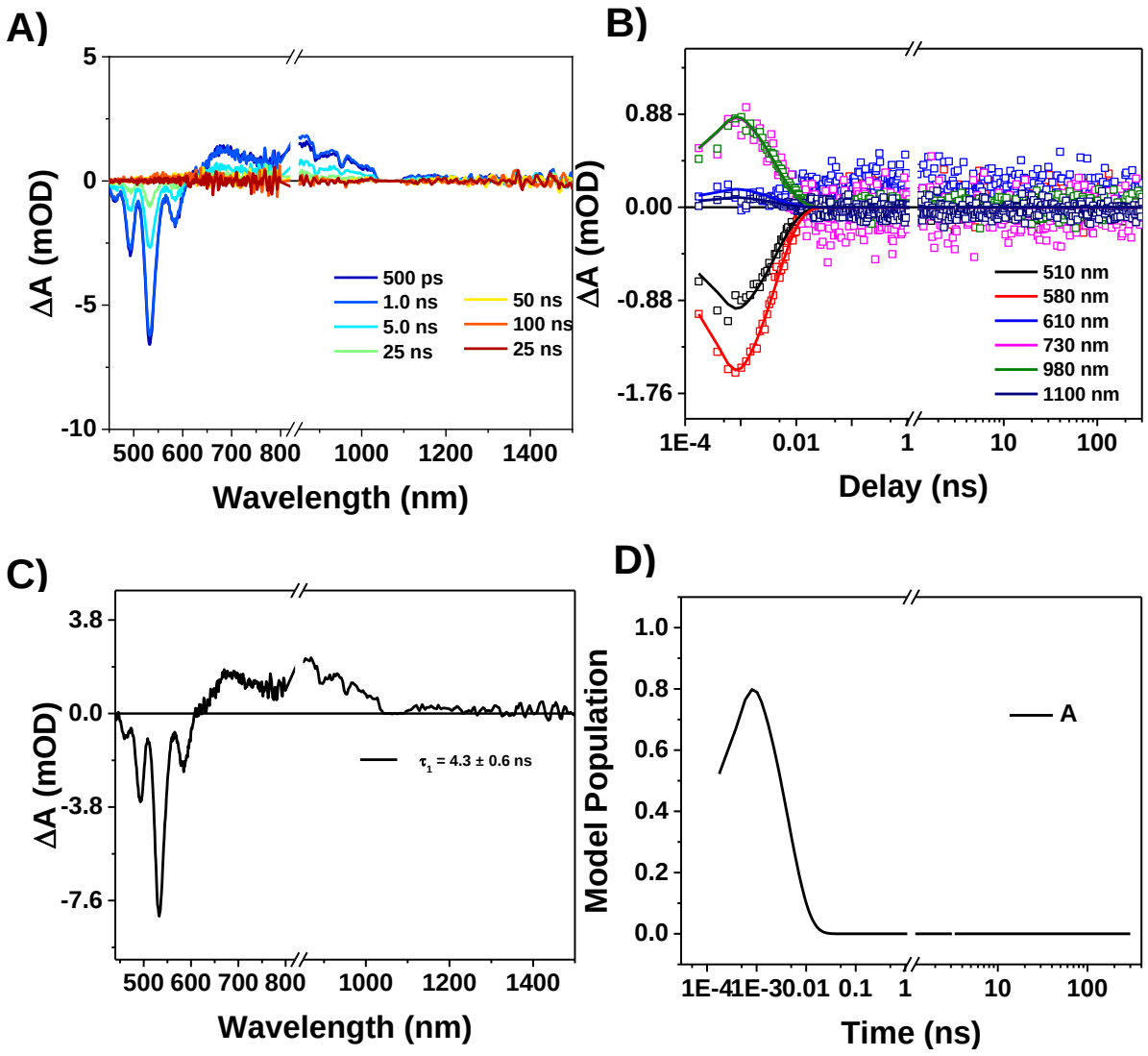

Figure 2.29. A) nsTA spectra of ***o*-PDI$_2$** in toluene following 430 nm excitation. B) Kinetics fits to the raw data at the indicated wavelengths with the kinetic model as described in the text. $\tau = 1/k$. C) Evolution-associated spectra. D) Model population kinetics, distribution of species in time. NIR spectra scaled by a factor of two for emphasis.

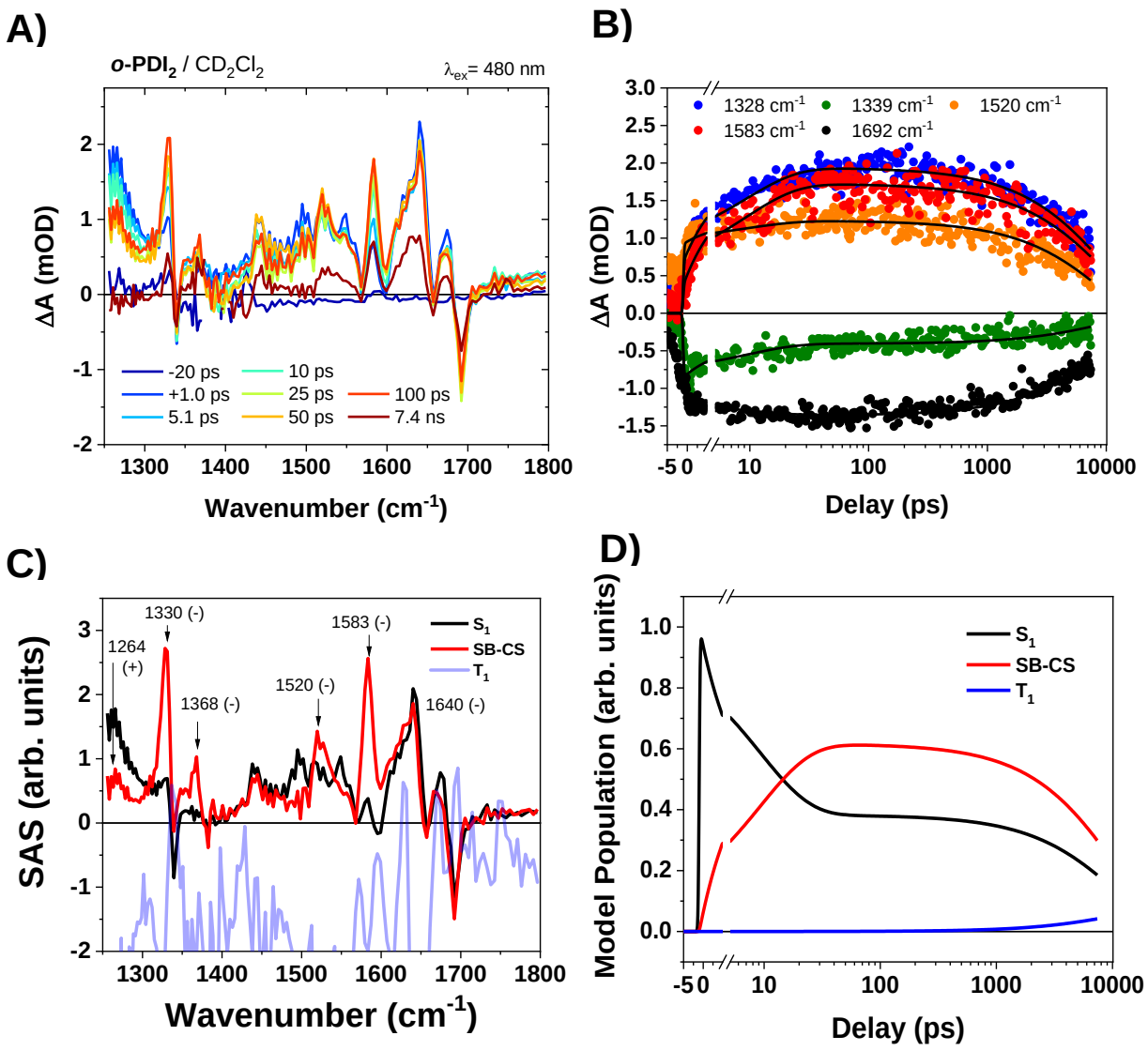

Figure 2.30. A) fsIR spectra of ***o*-PDI$_2$** in CD_2Cl_2 following 480 nm excitation. B) Kinetics fits to the raw data at the indicated wavelengths to the pseudoequilibrium model in the text. Species-associated spectra. D) Model population kinetics, distribution of species in time.

Modes at 1330, 1368, 1520, and 1583 cm^{-1} are assigned to **PDI-Ph$^{\bullet-}$** from comparison to FTIR spectra of chemically reduced PDI and DFT calculations (see below).[4,5]

The mode at 1264 cm^{-1} is assigned to **PDI-Ph$^{\bullet-}$** vibration (see below).

Modes at 1440, 1499, 1548, 1642, and 1677 cm^{-1} are assigned to PDI core vibrations[6] in ^{1*}**PDI-Ph**.

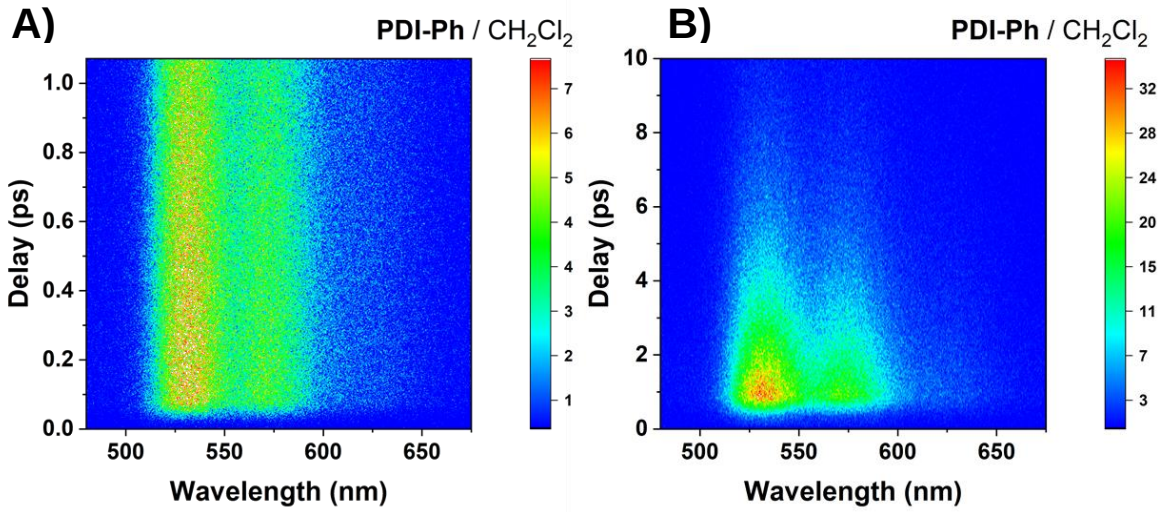

Figure 2.31. A) 1 ns and B) 10 ns psTRF spectra for **PDI-Ph** in CH_2Cl_2 following λ_{ex} = 480 nm, 1 nJ/pulse, ~50 fs excitation.

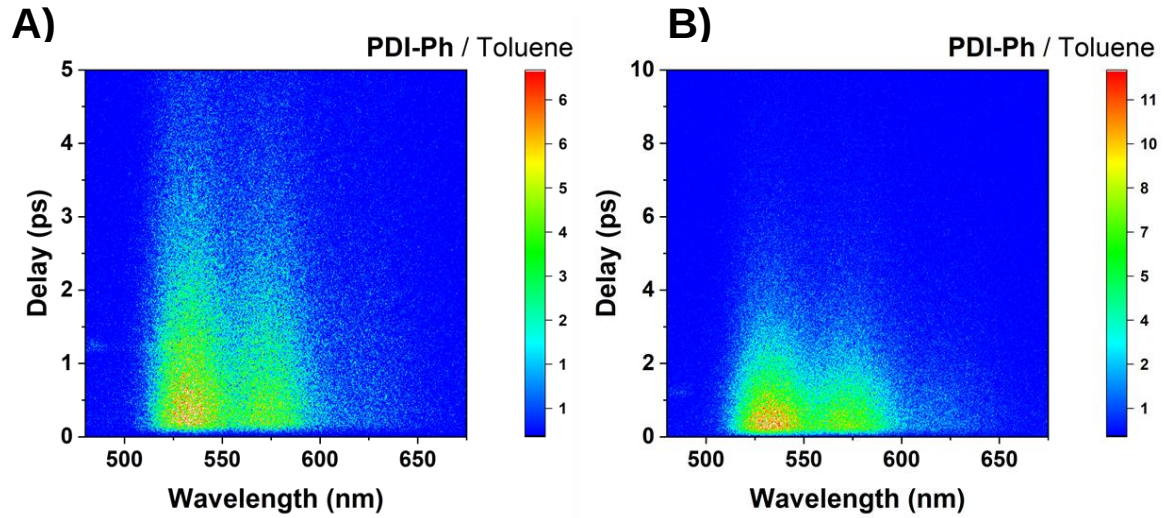

Figure 2.32. A) 5 ns and B) 10 ns psTRF spectra for **PDI-Ph** in toluene following λ_{ex} = 480 nm, 1 nJ/pulse, ~50 fs excitation.

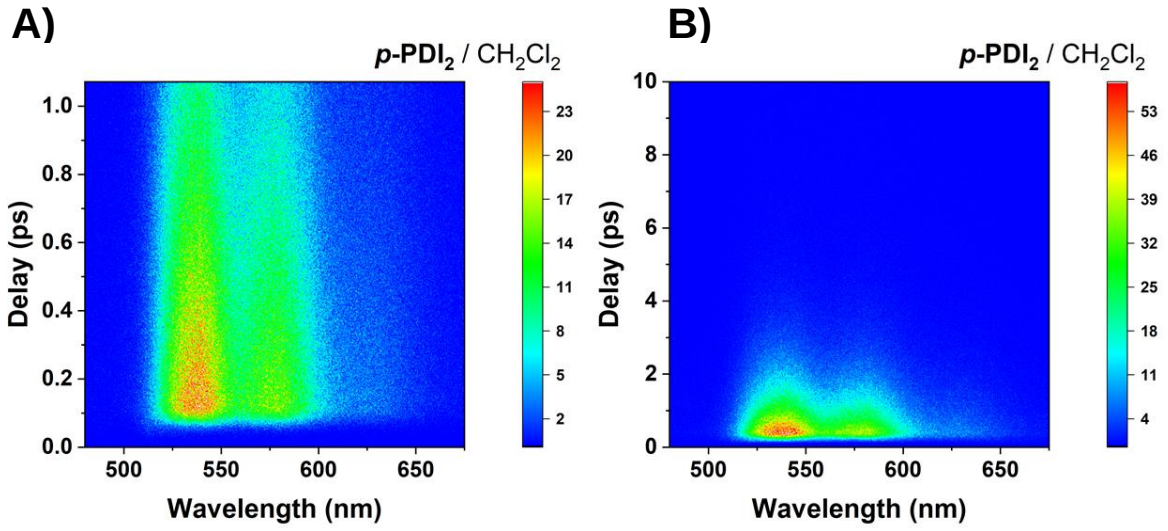

Figure 2.33. A) 1 ns and B) 10 ns psTRF spectra for ***p*-PDI$_2$** in CH_2Cl_2 following λ_{ex} = 480 nm, 1 nJ/pulse, ~50 fs excitation.

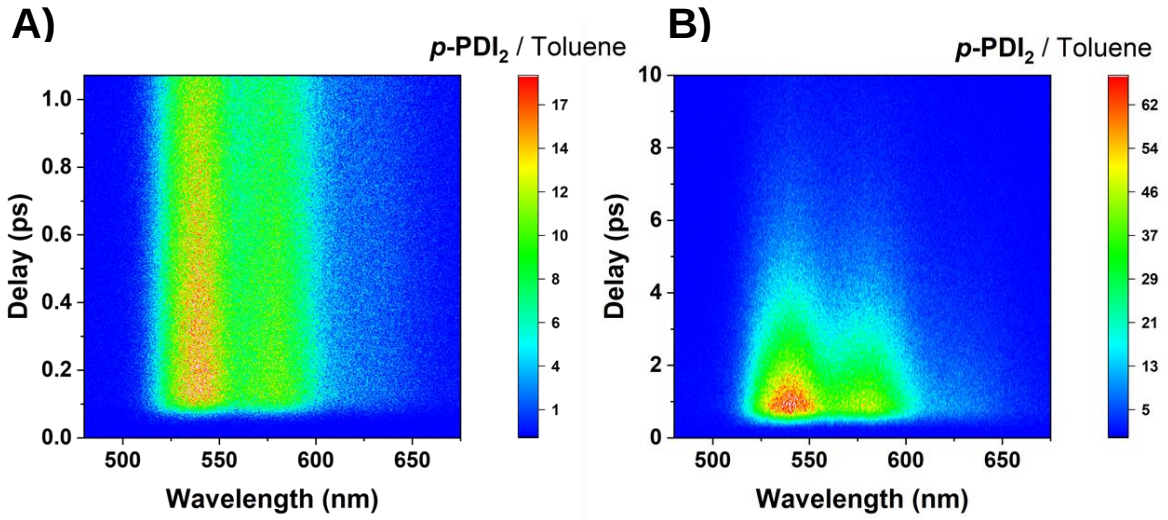

Figure 2.34. A) 1 ns and B) 10 ns psTRF spectra for ***p*-PDI$_2$** in toluene following λ_{ex} = 480 nm, 1 nJ/pulse, ~50 fs excitation.

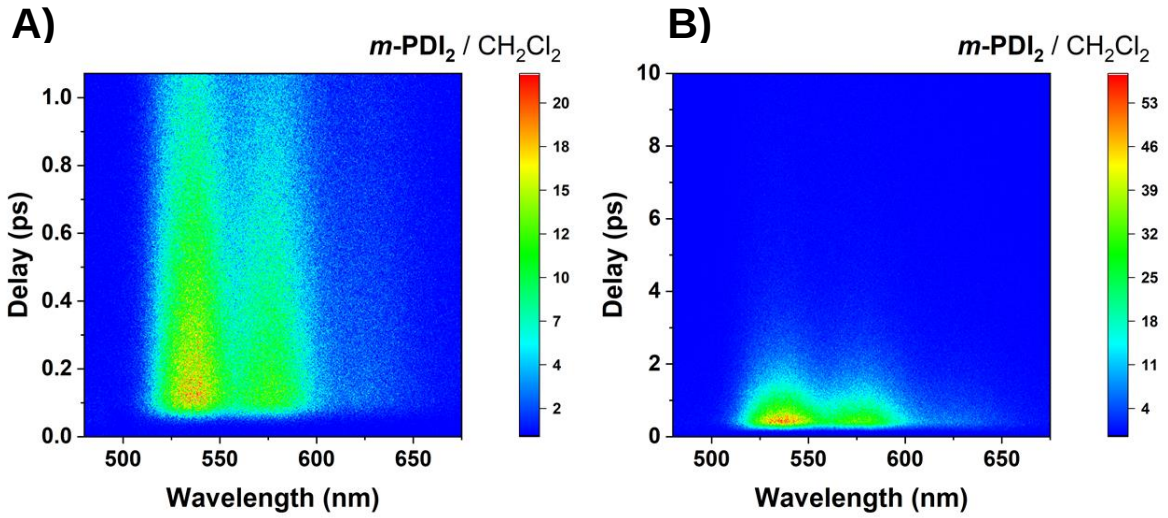

Figure 2.35. A) 1 ns and B) 10 ns psTRF spectra for ***m*-PDI$_2$** in CH_2Cl_2 following λ_{ex} = 480 nm, 1 nJ/pulse, ~50 fs excitation.

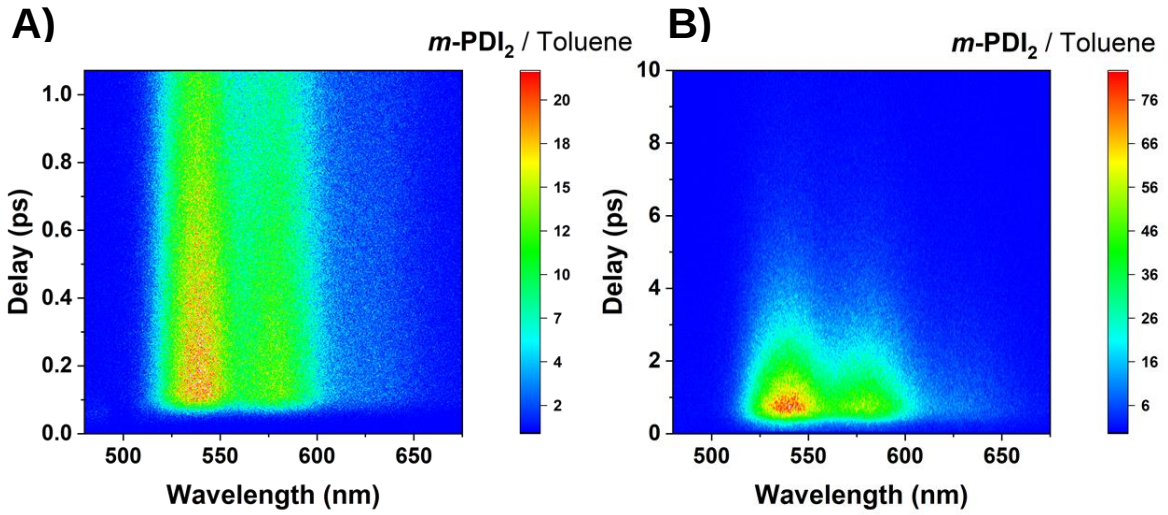

Figure 2.36. A) 1 ns and B) 10 ns psTRF spectra for ***m*-PDI$_2$** in toluene following λ_{ex} = 480 nm, 1 nJ/pulse, ~50 fs excitation.

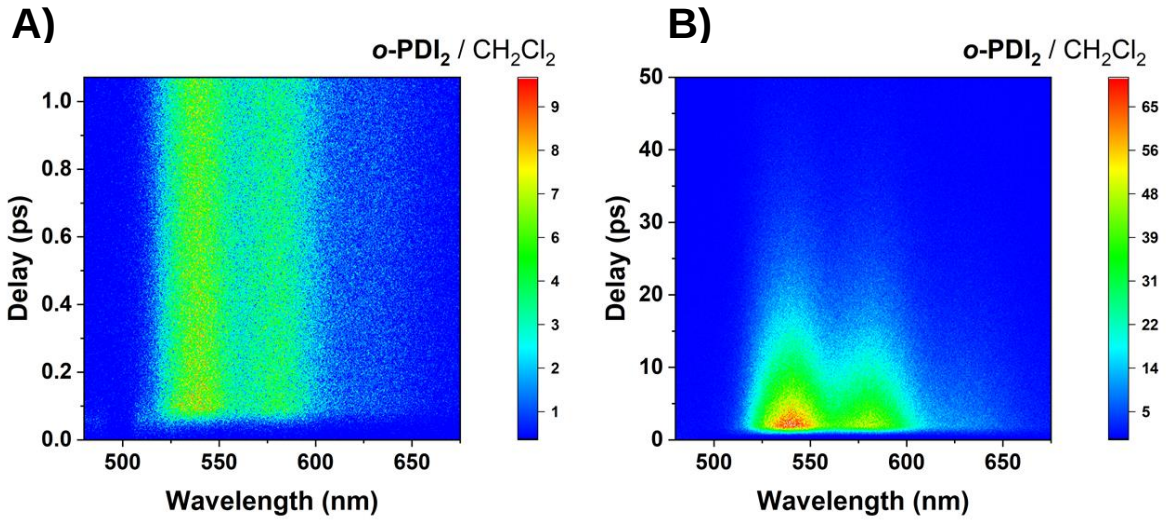

Figure 2.37. A) 1 ns and B) 50 ns psTRF spectra for ***o*-PDI$_2$** in CH_2Cl_2 following λ_{ex} = 480 nm, 1 nJ/pulse, ~50 fs excitation.

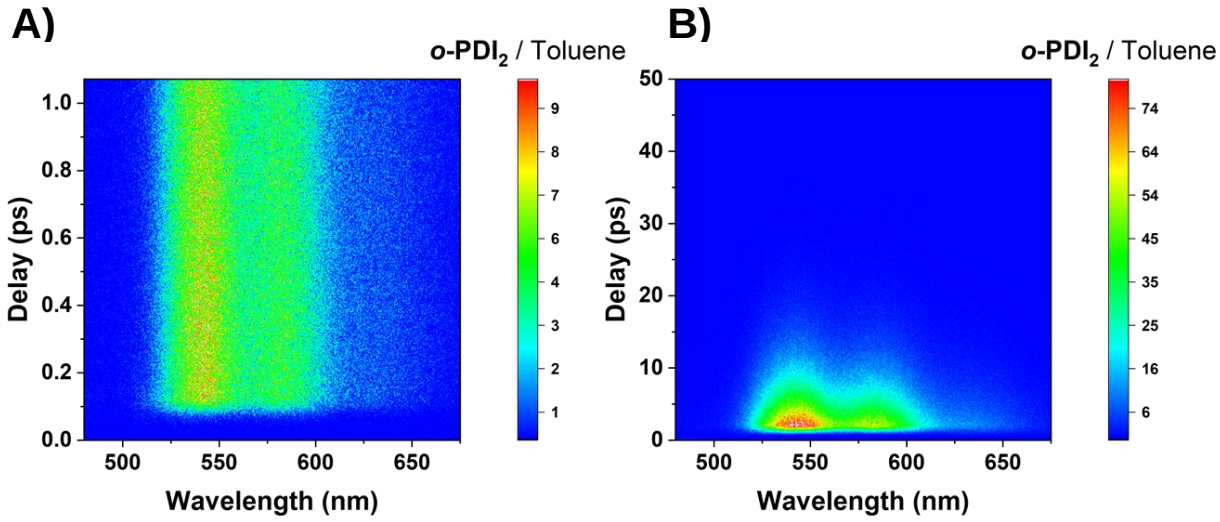

Figure 2.38. A) 1 ns and B) 50 ns psTRF spectra for ***o*-PDI$_2$** in toluene following λ_{ex} = 480 nm, 1 nJ/pulse, ~50 fs excitation.

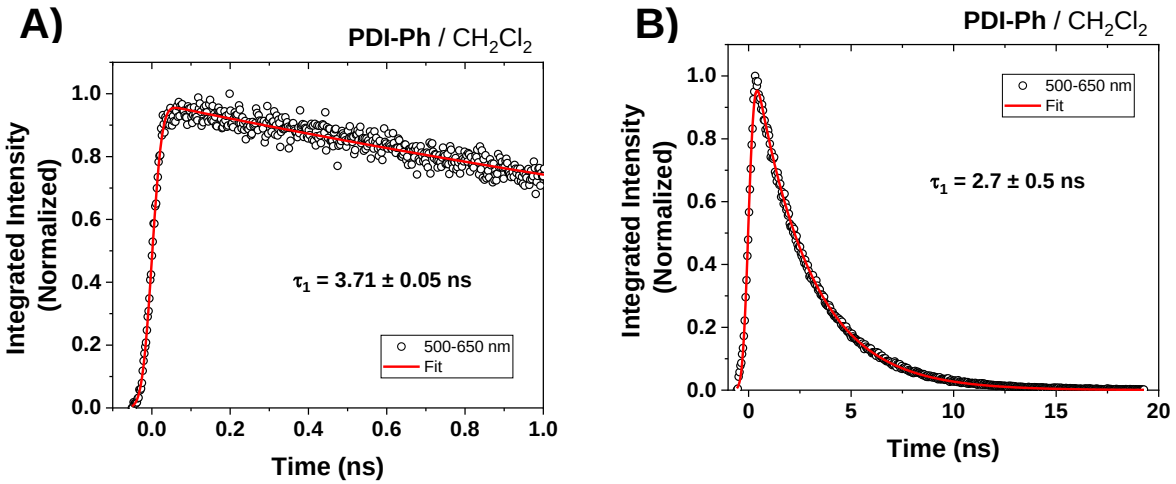

Figure 2.39. A) 1 ns and B) 10 ns psTRF windows and fits for **PDI-Ph** in CH_2Cl_2 following λ_{ex} = 480 nm, 1 nJ/pulse, ~50 fs excitation.

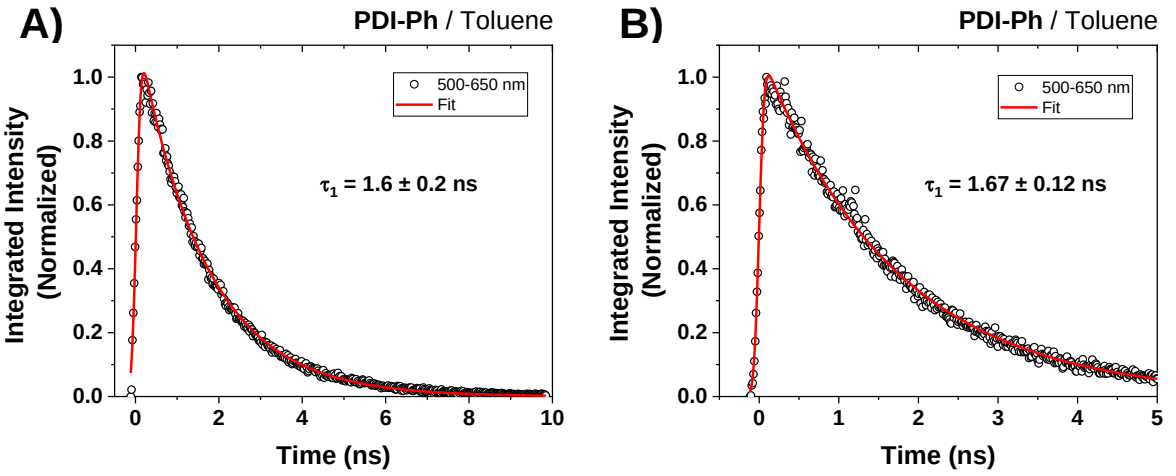

Figure 2.40. A) 5 ns and B) 10 ns psTRF windows and fits for **PDI-Ph** in toluene following λ_{ex} = 480 nm, 1 nJ/pulse, ~50 fs excitation.

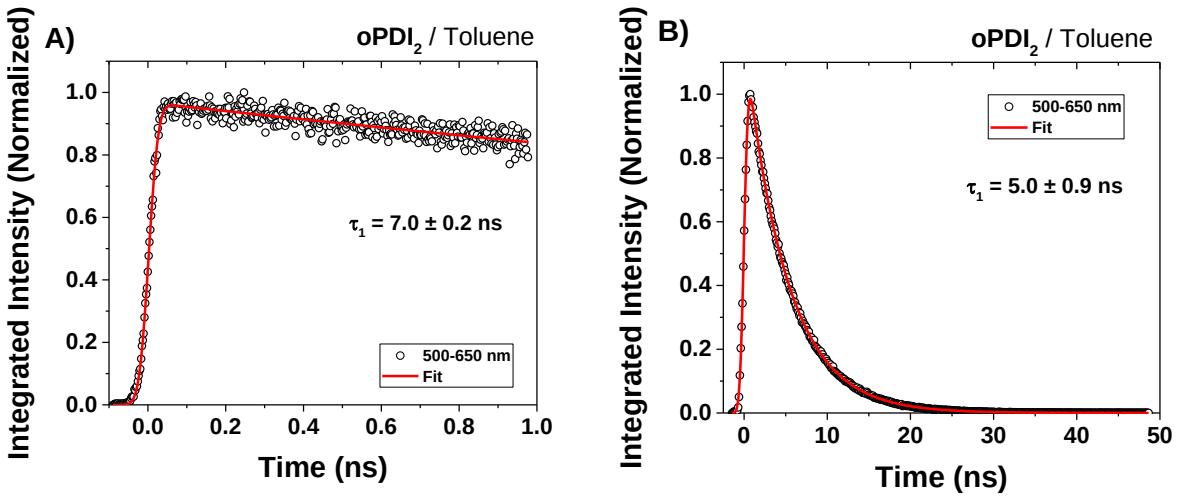

Figure 2.41. A) 1 ns and B) 50 ns picosecond TRF (psTRF) fits for ***o*-PDI₂** in toluene following λ_{ex} = 480 nm, 1 nJ/pulse, ~50 fs excitation.

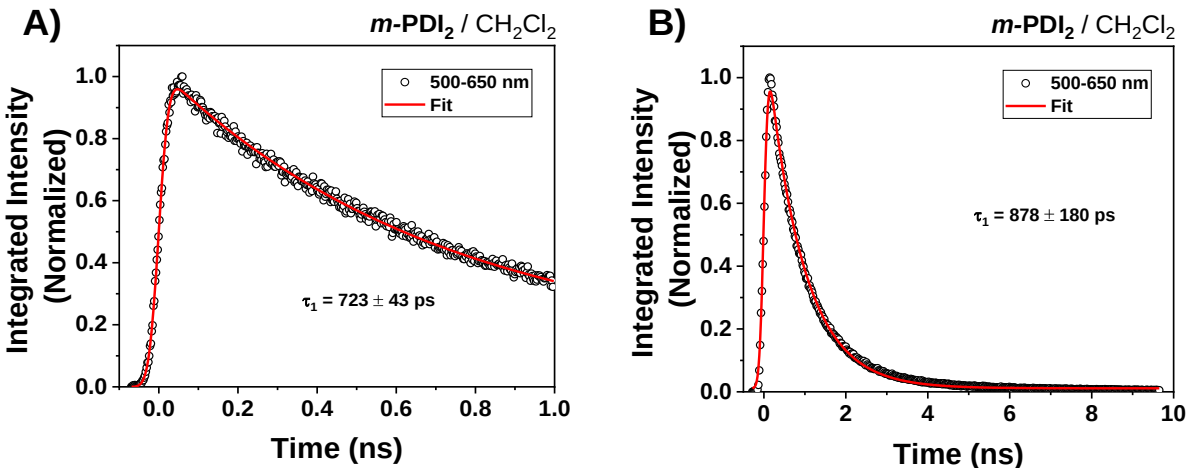

Figure 2.42. A) 1 ns and B) 10 ns picosecond TRF (psTRF) fits for ***m*-PDI₂** in CH_2Cl_2 λ_{ex} = 480 nm, 1 nJ/pulse, ~50 fs excitation.

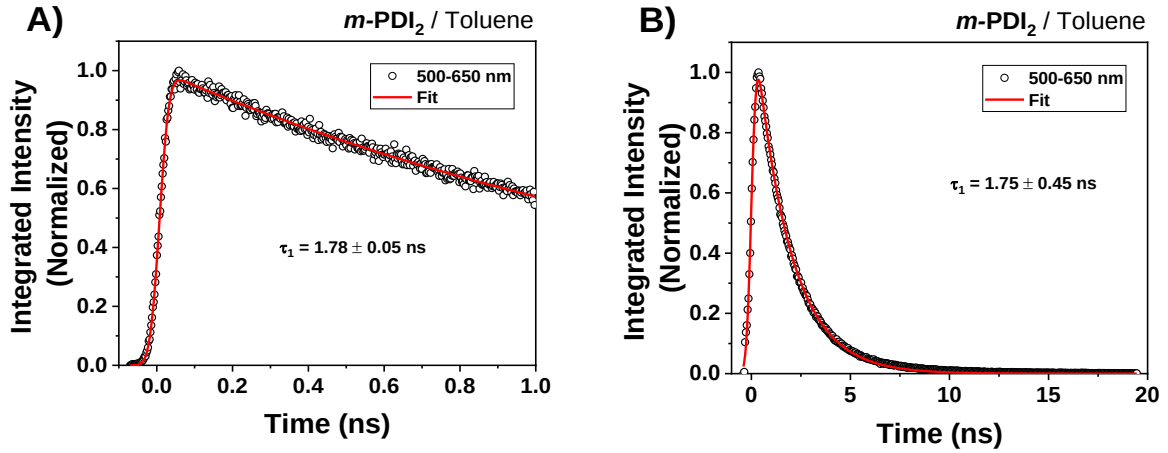

Figure 2.43. A) 1 ns and B) 1 ns and 20 ns picosecond TRF (psTRF) fits for ***m*-PDI$_2$** in toluene λ_{ex} = 480 nm, 1 nJ/pulse, ~50 fs excitation.

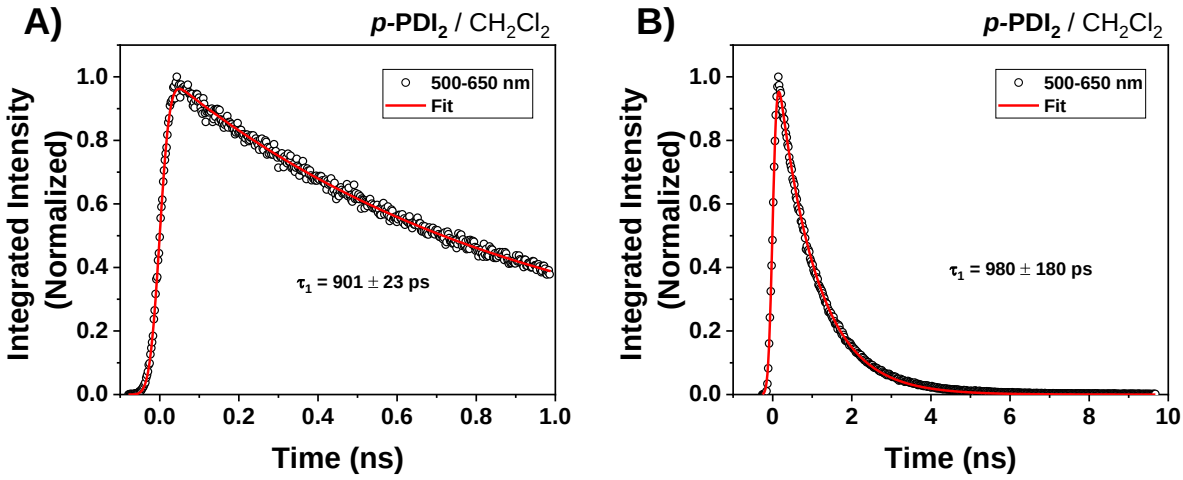

Figure 2.44. A) 1 ns and B) 10 ns picosecond TRF (psTRF) fits for ***p*-PDI$_2$** in CH_2Cl_2 λ_{ex} = 480 nm, 1 nJ/pulse, ~50 fs excitation.

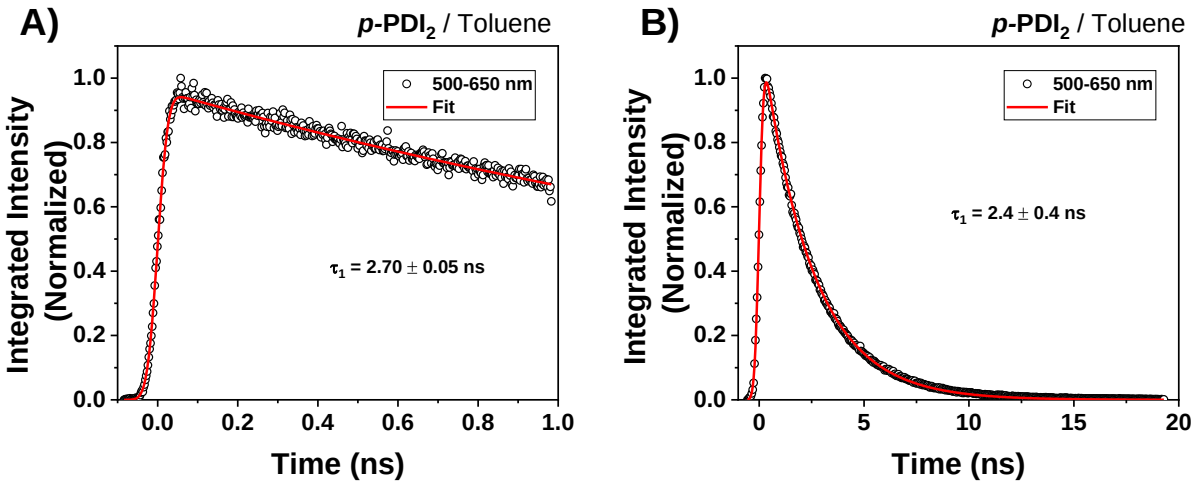

Figure 2.45. 1 ns and 20 ns picosecond TRF (psTRF) fits for ***p*-PDI$_2$** in toluene λ_{ex} = 480 nm, 1 nJ/pulse, ~50 fs excitation.

2.5.4. Computational Details

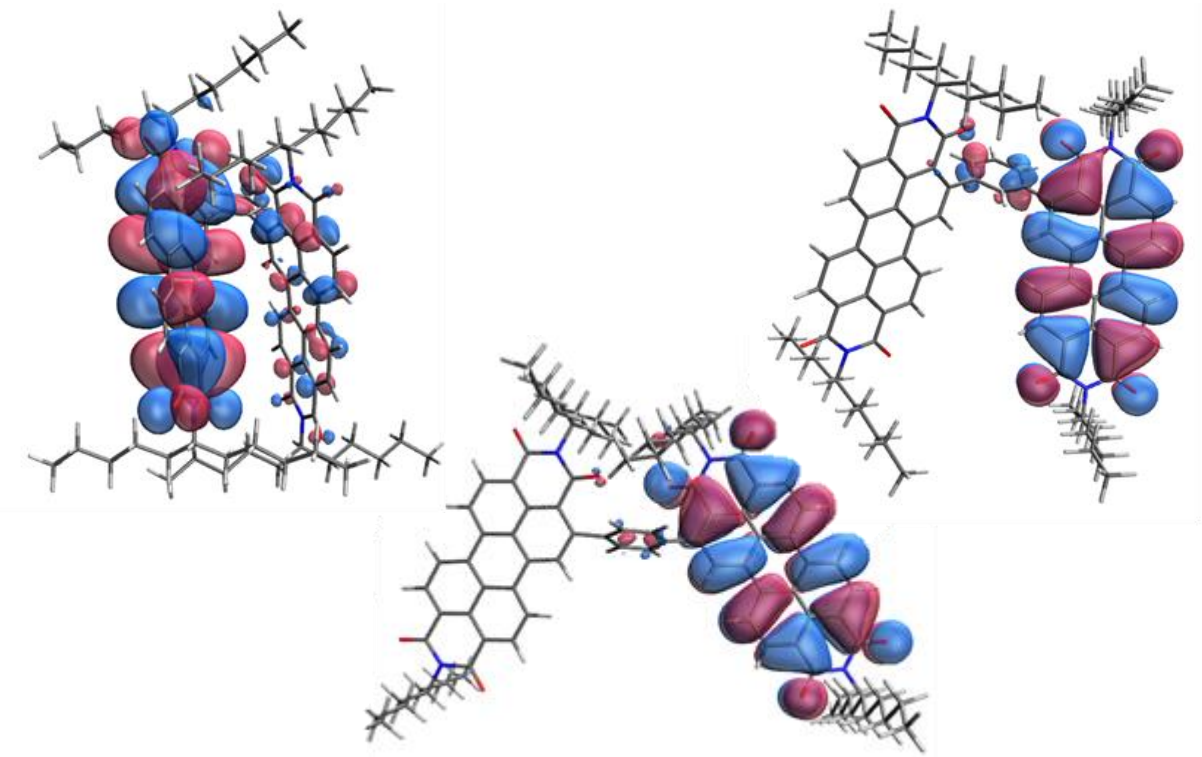

Figure 2.46. Visualizations of the highest-occupied molecular orbitals (HOMOs) for ***o*-PDI$_2$,** (left) ***m*-PDI$_2$** (right) and ***p*-PDI$_2$** (bottom).

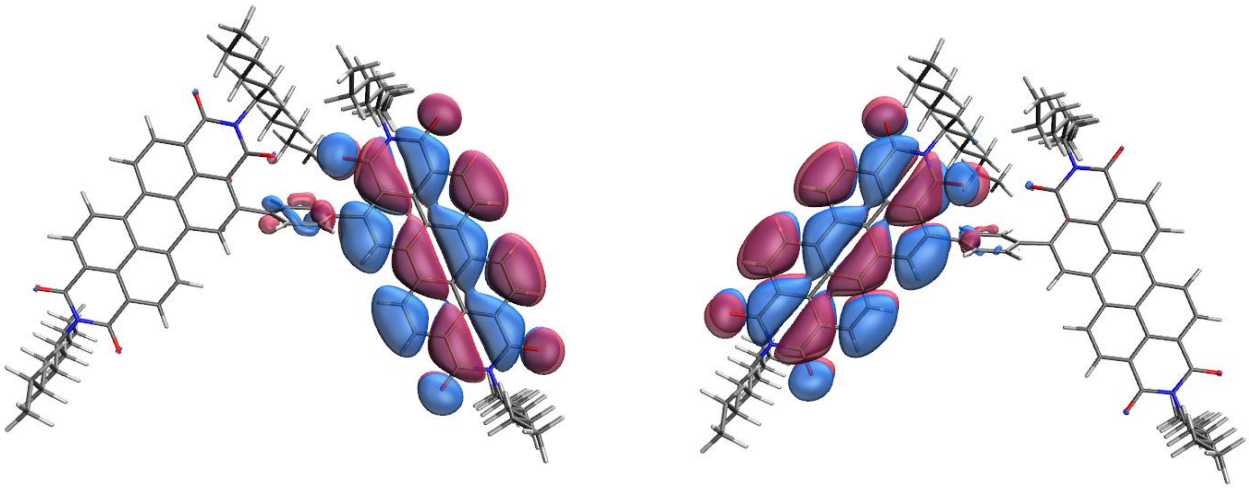

Figure 2.47. Visualizations of the lowest-unoccupied molecular orbital (LUMO, left) and LUMO+1 (right) for ***p*-PDI$_2$**.

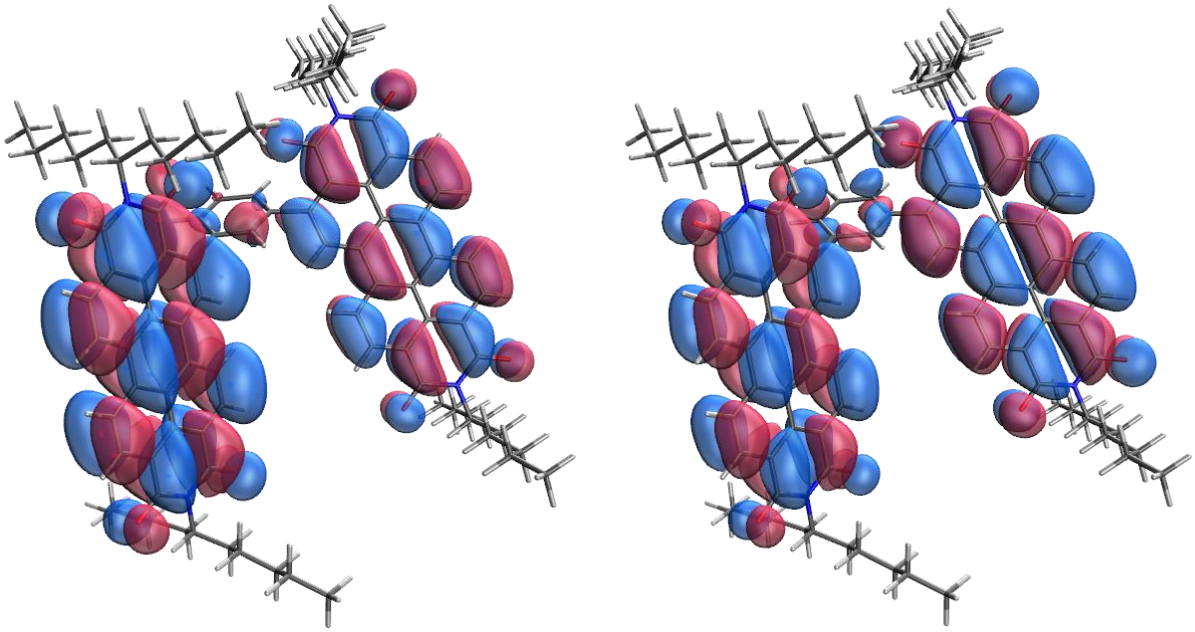

Figure 2.48. Visualizations of the lowest-unoccupied molecular orbital (LUMO, left)) and LUMO+1 (right) for ***m*-PDI$_2$**.

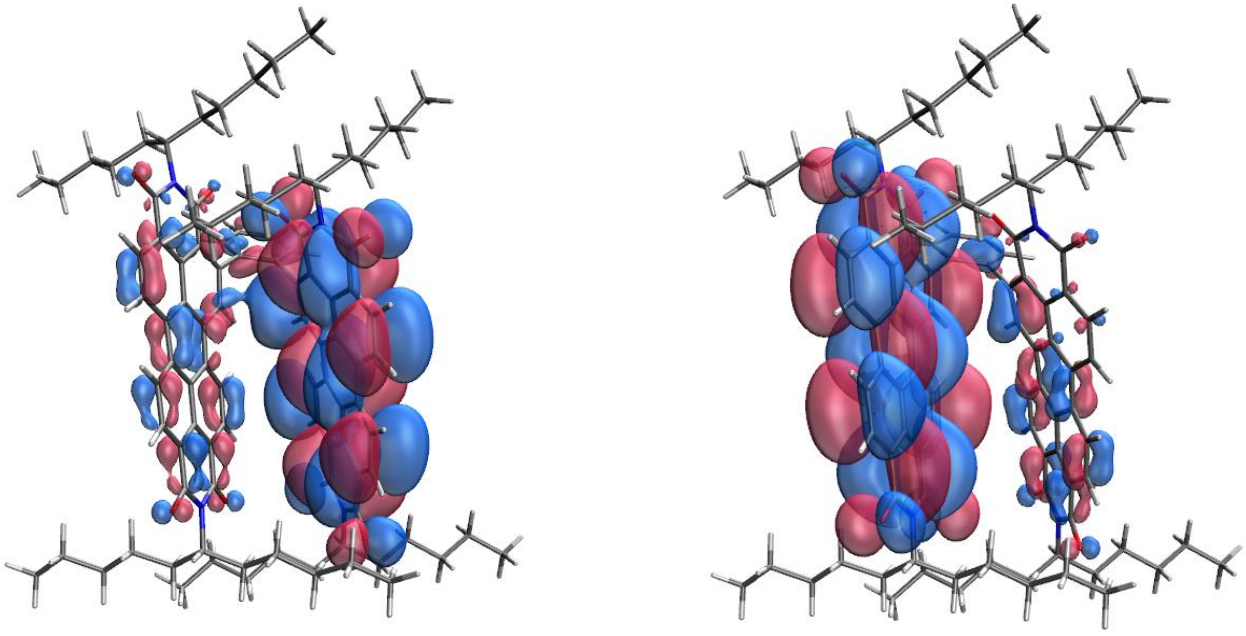

Figure 2.49. Visualizations of the lowest-unoccupied molecular orbital (LUMO, left) and LUMO+1 (right) for ***o*-PDI$_2$**.

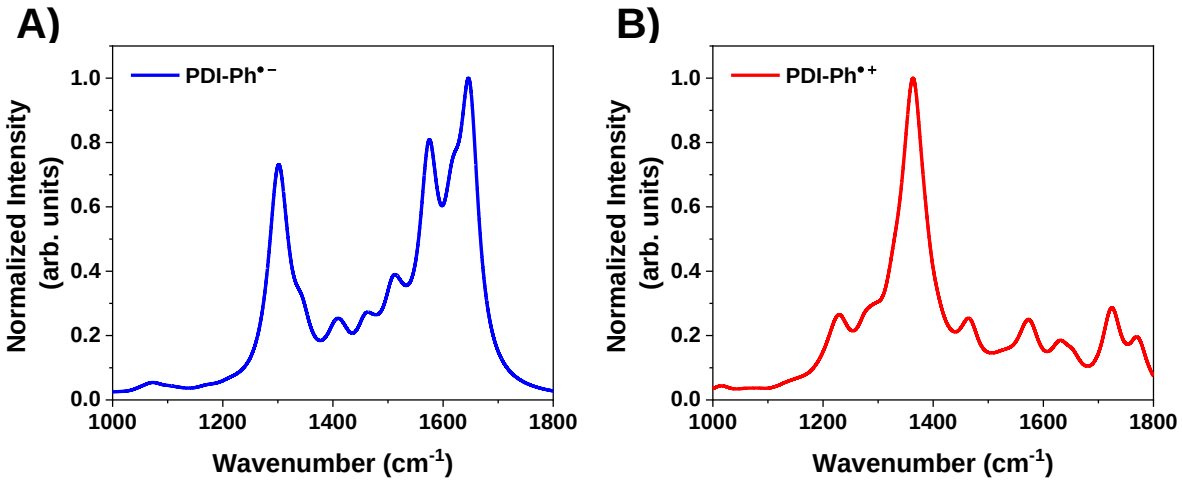

Figure 2.50. DFT-calculated IR spectra of **PDI-Ph** A) radical anion and B) radical cation states. were broadened using 40 cm^{-1} Lorentzian lineshapes and normalized. The frequency axis was scaled by 0.96 to best match the experimental data.

Table 2.3. Selected IR Peak Assignments for the **PDI-Ph** radical anion.

Exp. (cm^{-1})	Calc (cm^{-1})	Intensity (km/mol)	Assignment	Mode
1330	1354.6 1355.6	714.7 478.3	$\nu_{C=C}$ ω_{C-H}	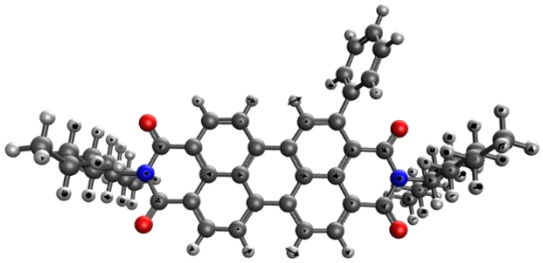
1368	1462.5	218.6	$\nu_{C=C}$ ω_{C-H}	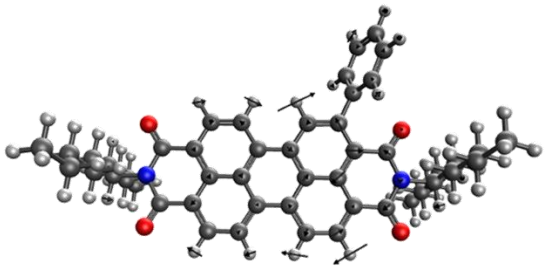

1520	1570.86	441.5	$\nu_{C=C}$ ω_{C-H}	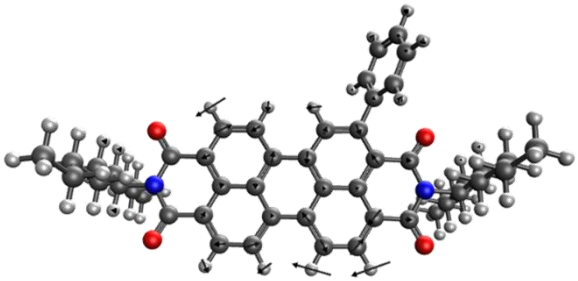
1583	1640.0	1482.9	$\nu_{C=C}$ ω_{C-H}	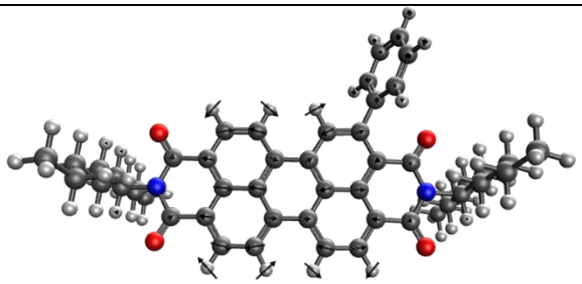
1640	1716.34	1938.4	$\nu_{C=O}$ $\nu_{C=O}$	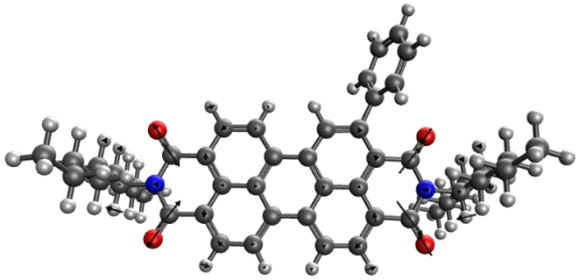

DFT / B3LYP; 6-31G(d), scaling factor: 0.96. ν = stretch, ω = wag.

Table 2.4. Selected IR Peak Assignments for the **PDI-Ph** radical cation.

Exp. (cm^{-1})	**Calc (cm^{-1})**	**Intensity (km/mol)**	**Assignment**	**Mode**
1264	1363.5	837.6	$\nu_{C=C}$ ω_{C-H}	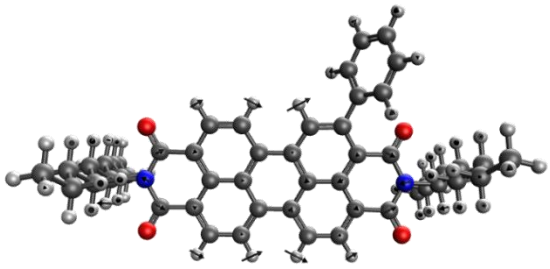

DFT / B3LYP; 6-31G(d), scaling factor: 0.96. ν = stretch, ω = wag.

Cartesian Coordinates

***o*PDI$_2$:**

C	-4.28604	-3.88893	1.51947	H	-7.75284	-0.05980	1.11354
C	-4.67458	-2.99175	0.54165	H	-9.30252	-0.91258	1.14861
C	-3.70789	-2.26735	-0.19524	C	-9.82297	1.56668	2.25982
C	-2.32233	-2.47663	0.09249	H	-10.40668	1.19600	0.20956
C	-1.94109	-3.36423	1.15000	H	-8.85568	2.02774	0.36918
C	-2.93605	-4.06804	1.82888	C	-10.51816	2.93957	2.38833
C	-0.51424	-3.50065	1.48719	H	-11.44030	2.96070	1.79566
C	0.45841	-2.85328	0.65903	H	-9.85977	3.73682	2.02151
C	0.08309	-2.02735	-0.44794	H	-10.77403	3.15958	3.43075
C	-1.34842	-1.78646	-0.69305	H	-8.90363	1.56732	2.85788
C	-0.07315	-4.23513	2.59094	H	-10.47267	0.78126	2.66787
C	1.28811	-4.37148	2.88517	H	-8.40620	-2.61060	-0.40880
C	2.24235	-3.78582	2.07346	C	6.06279	-3.65152	1.85304
C	1.84430	-3.02773	0.95221	C	6.66026	-4.64674	0.83390
C	2.82864	-2.44467	0.12324	C	5.85556	-5.95922	0.72097
C	2.44552	-1.68029	-0.96289	H	7.67965	-4.87733	1.17156
C	1.08957	-1.46373	-1.23568	H	6.73075	-4.16043	-0.14270
C	-1.79466	-0.89789	-1.66054	C	6.54889	-6.99552	-0.18996
C	-3.15745	-0.63246	-1.90760	H	4.85939	-5.74141	0.31461
C	-4.12663	-1.34234	-1.19464	H	5.70961	-6.38688	1.72200
C	-5.58301	-1.15410	-1.45974	C	5.73202	-8.29798	-0.33687
C	-6.12223	-2.84401	0.28895	H	7.53923	-7.23587	0.22193
N	-6.48756	-1.93389	-0.71219	H	6.70934	-6.55486	-1.18379
C	4.27295	-2.65398	0.37934	C	6.43100	-9.32681	-1.25174
C	3.67011	-3.96330	2.40805	H	6.57687	-8.91174	-2.25604
N	4.61270	-3.37729	1.53121	H	5.83773	-10.24353	-1.34253
O	4.03393	-4.61971	3.39831	H	7.41477	-9.59391	-0.84802
O	5.13444	-2.19928	-0.39865	H	4.74128	-8.05601	-0.74425
O	-6.01489	-0.37515	-2.32231	H	5.57457	-8.73605	0.65771
O	-6.96637	-3.50346	0.92198	C	6.91306	-2.36830	1.99572
C	-7.56247	-6.11076	-6.00283	H	6.00135	-4.14681	2.82391
C	-7.24330	-5.63546	-4.56896	C	6.42404	-1.39349	3.08806
H	-7.16625	-5.40240	-6.74012	H	6.95897	-1.85605	1.03298
H	-8.64627	-6.18504	-6.15083	H	7.92832	-2.69916	2.25314
H	-7.12134	-7.09391	-6.20108	C	7.37076	-0.17891	3.22171
C	-7.86236	-4.25464	-4.25902	H	6.36183	-1.91911	4.05096
H	-6.15479	-5.57947	-4.43381	H	5.41424	-1.03921	2.84288
H	-7.62164	-6.36862	-3.84430	C	6.93408	0.82470	4.31131
C	-7.54559	-3.76383	-2.82936	H	7.41875	0.35211	2.26186
H	-8.95205	-4.31070	-4.39059	H	8.38556	-0.53421	3.45019
H	-7.48658	-3.51973	-4.98496	C	7.85708	2.06526	4.34696
C	-8.15116	-2.37270	-2.54656	H	7.84919	2.56250	3.37045
H	-6.45614	-3.72239	-2.70204	H	8.88825	1.76948	4.57293
H	-7.93084	-4.48858	-2.09876	H	7.53379	2.78099	5.11211
C	-7.94853	-1.89023	-1.09019	H	6.92929	0.32644	5.28973
H	-9.23538	-2.41407	-2.71681	H	5.90237	1.14205	4.10483
H	-7.72809	-1.63138	-3.22950	H	-5.06104	-4.43671	2.03927
C	-8.57510	-0.49828	-0.85457	H	-2.67266	-4.77095	2.60677
C	-8.73773	-0.12351	0.63326	H	-1.07744	-0.35115	-2.25341
H	-9.57312	-0.52094	-1.31404	C	-3.43065	0.41770	-2.94086
H	-7.97964	0.24969	-1.38205	H	0.83158	-0.84070	-2.08039
C	-9.47601	1.22590	0.79397	H	3.21821	-1.24954	-1.58688

H	-0.78998	-4.70617	3.24925
H	1.62327	-4.93553	3.74600
C	-2.99072	1.73604	-2.72481
C	-4.03055	0.08898	-4.16206
C	-4.22352	1.05297	-5.14738
C	-3.19769	2.70535	-3.72007
C	-3.82343	2.37183	-4.91886
H	-4.69263	0.77932	-6.08468
H	-4.36294	-0.92700	-4.32598
H	-4.69542	-3.69767	5.87536
H	-4.55656	-2.11995	6.67885
C	-5.08623	-2.67379	5.89466
H	-6.14715	-2.71894	6.16709
H	7.99301	-4.92279	-2.83266
H	-3.84477	-1.96048	4.25563
C	-4.90867	-1.97973	4.52680
C	8.59780	-4.12344	-2.38888
H	8.82313	-4.40165	-1.35176
H	-5.42832	-2.55390	3.75009
H	9.54429	-4.06509	-2.93967
H	-4.95110	0.04069	5.31611
H	6.89961	-2.84154	-1.90990
H	7.63757	-2.51112	-3.48346
C	-5.45597	-0.53783	4.52983
H	-6.52551	-0.56187	4.78177
C	7.85644	-2.77004	-2.43824
H	-4.20010	0.21926	2.92885
C	-5.26884	0.18522	3.17655
C	8.68429	-1.62879	-1.80633
H	-5.77093	-0.38509	2.38274
H	8.86480	-1.85529	-0.74601
H	9.66385	-1.57043	-2.30212
H	-5.39399	2.17144	4.04985
H	6.99613	-0.34280	-1.41552
H	7.76399	-0.05791	-2.98289
C	-5.84176	1.61504	3.22528
H	-6.92303	1.55125	3.39969
C	7.96575	-0.26864	-1.92411
O	-3.64226	3.51405	3.53561
O	-4.76532	1.68675	-0.55738
C	-2.10301	2.10921	-1.57129
H	-0.50609	2.11554	-2.97676
C	-5.65715	2.41600	1.91710
C	-3.88860	2.14883	0.19013
C	-3.29423	3.06183	2.42892
C	8.78677	0.89632	-1.32425
C	-0.74557	2.26504	-1.93282
C	-2.47976	2.32699	-0.24697
N	-4.20821	2.53309	1.51458
H	1.39710	2.39697	-3.52257
H	8.80611	0.83200	-0.23238
H	-6.10172	1.85964	1.09008
H	9.82133	0.82999	-1.68819
C	-1.49014	2.70636	0.70235
C	0.25967	2.54817	-1.01741
C	2.11691	2.47548	-2.71967
C	-1.87424	3.04452	2.01985
H	3.81397	2.34529	-4.06706
C	-0.10842	2.76384	0.34700
C	1.68163	2.60360	-1.39817
C	3.47973	2.44237	-3.04227
C	-0.92507	3.40713	2.95728
C	0.86737	3.04452	1.35507
C	2.65823	2.74198	-0.36173
C	4.43661	2.51102	-2.04619
O	6.22810	2.32765	-3.60338
C	2.29151	2.93788	1.00798
C	4.04259	2.65849	-0.69953
C	0.43471	3.38512	2.63680
C	5.86716	2.42209	-2.41797
H	-5.85535	4.38200	2.79967
H	-7.37324	3.65457	2.23613
H	8.23857	2.34549	-2.82970
N	6.80224	2.43954	-1.36030
C	5.02545	2.69303	0.31429
C	3.29633	2.98265	1.97398
C	-6.31568	3.81280	1.98652
C	8.25564	2.28717	-1.73954
C	4.64704	2.84564	1.63392
C	6.46057	2.52324	-0.00586
H	3.03730	3.09739	3.01760
H	1.15280	3.64640	3.40203
H	5.41413	2.85286	2.39606
O	7.31753	2.42559	0.89363
C	-6.22582	4.59368	0.65663
C	9.11386	3.44704	-1.19271
H	10.13311	3.29052	-1.57189
H	-5.18926	4.91420	0.48844
H	-6.49650	3.92918	-0.17463
H	9.14313	3.39085	-0.10291
H	-6.87844	6.49426	1.48529
H	-8.18345	5.51691	0.79816
H	8.54682	4.86862	-2.73738
C	-7.14250	5.83653	0.64528
C	8.61545	4.83773	-1.64104
H	7.60517	5.00910	-1.24688
C	-7.04593	6.63182	-0.67465
H	10.55206	5.81677	-1.55388
C	9.54062	5.97410	-1.15336
H	-6.00693	6.95552	-0.82228
H	-7.29993	5.96792	-1.51152
H	9.61602	5.93304	-0.05782
H	-9.02289	7.55411	-0.55929
H	8.96164	7.41057	-2.67074
H	-7.72327	8.54516	0.13332
C	-7.97834	7.86250	-0.68590
C	9.03937	7.37260	-1.57599
H	8.02874	7.52724	-1.17473
H	-7.89623	8.41339	-1.62953
C	9.97006	8.50149	-1.08267

H	10.97941	8.37381	-1.49138	H	-2.86241	3.72051	-3.54234
H	10.04198	8.48940	0.01127	H	-3.98570	3.13182	-5.67382
H	9.59758	9.48471	-1.39110	H	-1.26820	3.69151	3.94363

***m*-PDI$_2$**

C	-1.51474	-7.15944	1.99817	C	-6.51022	-4.05710	2.31831
C	-2.30320	-6.14185	1.48720	C	-5.78549	-3.91896	3.66343
C	-1.70807	-5.07366	0.77212	H	-7.57534	-4.25332	2.50688
C	-0.28844	-5.05242	0.60245	H	-6.45733	-3.11448	1.76562
C	0.50901	-6.11670	1.13067	C	-6.40187	-2.83409	4.55655
C	-0.12949	-7.14859	1.81870	H	-4.72669	-3.67936	3.49158
C	1.96520	-6.09122	0.92750	H	-5.79842	-4.88268	4.19286
C	2.55376	-4.98029	0.24514	C	-5.68309	-2.66187	5.90067
C	1.76131	-3.90311	-0.26044	H	-7.46015	-3.07259	4.74072
C	0.30115	-3.95905	-0.10082	H	-6.39723	-1.87487	4.01753
C	2.80264	-7.11405	1.37768	C	-6.30951	-1.57900	6.78522
C	4.18862	-7.07389	1.18875	H	-7.35621	-1.81272	7.01595
C	4.77868	-6.00205	0.54088	H	-6.29221	-0.60134	6.28736
C	3.96980	-4.94569	0.06221	H	-5.77370	-1.47813	7.73610
C	4.57908	-3.85557	-0.60076	H	-4.62633	-2.41969	5.71797
C	3.79553	-2.81308	-1.06523	H	-5.68594	-3.62080	6.43830
C	2.40726	-2.83965	-0.89373	H	-6.13225	-6.14289	1.98910
C	-0.53984	-2.98818	-0.63215	C	8.29256	-4.87249	-0.50606
C	-1.94391	-3.01245	-0.50547	C	8.68528	-4.97783	-1.99134
C	-2.53271	-4.05070	0.22455	C	8.10377	-6.19720	-2.71882
C	-4.00498	-4.07884	0.46609	H	9.78252	-5.03643	-2.01767
C	-3.76657	-6.20998	1.70793	H	8.40733	-4.05790	-2.51515
N	-4.53665	-5.15931	1.18873	C	8.60764	-6.32532	-4.16224
C	6.04867	-3.80997	-0.81216	H	7.00660	-6.13322	-2.72939
C	6.25125	-5.98314	0.36036	H	8.34989	-7.11219	-2.16127
N	6.80709	-4.87846	-0.31532	C	8.01747	-7.52614	-4.91255
O	6.95286	-6.89539	0.77917	H	9.70512	-6.40429	-4.15976
O	6.57447	-2.87311	-1.40158	H	8.37163	-5.40210	-4.71206
O	-4.74224	-3.19035	0.06275	C	8.52551	-7.64638	-6.35294
O	-4.27500	-7.14024	2.32279	H	8.27564	-6.75189	-6.93680
C	-7.85268	-7.94047	-4.15134	H	8.08529	-8.51097	-6.86291
C	-6.92951	-7.80300	-2.93639	H	9.61593	-7.76376	-6.37980
H	-7.85320	-7.02367	-4.75381	H	6.92095	-7.44673	-4.91627
H	-8.88767	-8.13238	-3.84249	H	8.25292	-8.44844	-4.36267
H	-7.54053	-8.76621	-4.80093	C	8.97306	-3.68949	0.20757
C	-7.33193	-6.65680	-1.99952	H	8.60679	-5.79152	-0.00928
H	-5.89617	-7.64602	-3.27779	C	8.66516	-3.58204	1.70682
H	-6.92231	-8.74651	-2.37242	H	8.71621	-2.75329	-0.29657
C	-6.41300	-6.50669	-0.78028	H	10.05468	-3.83394	0.07574
H	-8.36596	-6.81491	-1.65837	C	9.45406	-2.46096	2.39610
H	-7.34110	-5.71270	-2.56430	H	8.88306	-4.54077	2.19947
C	-6.82313	-5.33846	0.12589	H	7.59098	-3.40158	1.85326
H	-5.38063	-6.36185	-1.12880	C	9.13925	-2.32004	3.89074
H	-6.41154	-7.44236	-0.20292	H	9.24542	-1.50678	1.88993
C	-6.01392	-5.21360	1.43022	H	10.53192	-2.64199	2.26891
H	-7.87059	-5.47590	0.42960	C	9.93051	-1.19850	4.57143
H	-6.77891	-4.39794	-0.43120	H	9.71664	-0.22634	4.11034

H	11.01098	-1.37089	4.49140
H	9.68366	-1.12340	5.63670
H	9.34677	-3.27401	4.39624
H	8.06261	-2.13737	4.01787
H	-2.00008	-7.96590	2.53695
H	0.44384	-7.96912	2.23323
H	-0.12448	-2.16844	-1.20557
C	-2.67181	-1.92038	-1.22524
H	1.83390	-2.00143	-1.27176
H	4.27919	-1.98099	-1.56572
H	2.38748	-7.97446	1.88893
H	4.82152	-7.87872	1.54668
C	-2.56630	-0.59800	-0.77818
C	-3.33289	-2.17859	-2.43123
C	-3.88799	-1.13032	-3.16298
C	-3.14173	0.45980	-1.49580
C	-3.79754	0.18011	-2.70183
H	-4.39236	-1.33688	-4.10285
H	-4.23078	0.99093	-3.27881
H	-2.05109	-0.39250	0.15663
H	-3.40741	-3.19870	-2.79637
H	-8.14247	1.94982	6.51165
H	-8.78970	3.48343	5.90669
C	-8.65566	2.42159	5.66576
H	-9.65356	1.97226	5.58960
H	6.47768	5.73721	7.70995
H	-6.86333	2.67517	4.48246
C	-7.86815	2.24490	4.36365
C	6.75692	6.40525	6.88712
H	6.30804	7.38611	7.08697
H	-7.71791	1.17334	4.16840
H	7.84652	6.52983	6.91437
H	-8.69931	3.96111	3.34301
H	5.20742	5.70609	5.54986
H	6.73419	4.85546	5.37806
C	-8.55083	2.88824	3.14956
H	-9.55733	2.45972	3.03085
C	6.29705	5.85184	5.53445
H	-6.75458	3.12309	1.98127
C	-7.76433	2.71106	1.84449
C	6.66859	6.75797	4.35387
H	-7.62959	1.63973	1.63935
H	6.23342	7.75599	4.51174
H	7.75927	6.90242	4.33790
H	-8.52684	4.46306	0.81324
H	5.11956	6.06624	3.02186
H	6.64742	5.22095	2.82800
C	-8.43810	3.38568	0.64189
H	-9.46118	2.99668	0.54075
C	6.20814	6.21501	2.99465
O	-6.80786	5.72601	-0.38756
O	-5.72433	1.30609	-0.84535
C	-2.91297	1.86495	-1.04632
H	-0.82570	1.46925	-1.07444
C	-7.74122	3.12480	-0.70658
C	-5.34966	2.46798	-0.79312
C	-5.95371	4.85134	-0.48668
C	6.57636	7.14390	1.83028
C	-1.56188	2.24114	-0.88835
C	-3.90274	2.83308	-0.82460
N	-6.29456	3.51334	-0.68047
H	1.04568	1.86628	-0.59016
H	6.11438	8.12572	1.97092
H	-7.70397	2.04572	-0.85844
H	7.66384	7.30379	1.83287
C	-3.51559	4.17291	-0.53620
C	-1.14660	3.52399	-0.55430
C	1.28769	2.91027	-0.42987
C	-4.50995	5.17021	-0.38279
H	3.41130	2.49681	-0.32213
C	-2.13908	4.53884	-0.40899
C	0.27152	3.86616	-0.37376
C	2.63518	3.25310	-0.27442
C	-4.14609	6.48248	-0.13075
C	-1.78182	5.89871	-0.14402
C	0.62778	5.22852	-0.12749
C	3.00304	4.57048	-0.05819
O	5.30337	4.04090	0.02606
C	-0.36074	6.25694	-0.02278
C	2.00667	5.57007	0.02060
C	-2.80141	6.84142	-0.01273
C	4.44054	4.90738	0.09044
H	-8.57765	4.82890	-1.76271
H	-9.51122	3.33977	-1.86629
H	6.70916	5.62433	0.32314
N	4.77079	6.26049	0.30537
C	2.39070	6.91170	0.24787
C	0.06515	7.56809	0.20007
C	-8.49075	3.74710	-1.89908
C	6.22442	6.59513	0.43525
C	1.41963	7.89478	0.33164
C	3.82030	7.28704	0.39218
H	-0.65780	8.37156	0.27639
H	-2.56767	7.88023	0.18759
H	1.73002	8.92005	0.50180
O	4.15305	8.45190	0.57771
C	-7.87556	3.43532	-3.26970
C	6.71724	7.50521	-0.70565
H	7.80308	7.60724	-0.56914
H	-6.86955	3.87359	-3.33206
H	-7.74351	2.34846	-3.37629
H	6.29063	8.50682	-0.59532
H	-8.86099	5.04869	-4.31969
H	-9.72566	3.52068	-4.38881
H	6.82020	5.93715	-2.19869
C	-8.71975	3.96400	-4.43655
C	6.44143	6.96609	-2.11568
H	5.35692	6.90621	-2.28408
C	-8.10744	3.67900	-5.81391
H	8.15567	7.87800	-3.07167

C	7.06618	7.83106	-3.21821	C	6.76879	7.32335	-4.63505
H	-7.10292	4.12342	-5.86229	H	5.68006	7.28194	-4.78260
H	-7.96574	2.59485	-5.92963	H	-8.49423	3.98964	-7.94288
H	6.70235	8.86459	-3.11967	C	7.39958	8.18718	-5.73183
H	-9.95618	3.75785	-6.97121	H	8.49181	8.21707	-5.63401
H	7.12740	6.28868	-4.73147	H	7.03547	9.22076	-5.68086
H	-9.08587	5.29661	-6.90497	H	7.16576	7.80076	-6.73049
C	-8.95643	4.20945	-6.97364	H	-4.93139	7.22341	-0.02727

***p*-PDI$_2$**

C	6.86286	3.94979	-0.32577	H	2.25545	4.51417	2.03065
C	5.48796	3.81792	-0.30391	H	2.44017	6.18867	2.56794
C	4.89806	2.53372	-0.23529	C	2.41166	6.09780	-0.28666
C	5.73071	1.37530	-0.15099	H	0.79388	6.93437	0.83650
C	7.15279	1.53051	-0.22246	H	0.51963	5.24434	0.36152
C	7.68542	2.81837	-0.30547	C	1.86989	6.46786	-1.68603
C	8.00115	0.32748	-0.19272	C	2.96671	6.62392	-2.76182
C	7.38476	-0.94963	0.00935	H	1.33084	7.41941	-1.57948
C	5.96666	-1.09973	0.13929	H	1.15250	5.70010	-1.99135
C	5.11411	0.09487	0.02048	C	2.39848	7.18523	-4.08328
C	9.38775	0.38524	-0.35248	H	3.42009	5.64355	-2.95827
C	10.18384	-0.76463	-0.29470	H	3.76368	7.27835	-2.38654
C	9.61053	-2.00200	-0.07011	C	3.45504	7.26581	-5.20607
C	8.21165	-2.11198	0.08320	H	1.98489	8.18764	-3.90337
C	7.63734	-3.38160	0.30917	H	1.56675	6.54872	-4.41684
C	6.26849	-3.50321	0.45305	C	2.86779	7.83343	-6.51640
C	5.44398	-2.37583	0.36380	H	2.48843	8.84996	-6.35850
C	3.72477	0.02862	0.09530	H	2.03513	7.21045	-6.86403
C	2.90322	1.16224	-0.04179	H	3.62451	7.86914	-7.30801
C	3.48556	2.41320	-0.23528	H	3.86043	6.26171	-5.38892
C	2.65020	3.61718	-0.50811	H	4.28959	7.89599	-4.87116
C	4.66478	5.04918	-0.27998	H	3.10644	6.87306	0.04336
N	3.27595	4.86496	-0.33785	C	10.75735	-5.63625	0.36532
C	8.47418	-4.60032	0.40209	C	10.66671	-6.27213	1.77102
C	10.48678	-3.19201	0.00474	C	11.04725	-5.30341	2.91038
N	9.85756	-4.43133	0.25469	H	11.35741	-7.12626	1.78168
O	11.71738	-3.10586	-0.13903	H	9.65336	-6.65321	1.92024
O	7.96491	-5.71789	0.60571	C	10.99015	-5.98411	4.29561
O	1.46254	3.54967	-0.85515	H	10.36140	-4.44636	2.90794
O	5.17530	6.18119	-0.21902	H	12.05872	-4.91103	2.73671
C	-0.26545	4.33057	5.34438	C	11.36420	-5.02526	5.44688
C	0.94717	4.62080	4.43398	H	11.67342	-6.84501	4.30730
H	-0.95292	3.63178	4.85262	H	9.97632	-6.37335	4.46430
H	-0.82065	5.25182	5.55688	C	11.28908	-5.71242	6.82720
H	0.04793	3.89170	6.29836	H	10.27386	-6.07956	7.01878
C	0.53209	5.26580	3.09411	H	11.55950	-5.01771	7.63017
H	1.47863	3.68117	4.22692	H	11.97368	-6.56786	6.86884
H	1.65339	5.28094	4.95481	H	10.68666	-4.16108	5.42866
C	1.72852	5.47101	2.13710	H	12.38007	-4.64302	5.28022
H	0.05287	6.23486	3.29498	C	10.47133	-6.65447	-0.76109
H	-0.21295	4.63538	2.59215	H	11.75526	-5.21618	0.22316
C	1.26542	5.94627	0.74391	C	10.62137	-6.06108	-2.17798

H	9.46449	-7.05760	-0.62563
H	11.18938	-7.47662	-0.63836
C	10.43035	-7.12929	-3.27700
H	11.61397	-5.60182	-2.28151
H	9.87876	-5.26568	-2.32105
C	10.55517	-6.54882	-4.70268
H	9.44094	-7.59341	-3.16117
H	11.17843	-7.92360	-3.14490
C	10.36522	-7.62809	-5.79027
H	9.37446	-8.08962	-5.70398
H	11.11891	-8.41722	-5.68397
H	10.45757	-7.19907	-6.79421
H	11.54270	-6.08196	-4.81516
H	9.80575	-5.75709	-4.83476
H	7.27886	4.94876	-0.35213
H	8.75657	2.96182	-0.33378
H	3.23042	-0.91805	0.26390
C	1.42401	1.01735	0.11283
H	4.37717	-2.51331	0.47310
H	5.85734	-4.48876	0.63023
H	9.87302	1.33507	-0.52894
H	11.25796	-0.71056	-0.41769
C	0.62038	0.60010	-0.94920
C	0.82930	1.38678	1.32760
C	-0.55487	1.43431	1.44720
C	-0.76793	0.63564	-0.82436
C	-1.36504	1.09527	0.35806
H	-1.00695	1.77661	2.36769
H	1.07520	0.31392	-1.89004
H	1.45410	1.68943	2.15979
H	-1.06026	6.17686	-6.55868
H	-2.54513	7.06246	-6.15155
C	-1.55219	6.77686	-5.78462
H	-0.96596	7.69154	-5.63708
H	-8.92871	-6.71430	-7.78584
H	-2.22221	5.05902	-4.62944
C	-1.66694	5.99121	-4.46082
C	-9.63129	-6.88629	-6.96286
H	-10.48586	-6.21216	-7.09467
H	-0.66284	5.71286	-4.11419
H	-9.99703	-7.91743	-7.03402
H	-3.37577	7.08980	-3.69211
H	-8.58041	-5.61373	-5.54818
H	-8.09242	-7.31102	-5.48638
C	-2.36925	6.80713	-3.35339
H	-1.80962	7.73809	-3.18515
C	-8.95787	-6.64395	-5.59505
H	-3.03767	5.10339	-2.19575
C	-2.47338	6.02895	-2.02346
C	-9.92771	-6.87889	-4.41597
H	-1.46580	5.73896	-1.69593
H	-10.79485	-6.21234	-4.52325
H	-10.30415	-7.91055	-4.45854
H	-4.19999	7.05820	-1.16717
H	-8.87848	-5.60485	-3.01619
H	-8.40315	-7.30475	-2.92631
C	-3.15712	6.85365	-0.91094
H	-2.63585	7.81548	-0.80920
C	-9.26384	-6.63220	-3.04367
O	-5.84171	5.81759	0.04449
O	-1.77334	3.82416	0.90191
C	-2.85887	1.16993	0.40302
H	-2.89767	-0.94844	0.26554
C	-3.10326	6.16678	0.47234
C	-2.97398	3.68355	0.61276
C	-5.16867	4.78377	0.21634
C	-10.24620	-6.84284	-1.87143
C	-3.52472	-0.06859	0.29283
C	-3.61443	2.34722	0.44612
N	-3.79005	4.82285	0.42685
H	-3.78621	-2.70102	0.28177
H	-11.07743	-6.13659	-1.94333
H	-2.06755	5.91485	0.70081
H	-10.65585	-7.86066	-1.92448
C	-5.02959	2.26185	0.30389
C	-4.90549	-0.19353	0.22211
C	-4.86144	-2.70736	0.17050
C	-5.79696	3.44671	0.21465
H	-4.95287	-4.87277	0.09309
C	-5.69497	0.99798	0.20706
C	-5.57002	-1.50384	0.13398
C	-5.50805	-3.94396	0.06738
C	-7.17000	3.38505	0.06620
C	-7.12038	0.95275	0.06941
C	-6.99395	-1.54604	0.00239
C	-6.88131	-4.00497	-0.07374
O	-6.86364	-6.38201	-0.17167
C	-7.78989	-0.35595	-0.02856
C	-7.64027	-2.81515	-0.10281
C	-7.82729	2.15475	0.01021
C	-7.52602	-5.33127	-0.19317
H	-4.69996	7.30621	1.39099
H	-3.07276	7.98663	1.59126
H	-8.73570	-7.38609	-0.41966
N	-8.92958	-5.34434	-0.33676
C	-9.04302	-2.89160	-0.24039
C	-9.17555	-0.48205	-0.15629
C	-3.65858	7.05733	1.60649
C	-9.57981	-6.69635	-0.48477
C	-9.79558	-1.73283	-0.26237
C	-9.73393	-4.19656	-0.36588
H	-9.80063	0.39966	-0.17687
H	-8.90263	2.15107	-0.09870
H	-10.86982	-1.82032	-0.36414
O	-10.96994	-4.26369	-0.49442
C	-3.53793	6.41111	3.00261
C	-10.55541	-6.98301	0.67848
H	-10.93301	-8.00443	0.53401
H	-4.15602	5.50478	3.04201
H	-2.49784	6.10336	3.17306

H	-11.40005	-6.29292	0.61211
H	-5.01968	7.67660	3.96113
H	-3.36216	8.27866	4.09527
H	-9.00066	-7.52371	2.09840
C	-3.97837	7.36903	4.13090
C	-9.89159	-6.88125	2.06824
H	-9.55346	-5.85055	2.23497
C	-3.85733	6.73099	5.53213
H	-11.17717	-8.32284	3.06068
C	-10.85413	-7.28253	3.20708
H	-4.47855	5.82614	5.57030
H	-2.81813	6.41402	5.69213
H	-11.75423	-6.65379	3.15863
H	-3.65780	8.60083	6.64323
H	-9.30809	-7.76471	4.64874
H	-5.32635	8.00822	6.52216
C	-4.28265	7.69994	6.65559
C	-10.21197	-7.14257	4.60474
H	-9.89518	-6.10118	4.75059
H	-4.18728	7.23024	7.64088
C	-11.17881	-7.55259	5.73612
H	-11.48558	-8.59871	5.61929
H	-12.08060	-6.92928	5.71582
H	-10.70753	-7.44153	6.71901
H	-1.39373	0.36197	-1.66601
H	-7.71177	4.31857	-0.01467

Chapter 3 – Photoinduced Electron Transfer from Zinc *meso*-Tetraphenylporphyrin to a One-Dimensional Perylenediimide Aggregate: Probing Anion Delocalization Effects

Reprinted (adapted) from *J. Porph. Phthalo*. **2019**, *24*(3), 143-152 doi: 10.1142/S1088424619500858 with the permission of WorldScientific Publishing.

3.1 Introduction

Organic photovoltaics (OPVs) provide a promising pathway to renewable energy that utilizes cost-effective, solution-processable materials.[101-103] Much of OPV research has centered on maximizing their power conversion efficiencies (PCEs) in order to compete with high-purity silicon cells that are the current industry standard. Historically, the best-performing OPVs have utilized a bulk heterojunction (BHJ) blend of interpenetrating networks of donor and acceptor materials.[104, 105] Considerable research has gone into the development of conjugated polymers as donor materials for OPV BHJ devices,[106, 107] while for many years development of acceptor materials has centered around buckminsterfullerene (C_{60}) and its derivatives.[108] The two highest performing fullerene derivatives, [6,6]-phenyl-C_{61}-butyric acid methyl ester ($PC_{61}BM$) and its C_{70} analogue ($PC_{71}BM$), have been optimized in BHJ devices with various polymer donors to achieve PCEs exceeding 10%.[109] Though fullerenes are ubiquitous in OPV research, several disadvantages inhibit their ultimate application, in particular their high cost, poor solar radiation absorption, and susceptibility to air and light-mediated degradation.[18, 110] These deficiencies have subsequently accelerated research into non-fullerene OPV acceptor materials.[19, 111, 112]

This laboratory and others have studied perylenediimide (PDI) derivatives, one of the emergent classes of non-fullerene OPV acceptor materials.[23, 24, 67, 113, 114] PDI is strongly light-absorbing, synthetically versatile and thermally/environmentally robust, making PDI-containing compounds attractive materials for OPVs. Moreover, PDI photophysics have been investigated extensively,[115] making PDI an optimal acceptor for studying the excited-state dynamics of donor-acceptor model compounds and active layer BHJ blends. Research into PDI-based acceptors has grown dramatically since their inception, and today PCEs for PDI-based devices now rival those

of fullerene-based devices.[116] The most promising PDI-based materials incorporate multiple connected PDI chromophores, the molecular orbitals of which are extensively delocalized as a result of fused aromatic ring structures, which increase the electronic coupling between acceptors and have been demonstrated to boost PCEs in related systems.[21, 41] In addition to possessing highly delocalized molecular orbitals, these PDI acceptors are substantially twisted with respect to one another, resulting in fewer cofacial interactions between the molecules that produce excimer-like trap states common in PDI-based OPV materials.[23] However, the mechanism of free carrier generation in these high-performing systems is not yet fully understood and further investigations are needed to elucidate their underlying electronic behavior.

Much of the work dedicated to understanding the mechanism of free carrier generation in OPVs has been performed on fullerene-based systems.[20, 30, 117] In a BHJ blend, the low dielectric environment does not provide sufficient stabilization to overcome the Coulombic binding energy of the exciton (electron-hole pair).[103] This situation results in the exciton forming a charge transfer (CT) state[118] in which the electron and hole remain bound at the donor-acceptor (D-A) interface.[119, 120] However, fullerene-based systems are known to easily overcome this binding energy, resulting in fully charge-separated (CS) states[121] characterized by spatially well-separated holes and electrons. Dissociation from the CT state is in competition with geminate recombination, in which the bound electron-hole pair cannot overcome the binding energy and recombines to the ground state, ultimately lowering the free-carrier yield and PCE.[122]

Savoie *et al*. and others have developed a quantum dynamical model to rationalize the high performance of OPVs containing large fullerene clusters in the active layer.[20, 26, 27, 30] Pure phases of fullerene clusters that interact with the donor are thought to form a band of high energy CS

states as a result of isotropic electronic coupling that is isoenergetic with the donor excited state ^{1*}D. This permits the exciton to transfer directly into this band, bypassing the Coulombically bound CT state, where the electron and hole remain tightly bound (<1 nm separation).[123] In contrast, non-fullerene materials lacking the structural and electronic properties of fullerenes[124] do not have the same accessible band of CS states, thus the excitons are instead believed to dissociate from the more strongly bound CT state.[20] Despite these differences in electronic structure, some PDI systems have nevertheless demonstrated high efficiency[24, 41] attributed to anionic and molecular

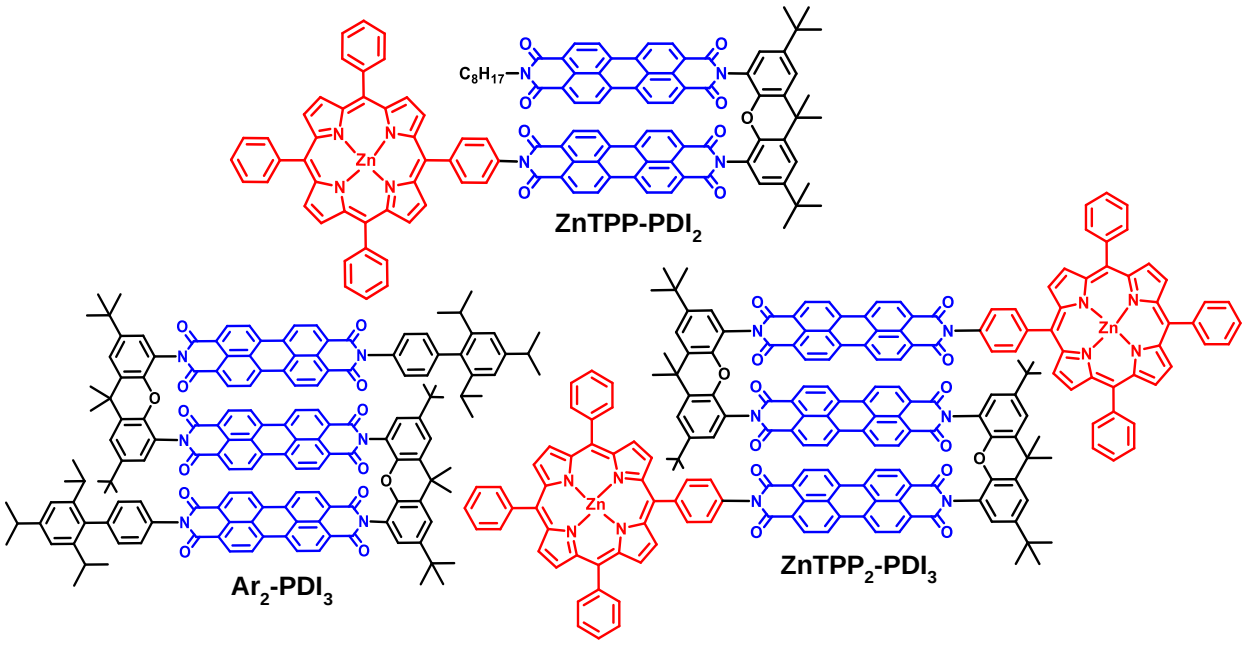

Figure 3.1. Molecular structures of **ZnTPP-PDI$_2$**, **ZnTPP$_2$-PDI$_3$** and **Ar$_2$-PDI$_3$**. Donor chromophores (ZnTPP) are colored red and acceptor chromophores (PDI) are colored blue.

orbital delocalization and even efficient generation of free carriers on picosecond timescales or less.[125]

Our recent work focused on investigating the effect of charge delocalization in PDI-based materials has yielded insights into this process. A rigidly oriented two-PDI acceptor system with zinc *meso*-tetraphenylporphyrin (ZnTPP) as the donor, **ZnTPP-PDI$_2$** (**Figure 3.1**), demonstrated an increase in the charge separation rate constant (k_{CS}) of 50% beyond the statistical sum of the

corresponding rates of two single PDI reference compounds.[44] The system was evaluated using the Marcus semi-classical electron transfer model,[92] which relates k_{CS} to the reorganization energy (λ) of the system, the free energy change for charge separation (ΔG_{CS}), and the electronic coupling (V_{DA}),

$$k_{CS} = \frac{2\pi}{\hbar}|V_{DA}|^2 \frac{1}{\sqrt{4\pi\lambda k_B T}} e^{-\frac{(\lambda+\Delta G_{CS})^2}{4\lambda k_B T}} \quad \textbf{(3.1)}$$

Values for λ and ΔG_{CS} were found to be approximately equal for **ZnTPP-PDI$_2$** and each of the single PDI reference compounds designed to individually evaluate through-bond and through-space electron transfer.[44] Furthermore, DFT calculations revealed a significantly lower SOMO + 1 energy for two cofacial PDI acceptors versus a single PDI, suggesting an increase in the electronic coupling between the acceptors via superexchange interactions[126] in which the ^{1*}ZnTPP state additionally couples to the SOMO + 1 level of the two interacting PDIs. However, it is currently unknown whether additional PDIs will continue to lower the SOMO + 1 of strongly coupled PDIs such that electron transfer can eventually occur directly to a band of excited states of aggregated PDIs, emulating the proposed model of charge separation in fullerenes.[20, 44]

In this work, we have prepared an extended donor-acceptor system **ZnTPP$_2$-PDI$_3$** (**Figure 3.1**) with three cofacially oriented PDIs to examine how the incorporation of an additional acceptor moiety might impact the charge transfer dynamics. Using the framework established by our previous observations, we analyze k_{CS} in this system as a function of the interactions between individual acceptors and monitor the effects of anion delocalization. The xanthene bridge maintains a fixed face-on interaction between the three PDI subunits as described previously,[44] while incorporating a second **ZnTPP** donor simplifies the synthesis of the system and does not participate in the excited-state dynamics. We have also prepared the reference system **Ar$_2$-PDI$_3$**

(**Figure 1**) which substitutes biphenyl groups for the ZnTPP donors as a template for correlating changes in PDI electronic spectra and for evaluating our system using the Marcus model.

3.2. Experimental Section

3.2.1. Materials Synthesis

ZnTPP$_2$-PDI$_3$ and **Ar$_2$-PDI$_3$** were prepared by the convergent synthesis detailed in **Scheme 3.1** and **Scheme 3.2**.

3.2.2. Electrochemistry

Oxidation and reduction potentials for the reference compound **Ar$_2$-PDI$_3$** were determined by differential pulse voltammetry, which was performed using a CH Instruments Model 622 electrochemical workstation on 0.5 mM solutions in anhydrous CH_2Cl_2 with 100 mM Bu_4N^+ PF_6^- supporting electrolyte. Measurements were performed using a Pt disc working electrode, Pt wire counter electrode, and Ag wire quasi-reference electrode. Potentials are referenced to ferrocene/ferrocenium as an internal standard and are reported vs. SCE.

3.2.3. Steady-State Optical Characterization

Absorption spectra were collected on a Shimadzu 1800 spectrophotometer. FTIR spectra were acquired on a Shimadzu IRAffinity-1 spectrophotometer in transmission mode with 2 cm^{-1} resolution. Samples with a maximum optical density of 1 were prepared in dichloromethane under an N_2 atmosphere contained in a liquid demountable cell (Harrick Scientific) with CaF_2 windows and a 500 μm Teflon spacer.

3.2.4. Computational Details

To reduce computational time, density functional theory (DFT) calculations were performed on **PDI$_3$** (with phenyls substituted for the porphyrin groups) in TeraChem (version 4.4) at the B3LYP-D3/6-31+G* level of theory for all geometry optimizations.[44]

3.2.5. Transient Absorption Spectroscopy

The experimental femtosecond transient absorption (fsTA) and nanosecond transient absorption (nsTA) apparatus has been previously described.[66, 67] Pump pulses at 590 nm generated by using the output of a laboratory-built collinear optical parametric amplifier were used to excite solution samples in 2 mm cuvettes.[127] The femtosecond transient IR (fsIR) spectroscopy apparatus has also been described previously.[128] Excitation pulses were tuned to 590 nm (4 μJ/pulse) and samples were prepared in the same manner as the FTIR samples in a demountable liquid cell with a 500 μm Teflon spacer. All samples for transient spectroscopy were dissolved in 1,4-dioxane to approximate the dielectric environment of the solid state.

3.3 Results

3.3.1. Electrochemistry

Differential pulse voltammetry experiments performed on the **Ar$_2$-PDI$_3$** reference molecule (**Figure 3.7**) show that the observed splitting of the first and second reduction potentials of PDI observed upon in a PDI dimer is not significantly enhanced in **Ar$_2$-PDI$_3$**,[44] the lowest energy reduction potential is -0.50 V vs SCE, which is approximately 40 mV more positive than the corresponding dimer acceptor. Using these reduction potentials and the reported oxidation potential of ZnTPP (E_{ox} = 0.83 V vs SCE), we calculate ΔG_{CS} for charge separation using **Equation 3.2**:[90]

$$\Delta G_{CS} = E_S - \left[e(E_{ox} - E_{red}) - \frac{e^2}{r_{DA}\varepsilon_S} + e^2\left(\frac{1}{2r_D} + \frac{1}{2r_A}\right) \times \left(\frac{1}{\varepsilon_S} - \frac{1}{\varepsilon_{SP}}\right)\right] \quad \textbf{(3.2)}$$

where E_{ox} and E_{red} are the first oxidation and reduction potentials of the electron donor and electron acceptor, respectively; r_D and r_A are the donor and acceptor radii, r_{DA} is the distance between donor and acceptor, ε_S is the dielectric constant of the solvent mediating the electron transfer event (ε_S (1,4-dioxane) = 2.25), and ε_{SP} is the dielectric constant of the electrochemical solvent (ε_{SP} (CH_2Cl_2) = 8.93). Using E_S = 2.06 eV for ^{1*}ZnTPP and distances taken from MM+ calculations, this equation gives the charge-separation free energy changes for **ZnTPP-PDI**, **ZnTPP-PDI$_2$**, and **ZnTPP$_2$-PDI$_3$** as ΔG_{CS} = -0.44, -0.43, and -0.46 eV, respectively. This calculation suggests that charge separation is slightly more favorable for charge injection directly into the trimer than it is for the dimeric and monomeric PDI acceptors. However, the charge separation rate also depends on the reorganization energy, λ. We estimated λ using the dielectric continuum model of the solvent ($\lambda_S \cong 0$ for 1,4-dioxane) and DFT calculations on the ion pairs in **ZnTPP$_2$-PDI$_3$** to be approximately 0.31 eV, compared to 0.33 eV for the dimer acceptor. With this reorganization energy, the charge separation process lies in the Marcus inverted region, and the small increase in ΔG_{CS} for the trimeric acceptor may indicate a lowered rate of charge transfer according to **Equation 3.1**. Details of this analysis are given in the Supplementary Information.

3.3.2. Femtosecond Transient Visible Absorption Spectroscopy

The ground-state absorption spectrum of **ZnTPP$_2$-PDI$_3$** in 1,4-dioxane (shown in black) displays a maximum absorption at 414 nm corresponding to the Soret band of ZnTPP[129] and broad features from 450-575 nm resulting from overlapping absorptions of the cofacially oriented

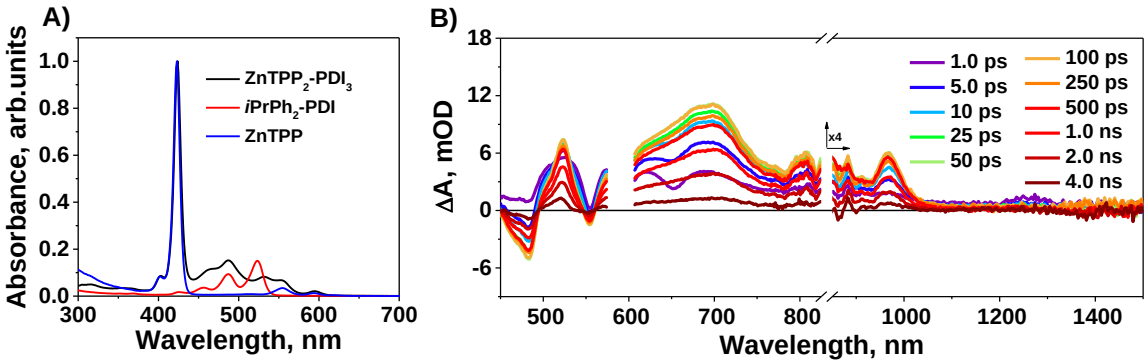

Figure 3.2. A) Steady-state absorption spectra in 1,4-dioxane. B) fsTA spectra for **ZnTPP$_2$-PDI$_3$** in 1,4-dioxane following excitation at 590 nm (~120 fs, 900 nJ/pulse). The values of ΔA for the near-IR features are expanded by a factor of 4.

PDIs[130, 131] (**Figure 3.2A**). The absorption bands of the PDIs are reminiscent of *H*-aggregates, expected by the structurally enforced cofacial overlap of the chromophores and evidenced by the increase in the ratio of the 1-0/0-0 vibronic bands compared to the absorption spectrum of a monomer PDI, *N*,*N*-(2,6-diisopropylphenyl)PDI (shown in blue), also seen in the three-acceptor model compound **Ar$_2$-PDI$_3$** (**Figure 3.8**). The lowest-energy band peak at 590 nm corresponds to the lowest energy Q-band of the ZnTPP chromophore, also seen in the absorption spectrum of ZnTPP (shown in red).[129] The PDI absorption is negligible at 590 nm, which permits selective photoexcitation of the ZnTPP chromophore. From the relative intensities of the Q bands, there is no obvious aggregation between ZnTPP chromophores.

The transient absorption spectra of **ZnTPP$_2$-PDI$_3$** in 1,4-dioxane (**Figure 3.2B**) show that its excited-state dynamics closely resemble those of the previously studied **ZnTPP-PDI$_2$**. At early times, we observe excited-state absorption (ESA) corresponding to the ZnTPP S_1 state (^{1*}ZnTPP) with broad features spanning 460-1000 nm as well as a near-IR ESA peak at 1250 nm and a stimulated emission (SE) feature at 650 nm.[132] The rapid decay of the ^{1*}ZnTPP ESA and SE features is accompanied by the formation of PDI$^{\bullet-}$ absorptions at 700, 790, and 975 nm and a PDI ground-state bleach at 490 nm, which indicates formation of the radical ion pair, **ZnTPP$^{\bullet+}$-PDI$^{\bullet-}$**.[133, 134] The PDI$^{\bullet-}$ features appear broadened relative to those of monomeric PDI$^{\bullet-}$, which has previously been attributed to fast anion delocalization over a cofacial two-acceptor system.[44]

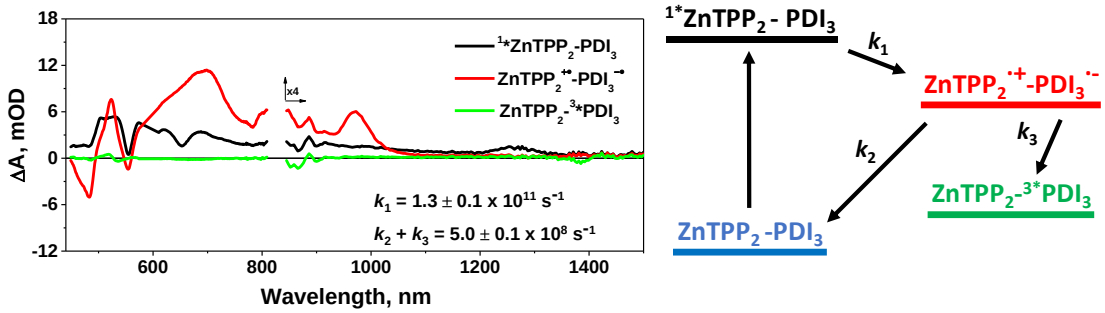

Figure 3.3. Evolution-associated spectra (left) and corresponding Jablonski diagram extracted from the fsTA spectra for **ZnTPP$_2$-PDI$_3$** in 1,4-dioxane following excitation at 590 nm (~120 fs, 900 nJ/pulse).

Qualitatively, the absorption band at 700 nm corresponding to the delocalized PDI$^{\bullet-}$ is similar in shape to the same band in **ZnTPP-PDI$_2$** and appears at similar times. The radical ion pair then undergoes charge recombination primarily to the ground state as indicated by the disappearance of PDI$^{\bullet-}$ absorption features, although a small amount of ^{3*}PDI is observed at long times. Global fitting of the fsTA spectra was performed at several selected wavelengths using a kinetic model in which the population of ^{1*}ZnTPP is depleted by formation of the charge-separated state with a rate k_1 (1.3×10^{11} s^{-1}), followed by charge recombination to the ground state and to ^{3*}PDI with an observed rate $k_{CR} = k_2 + k_3$ (5.0×10^8 s^{-1}).

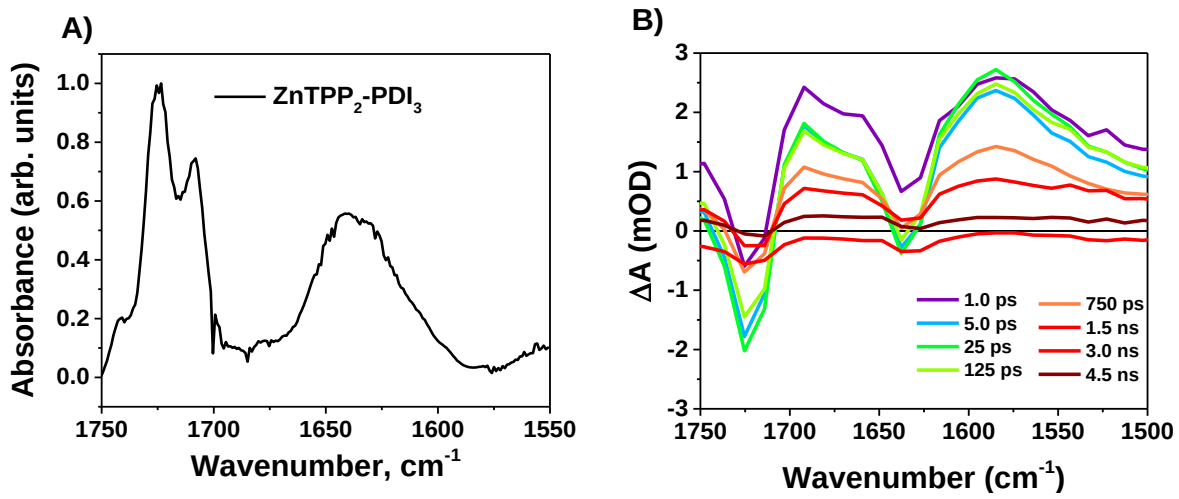

Figure 3.4. The A) steady-state FTIR spectrum and B) fsIR spectra at selected time points for **ZnTPP$_2$-PDI$_3$** in 1,4-dioxane following excitation at 590 nm.

The evolution-associated spectra (EAS) are given in **Figure 3.3** alongside a Jablonski diagram depicting the transitions in this system, while the corresponding kinetic fits to several wavelengths are given in **Figure 3.9A**. The EAS clearly show the transition from **^{1*}ZnTPP-PDI** to the radical ion pair **ZnTPP$^{\bullet+}$-PDI$^{\bullet-}$** followed by the persistence of **ZnTPP-^{3*}PDI** at long times. The contribution of ^{3*}PDI is minor, and so the value for k_{CR} is dominated by recombination to the ground state ($k_{CR} \approx k_2$). Importantly, the measured k_{CS} value for **ZnTPP$_2$-PDI$_3$** ($1.3 \pm 0.1 \times 10^{11}$ s^{-1}) is statistically identical to that previously reported for **ZnTPP-PDI$_2$** ($1.3 \pm 0.1 \times 10^{11}$ s^{-1}),[44] despite the small difference in ΔG_{CS}. The lack of further enhancement suggests that the third acceptor in **ZnTPP$_2$-PDI$_3$** is interacting electronically in a different manner compared to the two acceptors in **ZnTPP-PDI$_2$**.

3.3.3. Femtosecond Transient Infrared Spectroscopy

The ground-state FTIR spectrum of **ZnTPP$_2$-PDI$_3$** is given in **Figure 3.4A**. The feature at 1560 cm^{-1} is attributed to C=C stretching in ZnTPP[135-137] while the broad peak at 1637 cm^{-1} results

from the PDI C=C stretching modes and the ZnTPP stretching mode at about 1600 cm^{-1}[144], and the sharp peaks at 1707 and 1721 cm^{-1} originate from the PDI C=O stretching modes.[44]

The degree of delocalization can be further probed using fsIR spectroscopy. The steady-state IR spectra of ZnTPP and $ZnTPP^{\bullet+}$ do not have significant absorptions from ca. 1600-1800 cm^{-1}, and the change in absorption upon oxidation of ZnTPP at 1597 cm^{-1} is negligible. This allows direct observation of the changes in the IR transitions of PDI and $PDI^{-\bullet}$. The time-resolved IR spectra of **$ZnTPP_2$-PDI_3** are shown in **Figure 3.4B** and the global kinetic fits are given in **Figure 3.9B**. Photoexcitation results in the appearance of two bleach features at 1638 cm^{-1} and 1725 cm^{-1} which is accompanied by the rise of two broad ESA features centered at 1585 cm^{-1} and 1692 cm^{-1}. The broad peaks at 1585 cm^{-1} and 1692 cm^{-1} are assigned to the C=C and C=O stretches of $PDI^{\bullet-}$, respectively. The slight shift to higher frequencies observed after 5 ps may indicate electron transfer to a delocalized orbital between the PDIs. The shift is smaller than that observed in **ZnTPP-PDI**,[44] since the electron density is shared between at least two molecules and the subsequent weakening of the PDI C=O π bonds by $PDI^{\bullet-}$ formation is diminished.

3.4. Discussion

The transient visible and IR absorption data for **$ZnTPP_2$-PDI_3** show that its photophysics are analogous to those of **ZnTPP-PDI_2** and that increasing the number of acceptors in the system from two to three has a negligible effect on k_{CS}. Neither ΔG_{CS} (-0.46 eV) nor λ (0.31 eV) change dramatically upon addition of the third PDI, and as discussed above, the small change in ΔG_{CS} predicts a slight decrease in CS rate instead of the observed similar rate compared to the dimer. Therefore, there must be other factors influencing the CS dynamics, although with only minor contributions from the third PDI unit. It is possible that the diminished CS rate predicted by Marcus

theory is being compensated by an additional electron transfer pathway to the distal PDI or through enhanced delocalization of the acceptor state; these scenarios are discussed below.

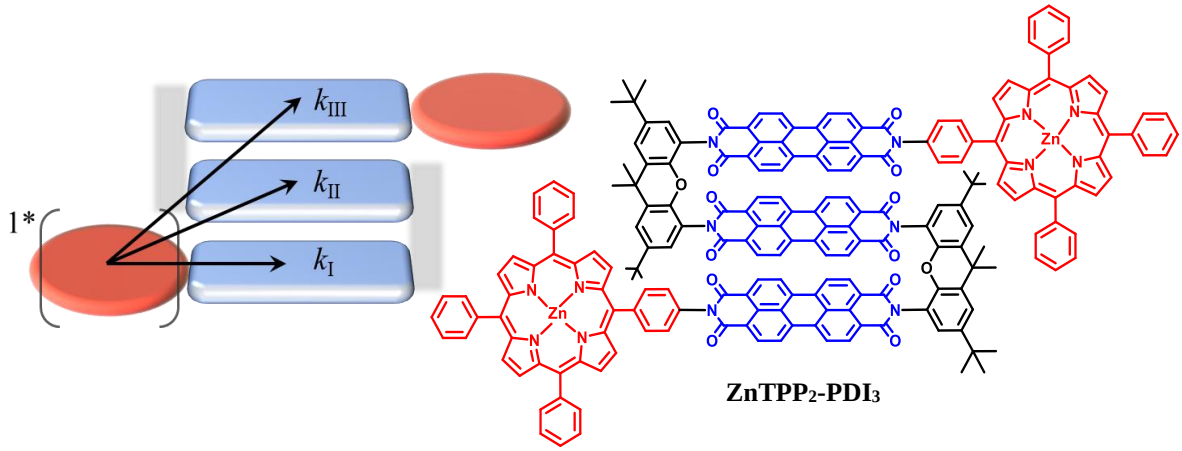

Figure 3.5. Schematic of electron transfer pathways available in **ZnTPP$_2$-PDI$_3$.** Rates k_I and k_{II} are taken from reference 36. Rate constant k_{III} is expected to be negligible due to the large spatial separation and number of bonds between the ZnTPP donor (red disk) and PDI acceptors (blue plates).

The lack of further substantial rate enhancement in **ZnTPP$_2$-PDI$_3$** suggests that the electronic coupling of the third distal PDI to ^{1*}ZnTPP must be weak. If we take the electron transfer to only involve PDI-centered (localized) acceptor orbitals, then the total observed electron transfer rate can be expressed as the sum of individual rates from ^{1*}ZnTPP to each localized state. These contributing pathways are shown schematically in **Figure 3.5**. Pathways I and II are discussed at length in our previous work[44] and have rate constants of $k_I = 8.1 \times 10^8$ s^{-1}, and $k_{II} = 1.0 \times 10^8$ s^{-1}, respectively. The ~8-fold decrease between the proximal and intermediate PDI acceptors suggests that the transfer to the distal PDI should be even slower, owing to the reduced donor-acceptor electronic coupling, as the differences in ΔG_{CS} between each donor-acceptor pair are insignificant (*vide supra*). The distance dependence of the electronic coupling for through-space electron transfer varies as $e^{-\beta r}$, where β is the damping factor (2-3 Å^{-1}).[138] MM+ force field calculations estimate the center-to-center distance to the third, distal PDI to be ca. 22 Å from the ^{1*}ZnTPP donor, compared to a donor-acceptor distance of 14.8 Å in **ZnTPP-PDI$_2$**.[44] Thus, the through-

space contribution to the CS rate in **ZnTPP$_2$-PDI$_3$** is likely negligible. While through-bond interactions experience significantly lower damping (b ~ 0.5/bond), the larger number of bonds between ^{1*}ZnTPP and the third distal PDI in **ZnTPP$_2$-PDI$_3$** ensures that this contribution will be similarly negligible. Thus, we do not expect direct electron injection into the distal PDI (k_{III} ~ 0) to enhance the overall observed rate.

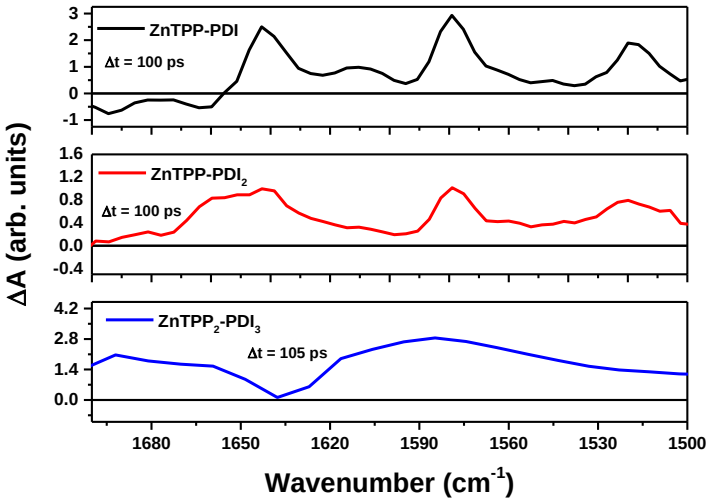

Figure 3.6. Comparison of the fsIR spectra for **ZnTPP-PDI**, **ZnTPP-PDI$_2$**, and **ZnTPP$_2$-PDI$_3$** at 100 ps in 1,4-dioxane (λex = 590 nm).

Therefore, as with **ZnTPP-PDI$_2$**, we observe a rate enhancement beyond what is expected from the statistical sum of rates of injection into the localized acceptor states. Electron delocalization in the trimer is evidenced by the line broadening observed in both the electronic spectra discussed above and is especially prominent in the vibrational spectra.

A comparison of the fsIR spectra of the different acceptors in the series at times long after charge separation is complete is shown in **Figure 3.6**. The most noticeable difference in the substantially increased broadening in **ZnTPP$_2$-PDI$_3$** compared to **ZnTPP-PDI$_2$** and **ZnTPP-PDI**. Similar to the visible spectra, the broadening of the IR peaks has previously been attributed to

delocalization of the anion between two chromophores,[44] although here the extended peak width is likely due to the presence of an additional neutral PDI species. Such peak broadening has also been observed in other PDI aggregates[139, 140], PDI dimer systems that form excimers,[128, 141, 142] and in solid films of extended aromatic systems, such as derivatives of tetracene.[143] In the solid state, this broadening has been attributed to the thermal phonon bath present that can obscure the relatively weak and narrow molecular transitions.[144] Even though the third PDI unit appears to be uninvolved in the charge-transfer dynamics, its influence on the transitions and behavior of its neighboring units can still be considerable, as shown in both the time-resolved electronic and vibrational spectra.

This delocalization does not appear to dramatically impact the energy of the SOMO based on the reported reduction potentials of **ZnTPP-PDI** and **ZnTPP-PDI$_2$**. However, the broadened and red-shifted anion absorption features in the fsTA spectra suggest that the energy difference between the SOMO and SOMO + 1 is lower in the dimer/trimer compared to the monomer acceptor. Specifically, the SOMO → SOMO + 1 transition of $PDI^{\bullet-}$ corresponds to the feature at ~975 nm in the fsTA spectrum of **ZnTPP$_2$-PDI$_3$** (**Figure 2B**), which shows no further shift to lower energy wavelengths, indicating no significant change in the SOMO + 1 energy. This suggests that the PDI SOMO + 1 and ^{1*}ZnTTP states can mix and enhance the overall donor-acceptor coupling via superexchange. In this formalism, the electronic coupling is described by **Equation 3.3** where ^{1*}ZnTPP (D)

$$V_{DA} = \frac{V_{DB}V_{BA}}{\Delta E_{DB}} \quad \textbf{(3.3)}$$

mixes with the SOMO+1 (B) and SOMO (A) of the PDI acceptors.[44] Delocalization of the orbitals lowers the energy of the anion excited state (SOMO + 1) and thus increases the effective coupling

between the donor and acceptors and enhances the charge separation rate. Since no further substantial rate enhancement beyond that observed in **ZnTPP-PDI$_2$** is seen, we conclude that the degree of delocalization in **ZnTPP$_2$-PDI$_3$** is quite similar, and that the electron density is confined mostly within a dimer unit. It is likely that this dimer unit is comprised of the PDI pair closest to the ZnTPP cation owing to the broken electrostatic symmetry.

The lifetime of the charge-separated states in this series gives some indication of how the partially delocalized anion is influenced by neighboring PDI sites. The charge recombination rate constant ($k_3 = 5.0 \times 10^8$ s^{-1}) in **ZnTPP$_2$-PDI$_3$** is smaller than the corresponding values in **ZnTPP-PDI$_2$** ($k_{CR} = 7.1 \times 10^8$ s^{-1}) and **ZnTPP-PDI** ($k_{CR} = 9.7 \times 10^8$ s^{-1}). The slightly lower ion pair energies (*vide supra*) do not track with the trend in recombination rates, which indicates that this is not simply an effect of the ΔG_{CR} for charge recombination. The decrease in recombination rate with increasing number of PDI units may imply that the electron density can hop between PDI dimers in **ZnTPP$_2$-PDI$_3$**. Electron hopping in PDI assemblies can occur with rates $>10^7$ s^{-1} such that if hopping of this magnitude occurs in competition with recombination, the lifetime of the charge-separated state can be moderately extended.[145] While the PDI trimer unit in **ZnTPP$_2$-PDI$_3$** appears insufficient for the electron to migrate far enough away prior to recombination to break the Coulomb barrier and produce a free carrier, the hopping process may provide such a pathway in the limit of extensive aggregation present in the solid state.

Despite the lack of large CS rate enhancement and the relatively short CS lifetime observed in this extended, one-dimensional PDI aggregate, both rapidly forming (<ps) and long-lived (~ms) charge-separated states in PDI aggregates have been observed previously. Logsdon *et al.*[36] and Hartnett *et al.*[35] have observed the formation of long-lived charge carriers in ordered oligomeric

films of donor-acceptor dyads and triads incorporating cofacial PDIs, implying that charge delocalization across more than two PDIs is possible in the presence of strong acceptor-acceptor interactions. As a result, upon photoexcitation, charge transfer from a donor to the PDI acceptor occurs into a series of potentially delocalized states formed by the interactions of several PDIs. The disorder present in films assists in this process as the energetic barrier to movement of the electron is far lower in a high-entropy system. In contrast, the xanthene spacers between the PDIs in **ZnTPP$_2$-PDI$_3$** prevent the PDI molecules from achieving optimal π-π stacking. The interplanar distance between each PDI molecule can be as large as 4.5 Å and rotations about the single bonds joining the PDIs to the xanthene spacers are required to achieve van der Waals stacking, which in turn, slips the short axes of the PDIs relative to one another. This observation supports the idea that the rigidity and accompanying low entropy of the structure in this study is preventing the chromophores from interacting in such a way that allows the electron to transfer into a fully delocalized orbital of three PDIs. Instead, delocalization of the anion still occurs between two PDIs as discussed above.

The interaction between molecular acceptor units is a prelude to the formation of a high density of states (DOS) arising from the coupling of individual molecular states in a solid medium[20, 30] and provides a framework for understanding why additional PDI acceptors in this geometry do not further increase the rate of charge separation to the same extent that other π-stacked PDI systems as well as ITIC derivatives have been shown to do.[32, 125, 146-148] Restricting the interactions of the PDIs using the xanthene spacer groups limits the coupling necessary to form a quasi-continuous band. Moreover, PDI only has a single LUMO level, which intrinsically limits how individual PDIs can couple to one another. In contrast, fullerenes have a threefold degenerate

LUMO which creates a corresponding increase in the number of pathways for electron transfer[124] and leads to a more rapid generation of band structure upon aggregation. Furthermore, the spherical structure and thus high symmetry of fullerenes enables the individual molecules to couple isotropically, which will dramatically increase the number of possible interactions.[20, 26, 30, 124] In this way, fullerenes have a high DOS within a cluster on the order of tens of nanometers that are encountered in OPVs,[20] whereas the density in one-dimensional π-stacked chromophores is limited. As a result, the path forward to observing electron transfer to an analogous band structure in non-fullerene acceptors requires increasing the degree of isotropic coupling between acceptors as well as the number of pathways available in the acceptors.

3.5. Conclusions

We have shown here that increasing the acceptor aggregate size of a donor-acceptor scaffold does not necessarily lead to an increase in the rate of photoinduced charge separation. Ultrafast time-resolved visible and mid-infrared spectroscopies show that the rate of charge separation in **ZnTPP$_2$-PDI$_3$** is nearly identical to those of **ZnTPP-PDI$_2$**, and the rate of charge recombination is decreased by ca. 30%. Accounting for ΔG_{CS} and λ in a Marcus framework points to similar electronic interactions of two PDI acceptors in both molecules, a conclusion that is qualitatively supported by the differential pulse voltammetry experiments indicating weak coupling to the distal PDI. As a result, covalent attachment of the ZnTPP donor to a single point on the PDI acceptor stack is insufficient to access a lower energy pathway for electron transfer in the three-acceptor model. These results imply the necessity of designing organic semiconductors with stronger electronic coupling in their anionic states, while at the same time avoiding excimer formation in their excited states. The initial extensive exciton delocalization observed in PDI

aggregates discussed previously suggests that delocalization over more than two chromophores is possible but may require a noncovalent method or a higher degree of symmetry and structural flexibility to observe. Thus, we are working towards designing several model oligomers incorporating two or more PDI cores through different bonding and organizational motifs to expound this discussion.

3.6. Supplementary Information.

3.6.1. Synthesis

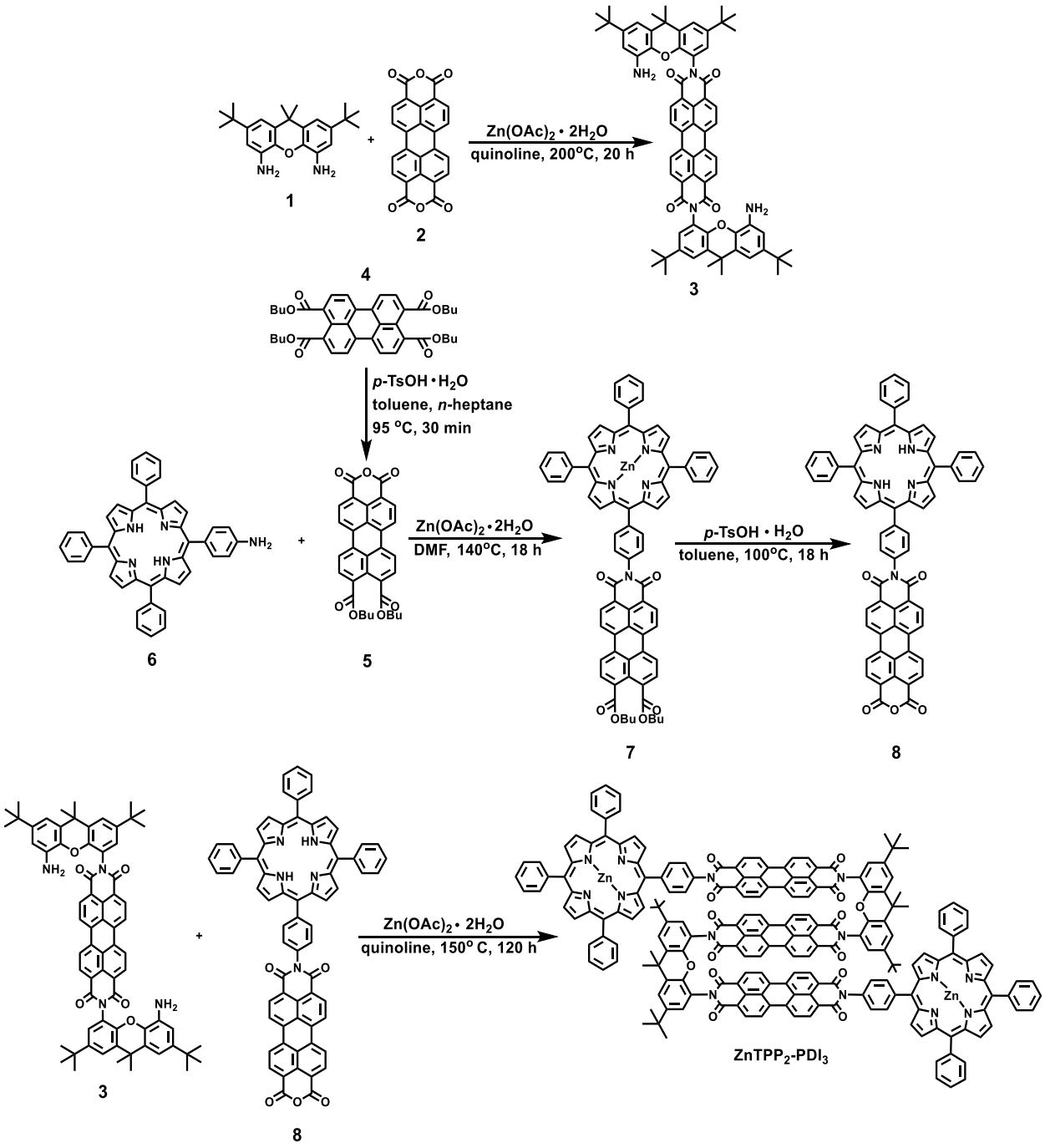

Scheme 3.1. Synthetic Scheme for **ZnTPP$_2$-PDI$_3$**.

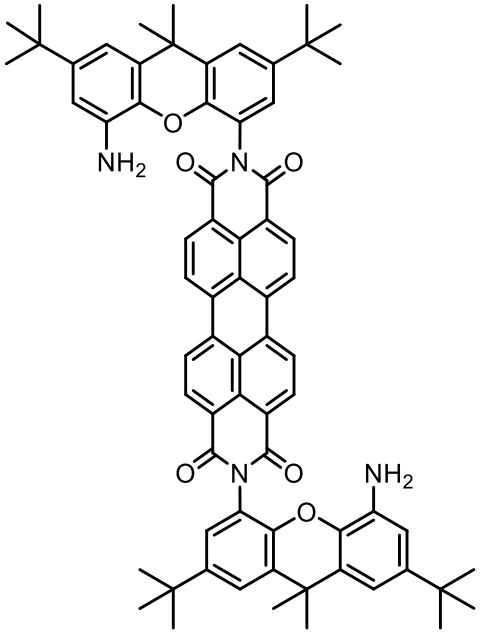

3: Compound **3** was synthesized according to a modified literature procedure[149].

To a 25 mL round-bottom flask charged with a magnetic stir bar were added **1** (283 mg, 0.803 mmol), **2** (150 mg, 0.382 mmol), $Zn(OAc)_2 \cdot 2H_2O$ (59 mg, 0.268 mmol), and distilled quinoline (13 mL). The mixture was stirred for 5 min at rt and then bubbled with N_2 for 10 min. The reaction was then stirred at 200 ^oC for 20 h. After cooling to rt, most of the quinoline was removed via vacuum distillation. The resulting red solid was dissolved in CH_2Cl_2, the resulting solution washed with 1M HCl, dried over anhyd. Na_2SO_4, filtered, and the solvent was removed *in vacuo*. Column chromatography (silica gel, 0.5-0.75% MeOH in CH_2Cl_2), followed by further column chromatography (silica gel, 1-1.5% acetone in $CHCl_3$) afforded **3** as a dark red solid (109 mg, 27%). Spectral data were in agreement with previously reported data[149].

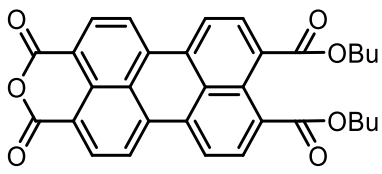

5: Compound **5** was synthesized according to a modified literature procedure[150].

To a 250 mL round-bottom flask charged with a magnetic stir bar were added **4** (5.00 g, 7.66 mmol), *p*-TsOH • H_2O (4.37 g, 23.0 mmol), toluene (20 mL), and *n*-heptane (102 mL). The reaction was brought to reflux under air and monitored via TLC until **4** was fully consumed (ca. 30 min). At this point, the reaction was immediately removed from heat and allowed to cool to rt. The precipitate was collected by filtration and washed with MeOH and H_2O, affording **5** (3.86 g, 96%) as a bright red solid. Spectral data were in agreement with previously reported data[150].

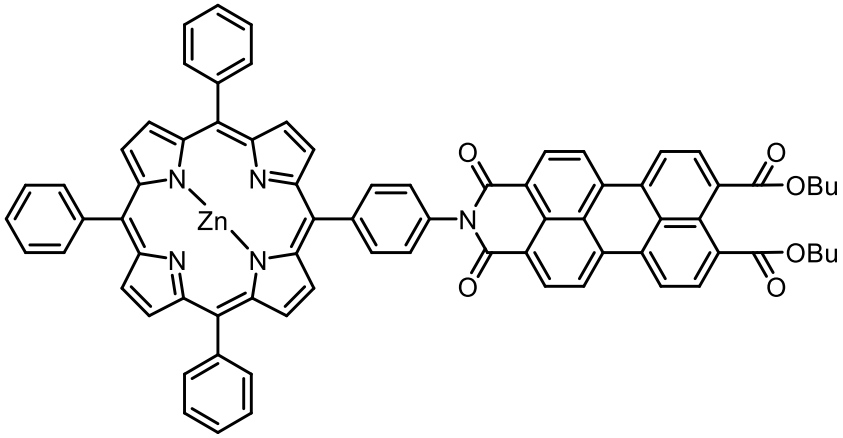

7: To a 10 mL screw cap vial charged with a magnetic stir bar were added **5** (130 mg, 0.249 mmol), **6** (181 mg, 0.261 mmol), $Zn(OAc)_2$ • $2H_2O$ (8 mg, 0.037 mmol), and DMF (5 mL). The reaction vessel was sealed with PTFE tape, sonicated for 5 min, and evacuated and then backfilled with N_2 three times at 30 second intervals before being stirred at 140 ^oC for 18 h. The reaction mixture was cooled and the solvent was removed *in vacuo*. Column chromatography (silica gel, 0.1% MeOH in $CHCl_3$) followed by further column chromatography (silica gel, 0.5% acetone in CH_2Cl_2) afforded **7** (212 mg, 71%) as a dark purple solid. ^1H NMR (500 MHz, $CDCl_3$): δ 9.15 (d, *J* = 4.3 Hz, 2H), 8.98 (d, *J* = 4.6 Hz, 2H), 8.95 (s, 4H), 8.48 (d, *J* = 7.5 Hz, 2H), 8.43 (d, *J* = 7.5 Hz, 2H) 8.26-8.22 (m, 8H), 8.14 (d, *J* = 7.9 Hz, 2H), 8.00 (d, *J* = 7.6 Hz, 2H), 7.82-7.70 (m, 11H), 4.32 (t,

J = 7.0 Hz, 4H), 1.86-1.78 (m, 4H), 1.58-1.48 (m, 4H), 1.04 (t, *J* = 7.3 Hz, 6H). ^{13}C NMR (125 MHz, $CDCl_3$): δ 168.1, 163.7, 150.2, 150.12, 150.10, 143.1, 142.8, 135.5, 135.3, 134.7, 134.5, 132.2, 132.1, 132.0, 131.9, 131.7, 131.5, 130.2, 129.2, 129.0, 128.8, 127.5, 126.9, 126.6, 125.7, 122.6, 121.9, 121.6, 121.20, 121.17, 120.0, 65.6, 53.4, 30.6, 19.3, 13.8. APPI HRMS *m*/*z* calcd. for $C_{76}H_{54}N_5O_6Zn$ $(M + H)^+$ 1196.3360, found: 1196.3345.

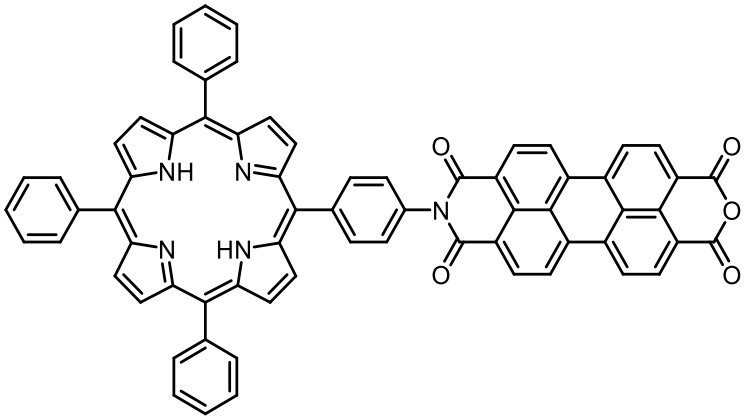

8: To a 50 mL round-bottom flask charged with a magnetic stir bar were added **6** (100 mg, 0.083 mmol), *p*-TsOH • H_2O (238 mg, 1.25 mmol), and toluene (8 mL). The mixture was stirred at 100 ^oC under air for 18 h. The reaction mixture was then cooled to rt, concentrated *in vacuo* and washed thoroughly with H_2O.The resulting green solid was used without further purification.

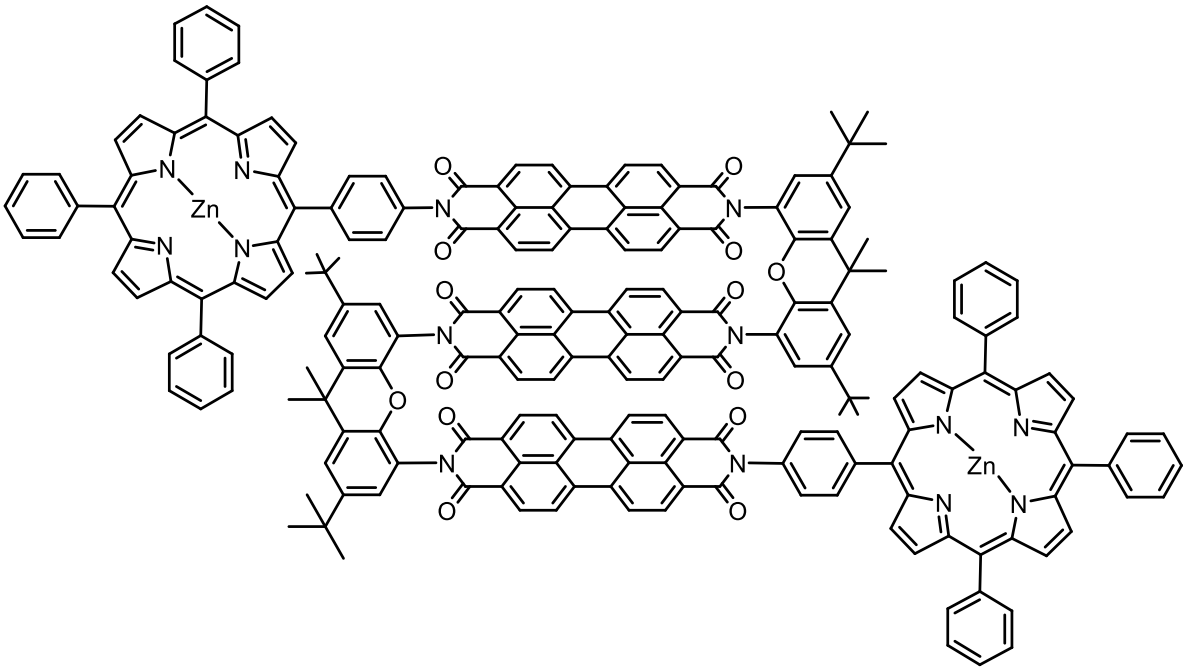

ZnTPP$_2$-PDI$_3$: To a 25 mL round-bottom flask charged with a magnetic stir bar were added **3** (31 mg, 0.029 mmol), **8** (73 mg, 0.073 mmol), $Zn(OAc)_2 \cdot 2H_2O$ (16 mg, 0.073 mmol), and distilled quinoline (3 mL). The mixture was bubbled with N_2 for 10 minutes and additional quinoline (0.5 ml) was added. The reaction was stirred at 150 ^oC for 120 h. Most of the quinoline was removed via vacuum distillation. The purple residue was dissolved in CH_2Cl_2, washed with distilled H_2O, dried over anhyd. Na_2SO_4, filtered, and the solvent was removed *in vacuo*. Column chromatography (silica gel, 1.5% MeOH in $CHCl_3$) followed by further column chromatography (silica gel, 6% acetone in $CHCl_3$, followed by size-exclusion chromatography (BioBeads SX-3, $CHCl_3$) afforded **ZnTPP$_2$-PDI$_3$** (10 mg, 3.2% over two steps) as a dark purple solid. ^{1}H NMR (600 MHz, $C_2D_2Cl_4$, 393.5 K): δ 9.16 (d, *J* = 4.0 Hz, 4H), 9.08 (d, *J* = 4.0 Hz, 4H), 9.05-9.00 (m, 8H), 8.59 (d, *J* = 7.3 Hz, 4H), 8.36 (d, *J* = 6.5 Hz, 8H), 8.31 (d, *J* = 6.1 Hz, 4H), 8.27 (d, *J* = 7.3 Hz, 4H), 8.11 (d, *J* = 7.3 Hz, 4H), 8.05-7.98 (m, 12H), 7.91-7.78 (m, 20H), 7.75 (d, *J* = 8.0 Hz, 4H), 7.65 (d, *J* = 7.0 Hz, 4H), 7.51 (s, 2H), 7.48 (s, 2H), 6.91 (s, 2H), 1.70 (s, 6H), 1.45 (s, 6H),

1.36 (s, 18H), 1.32 (s, 18H). APPI HRMS *m/z* calcd. for $C_{206}H_{134}N_{14}O_{14}Zn_2$ $(M)^+$ 3154.8790, found: 3154.8780.

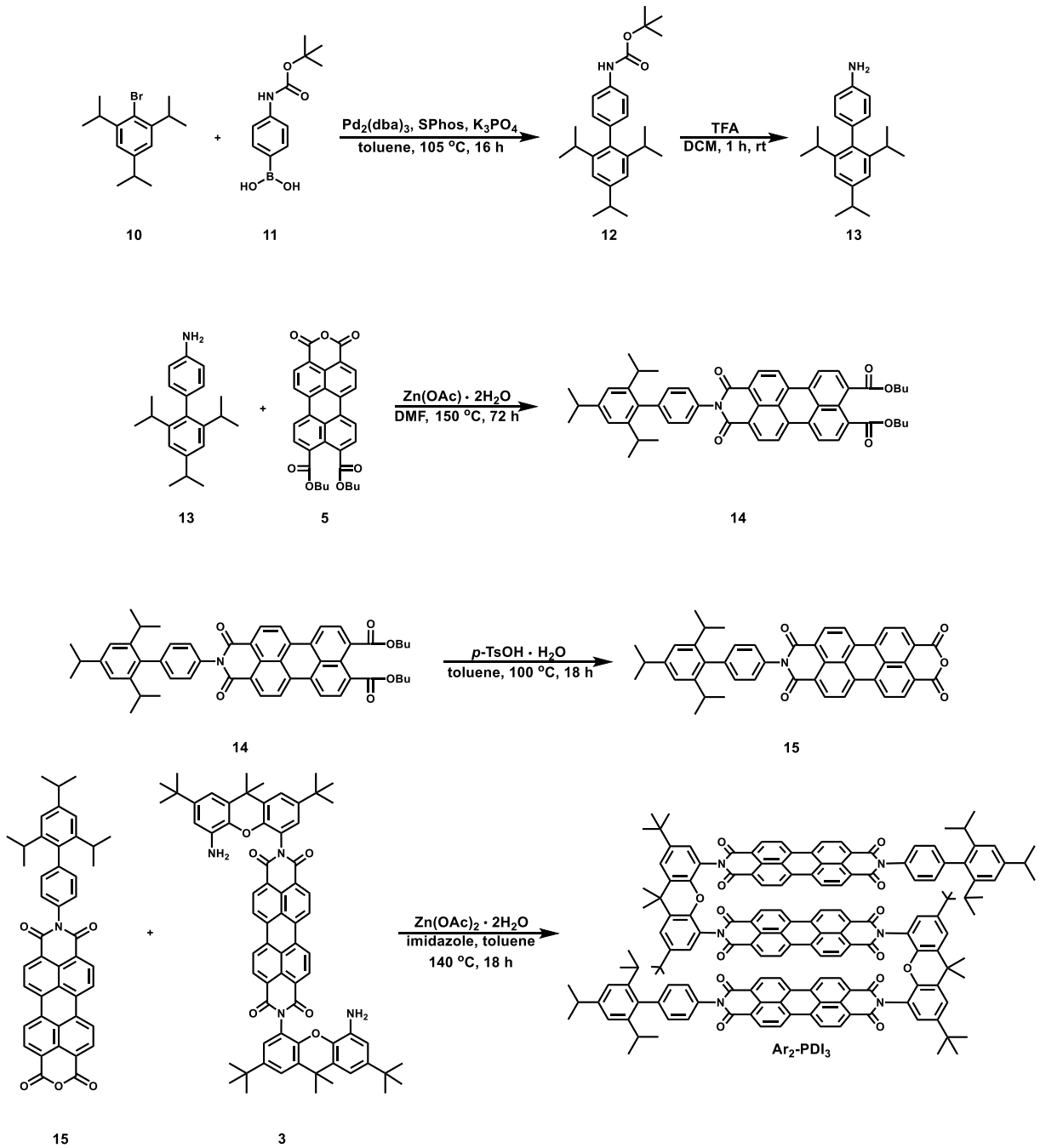

Scheme 3.2. Synthetic scheme for **Ar$_2$-PDI$_3$**.

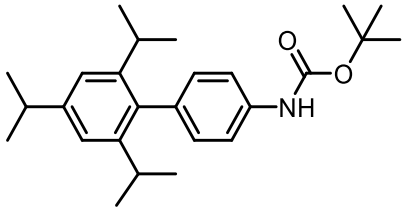

11: To a 50 mL round-bottom flask charged with a magnetic stir bar were added **10** (812 mg, 3.71 mmol), $Pd_2(dba)_3$ (91 mg, 0.099 mmol), SPhos (81 mg, 0.198 mmol), and K_3PO_4 (1.57 g, 7.41 mmol). The mixture was bubbled with N_2 for 20 min before adding toluene (25 mL) that had been separately bubbled with N_2 via cannula transfer. **9** (700 mg, 2.47 mmol, 0.63 ml) was added dropwise via syringe. The mixture was then bubbled with N_2 for an additional 10 min before stirring at 105 ^oC for 18 h. The reaction mixture was cooled to rt and filtered through a thin pad of silica gel (toluene), and the solvent was removed *in vacuo*. Column chromatography (silica gel, 50% CH_2Cl_2 in hexanes) afforded **12** (546 mg, 39%) as a white solid. ^1H NMR (500 MHz, DMSO-d_6): δ 9.38 (s, 1H), 7.48 (d, J = 8.1 Hz, 2H), 7.02 (s, 2H), 7.00 (s, 1H), 2.93-2.83 (m, 1H), 2.66-2.62 (2H, obscured), 1.49 (s, 9H), 1.23 (d, J = 7.0 Hz, 6H), 1.02 (d, J = 6.9 Hz, 12H). ^{13}C NMR (125 MHz, DMSO-d_6): δ 152.9, 147.3, 146.1, 138.0, 136.6, 133.7, 129.5, 120.0, 117.9, 79.0, 33.6, 29.7, 28.1, 24.1, 23.9. ESI HRMS *m*/*z* calcd. for $C_{26}H_{37}NO_2$ $(M)^+$ 395.2819, found: 395.2816.

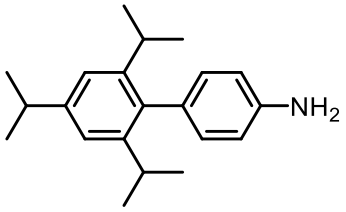

12: To a solution of **11** (550 mg, 1.39 mmol) in CH_2Cl_2 (11 mL) in a round-bottom flask charged with a magnetic stir bar was added TFA (3 ml) dropwise via syringe. The mixture was stirred at rt under air for 1 h before quenching with 1M K_2CO_3 solution. The solvent was removed *in vacuo*, and the precipitate was suspended in H_2O and collected by filtration before washing with

additional H_2O. **12** (411 mg, quant.) was afforded as a white solid. ^{1}H NMR (500 MHz, DMSO-d_6): δ 7.12 (s, 4H), 7.04 (s, 2H), 3.70 (br s, 2H), 2.94-2.84 (m, 1H), 2.54-2.45 (2H, obscured), 1.23 (d, *J* = 7.0 Hz, 6H), 1.02 (d, *J* = 7.0 Hz, 12H). ^{13}C NMR (125 MHz, DMSO-d_6): δ 147.6, 146.0, 136.2, 130.4, 120.1, 119.7, 33.6, 29.8, 24.0, 23.9. ESI HRMS *m*/*z* calcd. for $C_{21}H_{30}N$ $(M + H)^+$ 296.2373, found: 296.2364.

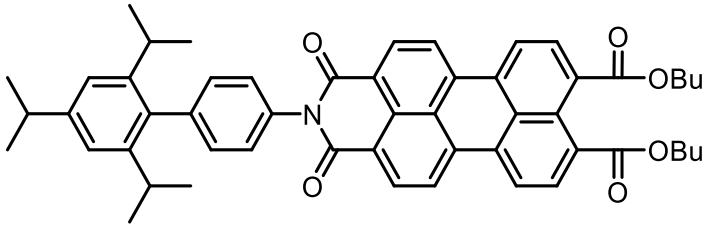

13: To a 10 mL sealed pressure vial charged with a magnetic stir bar were added **5** (210 mg, 0.402 mmol), **12** (148 mg, 0.502 mmol), $Zn(OAc)_2 \bullet 2H_2O$ (13 mg, 0.060 mmol), and DMF (6 mL). The reaction vessel was sealed with PTFE tape, sonicated for 5 min, evacuated and backfilled with N_2 three times at 30 sec intervals before being stirred at 150 ^{o}C for 72 h. The reaction mixture was cooled and the solvent was removed *in vacuo*. Column chromatography (silica gel, 1.5% MeOH in $CHCl_3$) afforded **13** (278 mg, 86%) as a bright red solid. ^{1}H NMR (500 MHz, $CDCl_3$): δ 8.69 (d, *J* = 8.0 Hz, 2H), 8.53 (d, *J* = 8.0 Hz, 2H), 8.48 (d, *J* = 8.0 Hz, 2H), 8.12 (d, *J* = 8.0 Hz, 2H), 7.37 (s, 4H), 7.08 (s, 2H), 4.34 (t, *J* = 6.7 Hz, 4H), 2.99-2.90 (m, 1H), 2.79-2.69 (m, 2H), 1.83-1.74 (m, 4H), 1.53-1.44 (m, 4H), 1.31 (d, *J* = 7.0 Hz, 6H), 1.12 (d, *J* = 6.9 Hz, 12H), 0.99 (t, *J* = 7.4 Hz, 6H). ^{13}C NMR (125 MHz, $CDCl_3$): δ 168.2, 163.9, 148.1, 146.7, 141.3, 136.2, 136.0, 133.6, 132.12, 132.11, 131.8, 130.6, 130.4, 129.7, 129.3, 129.2, 128.1, 126.3, 122.8, 122.3, 122.1, 120.7, 65.6, 34.3, 30.6, 30.3, 24.4, 24.1, 19.3, 13.8. APPI HRMS *m*/*z* calcd. for $C_{53}H_{54}NO_6$ $(M + H)^+$ 800.3946, found: 800.3928.

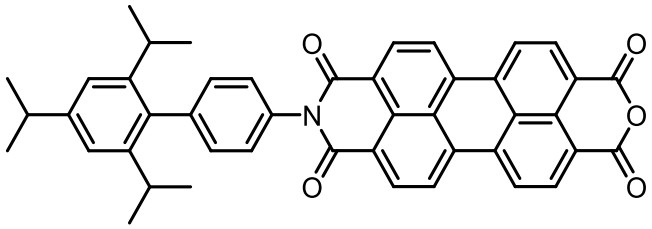

14: To a 25mL round-bottom flask charged with a magnetic stir bar was added **13** (210 mg, 0.263 mmol), *p*-TsOH • H_2O (0.268 mg, 1.13 mmol), and toluene (26 ml). The mixture was stirred at 100 ^oC under air for 18 h. The reaction mixture was then cooled to rt, and the solvent was removed *in vacuo*. The precipitate was suspended in H_2O, collected by filtration, washed with H_2O and MeOH and dried. The resulting dark red solid was used without further purification.

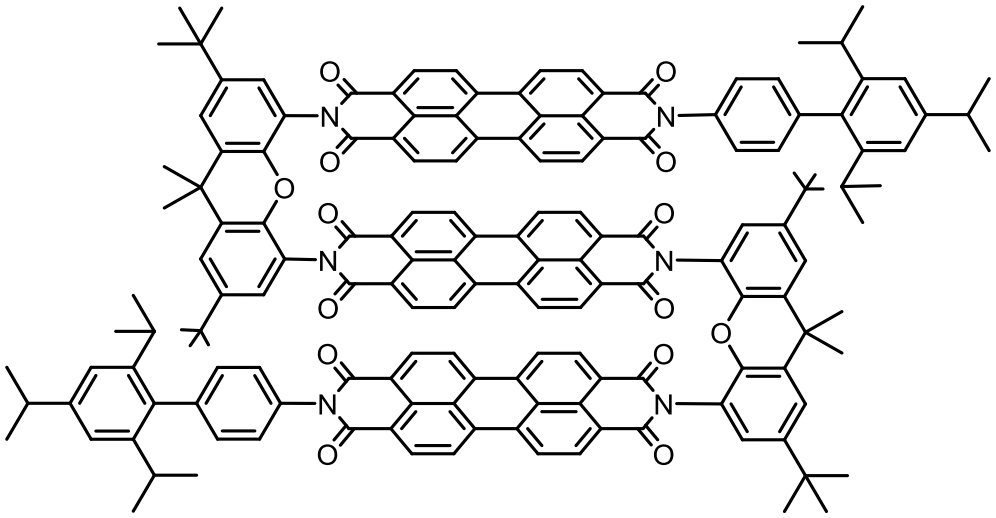

Ar$_2$-PDI$_3$: To a 25 mL round-bottom flask charged with a magnetic stir bar was added **3** (100 mg, 0.094 mmol), **14** (142 mg, 0.217 mmol), $Zn(OAc)_2$ • $2H_2O$ (10 mg, 0.047 mmol), imidazole (10.9 g, 160 mmol), and toluene (2 mL). The mixture was purged with N_2 for 10 min before stirring at 140 ^oC for 36 h. The reaction was removed from heat and 1M HCl (5 mL) was added. The reaction was then cooled to rt, dissolved in CH_2Cl_2, washed with distilled H_2O, dried over anhyd. Na_2SO_4, filtered, and the solvent was removed *in vacuo*. Column chromatography (silica gel, 1.5% MeOH

in $CHCl_3$), followed by further column chromatography (silica gel, 2-10% acetone in $CHCl_3$) afforded **Ar_2-PDI_3** (70 mg, 13.2% over two steps) as a dark red solid. ^{1}H NMR (600 MHz, $C_2D_2Cl_4$, 373.5 K): δ 8.50 (d, *J* = 7.4 Hz, 4H), 8.38 (d, *J* = 7.8 Hz, 2H), 8.29 (d, *J* = 7.8 Hz, 2H), 8.06 (d, *J* = 7.7 Hz, 4H), 7.97-7.90 (m, 12H), 7.77-7.73 (m, 4H), 7.67-7.63 (m, 4H), 7.61-7.59 (m, 2H), 7.58-7.53 (m, 2H), 7.25-7.19 (m, 4H), 7.14 (s, 2H), 6.88 (d, *J* = 2.0 Hz, 2H), 3.07-3.01 (m, 2H), 2.88-2.79 (m, 4H), 1.89 (s, 6H), 1.45 (s, 6H), 1.42 (d, *J* = 7.0 Hz, 18H), 1.41-1.33 (m, 36H), 1.23 (d, *J* = 6.7 Hz, 18H). APPI HRMS *m*/*z* calcd. for $C_{160}H_{135}N_6O_{14}$ $(M + H)^+$ 2364.0036, found: 2364.0018.

3.6.2. Marcus Analysis

3.6.2.1. Differential Pulse Voltammetry of Ar_2-PDI_3

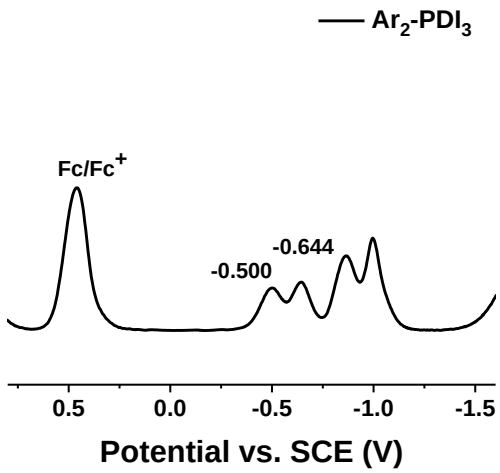

Figure 3.7. Differential pulse voltammogram for **Ar_2-PDI_3** in CH_2Cl_2 referenced to the ferrocene/ferrocenium redox couple.

Electron transfer processes for small molecules in solution such as **$ZnTPP_2$-PDI_3** can be evaluated using the semi-classical Marcus electron transfer model, where the rate of electron transfer, k_{CS},

depends on the reorganization energy λ, the driving force for charge transfer ΔG_{CS}, and the electronic coupling V[44, 92]:

$$k_{CS} = \frac{2\pi}{\hbar}|V|^2 \frac{1}{\sqrt{4\pi\lambda k_B T}} e^{-\frac{(\lambda+\Delta G_{CS})^2}{4\lambda k_B T}} \quad (3.1)$$

3.6.2.2. Free Energy Changes

The driving force ΔG_{CS} is given by the equation developed by Weller[90]:

$$\Delta G_{CS} = E_S - \left[e(E_{ox} - E_{red}) - \frac{e^2}{r_{DA}\varepsilon_S} + e^2\left(\frac{1}{2r_D} + \frac{1}{2r_A}\right) \times \left(\frac{1}{\varepsilon_S} - \frac{1}{\varepsilon_{SP}}\right)\right] \quad (3.4)$$

where E_{ox} and E_{red} are the first oxidation and reduction potentials of the electron donor and electron acceptor, respectively; r_D and r_A are the donor and acceptor radii, r_{DA} is the distance between donor and acceptor, ε_S is the dielectric constant of the solvent mediating the electron transfer event (ε_S (1,4-dioxane) = 2.25), and ε_{SP} is the dielectric constant of the electrochemical solvent (ε_{SP} (CH_2Cl_2) = 2.25). CH_2Cl_2 was chosen as the electrochemical solvent for its ability to dissolve sufficient material and supporting electrolyte needed for accurate measurements. MM+ force field calculations estimate r_{DA} = 16.1 Å by averaging the distances between the donor and each of the three acceptors (A_1-A_3), $r_{DA} = \frac{r_{DA1}+r_{DA2}+r_{DA3}}{3}$. r_D (ZnTPP) = r_A (PDI) = 7 Å as determined for model systems of both chromophores[151, 152]. From these values, ΔG_{CS} (**$ZnTPP_2$-PDI_3**) = -0.46 eV.

3.6.2.3. Reorganization Energy

The reorganization energy λ can be broken down into two components, $\lambda = \lambda_S + \lambda_I$, where λ_I is the internal reorganization energy and λ_S is the solvent contribution. The solvent reorganization energy λ_S is estimated using the dielectric continuum model[92, 93]:

$$\lambda_S = e^2\left(\frac{1}{2r_D} + \frac{1}{2r_A} - \frac{1}{r_{DA}}\right) \times \left(\frac{1}{\varepsilon_{op}} - \frac{1}{\varepsilon_S}\right) \quad (3.5)$$

where *e* is the charge of an electron, and ε_{op} and ε_S are the high-frequency and static dielectric constants of the solvent, respectively. For 1,4-dioxane, ε_{op} = 1.97 and ε_S = 2.25 at room temperature. Using the values for these parameters given above, λ_S = 0.07 eV. The internal reorganization energy λ_I can be calculated using DFT methods (see below), using[153]

$$\lambda_I = E(\text{anion at optimized neutral geometry}) - E(\text{optimized anion}) \quad (\mathbf{3.6})$$

PDI_3 (see below) with phenyl groups substituted in places of the porphyrins was used to reduce computational time. For PDI_3, λ_I = 0.10 eV. Using these values, plus λ_I = 0.14 eV for the oxidation of ZnTPP[154], λ_I = 0.24 eV and λ = 0.31 eV.

3.6.3 Additional Steady-State Optical Data and Global Analysis

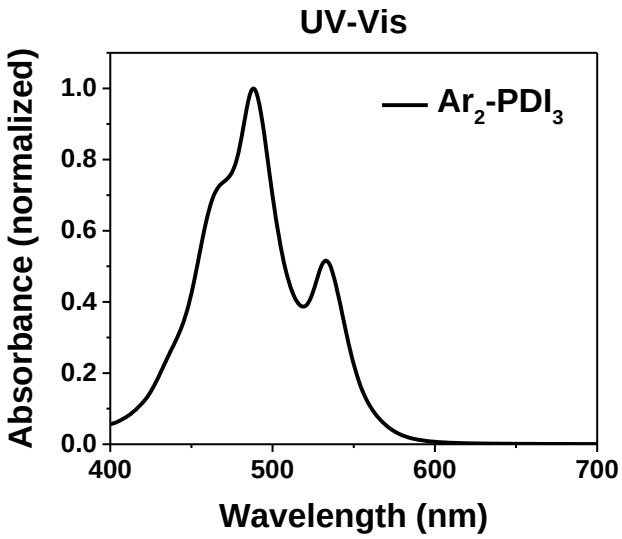

Figure 3.8. Normalized UV-Vis absorption spectrum for **Ar_2-PDI_3** in CH_2Cl_2.

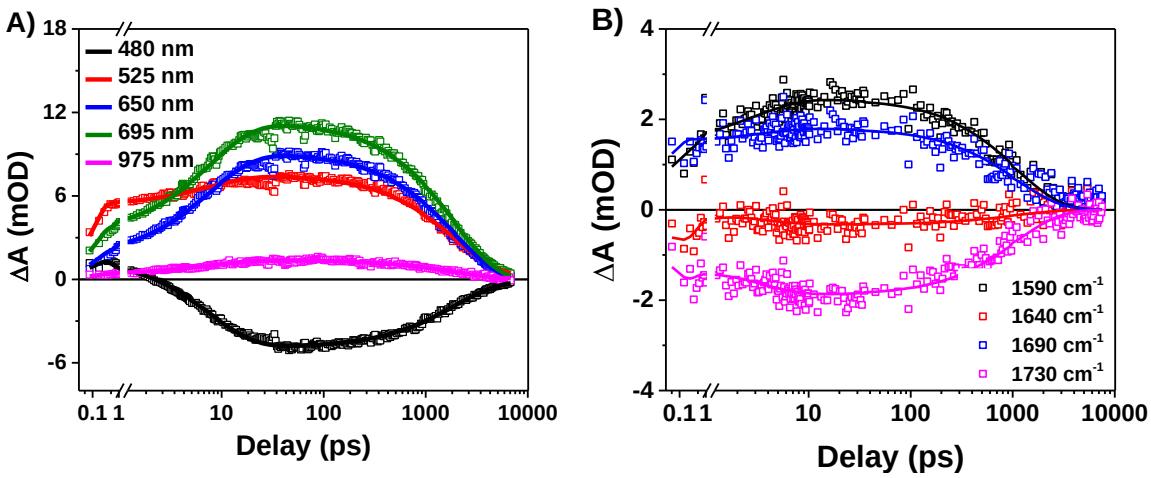

Figure 3.9. Global fit at several wavelengths using the kinetic model described in the main text for the A) fsTA spectra of **ZnTPP$_2$-PDI$_3$** in 1,4-dioxane and B) fsIR spectra of **ZnTPP$_2$-PDI$_3$** in 1,4-dioxane.

3.6.4. Computational Data

The total energy in hartrees (1 hartree = 27.2114 eV) was computed at the B3LYP-D3/6-31+G(d) level of theory using TeraChem 4.4 as previously reported[44].

PDI$_3$ (0)

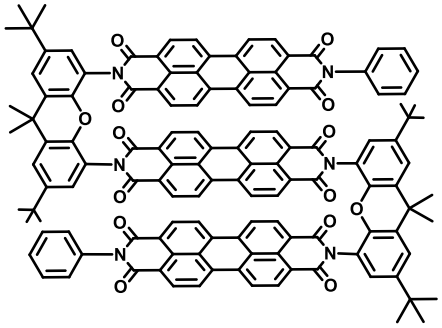

Cartesian Coordinates:

C	1.4032494723	0.6763094775	-1.3060138640	C	2.7770007289	-1.2962030047	-1.6226786625
C	1.6012995051	-0.6913015175	-1.1727641252	C	-1.4383104313	-1.9930847462	0.2139898584
O	0.6868232180	-1.5502295788	-0.6263885868	C	-2.6768472189	-1.5993362587	0.6997319339
C	-0.5088642450	-1.0471187732	-0.2082496162	C	-3.0148807812	-0.2436815186	0.7673079534
C	-0.8175015813	0.3136233446	-0.1990605792	C	-2.0675995501	0.6795220747	0.3069886588
C	0.1512308104	1.3590505934	-0.7553430942	C	-0.5555242461	2.1352606059	-1.8923685556
C	2.4067338400	1.4070609629	-1.9615686489	C	0.5665294815	2.3350901232	0.3695497499
C	3.5659084222	0.8221452239	-2.4740576740	C	-4.3608730142	0.2485532527	1.3130697280
C	3.7445023297	-0.5574082064	-2.2721861021	C	-4.1153118118	1.0989333223	2.5776257964

C	-5.0695441823	1.1091437013	0.2446658392	C	7.7865935906	-18.3940577616	-5.3910438706
C	-5.2939744684	-0.9152944752	1.6843158212	C	5.6242263982	-18.2125532850	-6.6753822730
C	4.6084167251	1.6003412787	-3.2869765440	C	7.2892954269	-16.3521397841	-6.7403661524
C	4.2602390396	3.0937640883	-3.3931677997	C	2.1741364051	-18.1495476767	3.2513947448
C	6.0000301350	1.4700374830	-2.6360702920	C	2.1107427258	-19.6722202982	3.0483276448
C	4.6547484070	1.0037923152	-4.7117610864	C	3.1873059299	-17.8360373747	4.3740780749
C	1.6666729837	-5.8724923161	-2.9330762383	C	0.7720135339	-17.6698836135	3.6776419921
C	1.6704585689	-7.2470600108	-2.6863989375	C	0.1839164081	-11.8089934444	2.4939077377
C	2.2233207987	-7.7831099174	-1.5230139911	C	0.2800047530	-10.4170168943	2.4011147843
C	2.7600259262	-6.8940578627	-0.5441048996	C	-0.1644654927	-9.7232564337	1.2758316264
C	2.7661454832	-5.4921368886	-0.8114706842	C	-0.7156981427	-10.4650528825	0.1857846260
C	2.2267174765	-4.9966966486	-2.0204921355	C	-0.7892272722	-11.8871978719	0.2789686239
C	3.3111775446	-7.3717458633	0.6845200790	C	-0.3506442768	-12.5462616681	1.4522643496
C	3.8431310281	-6.4437027272	1.5805136843	C	-1.1913056344	-9.8208772017	-0.9979555668
C	3.8491871444	-5.0728454219	1.3107429714	C	-1.6481154919	-10.6129453203	-2.0520932753
C	3.3237551362	-4.5921019571	0.1240082963	C	-1.6900045541	-12.0074379446	-1.9625125504
C	2.2757064381	-9.2261322137	-1.2795627133	C	-1.2854472492	-12.6468790055	-0.8048201258
C	3.3125035493	-8.8134508474	0.9541330577	C	-0.0989588679	-8.2610828050	1.1812593612
C	2.2654644078	-3.5521866129	-2.3429353695	C	-1.2030088865	-8.3556369204	-1.0560676636
C	3.3810316669	-3.1403011566	-0.1573464354	C	-0.4731428841	-14.0171260099	1.5924970929
C	1.8196173345	-10.1522361310	-2.2163552570	C	-1.3905811847	-14.1220214179	-0.7209597338
C	1.8152176984	-11.5241515663	-1.9561166103	C	0.4730327674	-7.4750055768	2.1807698572
C	2.3027759925	-12.0022247139	-0.7538125869	C	0.4433198412	-6.0781383062	2.1288110641
C	2.8394673437	-11.1087673381	0.1997487554	C	-0.1700329820	-5.4314034590	1.0723559077
C	2.8126777942	-9.7044768279	-0.0444400503	C	-0.7093892849	-6.1867342502	0.0037239166
C	3.3765157943	-11.6156203025	1.4045747717	C	-0.6647428871	-7.6128607790	0.0396981446
C	3.8375358022	-10.7358456180	2.3683905477	C	-1.3194917062	-5.5227326726	-1.0864696148
C	3.7889104128	-9.3550492255	2.1500031594	C	-1.8113995838	-6.2583708287	-2.1493564697
N	2.8960153882	-2.7162979025	-1.4032933955	C	-1.7443217716	-7.6551605405	-2.1349998977
C	2.1905972046	-13.4407766404	-0.4546479907	N	-1.0037711487	-14.7102388185	0.5005488070
N	2.8910304266	-13.9118711374	0.6745698823	C	-0.3213628756	-3.9581109950	1.1194258529
C	3.4783553381	-13.0763990333	1.6447014324	C	-1.5209273097	-4.0543328024	-1.0673594425
O	3.8527460390	-2.3464494910	0.6428862901	O	-1.8233127896	-14.8018138329	-1.6339514035
O	1.7989978534	-3.0978845343	-3.3737697032	O	-0.1394040313	-14.5990805770	2.6154543621
O	1.5268190561	-14.1948667579	-1.1503901379	O	0.1518273635	-3.2715703564	2.0089205640
O	4.0321158458	-13.5356744222	2.6299317450	O	-2.0576177390	-3.4496531510	-1.9793221596
C	3.6301899189	-17.4255972494	-0.2689569291	C	-1.0989583480	-16.1488229359	0.5893345896
C	3.5799954792	-16.0377015710	-0.2618317315	C	-2.1558312197	-16.7191147957	1.2937495356
O	4.0460980716	-15.2608094100	-1.2807314450	C	-2.2636889858	-18.1071953360	1.3615786870
C	4.6809244949	-15.8482585253	-2.3316064694	C	-1.3174956743	-18.9112487972	0.7225844306
C	4.7350268497	-17.2282036954	-2.5187753147	C	-0.2599366174	-18.3256618898	0.0250445851
C	4.1390300312	-18.1945828391	-1.4917661532	C	-0.1425667743	-16.9380521761	-0.0437826523
C	3.1521465395	-18.0885150392	0.8715441351	N	-1.1132478744	-3.3901623025	0.1062565146
C	2.6326933905	-17.4197857778	1.9822959531	C	5.5177656289	-4.6843020083	-3.0916639175
C	2.5550823421	-16.0196336093	1.9246100053	C	5.2011040587	-6.0214539118	-3.3549915429
C	3.0077055827	-15.3386615650	0.8089144330	C	5.5209689541	-7.0439779422	-2.4616467055
C	5.3156904442	-14.9732060421	-3.2140283364	C	6.1416535322	-6.6981791042	-1.2194941426
C	5.9539479185	-15.4624282986	-4.3464377584	C	6.4164128070	-5.3269023432	-0.9380778192
C	5.9809234684	-16.8362698959	-4.6066495435	C	6.1323550361	-4.3322455254	-1.9029212143
C	5.3765609869	-17.6873883122	-3.6713415506	C	6.5016821807	-7.6883874147	-0.2545209482
C	2.9500378853	-18.9493299021	-2.1327081818	C	7.0690986544	-7.2750127297	0.9519637115
C	5.2233691917	-19.2066428899	-1.0582928727	C	7.2869285091	-5.9249388539	1.2388370737
C	6.6653519261	-17.4339898038	-5.8430833669	C	6.9747501500	-4.9526193905	0.3058602853

C	5.2739977907	-8.4589245912	-2.7650446894	H	5.3817675434	1.5473025613	-5.3270775791
C	6.2882828142	-9.1023560854	-0.5742024140	H	1.2374704753	-5.4663427561	-3.8420314054
C	6.5360168939	-2.9261398396	-1.6773691815	H	1.2243651401	-7.8995212334	-3.4251700530
C	7.2135373704	-3.5284663532	0.6377044779	H	4.2826938198	-6.7791338915	2.5111610560
C	4.6523996908	-8.8772194112	-3.9429067104	H	4.2799380168	-4.3681291836	2.0127180990
C	4.4733511311	-10.2321820894	-4.2426983083	H	1.4414976746	-9.8172467487	-3.1729177737
C	4.9238175829	-11.2108361546	-3.3732832898	H	1.4215842077	-12.2298459791	-2.6777482071
C	5.5355643691	-10.8310815338	-2.1569216759	H	4.2416712657	-11.1412321035	3.2896505258
C	5.6984371395	-9.4509388716	-1.8294011591	H	4.1518934759	-8.7010686823	2.9336841302
C	6.0080568681	-11.8275280747	-1.2727331439	H	3.1834898414	-19.1705781147	0.8764266361
C	6.5403339108	-11.4705289396	-0.0480322130	H	2.1152791529	-15.4526723037	2.7321523397
C	6.6578909391	-10.1228298114	0.3008064090	H	6.4295047888	-14.7529892922	-5.0103861902
N	7.0068078699	-2.6007798083	-0.4022501361	H	5.4105393821	-18.7581263298	-3.8431638730
C	4.7482541466	-12.6420781361	-3.7286022026	H	2.1654234456	-18.2483587145	-2.4330351464
C	6.0177777593	-13.2514449187	-1.6661053603	H	2.5221064393	-19.6646403064	-1.4220391340
O	7.5916143869	-3.1661873799	1.7385935402	H	3.2733335361	-19.5053092883	-3.0196259239
O	6.4649332841	-2.0822369348	-2.5623046533	H	6.0837665308	-18.6877136666	-0.6259014025
O	4.1395704552	-12.9982983939	-4.7246668090	H	5.5708955562	-19.7983354383	-1.9108004066
O	6.5752428461	-14.1049186814	-0.9987010516	H	4.8299642246	-19.9029156109	-0.3117401252
C	7.3252089447	-1.2166104763	-0.1248165878	H	7.3980914855	-19.2020702632	-4.7632839871
C	6.3919938860	-0.4124303448	0.5239770495	H	8.5470554927	-17.8578640517	-4.8128356243
C	6.7325085610	0.9066798534	0.8227647212	H	8.2741732331	-18.8499201517	-6.2608897183
C	7.9820036924	1.4128301607	0.4618813325	H	5.1658394687	-19.0209799764	-6.0964774975
C	8.8991705816	0.5999468065	-0.2064673236	H	6.0986431550	-18.6582764882	-7.5576686622
C	8.5731089231	-0.7238097255	-0.4966927860	H	4.8234138648	-17.5468154108	-7.0143841403
N	5.3586427486	-13.5773492718	-2.8721510909	H	8.0683938353	-15.7913060312	-6.2124810795
H	2.2546862025	2.4724529972	-2.0821403381	H	6.5370810775	-15.6425602362	-7.1014065751
H	4.6341131190	-1.0592398930	-2.6276267256	H	7.7524294939	-16.8224489293	-7.6143364544
H	-3.3672198334	-2.3706511075	1.0167898092	H	3.0934045712	-20.1019528149	2.8226296915
H	-2.3136406272	1.7359886723	0.3353983444	H	1.4201388492	-19.9334864150	2.2383589459
H	-0.8626901807	1.4498383610	-2.6875851624	H	1.7473584602	-20.1498360724	3.9644536140
H	0.1078765523	2.8900018175	-2.3262737818	H	4.1901018193	-18.1877808768	4.1064298881
H	-1.4459644701	2.6512924547	-1.5194594314	H	2.8879307902	-18.3258674141	5.3087734154
H	1.0551805242	1.7943380635	1.1856556294	H	3.2490953316	-16.7583248854	4.5583010089
H	-0.3057580397	2.8578606018	0.7764789133	H	0.0353043498	-17.8818472002	2.9006274589
H	1.2661135355	3.0851694962	-0.0131186013	H	0.7372718276	-16.5974594898	3.8768111681
H	-3.4890939600	1.9708794826	2.3610500799	H	0.4671188048	-18.1919601702	4.5930988569
H	-3.6113921109	0.5092413809	3.3512385197	H	0.5220578971	-12.3316084793	3.3817546218
H	-5.0668537422	1.4607121666	2.9856230957	H	0.7104727086	-9.8811162276	3.2370513345
H	-4.4849949713	1.9972437220	-0.0155572165	H	-1.9869696996	-10.1521222814	-2.9720181556
H	-6.0431638469	1.4488169553	0.6168186418	H	-2.0496147729	-12.6111100288	-2.7884499099
H	-5.2325799533	0.5340961122	-0.6731011505	H	0.9543294972	-7.9443279155	3.0294837843
H	-4.8667938625	-1.5443467217	2.4733976532	H	0.8740218094	-5.4811482506	2.9244559704
H	-5.5120486058	-1.5490029357	0.8176229491	H	-2.2737654510	-5.7304223811	-2.9761702332
H	-6.2455109586	-0.5208744710	2.0567381950	H	-2.1659278603	-8.1914884697	-2.9765415204
H	4.2217892092	3.5669407750	-2.4053065751	H	-2.8821088702	-16.0775510860	1.7820341790
H	3.2983695772	3.2557039226	-3.8927895538	H	-3.0837378362	-18.5587140582	1.9117573704
H	5.0289362332	3.6099710557	-3.9781926757	H	0.4793236274	-18.9476094625	-0.4674625415
H	6.0046042256	1.9085840995	-1.6347763853	H	0.6723766220	-16.4610082848	-0.5753588037
H	6.7466167574	1.9979207705	-3.2420620318	H	5.2933484922	-3.9085294447	-3.8153364713
H	6.3163592753	0.4284382357	-2.5433712569	H	4.7106023172	-6.2494209316	-4.2926731367
H	3.6733224542	1.0709342214	-5.1940906970	H	7.3510776472	-8.0050354608	1.7004089904
H	4.9522592542	-0.0492469832	-4.6908431808	H	7.7084902350	-5.6161051800	2.1893263490

H	4.2975879290	-8.1457451812	-4.6585197903	H	9.2761775769	-1.3750280137	-1.0060058420
H	3.9898282946	-10.5377051407	-5.1641561579	H	8.2394688114	2.4425326541	0.6928537780
H	6.8781291607	-12.2530033200	0.6221426073	H	-1.4024916256	-19.9931438932	0.7732007025
H	7.0737168990	-9.8849466385	1.2714375788		**Energy at this geometry:**		
H	5.4210442359	-0.8189637957	0.7788072392		***E*(charge = 0) = -6390.9787554406**		
H	6.0130228002	1.5411372170	1.3321313408		***E*(charge = -1) = -6391.0786248221**		
H	9.8688737262	0.9929188814	-0.4969750253				

PDI_3 (-)

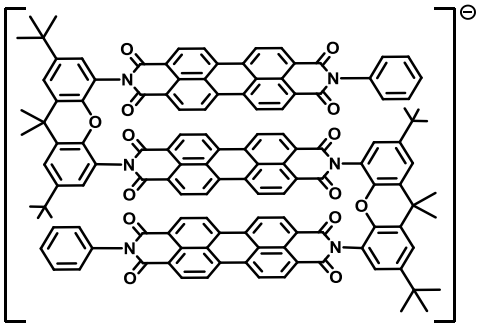

Cartesian Coordinates:

C	1.4070363320	0.6674140801	-1.2845675323	C	3.3505966161	-7.3805348290	0.7096660353
C	1.6057864578	-0.6993329284	-1.1417011355	C	3.8672267519	-6.4494079390	1.6284908760
O	0.6777017462	-1.5562145757	-0.6152584555	C	3.8626733112	-5.0853731190	1.3703027872
C	-0.5204007400	-1.0553025559	-0.2146315252	C	3.3448129696	-4.5909886515	0.1765556194
C	-0.8249184216	0.3073588790	-0.1976249614	C	2.2668479418	-9.2115712435	-1.2449963456
C	0.1512392291	1.3517632587	-0.7437230252	C	3.3824623783	-8.8158656117	0.9505207007
C	2.4156715160	1.3960956144	-1.9355271792	C	2.2822484785	-3.5533231211	-2.2912158532
C	3.5807350756	0.8072545364	-2.4291268789	C	3.3967179984	-3.1479453402	-0.0916898960
C	3.7634546579	-0.5688428291	-2.2062126368	C	1.7418342237	-10.1305501813	-2.1674157837
C	2.7908419485	-1.3071964843	-1.5633986425	C	1.7344795990	-11.4957702019	-1.9147453119
C	-1.4608533343	-2.0031861286	0.1839018280	C	2.2785177229	-11.9924661134	-0.7361948170
C	-2.7004102420	-1.6048112131	0.6633082178	C	2.8661099286	-11.1113286939	0.2009509582
C	-3.0313226961	-0.2478577875	0.7459023424	C	2.8431138908	-9.7018572841	-0.0355079378
C	-2.0773441652	0.6756452324	0.3007082825	C	3.4414944790	-11.6248453255	1.3851966006
C	-0.5488011224	2.1325741524	-1.8819361891	C	3.9738948552	-10.7468623604	2.3260692508
C	0.5605337809	2.3276133119	0.3840180771	C	3.9295910406	-9.3728988845	2.1192939929
C	-4.3740516811	0.2474873074	1.2977040936	N	2.9098525951	-2.7228088303	-1.3412604376
C	-4.1212505896	1.0897001529	2.5665011335	C	2.1730741250	-13.4251143259	-0.4504615954
C	-5.0839173847	1.1202061459	0.2400268317	N	2.8886097556	-13.9000222678	0.6719347221
C	-5.3124383223	-0.9133476372	1.6651632836	C	3.5181296691	-13.0744703047	1.6293297896
C	4.6213813838	1.5748842187	-3.2546272569	O	3.8598613520	-2.3388461083	0.7056849653
C	4.2739705977	3.0671436040	-3.3808865102	O	1.8210566686	-3.0795454090	-3.3209630769
C	6.0171323006	1.4509453222	-2.6123490950	O	1.5075252301	-14.1915191668	-1.1399994879
C	4.6601264041	0.9592425690	-4.6717030037	O	4.0826870614	-13.5584719184	2.6025617974
C	1.6833420177	-5.8637765817	-2.8928269844	C	3.6235372171	-17.4167853758	-0.2651361107
C	1.6811947481	-7.2327161280	-2.6535580925	C	3.5785864876	-16.0282126197	-0.2580330124
C	2.2379866309	-7.7763861472	-1.4865379247	O	4.0662442359	-15.2538028249	-1.2668706394
C	2.7888264451	-6.8919004703	-0.5104545469	C	4.7003122652	-15.8405005662	-2.3142452248
C	2.7903673246	-5.4848896459	-0.7679930049	C	4.7420914807	-17.2207834293	-2.5088608626
C	2.2439008764	-4.9870575495	-1.9734395411	C	4.1450623076	-18.1871357046	-1.4818142554

C	3.1369384268	-18.0788022591	0.8728987424	N	-1.1423451866	-3.3992021360	0.0673942315
C	2.6167572600	-17.4051199489	1.9795893859	C	5.5651329873	-4.7072489099	-3.1289875326
C	2.5410525616	-16.0045785640	1.9179017894	C	5.2330723698	-6.0373197394	-3.3770470137
C	2.9979381200	-15.3236504877	0.8047378337	C	5.5269433832	-7.0546746782	-2.4587170313
C	5.3440093449	-14.9643951581	-3.1909273593	C	6.1495912559	-6.6990015658	-1.2218961609
C	5.9728498948	-15.4564145330	-4.3268698483	C	6.4399442183	-5.3257252833	-0.9543329604
C	5.9838379968	-16.8291604750	-4.5974682468	C	6.1764907378	-4.3413076777	-1.9357505863
C	5.3754461757	-17.6808315179	-3.6658998427	C	6.4930813622	-7.6860145933	-0.2450357348
C	2.9674023395	-18.9581176938	-2.1248602185	C	7.0204830451	-7.2616273734	0.9814689726
C	5.2363787116	-19.1876279349	-1.0369564533	C	7.2537275646	-5.9156088311	1.2511899056
C	6.6462169511	-17.4227386613	-5.8483443844	C	6.9936759600	-4.9473757723	0.2919515885
C	7.7435883126	-18.4226814422	-5.4251406853	C	5.2514402726	-8.4636987006	-2.7358128876
C	5.5796199867	-18.1579141094	-6.6882890114	C	6.3121997513	-9.0952446108	-0.5670626499
C	7.2939105156	-16.3418245968	-6.7299937171	C	6.5748318281	-2.9404939439	-1.7184232840
C	2.1616443485	-18.1261758752	3.2549510627	C	7.2656542333	-3.5364860152	0.6050250264
C	2.1160753002	-19.6520380370	3.0722069870	C	4.5849235253	-8.8872754586	-3.8936748093
C	3.1698563815	-17.7896951946	4.3757035454	C	4.4061514584	-10.2389520794	-4.1828153577
C	0.7532397148	-17.6579073723	3.6732948271	C	4.9090591481	-11.2189181644	-3.3348941513
C	0.2387073662	-11.8047086408	2.4224802406	C	5.5507971531	-10.8371983851	-2.1346615087
C	0.3426522446	-10.4184424694	2.3179350826	C	5.7035796116	-9.4529108157	-1.8090976480
C	-0.1506375198	-9.7242331757	1.2082769344	C	6.0626914126	-11.8271934118	-1.2630165206
C	-0.7519944447	-10.4669467864	0.1453323337	C	6.6355823501	-11.4576563693	-0.0537912412
C	-0.8301225120	-11.8897403001	0.2476973639	C	6.7421916388	-10.1153196895	0.2934913535
C	-0.3511702185	-12.5452550518	1.4082460732	N	7.0553428318	-2.6142939335	-0.4441371566
C	-1.2589212378	-9.8236749169	-1.0257685110	C	4.7589871838	-12.6407885696	-3.7006669893
C	-1.7752621985	-10.6183642643	-2.0568971035	C	6.0652992199	-13.2455723660	-1.6482897990
C	-1.8181026022	-12.0071392763	-1.9609635214	O	7.6736552601	-3.1559122292	1.6933524704
C	-1.3645168898	-12.6492969547	-0.8173860720	O	6.5003487139	-2.0852572473	-2.5988338613
C	-0.0869702804	-8.2669868885	1.1099402750	O	4.1594087567	-13.0137139909	-4.7002854072
C	-1.2527197356	-8.3616198016	-1.0940456583	O	6.6300789760	-14.1107274490	-0.9952206761
C	-0.4848407062	-14.0058776109	1.5640704510	C	7.3582614978	-1.2316985516	-0.1589745507
C	-1.4578974709	-14.1191372296	-0.7318783350	C	6.4259124043	-0.4555102463	0.5255493048
C	0.5194449094	-7.4787313419	2.0914188156	C	6.7488667929	0.8624809373	0.8467841561
C	0.4757316708	-6.0845404020	2.0470788418	C	7.9829235585	1.3988213867	0.4761959517
C	-0.1746526132	-5.4350545624	1.0124496893	C	8.9001975046	0.6157628980	-0.2267305364
C	-0.7363967339	-6.1895316278	-0.0467625758	C	8.5902420011	-0.7067669598	-0.5410252153
C	-0.6877883796	-7.6169897412	-0.0133937154	N	5.3904522920	-13.5717261525	-2.8492701929
C	-1.3720611979	-5.5269434413	-1.1223231935	H	2.2617310021	2.4600738863	-2.0684756588
C	-1.8821489835	-6.2661061486	-2.1788170950	H	4.6588450018	-1.0743113018	-2.5435600657
C	-1.8136993049	-7.6587131998	-2.1668790654	H	-3.3960293796	-2.3774726208	0.9659614078
N	-1.0413662795	-14.7017465029	0.4840844739	H	-2.3181442714	1.7335151017	0.3364492436
C	-0.3355055590	-3.9689087011	1.0722413559	H	-0.8602732624	1.4480527588	-2.6762032500
C	-1.5793078375	-4.0637919203	-1.0969238532	H	0.1202235291	2.8820945714	-2.3167160679
O	-1.9116853294	-14.8120901764	-1.6289738041	H	-1.4363999967	2.6550387056	-1.5095583552
O	-0.1452760062	-14.5938072817	2.5854890890	H	1.0491261340	1.7866107160	1.1998912280
O	0.1338367651	-3.2756780667	1.9610249684	H	-0.3139549904	2.8485349744	0.7900191712
O	-2.1464558045	-3.4530648269	-1.9897319530	H	1.2604168294	3.0790922999	0.0037785614
C	-1.1213075880	-16.1382795388	0.5750252336	H	-3.4878766062	1.9570169024	2.3520486791
C	-2.1690373491	-16.7220076846	1.2828269101	H	-3.6190740781	0.4925576706	3.3354001741
C	-2.2610056806	-18.1111576231	1.3534566263	H	-5.0691611984	1.4576233247	2.9790418782
C	-1.3066449642	-18.9052436268	0.7139103083	H	-4.4947984446	2.0068933689	-0.0148558481
C	-0.2570263880	-18.3075796424	0.0141196553	H	-6.0548448812	1.4618717063	0.6192765405
C	-0.1564583505	-16.9186304514	-0.0569840331	H	-5.2529378115	0.5536932009	-0.6818993169

H	-4.8836018353	-1.5514693399	2.4457722596	H	6.5582051429	-15.6068455609	-7.0729219435
H	-5.5375323675	-1.5395364238	0.7949667037	H	7.7416066223	-16.8078302265	-7.6149794969
H	-6.2601662896	-0.5161646205	2.0458382765	H	3.1031940882	-20.0716059050	2.8458757395
H	4.2314424518	3.5530871612	-2.3992668422	H	1.4252232839	-19.9320460373	2.2686726678
H	3.3133278083	3.2224700951	-3.8855346046	H	1.7627950963	-20.1220993983	3.9969381068
H	5.0451236337	3.5756308564	-3.9703282977	H	4.1768018014	-18.1317462577	4.1100608489
H	6.0290549503	1.8942759992	-1.6131752969	H	2.8763784944	-18.2737838429	5.3160363209
H	6.7593307858	1.9757225837	-3.2274088825	H	3.2202628855	-16.7096766391	4.5476130789
H	6.3339613440	0.4098904436	-2.5175225053	H	0.0156208486	-17.9213730856	2.9125414373
H	3.6749794947	1.0169285726	-5.1481341852	H	0.6957586825	-16.5784206845	3.8195302658
H	4.9591199032	-0.0926206988	-4.6353377915	H	0.4662524831	-18.1445642069	4.6146713203
H	5.3822923362	1.4951668404	-5.3004739107	H	0.6180664828	-12.3266206108	3.2936397952
H	1.2545144371	-5.4503580815	-3.7989154873	H	0.8307401386	-9.8825782745	3.1215349126
H	1.2285826582	-7.8824775722	-3.3902292235	H	-2.1504022721	-10.1569986693	-2.9624523717
H	4.2902592476	-6.7917114342	2.5639628645	H	-2.2111213516	-12.6132872273	-2.7697027467
H	4.2820930729	-4.3811770572	2.0799409940	H	1.0368332109	-7.9476702679	2.9184383334
H	1.3175047908	-9.7811409070	-3.0985343706	H	0.9348114933	-5.4883735149	2.8269051592
H	1.2992002553	-12.1955184284	-2.6179245995	H	-2.3564421652	-5.7367405756	-2.9979972983
H	4.4167214652	-11.1645815976	3.2236503019	H	-2.2428982060	-8.1966701963	-3.0035693683
H	4.3475742399	-8.7237635607	2.8790593929	H	-2.9002149910	-16.0868157352	1.7723190226
H	3.1651747264	-19.1614903459	0.8784751645	H	-3.0742126641	-18.5713074347	1.9078886752
H	2.0989505861	-15.4321278545	2.7201297075	H	0.4904537439	-18.9209413771	-0.4771149266
H	6.4506911898	-14.7458446474	-4.9877239471	H	0.6523859426	-16.4292956207	-0.5873585835
H	5.3956586995	-18.7514765649	-3.8438936708	H	5.3507827584	-3.9369415444	-3.8614996667
H	2.1787145919	-18.2659960862	-2.4344585305	H	4.7502867153	-6.2757115036	-4.3160538090
H	2.5407042486	-19.6711052391	-1.4106101730	H	7.2526788780	-7.9859676511	1.7522728141
H	3.2998070869	-19.5189358748	-3.0059869828	H	7.6512674275	-5.5975728653	2.2089221556
H	6.0866714522	-18.6567031390	-0.5989682579	H	4.1891603263	-8.1556558146	-4.5871558656
H	5.5983842400	-19.7768354988	-1.8859013495	H	3.8907077297	-10.5512828619	-5.0844164123
H	4.8445620877	-19.8855520566	-0.2904365806	H	6.9990671189	-12.2374037941	0.6060990166
H	7.3347101929	-19.2347192702	-4.8157438777	H	7.1928486749	-9.8684694903	1.2458725064
H	8.5186347262	-17.9205949613	-4.8358332451	H	5.4679066465	-0.8873519711	0.7907229783
H	8.2175246236	-18.8706390805	-6.3075017453	H	6.0269322463	1.4721557787	1.3828229874
H	5.1054744319	-18.9634761724	-6.1181331942	H	9.8589993742	1.0307260659	-0.5248984601
H	6.0352445127	-18.5993335638	-7.5834091077	H	9.2953606957	-1.3344702291	-1.0765576887
H	4.7937138204	-17.4646768332	-7.0059971135	H	8.2272171429	2.4278480222	0.7267018273
H	8.0877099753	-15.8098897987	-6.1943054135	H	-1.3776868378	-19.9884948308	0.7671542292

Energy at this geometry:
***E*(charge = 0) = -6390.9752076786**
***E*(charge = -1) = -6391.08240479**

Chapter 4 - Fluorine Tuning of Morphology, Energy Loss, and Carrier Dynamics in Perylenediimide Polymer Solar Cells

4.1 Introduction

Solar cells incorporating solution-processable organic semi-conductors as photoactive layers hold promise as inexpensive, lightweight, and renewable sunlight-to-energy harvesting technologies.[46, 155-157] In one embodiment, polymer solar cells (PSCs) are fabricated by blending a p-type (electron-donor) conjugated polymer with an n-type (electron-acceptor) small-molecule semiconductor to create a bulk-heterojunction (BHJ) photoactive layer.[157] For more than a decade, the search for new donor polymers and/or fine-tuning of promising backbones has dominated strategies for advancing the field,[155] whereas the superiority of fullerenes as acceptors seemed unassailable.[156] However, nonfullerene acceptors (NFAs) have recently enabled PSCs with power conversion efficiencies (PCEs)[21, 45, 158] as high as 16%[46] via mechanisms that are not entirely understood.[159-162] During the past 5 years, many hundreds of successful and unsuccessful NFAs have been reported.[45, 158, 111, 163-165] Among them, indacenodithienothiophene (IDTT)[45] and perylenediimide (PDI)[125, 166] acceptors frequently outperform fullerenes[156] and many other NFAs.[167] Compared to IDTTs, which are only accessible via complex, multistep syntheses[168, 169] and possess labile end-groups,[163] PDIs are readily synthesized robust alternatives (the cores are used in automotive paints) that exhibit efficient and stable electron transport in ambient,[170, 171] have unique photophysical and spintronic properties,[172, 173] and intense, high-energy visible range optical absorption. The latter is attractive because many polymers developed for fullerene-based PSCs have absorption complementary to that of PDIs. Despite these attractions, PDI-based PSCs are far less investigated than IDTT acceptors, with only a handful enabling PCEs $\geq$ 9%.[21, 125 , 25, 41, 174-177] While these empirical results demonstrate that synthetic modulation of PDIs can significantly enhance solar cell

performance, the fundamentals underlying PSC differences between PDIs are not well understood. While only one system has provided insight into PDI energetics and photophysics by probing exciton and charge dynamics via photoinduced electron transfer,[125] broader analysis of a BHJ blend nanostructure and its effects on these parameters is lacking. BHJ morphology remains a major challenge for PDI-based PSC development, especially considering the pronounced tendency of PDIs to aggregate and form large crystalline domains, which risks excessive BHJ phase segregation, reduced charge mobilities, and lower performance.[23, 177, 178] Although previous studies have addressed this issue using twisted geometry PDIs intended to suppress aggregation and optimize nanoscale BHJ morphology,[24, 41] such strategies risk impure BHJ domains that inhibit phase segregation and reduce carrier generation and mobility.[24, 25, 177] Therefore, it is imperative to explore alternative strategies for optimizing PDI-based BHJ active layer morphology. Fluorinating semiconducting polymers effectively lowers frontier molecular orbital (FMO) energies, enhances environmental stability, increases backbone planarity, promotes denser packing and hence crystallinity and mobility, and enhances self-assembly through intermolecular C–F···H, F···S, and F···πinteractions.[29, 179-181] While such donor polymer fluorination effects have proven promising in modifying BHJ fullerene- and IDTT-based PSC performance, the application to PDI PSCs has been barely explored with respect to BHJ film morphology, charge carrier dynamics, and device performance.[29]

Here we investigate fluorination effects on BHJ performance by comparing/contrasting the fluorine-poor donor polymer **PBDTT-FTTE** with the fluorine-rich analogue **PBDTTF-FTTE** (**Figure 4.1A**), paired for the first time with a twisted PDI acceptor, **Ph(PDI)$_3$** (**Figure 4.1A**).[41] The present systems are characterized experimentally by optical absorption

spectroscopy, cyclic voltammetry, ultraviolet photoelectron spectroscopy (UPS), photovoltaic response, space-charge-limited current (SCLC), AFM, TEM, GIWAXS, and fs/ns transient absorption (TA) spectroscopy and theoretically with ground-state and excited-state electronic structure to probe local differences arising from backbone fluorination. The data reveal that additional fluorination dramatically modifies BHJ morphology and semiconductor phase separation, leading to higher electron mobility (μ_e), longer free charge (FC) lifetimes, higher FC yields, and lower FC bimolecular recombination (BR) in **PBDTTF-FTTE**:**Ph(PDI)$_3$** blends, affording significantly enhanced PSC performance. Moreover, the computed dipole differences between the ground and excited state, p_{eg}, is known to be associated with lower exciton binding energies and hence greater FC lifetimes and yields.[181-184] Here our computed interpretation of polymer p_{eg} trends requires systems larger than dimers, and the dipolar orientation angle between the two moments provides a key measure of polarization forces acting against the Coulomb potential,[185] especially when polymer backbone conformations are nearly identical. We find that **PBDTTF-FTTE** has overall larger dipole moments due to the heavier fluorination and exhibits antiparallel directionality between the excited- and ground-state dipoles, an arrangement that should afford lower exciton binding energies and higher FC lifetimes due to less recombination, in agreement with experimental results.

4.2. Experimental Methods

4.2.1. Materials Synthesis.

The donor polymers **PBDTT-FTTE** and **PBDTTF-FTTE** were synthesized according to reported procedures.[186, 187] The acceptor material **Ph(PDI)$_3$** was prepared according to **Scheme 4.1.**

4.2.2. Ultraviolet Photoelectron Spectroscopy.

Ultraviolet photoelectron spectroscopy (UPS) measurements were conducted on a Thermo Scientific Escalab 250Xi ultra photoelectron spectrometer (NUANCE) with an analysis pressure of 2×10^{-8} mbar. Measurements were made with HeI photon source ($h\nu$ = 21.22 eV) with a pass energy of 2.0 eV. Clips were used to electrically connect the ITO and the instrument station, a sample bias of -5.0 V was therefore applied to accurately acquire the high binding energy cutoff (E_{cutoff}). Gold (Au) was used for calibration of the instrument under the same bias of -5.0 V, and a shift value of 4.5 eV was therefore obtained to calibrate the gold that has a Fermi edge at 0.0 eV.[188] This shift value was then applied to calibrate all the recorded UPS spectra from sample films.

4.2.3. Electrochemical Characterization.

The electrochemical properties of the materials were investigated as **thin films** in deoxygenated anhydrous acetonitrile under nitrogen at a scan rate of 100 mV s^{-1} using 0.1 M tetrakis(*n*-butyl)ammonium hexafluorophosphate [$(n\text{-Bu})_4N^+PF_6^-$] as the supporting electrolyte. Pt electrodes were used as both the working and counter electrodes, and with Ag/Ag^+ (sat. NaCl) as the pseudoreference electrode. **Ph(PDI)$_3$** films were drop-cast onto the Pt working electrode from a 5 mg mL^{-1} $CHCl_3$ solution. A ferrocene/ferrocenium (Fc/Fc^+) redox couple was used as internal standard and was assigned an absolute energy level of –4.88 eV vs vacuum.[189]

4.2.4. Thermal Analysis.

The TGA measurements were performed on a SDT Q600 instrument (TA Instruments). The samples (weight range 1.0-2.0 mg) were heated with a rate of 10 °C/min under N_2. The thermal decomposition temperature (T_d) was measured at 5% mass loss of the samples. DSC measurements

were performed on a DSC 250 instrument (TA Instruments, Materials Characterization and Imaging Facility, MatCI). The samples were placed in lidded Al zero pans (TA Instruments) and thermally cycled twice (heating-cooling-heating-cooling) under N_2 with a heating/cooling rate of 10 °C/min. All the data are reported using the second cycle and exotherm up.

4.2.5. Solar Cell Device Fabrication and Measurements.

Photovoltaic performance was studied using the "inverted" device structure: indium tin oxide (ITO)/zinc oxide (ZnO) (~22 nm)/active layer/molybdenum oxide (MoO_3) (10 nm)/Ag (100 nm). All the solar cells were tested in ambient at room temperature by a Keithley 2400 source-measure unit under simulated AM 1.5G irradiation (**100 mW cm^{-2}**) using Xe arc lamp of a Spectra-Nova 300W Class-A solar simulator (Spectra-Solaris Inc.). All the solar cells were put in custom designed contacting testing jig (Spectra-Solaris Inc.). The active area of all the solar cells was 6 mm^2 (3 mm × 2 mm). The solar cell testing and automation program used (Agilent VEE) was developed by Spectra-Solaris Inc. All the current density-voltage (*J*-*V*) plots were scanned in the reverse direction (from positive voltage to negative voltage). Light intensity dependence measurements were conducted on the same home solar cell testing setup, using a series of density filters (New Focus, diameter ~ 2.5 cm) and a home-designed black box holder. In the experiments, different density filters were applied to AM 1.5G light (100 mWcm^{-2}), and *J*-*V* curves were recorded. External quantum efficiency (EQE) spectra of solar cells were recorded in ambient at room temperature on a Newport QE-PV-SI setup. Incident light from Xe lamp (300 W) sequentially passing through motorized filter wheel, chopper wheel and monochromator (Newport Cornerstone 260) was focused on the active area of solar cells. The spot of output light was similar as the active area of sample cells. The incident light was perpendicular to (~90°) ITO/glass

substrate. The frequency of chopper wheel was set as 30 Hz. The current was obtained using a current pre-amplifier (Newport, 70710QE) and a lock-in amplifier (Newport, 70105 Dual channel Merlin).

4.2.6. Space-Charge-Limited Current (SCLC) Measurements.

Space-charge-limited current (SCLC) hole and electron mobilities were measured using ITO/MoO_3 (8 nm)/Organics/MoO_3 (8 nm)/Ag (100 nm) and ITO/ZnO (~22 nm)/Organics/LiF (1 nm)/Al(100 nm) single carrier diode structure, respectively. All the vertical diodes were measured in ambient at room temperature by a Signatone H100 series probe station (with assembled a Motic MLC-150C fiber optic illuminator and an Olympus SZ60 microscope) and an Agilent B1500A semiconductor device parameter analyzer. The tungsten probe tips (SE-20T, Signatone Corporation) were carefully cleaned by isopropanol or acetone before measurements, to insure we removed any contact resistance effects that could largely limit the current. In the hole-only diodes, ITO was the hole injection electrode, and MoO_3/Ag was the hole extraction electrode, while in the electron-only diodes, LiF/Al was the electron injection electrode, and ZnO/ITO was the electron extraction electrode. The applied voltage scan (Power SMU) was from 0 V to + 3.5 V (too high applied voltage leads to the breakdown of vertical diodes, and linear current-voltage characterstics with large current were observed if we scanned the broken diodes for the second time), with another probe connected to the instrument ground (GNDU, potential of 0 V). The current-voltage curves of single carrier diodes were therefore obtained.

4.2.7. Microscopy Measurements.

Standard tapping-mode AFM measurements in ambient were performed on a Scanned Probe Imaging and Development (SPID) Bruker ICON using a TESPA probe (NU Atomic and

Nanoscale Characterization Experimental Center, NUANCE). The AFM images were confirmed from different samples and scan areas. The root-mean-square roughness (R_q) values of height images were obtained from the whole scan area (3 μm × 3 μm) in the NanoScope Analysis 1.9 software. All the AFM images were flattened and exported from the software. TEM images were obtained on a Hitachi HT7700 microscope (Northwestern University Atomic and Nanoscale Characterization Experimental Center, Electron Probe Instrumentation Center, NUANCE EPIC) at an acceleration of 120 kV to gain sufficient transmission. TEM images were taken perpendicular to the plane of the films, and confirmed from different samples and areas, to make sure they are representative.

4.2.8. X-Ray Diffraction and Scattering.

GIWAXS measurements were performed using Beamline 8-ID-E at the Advanced Photon Source (APS) at Argonne National Laboratory.[190] The photon energy is 10.92 keV (λ = 1.13938 Å). Samples were examined under vacuum, with a Pilatus 1M detector (Dectris) having a pixel size of 172 μm × 172 μm used to collect the two-dimensional (2D) scattering images. Two images with a vertical offset were used to avoid gaps in the detector, which consists of 10 modules. The sample-detector distance is 204 mm and the beam size is 200 μm (h) × 20 μm (v). Flat field, solid angle, and detector efficiency corrections were applied to the images and the images were combined and converted to q-space with the GIXSGUI package for Matlab.[191] Further processing used local Origin software. Out-of-plane (OoP) grazing incidence 2θ X-ray diffraction (GIXRD) measurements were conducted on a Rigaku Smartlab (Jerome B. Cohen X-ray Diffraction Facility, NU) with monochromated CuKα radiation (λ = 1.541 Å). X-ray beam was aligned sequentially by performing θ/2θ, Z, Ry, Z scans, and the final Z scan value was set at 50% of maximal intensity.

The slit was then changed from PSA open to PSA 0.5 deg. Omega was set as 0.2, and 2θ was scanned from 3° to 30°. Step was set as 0.03°, and speed was set as 10°/min.

4.2.9. Transient Absorption Spectroscopy.

Transient absorption (TA) experiments for thin films were performed as described previously.[192] Briefly, ~ 40% of the output of a 1 kHz amplified Ti:sapphire system at 827 nm (1 W, 100 fs, Spitfire, Spectra Physics) is used to pump a laboratory-constructed optical parametric amplifier that is then tuned to the specific excitation wavelength. The pump is depolarized to minimize polarization-specific dynamics. The pump spot size was set to 1 mm diameter (1/*e*) and the pulse energy is attenuated to be <100 nJ/pulse to minimize singlet-singlet annihilation. The probe in the fsTA experiment is generated using 10% of the remaining output by driving continuum generation in a sapphire plate (430-850 nm) or a proprietary crystal from Ultrafast Systems (850-1600 nm). In the nsTA experiment, the probe is generated in a separately delayed broadband laser system (EOS, Ultrafast Systems, LLC). Pump and probe are spatially and temporally overlapped at the sample. The transmitted probe is detected on a commercial spectrometer (customized Helios-EOS, Ultrafast Systems, LLC).

4.2.10. Computational Details.

The ground state dipole moment ($\boldsymbol{p}_g$) was calculated using the optimized geometry for each oligomer (monomer, $N = 1$; dimer, $N = 2$; trimer, $N = 3$; tetramer, $N = 4$) using a B3LYP functional and 6-31G(d) basis set. The excited state dipole moment ($\boldsymbol{p}_e$) was calculated using the same optimized geometry linear-response TDDFT with a wB97X-D3 functional to get the CT nature of the exciton modeled with a range-tuned functional. The cc-pVDZ basis set was used. A cc-pVTZ basis was used on the smaller oligomers ($N = 1,2$), but the dipole moments did not change by more

than 10%. The Q-Chem electronic structure package was used for the DFT and TDDFT calculations.[193, 194] The electron-hole separation was calculated from the spatial distance between the center of the hole and electron positions from the decomposed TDDFT wavefunction.[195] The potential energy surface calculations were run using an optimized geometry search at each torsion angle. The angles were chosen in 10˚ steps over the full range -180˚ to 180˚ due to the asymmetry of the fluorination. The functional used was B3LYP and a 6-31G(d) basis set.

4.3. Results and Discussion

PBDTT-FTTE is a well-established PSC donor polymer, delivering good PCEs when paired with fullerenes (9.94%)[196, 197] or IDTTs (6.80%),[21] and is chosen here to investigate the effects of additional backbone fluorination as the highly fluorinated analogue **PBDTTF-FTTE** has only recently been reported.[186]Both **PBDTT-FTTE** and **PBDTTF-FTTE** were synthesized via green DARP protocols developed by this laboratory,[186, 198] with number-average molecular masses (M_n) and dispersities (Đ) estimated by high-temperature GPC as 25.5 kg/mol (Đ = 1.93) and 25.6 kg/mol (Đ = 2.45), respectively. **Ph(PDI)$_3$**[41] was synthesized by a new two-step halogen lamp photocyclization method, first illuminating compound **1** in CH_2Cl_2 with catalytic amount of I_2 and then evaporating the CH_2Cl_2, redissolving in toluene, and illuminating with additional I_2

(see the Materials Synthesis section and **Scheme 4.1** in the Supporting Information).

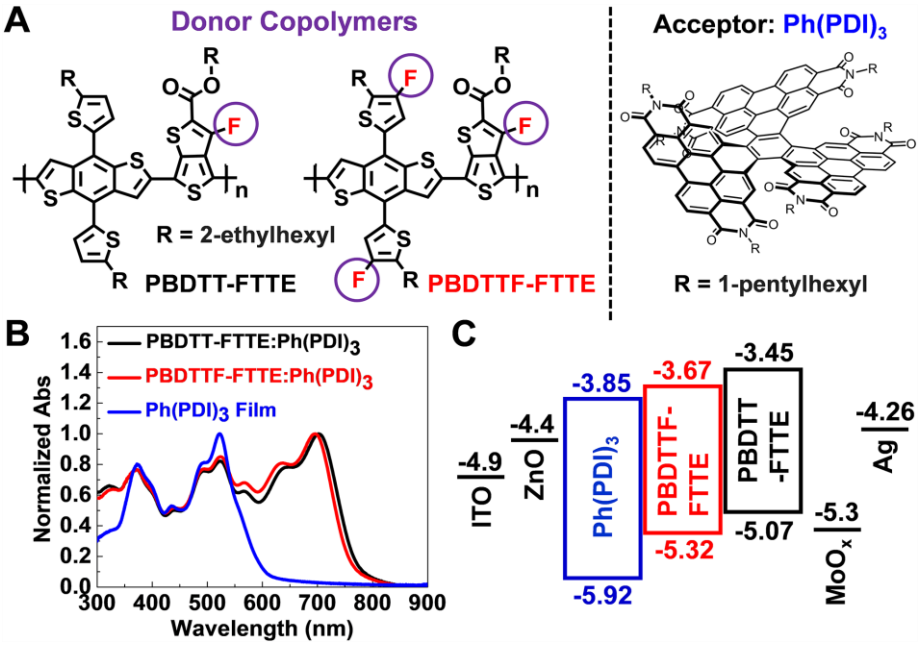

Figure 4.1. A. Chemical structures of **PBDTT-FTTE**, **PBDTTF-FTTE**, and **Ph(PDI)$_3$**; B. Optical absorption spectra of the indicated films (absorbance data were normalized to the maximal peak); C. Inverted PSC structure and orbital energetics.

The polymer:**Ph(PDI)$_3$** BHJ films exhibit broad optical absorption from 300 to 800 nm (**Figure 4.1B**), indicating potential for efficient solar light capture. HOMO energies were determined from UPS data (**Figures 4.6** and **4.7**), and LUMO energies were calculated as $E_{LUMO} = E_{HOMO} + E_g$. The optical bandgaps ($E_g$s) of **PBDTT-FTTE**, **PBDTTF-FTTE**, and **Ph(PDI)$_3$** films are 1.62, 1.65, and 2.07 eV, respectively (**Table 4.3**), with estimated HOMO/LUMO levels lying at −5.07/−3.45, −5.32/−3.67, −5.92/−3.85 eV, respectively (**Figure 4.1C**). The photovoltaic response of the present systems was assessed in ITO/ZnO/Al/MoO_3/Ag PSC architectures. From extensive fabrication/screening experiments, optimal BHJ films are achieved by blending **PBDTT-FTTE**or **PBDTTF-FTTE** with **Ph(PDI)$_3$** in a 1:1 mass ratio inadditive-free o-dichlorobenzene. Interestingly, the optimized **PBDTT-FTTE**:**Ph(PDI)$_3$** PSCs yield an average PCE of 5.50%, while in sharp contrast, the more heavily fluorinated **PBDTTF-FTTE**:**Ph(PDI)$_3$**

devices exhibit simultaneously enhanced V_{OC} (0.845 → 1.058 V), J_{SC} (13.85 → 14.66 mA cm^{-2}), and FF (47.04 → 56.36%), yielding a higher average PCE of 8.74% (**Table 4.1**). The champion **PBDTTF-FTTE**:**Ph(PDI)$_3$** blend PCE achieves 9.10% (**Figure 4.2B**), rivaling those of the most efficient PDI-based (9.15−10.6%)[21, 41, 125, 174] and **PBDTT-FTTE**:fullerene (8.40%) PSCs reported to date.[198, 199] Note that such a fluorination-related PCE increase is not observed in the corresponding polymer:ITIC-Th (8.02 vs 7.90%)[186] and polymer:$PC_{71}BM$ (8.21[186] vs 6.48%) BHJ blends. The larger V_{OC} of **PBDTTF-FTTE**:**Ph(PDI)$_3$** vs **PBDTT-FTTE**:**Ph(PDI)$_3$** is consistent with the FMO energetics (**Figure 4.1C**). Note that the energy loss (E_{loss}) calculated from $E_{loss} = E_g - eV_{OC}$[200, 201] is 0.59 eV for **PBDTTF-FTTE**:**Ph(PDI)$_3$**, which is significantly lower than 0.78 eV for the **PBDTT-FTTE**:**Ph(PDI)$_3$**-based devices. The former E_{loss} approaches that of c-Si and perovskite cells (0.40−0.55 eV)[201] and is among the lowest reported for PSCs.[21, 159, 201-206] The smaller E_{loss} minimizes the V_{OC}−J_{SC} trade-off in the **PBDTTF-FTTE**:**Ph(PDI)$_3$**-based devices, yielding both high J_{SC} and V_{OC} values. External quantum efficiency (EQE) spectra (**Figure 4.2A**) demonstrate strong response from 300 to 800 nm, which significantly increases in the **PBDTTF-FTTE**:**Ph-(PDI)$_3$** cells, in agreement with the J−V data.

Table 4.1. Donor:Ph(PDI)$_3$ BHJ Blend OPV and SCLC Device Metrics.

Blend[a]	V_{OC} (V)	J_{SC} (mA cm^{-2})	FF (%)	PCE (%)	EQE J_{SC} (mA cm^{-2})	E_{loss} (eV)	μ_h (cm^2 V^{-1} s^{-1})	μ_e (cm^2 V^{-1} s^{-1})	μ_h / μ_e
PBDTT-FTTE	0.845 ± 0.006 (0.853)	13.85 ± 0.45 (14.31)	47.04 ± 1.73 (48.59)	5.50 ± 0.24 (5.93)	13.61	0.78	30.9 ± 8.8 × 10^{-4}	2.2 ± 2.0 × 10^{-4}	14.29
PBDTTF-FTTE	1.058 ± 0.008 (1.058)	14.66 ± 0.45 (15.31)	56.36 ± 1.03 (56.18)	8.74 ± 0.19 (9.10)	14.06	0.59	13.9 ± 3.2 × 10^{-4}	9.8 ± 6.9 × 10^{-4}	1.42

[a] Averages with one standard deviation (1σ) are from ≥ 13 separate PSCs. Values in parentheses are from the champion cells.

Single-carrier diodes were next fabricated to evaluate charge transport in the vertical direction relative to the substrate.[207, 208] The **PBDTT-FTTE**:**Ph(PDI)$_3$** and **PBDTTF-FTTE**:**Ph(PDI)$_3$** blends exhibit SCLC hole mobilities (μ_hs) of $(30.9 \pm 8.8) \times 10^{-4}$ and $(13.9 \pm 3.2) \times 10^{-4}$ cm^2 V^{-1} s^{-1}, respectively (**Tables 4.1** and **4.6**), implying slightly more efficient hole transport in the fluorine-poor blend. In contrast, the corresponding electron mobilities (μ_es) favor the fluorine-rich blend, $(2.2 \pm 2.0) \times 10^{-4}$ and $(9.8 \pm 6.9) \times 10^{-4}$ cm^2 V^{-1} s^{-1}, respectively. Thus, the hole to electron transport ratio, μ_h/μ_e, increases by 10-fold (14.29 → 1.42) in the **PBDTTF-FTTE**:**Ph(PDI)$_3$** blend. The enhanced μ_e and therefore more balanced charge transport in the **PBDTTF-FTTE**:**Ph(PDI)$_3$** blend are consistent with the superior FC extraction (*vide infra*) and higher J_{SC}, FF, and PCE. BHJ film morphology was investigated by AFM, TEM, and GIWAXS. Tapping mode AFM images (**4.3A, 4.3B** and **4.12**)reveal smooth surfaces with the RMS roughness (R_q) of the **PBDTT-FTTE**:**Ph(PDI)$_3$** blend (0.71 nm) being slightly smaller than that of the **PBDTTF-FTTE**:**Ph(PDI)$_3$** blend (1.05 nm).

Similar continuous networks are visible in the phase images of both blends. Bulk morphology was further probed by TEM (**Figures 4.3A**, **4.3B**, and **4.14**), where the greater **Ph(PDI)$_3$** electron density vs the polymers enhances the contrast, with the darker regions corresponding to **Ph(PDI)$_3$**-rich domains.[209-211] Both blends exhibit similar **Ph(PDI)$_3$** domain sizes of ~3.5 nm, smaller than those observed with fullerene (~10 nm)[198] and other PDI (~5−100

nm) acceptors,[23] consistent with the 3D **Ph(PDI)$_3$** geometry suppressing aggregation.

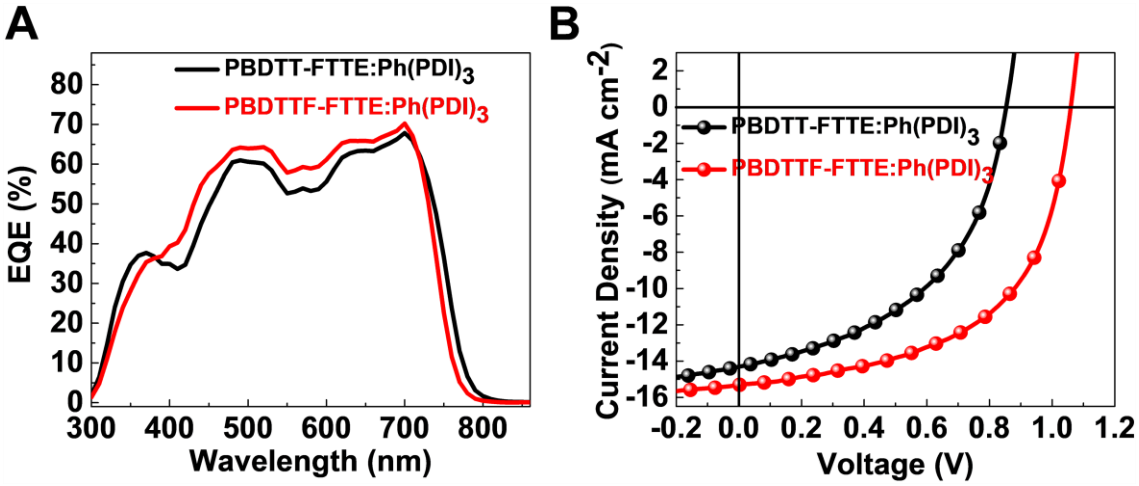

Figure 4.2. A. EQE spectra and **B**. *J*–*V* responses of the champion cells.

Importantly, the **PBDTTF-FTTE**:**Ph(PDI)$_3$** blends clearly show better separated polymer/acceptor domains, while the **PBDTT-FTTE**:**Ph(PDI)$_3$** blend reduced contrast indicates a more homogeneous/mixed morphology.[210] Thus, fluorine-rich **PBDTTF-FTTE** more effectively templates the BHJ morphology, affording higher-purity donor and acceptor domains. In such blends, geminate recombination can, in principle, be reduced (see more below), and the primary separated electrons and holes are expected to overcome Coulombic attraction and generate FCs more efficiently.[212] The differing TEM contrasts are also consistent with higher **PBDTTF-FTTE**:**Ph(PDI)$_3$** electron mobility, as noted above (**Table 4.1**). GIWAXS measurements were next used to assess the relevant film ordering characteristics. The 2D scattering patterns are shown in **Figure 4.3C** and **4.3D**, with vertical and horizontal linecuts, relevant d-spacings, and correlation lengths (CLs) provided in **Figure 4.14** and **Table 4.7.** Neat **PBDTT-FTTE** and **PBDTTF-FTTE** exhibit in-plane (IP) lamellar (100) peaks with d_{100} = 25.8 and 26.3 Å, as well as out-of-plane (OoP) π–π stacking (010) peaks with d_{010} = 3.86 and

3.82 Å, respectively, suggesting preferential "π-face-on" polymer orientation relative to the substrate.[177, 186] The corresponding CLs of OoP (010) peaks are 1.78 and 1.83 nm, respectively. Neat **Ph(PDI)$_3$** films exhibit peaks at around 0.28 and 0.4 $Å^{-1}$in both IP and OoP directions.[41]

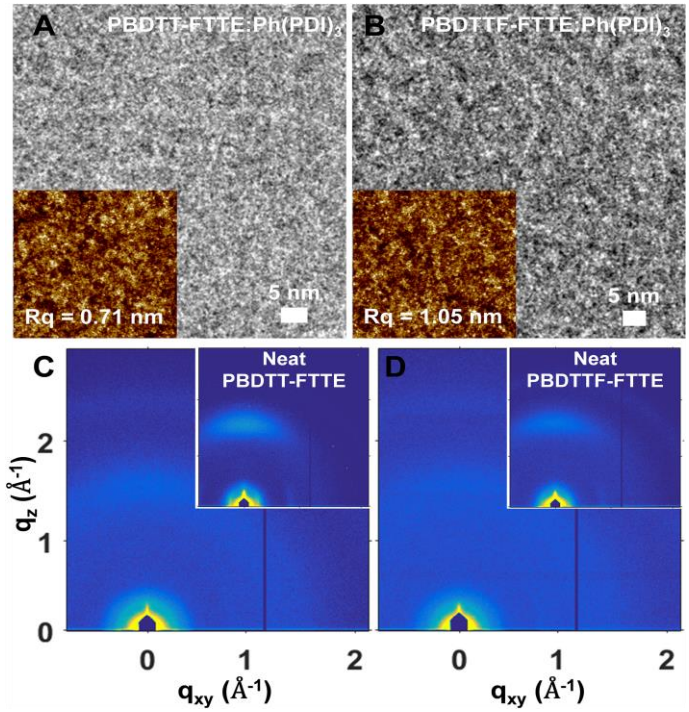

Figure 4.3. TEM and inset AFM images of **A**. **PBDTT-FTTE:Ph(PDI)$_3$** and **B**. **PBDTTF-FTTE:Ph(PDI)$_3$** blends; 2D GIWAXS patterns of **C**. **PBDTT-FTTE:Ph(PDI)$_3$** and **D**. **PBDTTF-FTTE:Ph(PDI)$_3$** blends with inset images of pristine polymer.

In sharp contrast, the two BHJ blends exhibit much weaker scattering with comparable intensities, suggesting comparable and lower degrees of ordering. Overall, the GIWAXS results indicate that the neat and BHJ blend films are largely amorphous, with no obvious correlation between crystallographic parameters, mobilities, and PSC performance metrics.

Charge photogeneration and recombination are central limits to PSC efficiency and remain unresolved in most NFA-based PSCs,[28, 32, 213] especially in PDIs.[28, 34, 160] Femtosecond transient absorption (fsTA) and nanosecond transient absorption (nsTA) spectroscopies *in*

vacuo along with light intensity dependence experiments were employed here to probe differences in charge photogeneration yields and recombination mechanisms for the first time in PDI-based PSCs.[34] Charge separation was monitored by TA of the **Ph(PDI)$_3$** bleach at 525 nm following BHJ blend excitation at 700 nm (**Figure 4.4A and 4.4B**). Because **Ph(PDI)$_3$** does not absorb at 700 nm, charge generation upon photoexcitation at this wavelength must occur purely by electron transfer (polymer → **Ph(PDI)$_3$**), with negligible probability of Förster resonant energy transfer. Full blend data sets were globally fit at selected wavelengths to two successive first-order decays and a long-lived bimolecular process attributed to FC recombination (see the Supplementary Information). Multiple decay components are common in PSC systems because disordered morphologies can have several populations.[32] Ultrafast electron transfer is observed in each blend, with the fastest component having a time constant < 500 fs, far faster than previously reported (3 ps).[34] Additionally, both the **PBDTT-FTTE**:**Ph(PDI)$_3$** and **PBDTTF-FTTE**:**Ph(PDI)$_3$** blends behave similarly at early times, indicated in the full fsTA data sets (**Figure 4.16-4.22**). This may reflect competition between the higher driving force (ΔE_{LUMO}, see **Table 4.4**) for charge separation in **PBDTT-FTTE**:**Ph(PDI)$_3$** vs the more optimal BHJ morphology in **PBDTTF-FTTE**:**Ph(PDI)$_3$**. By 6.6 ns, both blends produce similar amounts of FCs, as evidenced by the comparable 525 nm **Ph(PDI)$_3$** bleach magnitudes (**Figure 4.4C**). The bleach features in both blends maximize near 20 ps, and by comparing this value to that at the experimental end, the overall FC yield in both blends is determined to be ca. 20% by 6 ns.

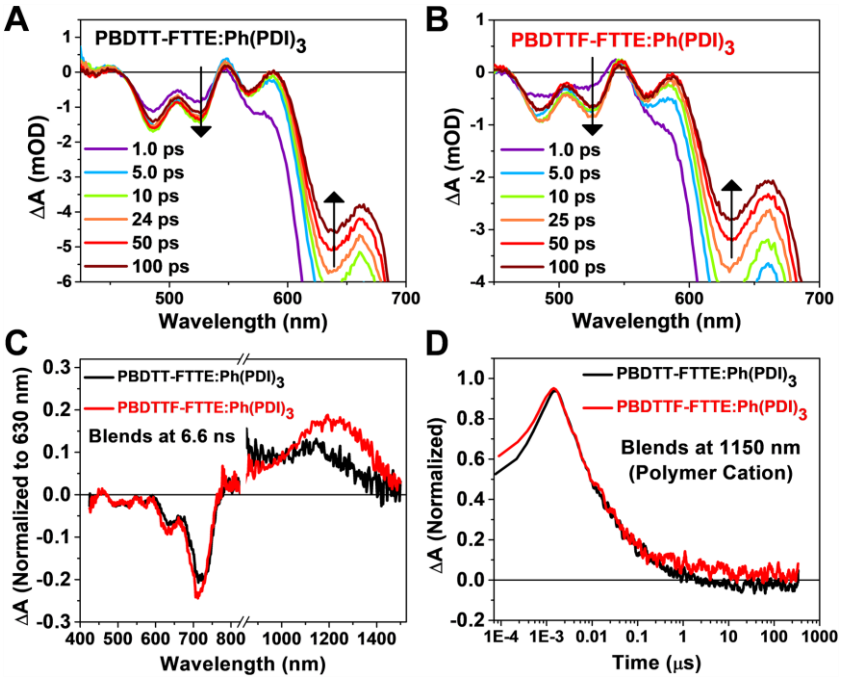

Figure 4.4. Time-resolved spectra of **A**. **PBDTT-FTTE:Ph(PDI)$_3$** and **B**. **PBDTTF-FTTE:Ph(PDI)$_3$** BHJ blends with λ_{ex} = 700 nm showing ultrafast electron transfer. **C**. Transient absorption spectra at 6.6 ns for blends excited at 700 nm in fsTA experiments, normalized to polymer bleach at 630 nm immediately after excitation. **D**. FC decay dynamics monitored at the polymer cation absorption (λ = 1150 nm) with λ_{ex} = 520 nm in nsTA experiments.

FC decay was next monitored at the polymer cation absorption (λ = 1150 nm)[28] following excitation at 520 nm and probing in the ns regime (**Figures 4.23** and **4.24**). The FC lifetime is somewhat longer in **PBDTTF-FTTE**:**Ph(PDI)$_3$** (**Figure 4.4D**) and hence at long times (>1 μs) generates a higher yield of FCs than does **PBDTT-FTTE**:**Ph(PDI)$_3$**, indicating that the charge carriers more easily diffuse and avoid BR. This observation is consistent with the higher μ_e and more balanced mobilities in that blend (vide supra), although note that the TA measurements are done in the absence of an external electrical bias. The small difference in the observed BR rate correlates with the TEM images showing clearer phase separation and the higher PCE for **PBDTTF-FTTE**:**Ph(PDI)$_3$**. It is likely that the optimal morphology and balanced charge transport in **PBDTTF-FTTE**:**Ph(PDI)$_3$** account for the increased FCs at long

times and the reduced recombination rates in the TA experiments. FC recombination was further evaluated by light intensity (I) dependence measurements (**Figure 4.10**). All the plots of J_{SC} vs I follow a function $J_{SC} \approx I^{\alpha}$, where α is related to BR loss.[214] Plots of the **PBDTT-FTTE**:**Ph(PDI)$_3$** and **PBDTTF-FTTE**:**Ph(PDI)$_3$** blends yield α values of 0.862 and 0.959, respectively. The α value of the **PBDTTF-FTTE**:**Ph(PDI)$_3$** blend is similar to those of other high-PCE PDI blends.[43, 174] In the same experiment, V_{OC} vs ln(I) plots are linear, and the ideality factor n is calculated fromthe slope nk_BT/q, where k_B is the Boltzmann constant, T temperature, and q the elementary charge.[214] The n deviation from 2 to 1 reflects lower importance of Shockley−Read−Hall recombination vs BR. The **PBDTT-FTTE**:**Ph(PDI)$_3$** and **PBDTTF-FTTE**:**Ph(PDI)$_3$** blends yield slopes of 1.24k_BT/q and 1.43k_BT/q, respectively. Thus, there is significantly less BR loss in the **PBDTTF-FTTE**:**Ph(PDI)$_3$** devices, consistent with the TA results.

Table 4.2. Computed **PBDTT-FTTE** and **PBDTTF-FTTE** Oligomer Dipolar Parameters.

	PBDTT-FTTE				**PBDTTF-FTTE**			
N	**1**	**2**	**3**	**4**	**1**	**2**	**3**	**4**
p_g [a]	2.51	4.51	4.88	6.30	3.05	4.37	6.81	8.65
p_e [b]	5.28	3.35	3.94	5.17	4.55	3.21	5.60	7.59
Δp_{ge}	2.81	1.16	5.37	8.00	1.51	1.26	11.31	14.88

θ_{eg} (°)	7.64	0.70	74.13	87.92	1.29	7.45	131.11	132.78
p_{tr}	3.23	5.67	7.03	8.02	3.25	5.49	7.07	8.07
f **(a.u)**	0.88	2.28	3.25	4.09	0.89	2.13	3.28	4.16

[a]Ground-state dipole calculations with DFT using B3LYP and a 6-31(d) basis set.
[b] The excited-state dipole calculations with B97X-D3 and cc-pVDZ basis set.

To better understand the experimental PSC metrics, photogeneration/recombination dynamics, and charge trans- port of **PBDTT-FTTE**:**Ph(PDI)$_3$** versus **PBDTTF-FTTE**:**Ph-(PDI)$_3$**, ground-state and excited-state electronic structure computation was used to probe the local effects of backbone fluorination. The internal polarization arising from changes in excited- and ground-state dipole moments was computed because the degree of intramolecular charge transfer (ICT) and, hence, the exciton binding energy are related to the difference between the ground- (p_g) and excited-state (p_e) dipole moments (Δp_{ge}).[182, 183, 215]

The expectation is that the larger Δp_{ge} correlates with local charge separation and therefore leads to a greater likelihood of charge generation. While previous studies focused on monomers or dimers,[183, 216] here the dipole moments for an oligomer series, monomer−tetramer, $N = 1-4$, were computed because larger oligomers (trimers/tetramers) were found necessary for meaningful dipole comparisons. Additionally, determining differences in dipole orientation between p_g and p_e was found critical in elucidating Δp_{ge} trends. Trends for the **PBDTT-FTTE** and **PBDTTF-FTTE** $N = 1-4$ oligomers are compiled in **Table 4.2** (see geometries for each in **Figure 4.24-4.28**). Note the abrupt rise in Δp_{ge} and change in dipole orientation difference between ground and excited states (θ_{eg}) for $N > 2$.

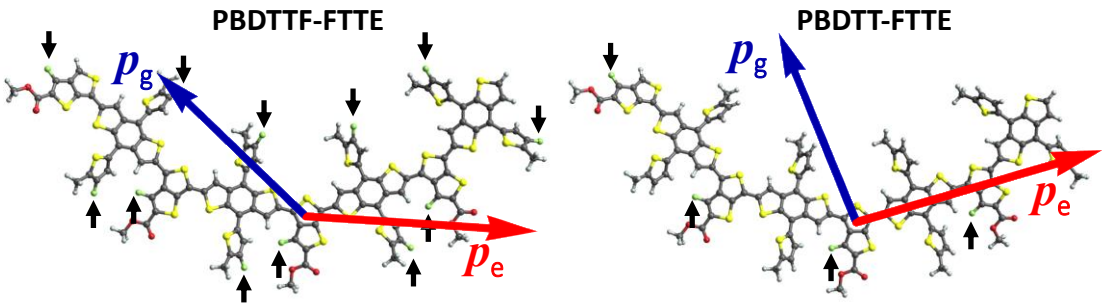

Figure 4.5. Dipole moment computation. Optimized **PBDTTF-FTTE** tetramer geometry with ground (blue) and excited-state dipole (red) vectors overlayed (left). Optimized **PBDTT-FTTE** tetramer geometry with ground (blue) and excited-state dipole (red) vectors overlayed (right).

We attribute this change in dipole orientation to the backbone curvature of the cis inward-oriented FTTE units (**Figure 4.4**). Interestingly, the **PBDTTF-FTTE** trimer and tetramer show antiparallel ground- and excited-state dipole orientations, ideal for exciton scission. As with previous dipole calculations that compare the performance of fluorinated and nonfluorinated acceptors and polymers,[182, 183, 215, 216] the magnitude of Δp_{ge} is also greater for **PBDTTF-FTTE** compared to that of **PBDTT-FTTE** due to the overall larger dipole moments of both p_g and p_e (see **Table 4.2.** for comparison). Yet, even if only the magnitude of Δp_{ge} mattered for the efficacy of exciton separation in a given polymer (which for the 1D excitontransport polarization direction certainly does matter), in order for **PBDTT-FTTE** to have the same Δp_{ge} as **PBDTTF-FTTE**, it would require a ~2.5× larger p_g or p_e. The fluorination of the thiophene side-chains in this study changes the dipole magnitudes of p_g or p_e by at most only 1.5×. The cis configuration is the minimum-energy configuration for both polymers (**Figures 4.33-4.36**), with the **PBDTTF-FTTE** oligomer demonstrating slightly greater stability. Pronounced curvature in polymer backbones is known to depress hole mobility due to suboptimal film morphologies and increased disorder.[217, 218] This may explain the modest **PBDTTF-FTTE**:**Ph(PDI)$_3$** μ_h = 13.9 × 10^{-4} cm^2 V^{-1} s^{-1} versus **PBDTT-FTTE**:**Ph(PDI)$_3$** μ_h = 30.9 × 10^{-4} cm^2 V^{-1} s^{-1}. In contrast,

modest curvatures afford more favorable domain dimensions and hence smaller BR values.[218] In a solid film environment, there will certainly be a distribution of torsion angles with some conformations of torsions in the trans orientation, i.e., the FTTE group alternating up and down. This will lead to a dispersion in dipole moments,[219] but when including interchain exciton diffusion, there will be pathways to avoid trans domains.[220, 221] We next investigated exciton delocalization for each oligomer to probe the degree of electron−hole charge separation within the exciton. The electron−hole (R_{eh}) separation distance is ∼20% greater for $N > 2$ **PBDTTF-FTTE** (see the Supplementary Information for details). Together with the greater dipole difference between the ground state (higher Δp_{ge} and θ_{eg} in **Table 4.2**) in **PBDTTF-FTTE** affording reduced geminate recombination, this analysis provides a plausible explanation for the higher FC yield and greater μ_e in the **PBDTTF-FTTE**:**Ph(PDI)$_3$** films.

4.4 Conclusions

In summary, two polymer donors, fluorine-poor **PBDTT-FTTE** and fluorine-rich **PBDTTF-FTTE**, are blended with theacceptor **Ph(PDI)$_3$** to investigate donor backbone fluorination effects in PDI-based BHJ PSCs. An unexpected, remarkable PCE increase from 5.93% for **PBDTT-FTTE**:**Ph(PDI)$_3$** to 9.10% for **PBDTTF-FTTE**:**Ph(PDI)$_3$** is achieved, while such a PCE increase is not observed in the analogous pairs, **PBDTT-FTTE**:ITIC-Th vs **PBDTTF-FTTE**:ITIC-Th (8.02 vs 7.90%, respectively)[186] and **PBDTT-FTTE**:$PC_{71}BM$[186, 198] vs **PBDTTF-FTTE**:$PC_{71}BM$ (8.21 vs 6.48%, respectively). Detailed film morphological, carrier photogeneration, recombination, and transport analysis reveals that the latter material has more suitable semiconductor phase separation, larger μ_e, longer-lived and higher yields of FC carriers, and slower bimolecular recombination than **PBDTT-FTTE**:**Ph(PDI)$_3$**. Moreover, the lower-

lying **PBDTTF-FTTE** HOMO affords a larger V_{OC} and a significantly lower E_{loss} of 0.59 eV, among the lowest recorded for PSCs. Ground- and excited-state dipole orientation computation shows that fluorination alters the dipole orientation and reduces exciton binding energies. The **PBDTTF-FTTE** oligomers support nearly antiparallel ground-and excited-state dipole moments, explaining the increased FC lifetimes and yields. Thus, pairing PDIs with highly fluorinated donor polymers is promising for enhancing PDI-based PSC performance.

4.5. Supplementary Information

4.5.1. Synthesis

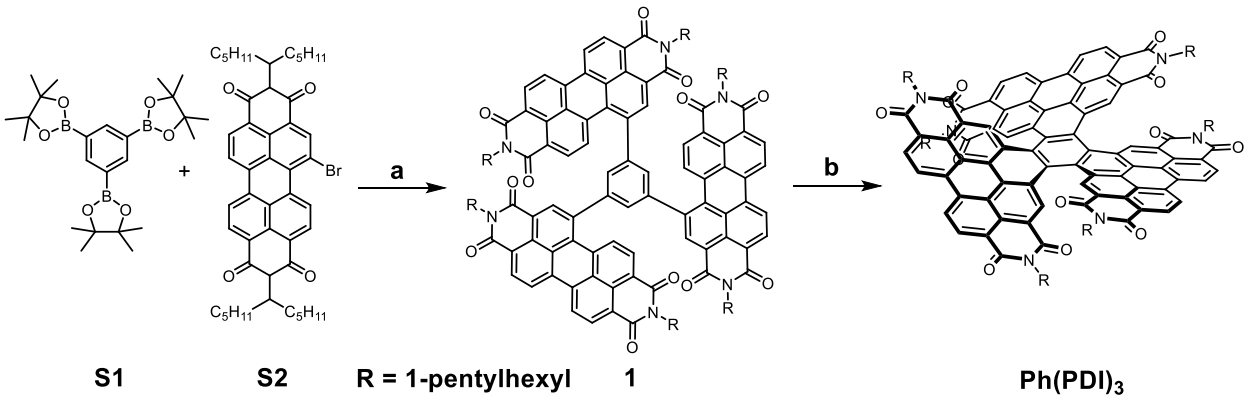

Scheme 4.1. Synthesis of molecules **1** and **Ph(PDI)**$_3$. (a) $Pd(PPh_3)_4$, 2M Na_2CO_3, THF; (b) (1) I_2, CH_2Cl_2, *hv*, O_2 (2) I_2, Toluene, *hv*, O_2.

1: Compound **1** was synthesized following a literature procedure. Spectral data were consistent with previously reported data.[3]

Ph(PDI)$_3$: Compound **1** (200 mg, 0.092 mmol) was dissolved in CH_2Cl_2 (200 mL) along with I_2 (5 mg, 0.018 mmol). The deep red solution was bubbled with air and irradiated with a 500 W halogen lamp for 6 h, periodically refilling with CH_2Cl_2. Then, the remaining CH_2Cl_2 was evaporated and the crude was re-dissolved in toluene (200 mL) with an additional 5 mg I_2 and irradiated while bubbling with air for an additional 24 h to result in an orange-red solution. The

solvent was evaporated under reduced pressure and the crude material was purified by silica gel column chromatography (CH_2Cl_2), followed by further silica gel column chromatography (acetone:toluene 3.5:96.5) to give **Ph(PDI)$_3$** as a bright red solid (88 mg, 44%). Spectral data were consistent with previously reported data.[3]

4.5.2. UPS Spectroscopy.

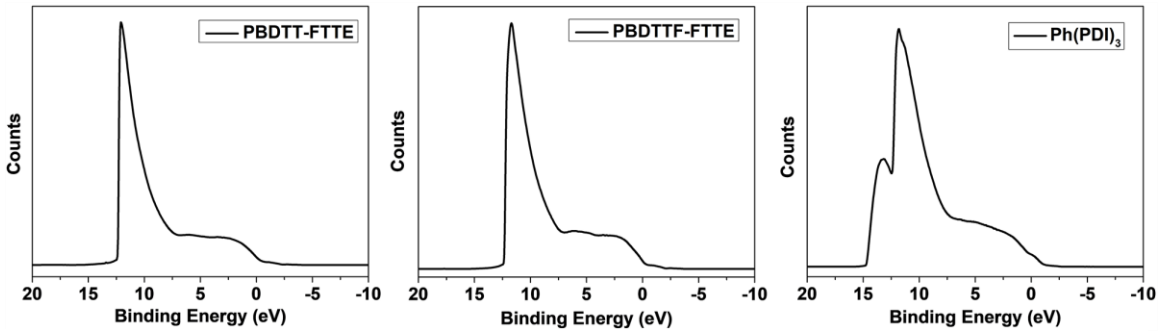

Figure 4.6. Raw UPS spectra recorded from neat **PBDTT-FTTE**, **PBDTTF-FTTE**, and **Ph(PDI)$_3$** films.

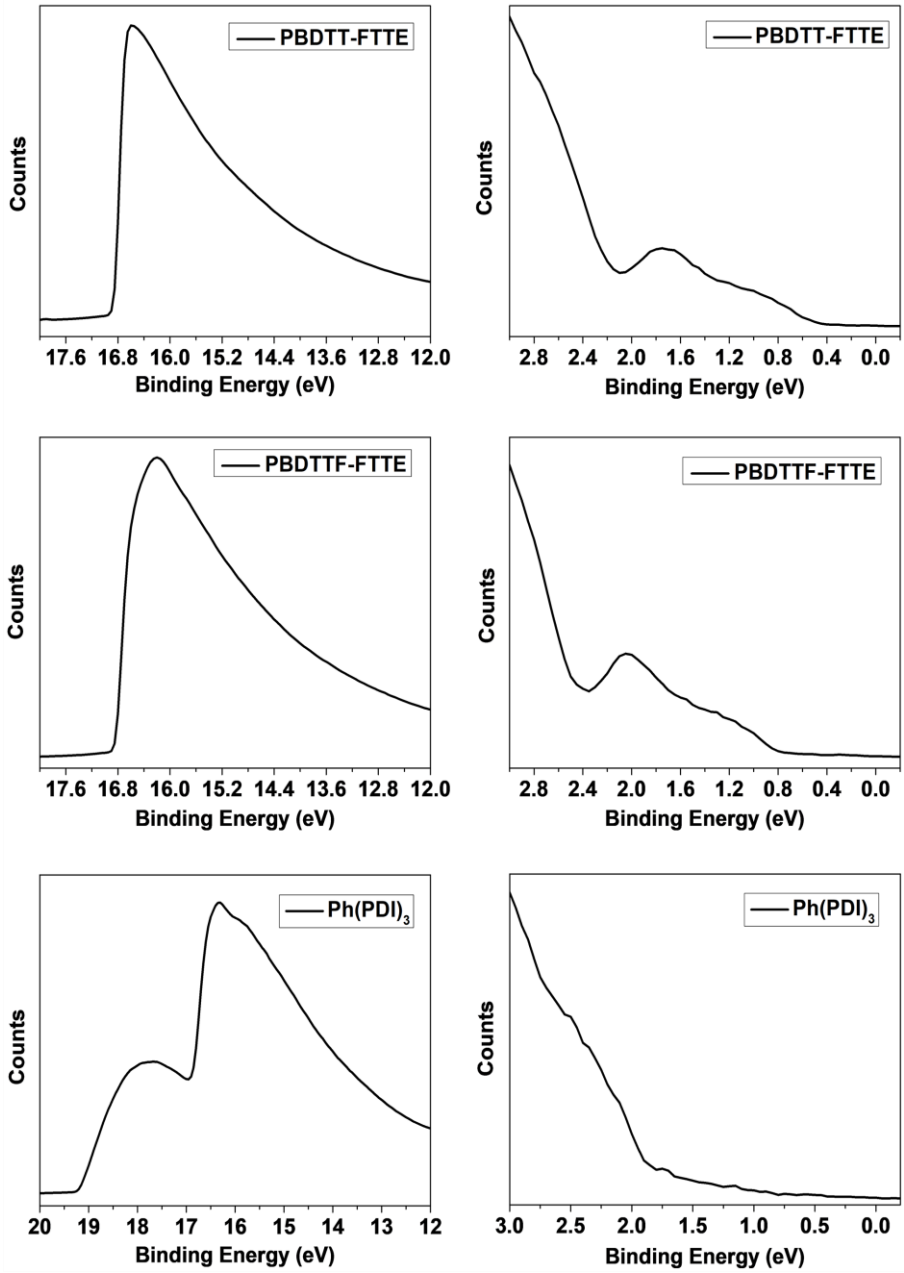

Figure 4.7. The shifted UPS spectra of neat **PBDTT-FTTE**, **PBDTTF-FTTE**, and **Ph(PDI)$_3$** films. The high binding energy cutoff (E_{cutoff}) and the onset of the peak with a lowest binding energy (E_{onset}) were extracted for the IP estimation.

4.5.3. Optical and Electrochemical Characterization.

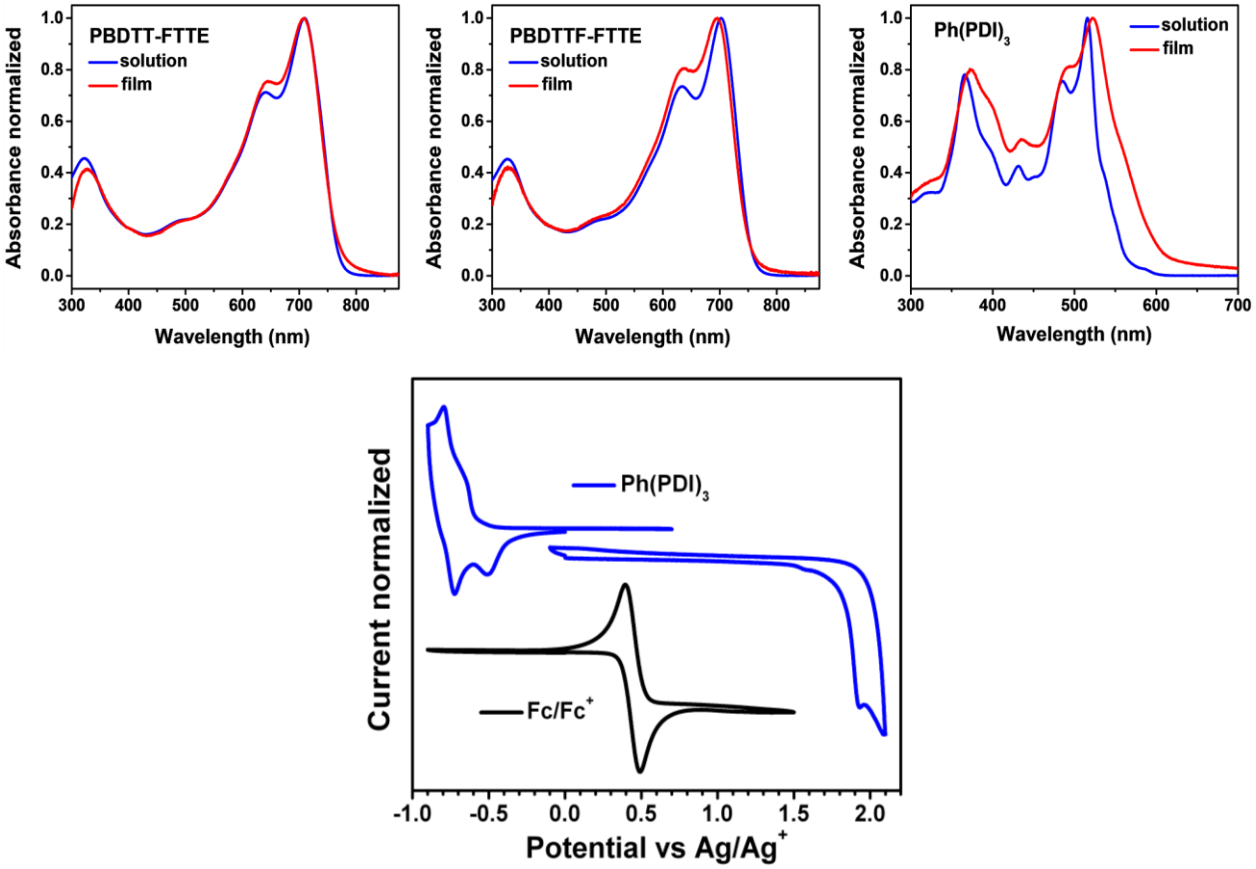

Figure 4.8. UV-vis absorption spectra of the donor and acceptor materials (top) and cyclic voltammograms of a **Ph(PDI)$_3$** film (bottom).

Table 4.3. Physicochemical Properties of **PBDTT-FTTE**, **PBDTTF-FTTE**, and **Ph(PDI)$_3$**.

Material	E_{HOMO}^{UPS} (eV)	E_g† (eV)	E_{LUMO}‡ (eV)	E_{LUMO}^{CV} (eV)	E_{HOMO}^{CV} (eV)	E_{HOMO}§ (eV)
PBDTT-FTTE	-5.07	1.62	-3.45	/	/	/
PBDTTF-FTTE	-5.32	1.65	-3.67	/	/	/
Ph(PDI)$_3$	-5.92	2.07	-3.85	-3.85	-6.27	-5.92

† Optical bandgap E_g was determined by the absorption edge of thin film;

‡ Calculated from $E_{LUMO} = E_{HOMO}^{UPS} + E_g$, E_{HOMO}^{UPS} is the HOMO estimated from UPS;

§ Calculated from $E_{HOMO} = E_{LUMO}^{CV} + E_g$, E_{LUMO}^{CV} is the LUMO estimated from CV.

4.5.4. Thermal Analysis.

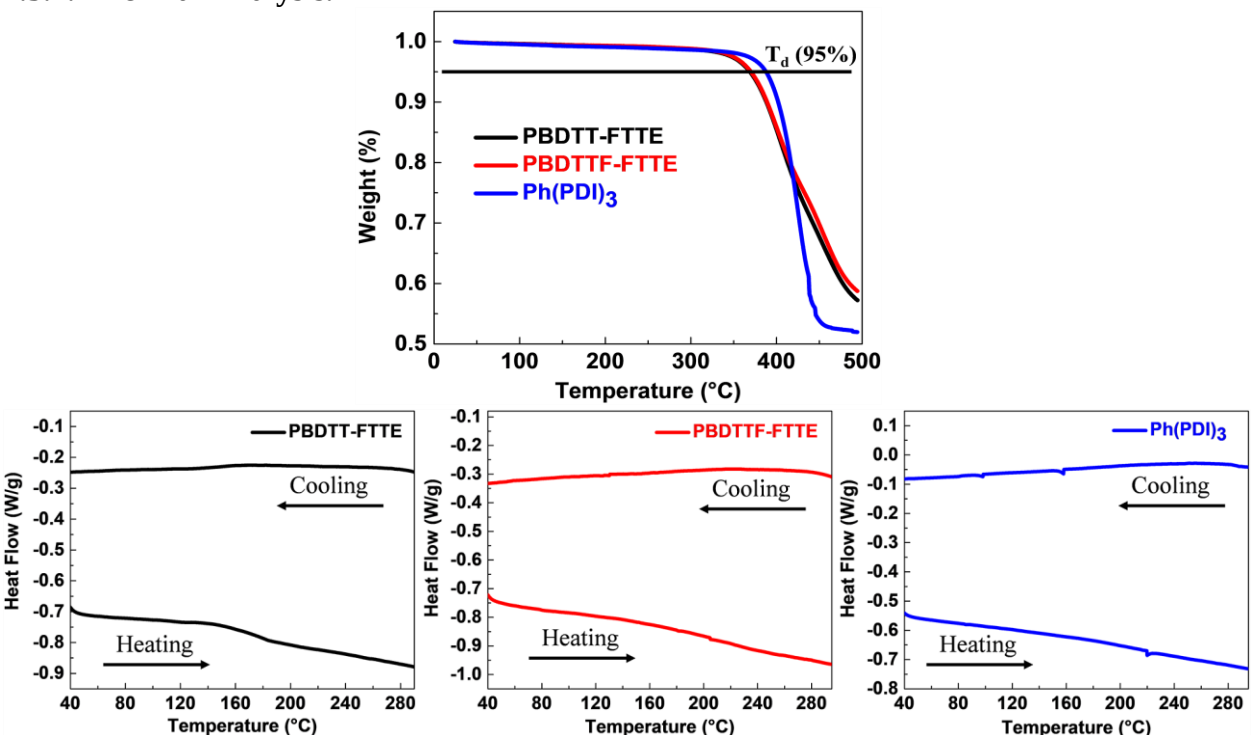

Figure 4.9. TGA heating traces of **PBDTT-FTTE**, **PBDTTF-FTTE**, and **Ph(PDI)$_3$** (top) and DSC heating and cooling traces of **PBDTT-FTTE**, **PBDTTF-FTTE**, and **Ph(PDI)$_3$** (bottom).

4.5.5. Solar Cell Device Characterization.

Table 4.4. Fully Optimized Photovoltaic Performance of **polymer:Ph(PDI)$_3$** Blends.

BHJ Blend	Experimental details	V_{OC} (V)	J_{SC} (mA cm^{-2})	FF (%)	PCE (%)	Number of devices	EQE J_{SC} (mA cm^{-2})
PBDTT-FTTE:Ph(PDI)$_3$	1:1, *o*-DCB, 11mg/mL	0.845 ± 0.006 (0.853)	13.85 ± 0.45 (14.31)	47.04 ± 1.73 (48.59)	5.50 ± 0.24 (5.93)	13	13.61
PBDTTF-FTTE:Ph(PDI)$_3$	1:1, *o*-DCB, 11mg/mL	1.058 ± 0.008 (1.058)	14.66 ± 0.45 (15.31)	56.36 ± 1.03 (56.18)	8.74 ± 0.19 (9.10)	13	14.06

The photovoltaic data are reported as averages taken over 13 separate devices ± one standard deviation (1σ), and the numbers in parenthesis are from the champion cells. The mismatch between average J_{SC} and corresponding EQE is **within or near 4%**.

Table 4.5. Energy Loss of BHJ **Polymer:Ph(PDI)$_3$** Blend Films.

BHJ Blend	V_{OC} (V)	E_g of polymer film (eV)	$E_{loss} = E_g - eV_{OC}$ (eV)
PBDTT-FTTE:Ph(PDI)$_3$	0.845 ± 0.006 (0.8529)	1.62	1.62 - 0.845 = 0.78 (0.77)
PBDTTF-FTTE:Ph(PDI)$_3$	1.058 ± 0.008 (1.0804)	1.65	1.65-1.058 = 0.59 (0.57)

The V_{OC}s are reported as averages taken over 13 separate devices ± one standard deviation (1σ), and the numbers in parenthesis are maximal V_{OC}s and the corresponding minimal E_{loss}s.

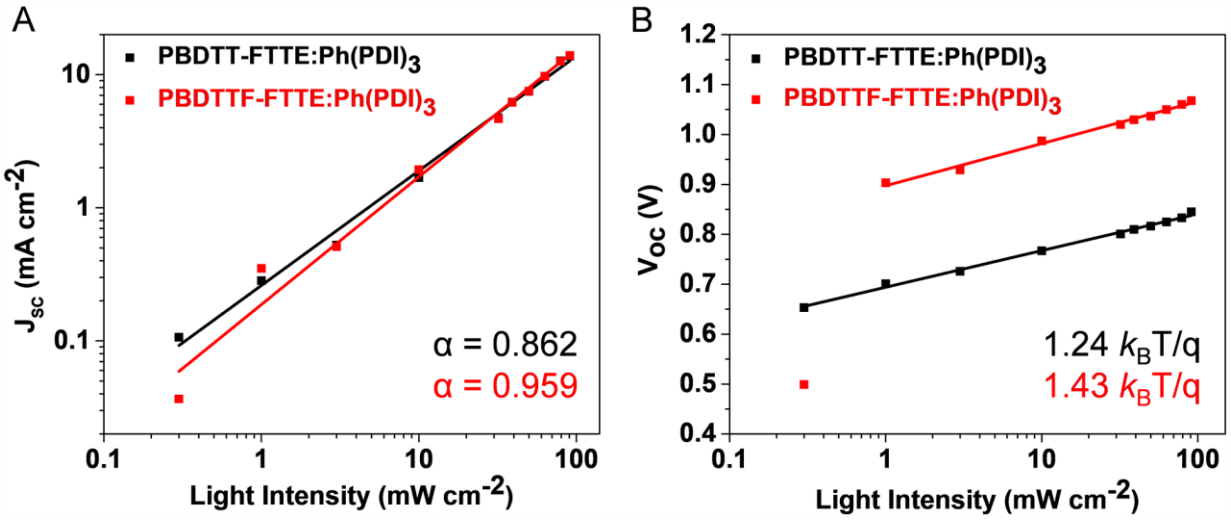

Figure 4.10. (a) J_{SC} versus light intensity (I_{light}) and (b) V_{OC} versus I_{light} measurements of the polymer:**Ph(PDI)$_3$** solar cell devices. Note that nk_BT/q values were extracted from the corresponding V_{OC} ~ ln(I_{light}) plots. The detailed fitting parameters from the above curves are as follows: (a) α = 0.862 for the **PBDTT-FTTE:Ph(PDI)$_3$** blend; α = 0.959 for the **PBDTTF-FTTE:Ph(PDI)$_3$** blend; (b) n = 1.24 for the **PBDTT-FTTE:Ph(PDI)$_3$** blend; n = 1.43 for the **PBDTTF-FTTE:Ph(PDI)$_3$** blend; At lower light intensities (I_{light} < 1 mW cm^{-2}), the **PBDTTF-FTTE:Ph(PDI)$_3$**-based devices exhibit a much stronger V_{OC} dependence on I_{light}.

4.5.6. Space Charge-Limited Current (SCLC) Measurements.

Table 4.6. SCLC Zero-Field mobilities of Blend and Neat Films.

Films	Experimental details	μ_h (10^{-4} cm^2/Vs)	Number of devices for μ_h	μ_e (10^{-4} cm^2/Vs)	Number of devices for μ_e	μ_h / μ_e
Blend PBDTT-FTTE:$Ph(PDI)_3$	1:1, *o*-DCB, 11mg/mL	30.86 ± 8.80	19	2.16 ± 2.03	7	14.29
Blend PBDTTF-FTTE:$Ph(PDI)_3$	1:1, *o*-DCB, 11mg/mL	13.91 ± 3.18	15	9.81 ± 6.89	8	1.42
Neat PBDTT-FTTE	*o*-DCB, 11mg/mL	9.31 ± 2.17	7	/	/	/
Neat PBDTTF-FTTE	*o*-DCB, 11mg/mL	3.68 ± 3.17	5	/	/	/
Neat $Ph(PDI)_3$	*o*-DCB, 22mg/mL	/	/	3.64 ± 1.41	5	/

The SCLC zero-field mobilities of the holes (electrons) μ_h (μ_e)s are reported as averages taken over 5 or more separate devices ± one standard deviation (1σ). The μ_h / μ_e values were calculated from the average mobilities.

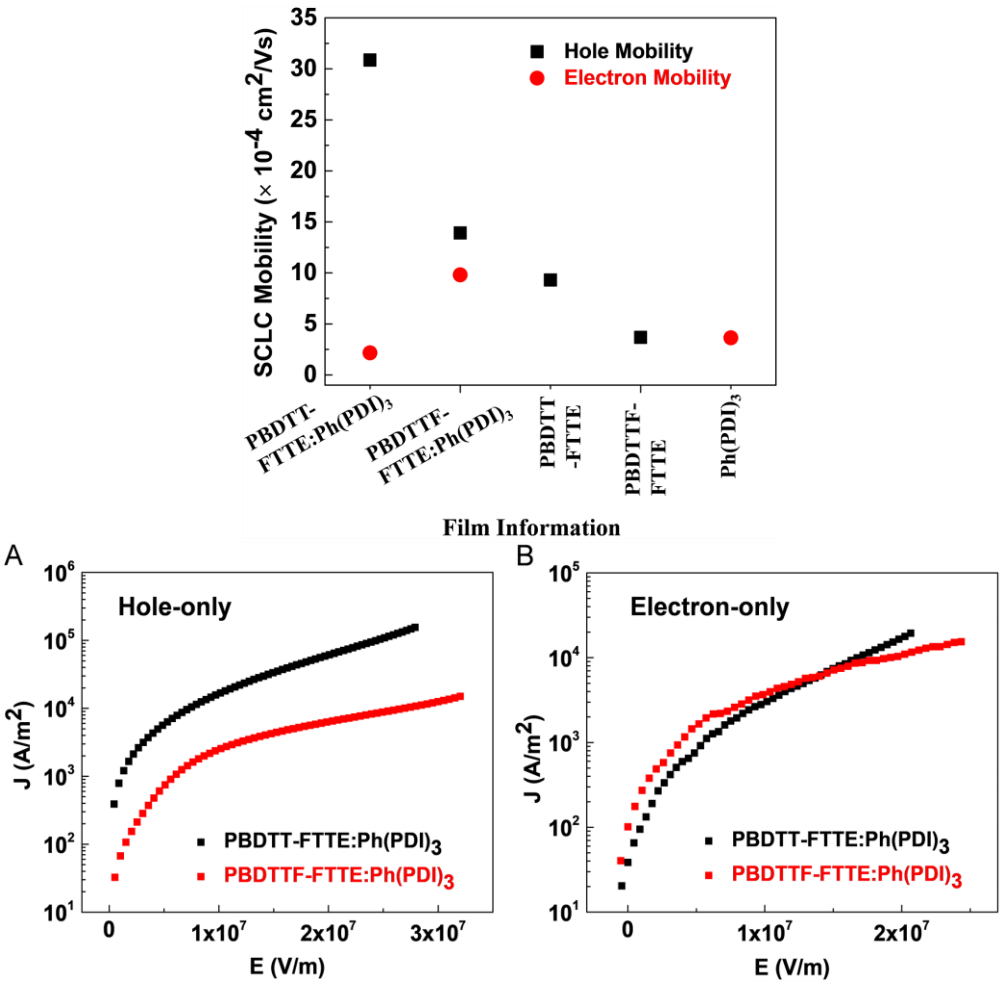

Figure 4.11. Average SCLC zero-field mobilities of blend and neat films top) and representative *J-E* curves of hole-only (bottom left) and electron-only diodes (bottom right) for blends. Average fitting parameters obtained from 7 or more separate devices are shown in **Table 4.4**.

4.5.7. Atomic Force Microscopy.

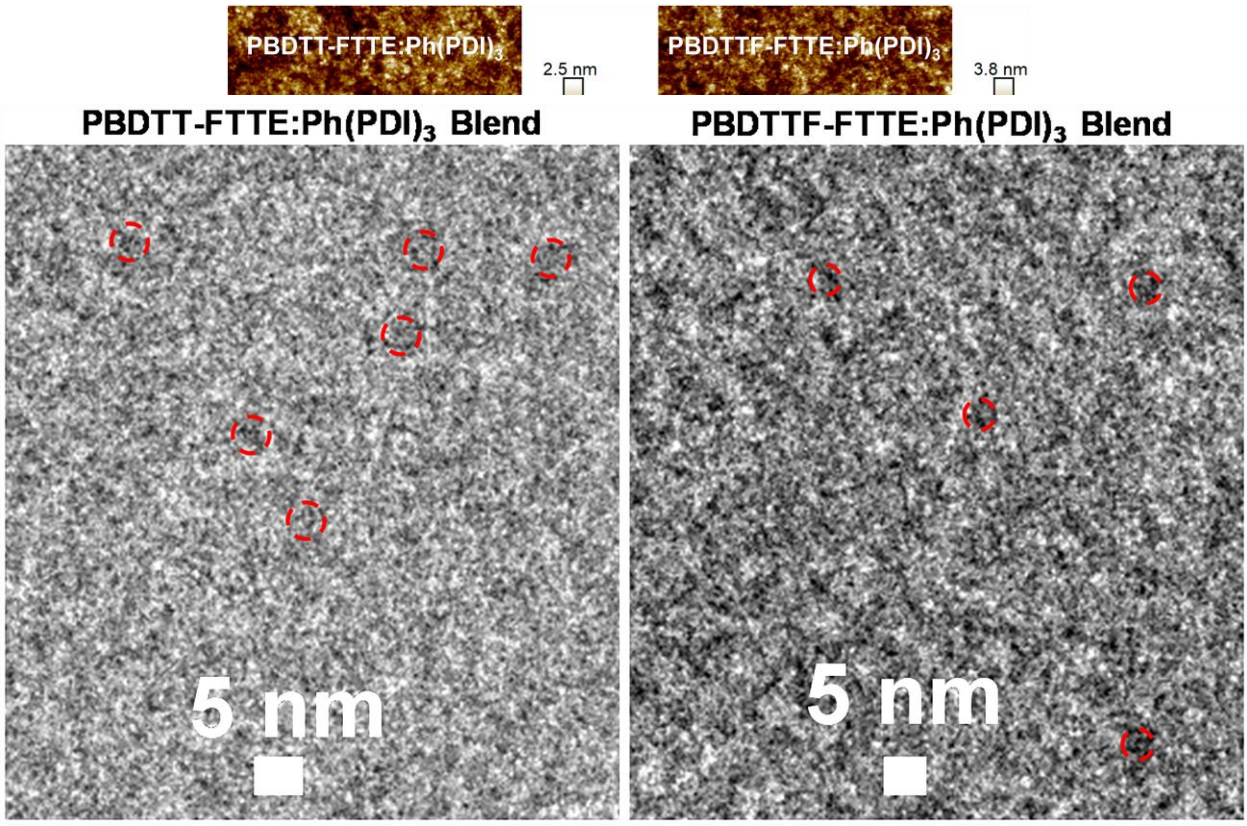

Figure 4.14. Typical TEM images of **PBDTT-FTTE:Ph(PDI)$_3$** and **PBDTTF-FTTE:Ph(PDI)$_3$** blend films with size of **Ph(PDI)$_3$**-rich domains (red circles ~ 3.5 nm).

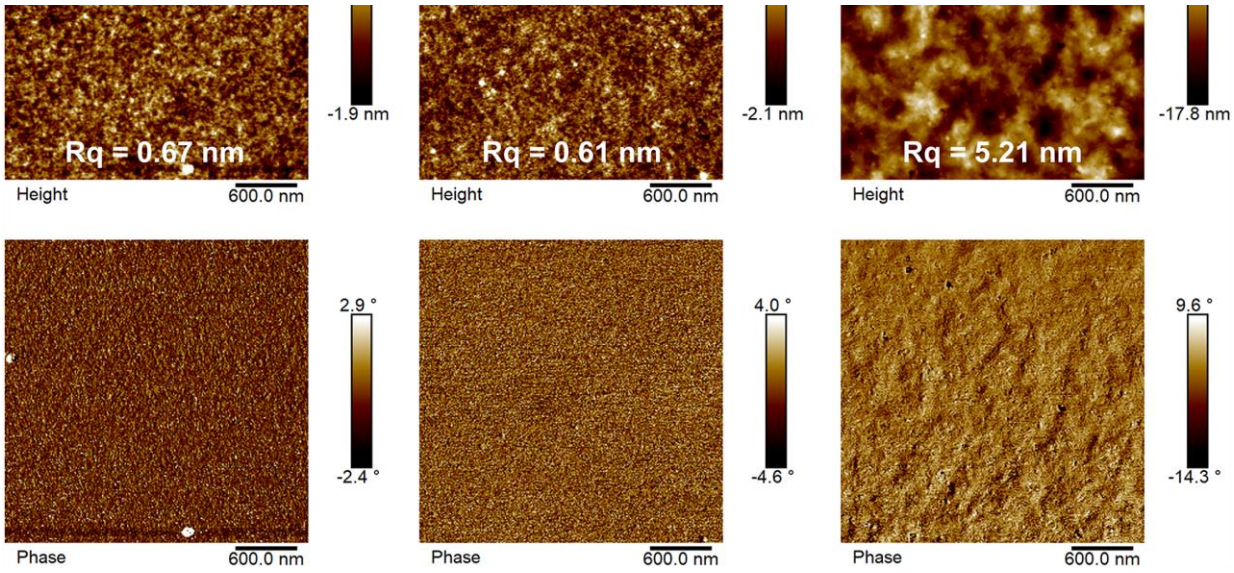

Figure 4.13. AFM images of neat **PBDTT-FTTE**, **PBDTTF-FTTE**, and **Ph(PDI)$_3$** films.

4.5.8. Transmission Electron Microscopy.

4.5.9. Grazing Incidence Wide-angle X-ray Scattering (GIWAXS)

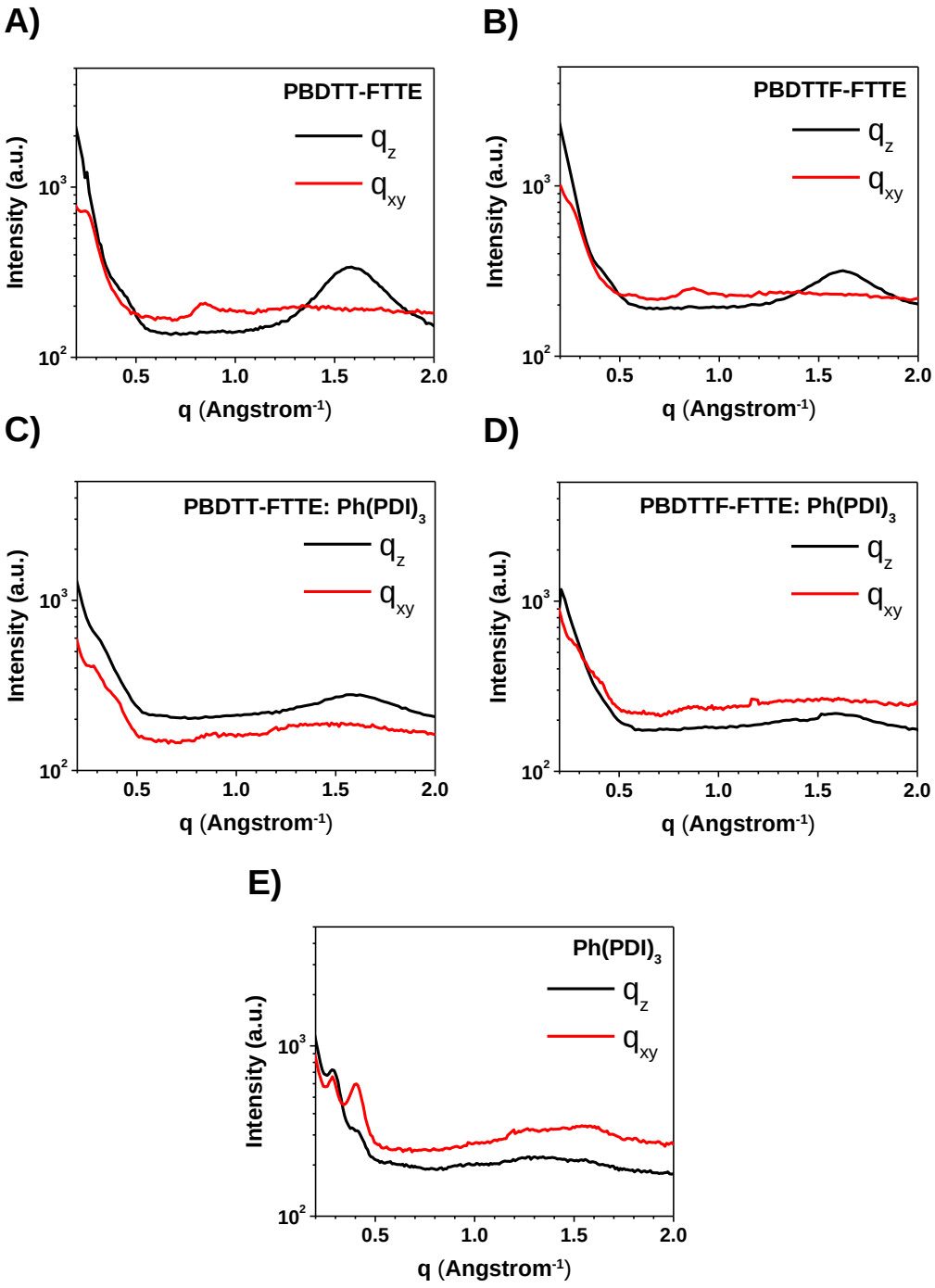

Figure 4.15. GIWAXS linecuts of (a) pristine **PBDTT-FTTE**, (b) pristine **PBDTTF-FTTE**, (c) BHJ blend **PBDTT-FTTE**:**Ph(PDI)$_3$**, (d) BHJ blend **PBDTTF-FTTE**:**Ph(PDI)$_3$**, and (e) pristine **Ph(PDI)$_3$** films showing in-plane (IP, q_{xy}) and out-of-plane (OoP, q_z) crystalline scattering peaks.

Table 4.7. *d*-Spacings and Correlation Lengths of Pristine and Blend Films.

Film	*d*-spacing (Å)		Correlation Length (nm)	
	IP (100)	**OoP (010)**	**IP (100)**	**OoP (010)**
Neat **PBDTT-FTTE**	25.76 ± (1.52)	3.91 ± (0.05)	4.6 ± (0.3)	1.78 ± (0.03)
Blend **PBDTT-FTTE:Ph(PDI)$_3$**	-	3.98 ± (0.02)	-	1.49 ± (0.08)
Neat **PBDTTF-FTTE**	26.32 ± (2.23)	3.85 ± (0.03)	4.0 ± (0.7)	1.83 ± (0.09)
Blend **PBDTTF-FTTE:Ph(PDI)$_3$**	-	3.98 ± (0.03)	-	1.30 ± (0.03)
Neat **Ph(PDI)$_3$**	22.3	4.66 ± (0.07)	24.3	0.98 ± (0.01)

All the values are reported as averages from 3 separate datasets.

4.5.10. Transient Absorption Spectroscopy.

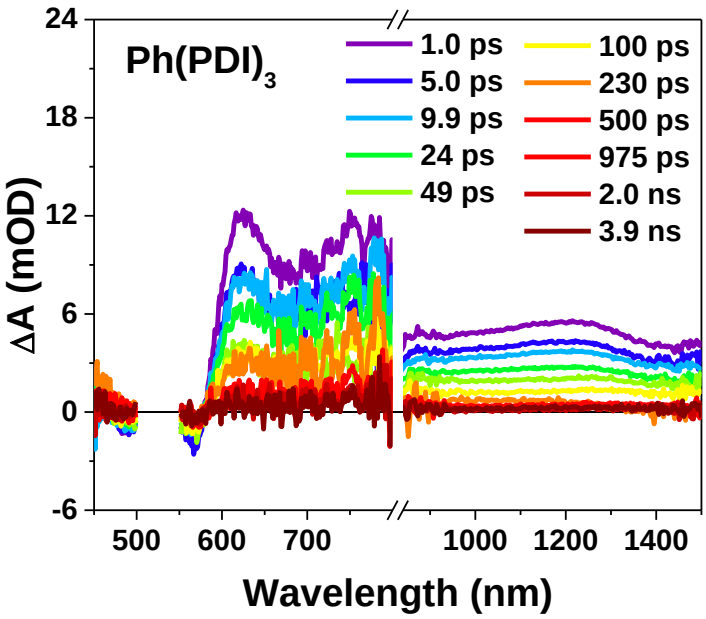

Figure 4.16. Time-resolved fsTA spectra at selected time points of film **Ph(PDI)$_3$** with λ_{ex} = 520 nm.

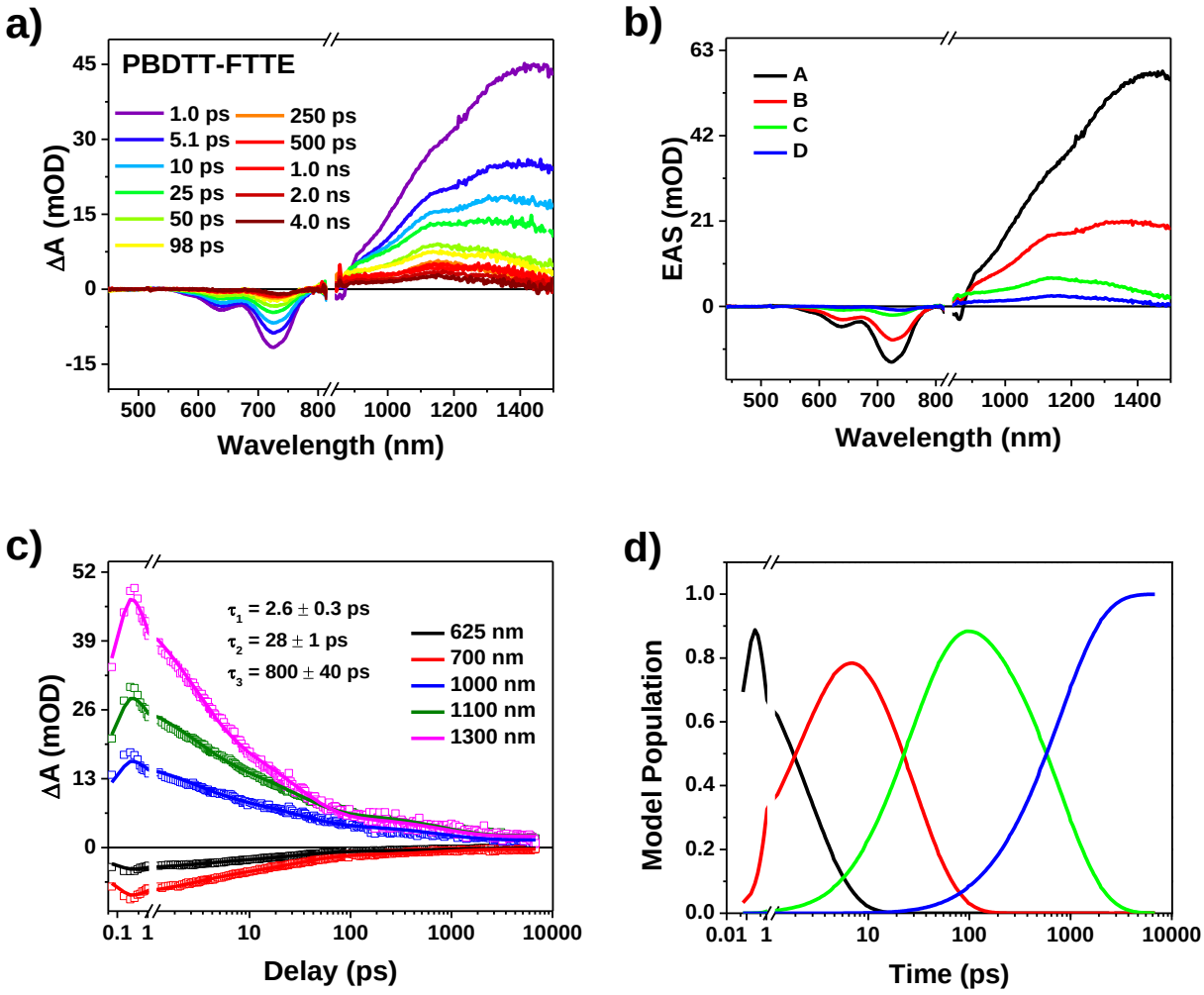

Figure 4.17. Analysis of the raw **PBDTT-FTTE** pristine film data with λ_{ex} = 700 nm as described in the text. (a) Time-resolved spectra at selected time points of film **PBDTT-FTTE** with λ_{ex} = 700 nm. (b) Evolution-associated spectra, τ_1 is the decay of species A to species B, etc. with time constants $\tau = 1/k$ shown in (c). (c) Kinetic fits to the raw data at the indicated wavelengths with the kinetic model described by **Eqn. S1**[40]. (d) Model population kinetics, distribution of species in time.

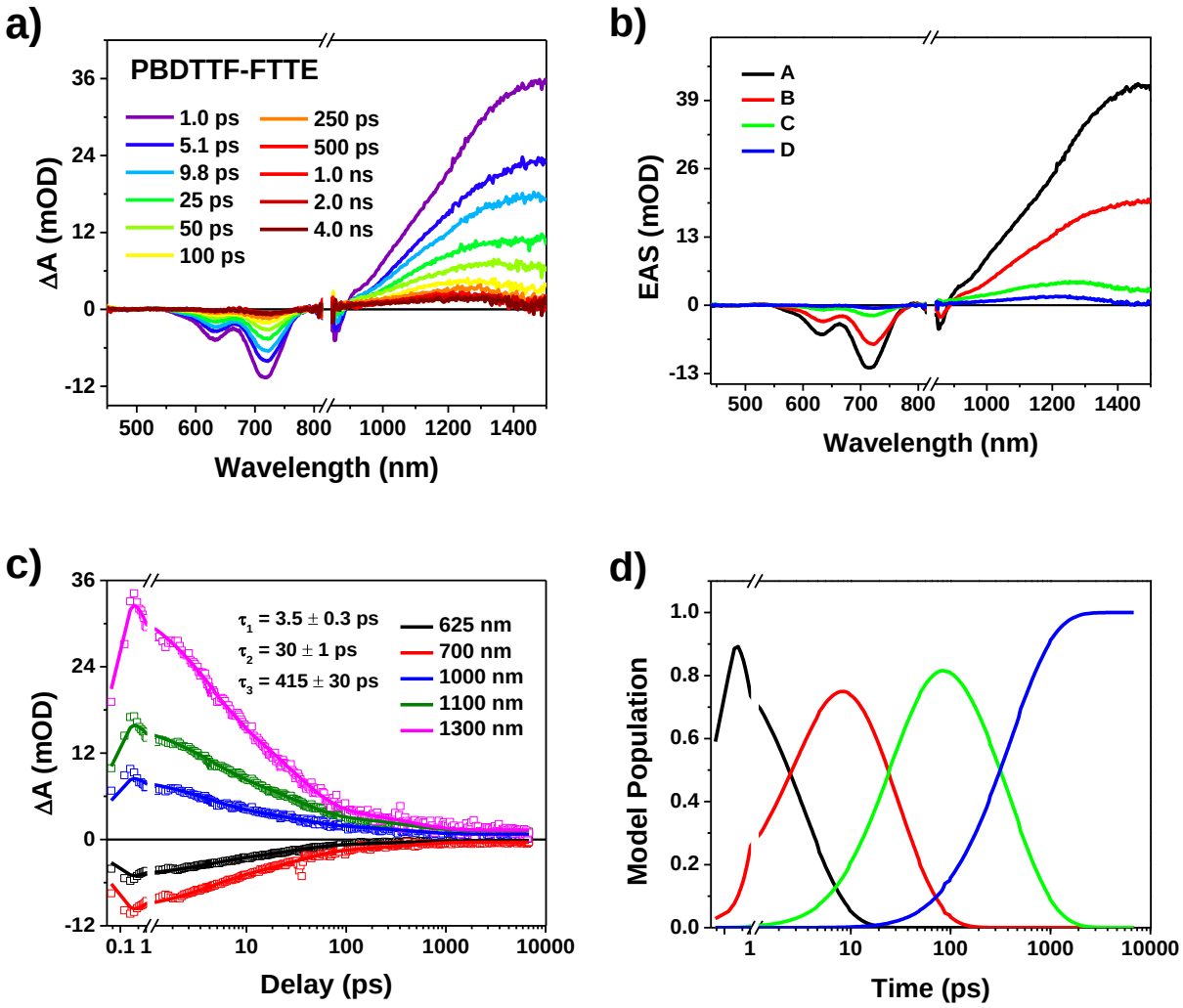

Figure 4.18. Analysis of the raw **PBDTTF-FTTE** pristine film data with λ_{ex} = 700 nm as described in the text. (a) Time-resolved spectra at selected time points of film **PBDTTF-FTTE** with λ_{ex} = 700 nm. (b) Evolution-associated spectra, τ_1 is the decay of species A to species B, etc. with time constants $\tau = 1/k$ shown in (c). (c) Kinetic fits to the raw data at the indicated wavelengths with the kinetic model described by **Eqn. S1**[40]. (d) Model population kinetics, distribution of species in time.

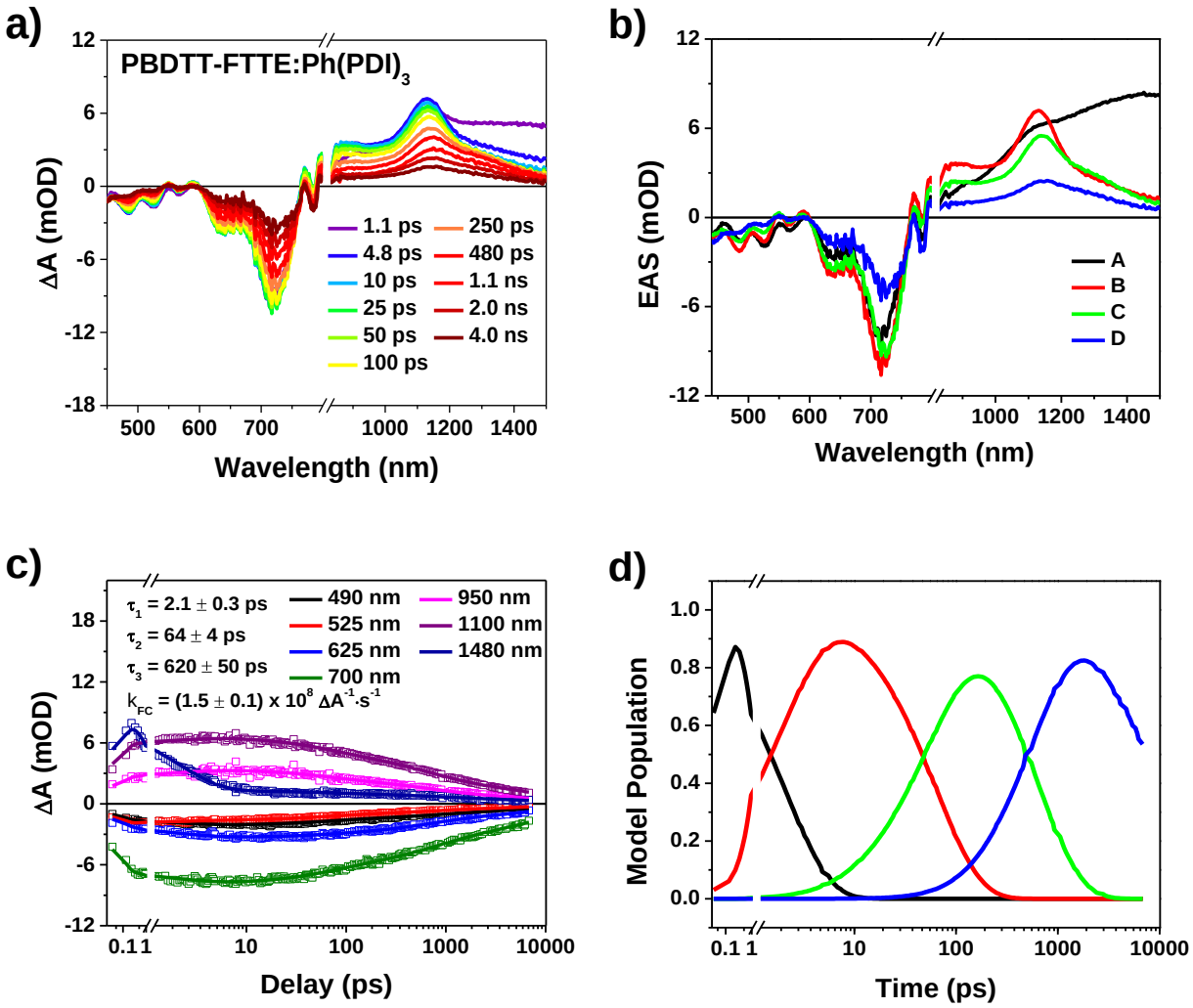

Figure 4.19. Analysis of the raw **PBDTT-FTTE:Ph(PDI)$_3$** blend film data with λ_{ex} = 520 nm as described in the text. (a) Time-resolved spectra at selected time points of **PBDTT-FTTE:Ph(PDI)$_3$** blend film with λ_{ex} = 520 nm. (b) Evolution-associated spectra, τ_1 is the decay of species A to species B, etc. with time constants $\tau = 1/k$ shown in (c). (c) Kinetic fits to the raw data at the indicated wavelengths with the kinetic model described by **Eqn. S2**[40]. (d) Model population kinetics, distribution of species in time.

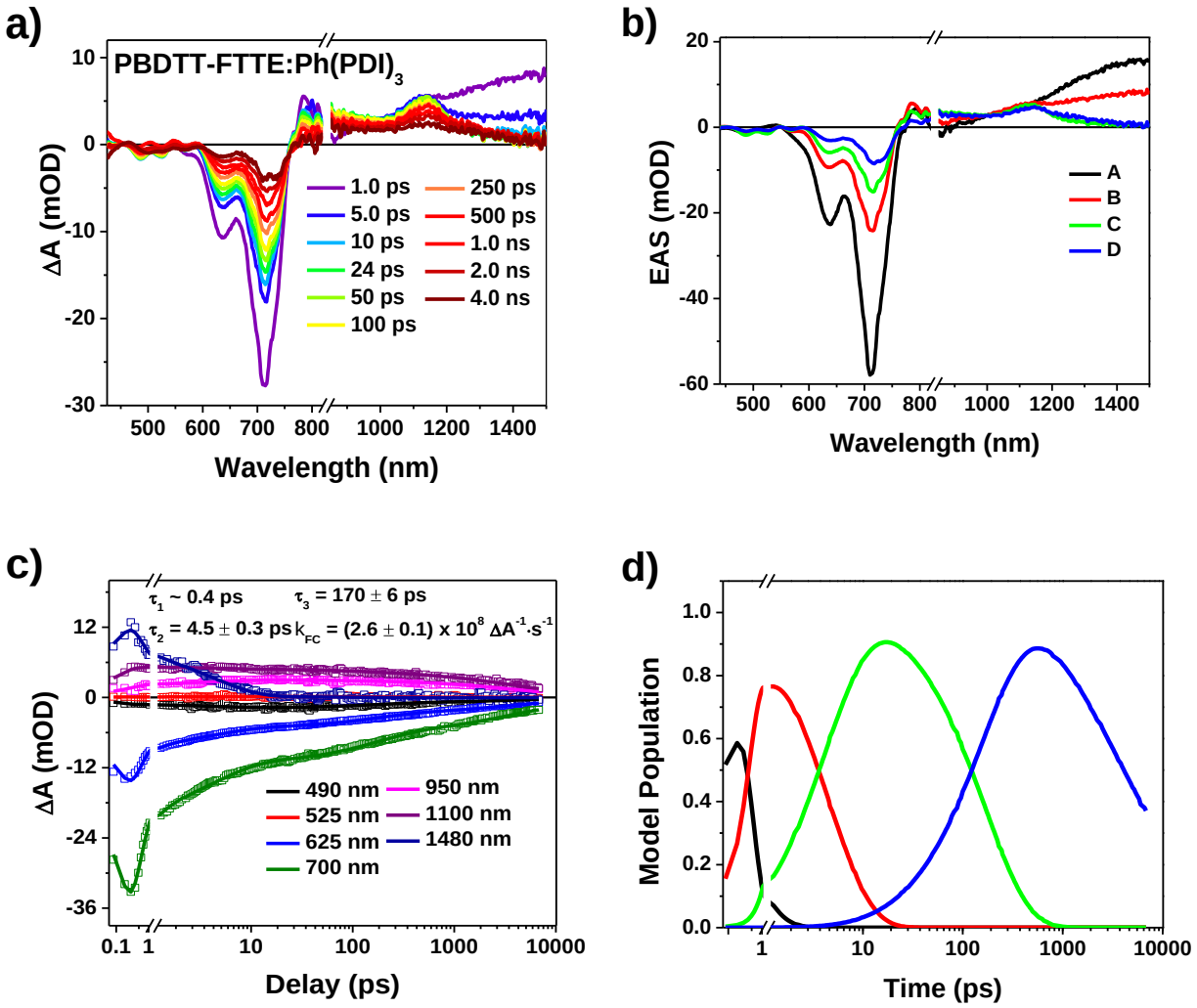

Figure 4.20. Analysis of the raw **PBDTT-FTTE:Ph(PDI)$_3$** blend film data with λ_{ex} = 700 nm as described in the text. (a) Time-resolved spectra at selected time points of **PBDTT-FTTE:Ph(PDI)$_3$** blend film with λ_{ex} = 700 nm. (b) Evolution-associated spectra, τ_1 is the decay of species A to species B, etc. with time constants $\tau = 1/k$ shown in (c). (c) Kinetic fits to the raw data at the indicated wavelengths with the kinetic model described by **Eqn. S2**[40]. (d) Model population kinetics, distribution of species in time.

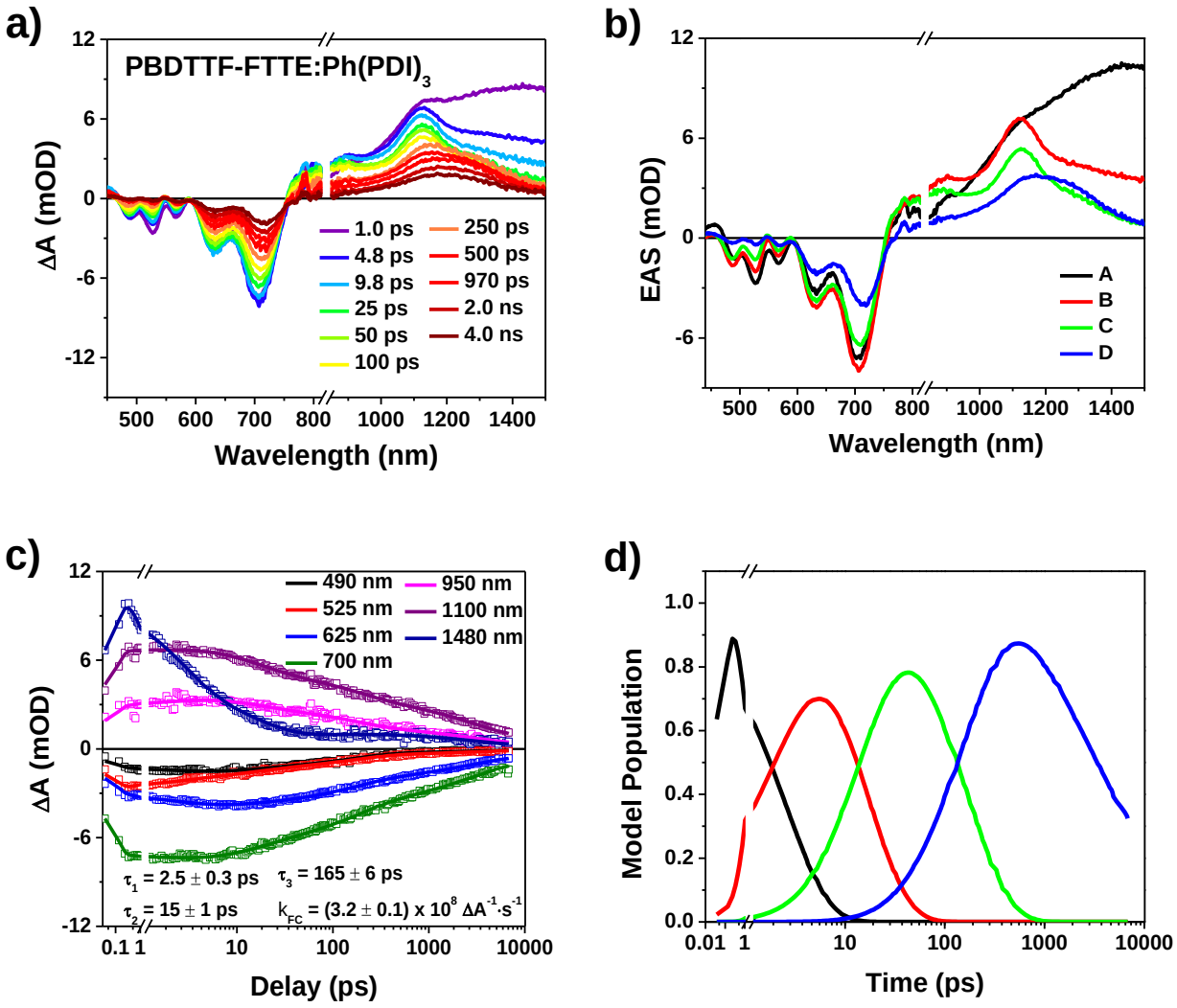

Figure 4.21. Analysis of the raw **PBDTTF-FTTE:Ph(PDI)$_3$** blend film data with λ_{ex} = 520 nm as described in the text. (a) Time-resolved spectra at selected time points of **PBDTTF-FTTE:Ph(PDI)$_3$** blend film with λ_{ex} = 520 nm. (b) Evolution-associated spectra, τ_1 is the decay of species A to species B, etc. with time constants $\tau = 1/k$ shown in (c). (c) Kinetic fits to the raw data at the indicated wavelengths with the kinetic model described by **Eqn. S2**[40]. (d) Model population kinetics, distribution of species in time.

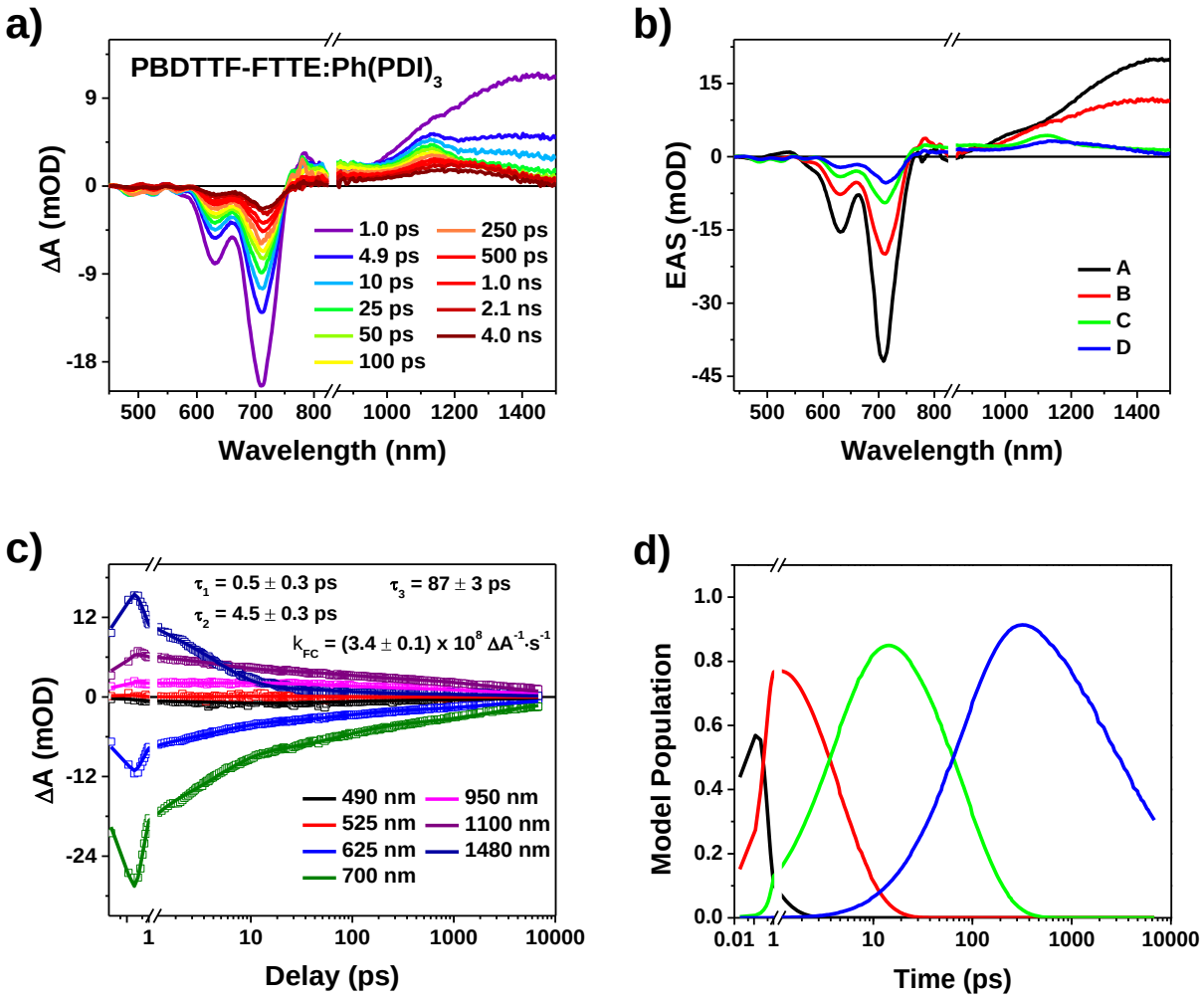

Figure 4.22. Analysis of the raw **PBDTTF-FTTE:Ph(PDI)$_3$** blend film data with λ_{ex} = 700 nm as described in the text. (a) Time-resolved spectra at selected time points of **PBDTTF-FTTE:Ph(PDI)$_3$** blend film with λ_{ex} = 700 nm. (b) Evolution-associated spectra, τ_1 is the decay of species A to species B, etc. with time constants $\tau = 1/k$ shown in (c). (c) Kinetic fits to the raw data at the indicated wavelengths with the kinetic model described by **Eqn. S2**[40]. (d) Model population kinetics, distribution of species in time.

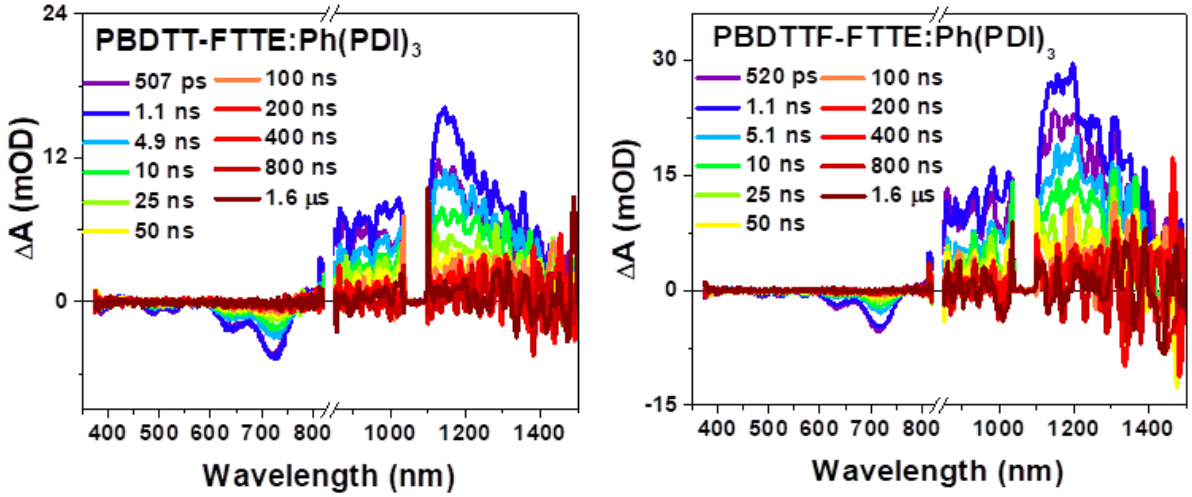

Figure 4.23. nsTA spectra at selected time points of **PBDTT-FTTE:Ph(PDI)$_3$** blend film with λ_{ex} = 520 nm (left) and nsTA spectra at selected time points of **PBDTTF-FTTE:Ph(PDI)$_3$** blend film with λ_{ex} = 520 nm (right).

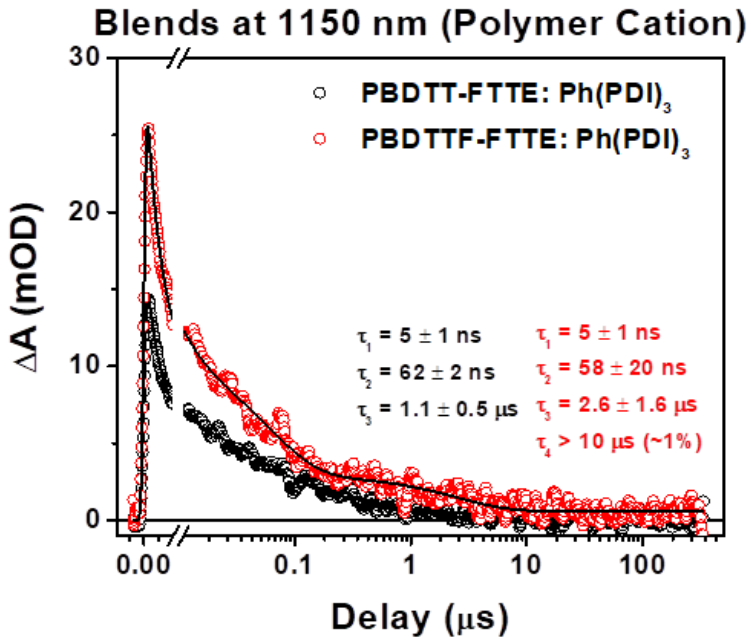

Figure 4.24. Raw kinetic traces for the polymer cation decay of **PBDTT-FTTE:Ph(PDI)$_3$** and **PBDTTF-FTTE:Ph(PDI)$_3$** blends monitored at 1150 nm in the nanosecond regime with their kinetic fits. λ_{ex} = 520 nm. The kinetics were fit to a sum of three exponential decays convoluted with a Gaussian instrument response.

4.5.11. Computational Data.

Table 4.8. Monomer (N = 1) Dipole Moments.

Isomer	PBDTT-FTTE	PBDTTF-FTTE
	x y z	x y z
$\mathbf{p}_g$ (Debye)	-2.4000, -0.7197, 0.1621	-2.4987, -1.7446, 0.1498
$\mathbf{p}_e$ (Debye)	-4.7969, -2.1702, 0.3278	-3.6705, -2.6854, 0.2432
$\mathbf{p}_{tr}$ (Debye)	2.3158, 2.2564, 0.0296	1.9927, 2.5634, -0.0140
	Total	Total
$\lvert\mathbf{p}_g\rvert$ (Debye)	2.51083	3.05116
$\lvert\mathbf{p}_e\rvert$(Debye)	5.27517	4.55446
$\lvert\mathbf{p}_{tr}\rvert$(Debye)	3.23344	3.24686
Δp_{eg} (Debye)	2.80652	1.50564
θ_{eg} (°)	7.63601	1.28915
Gap (eV)	3.4237	3.4454

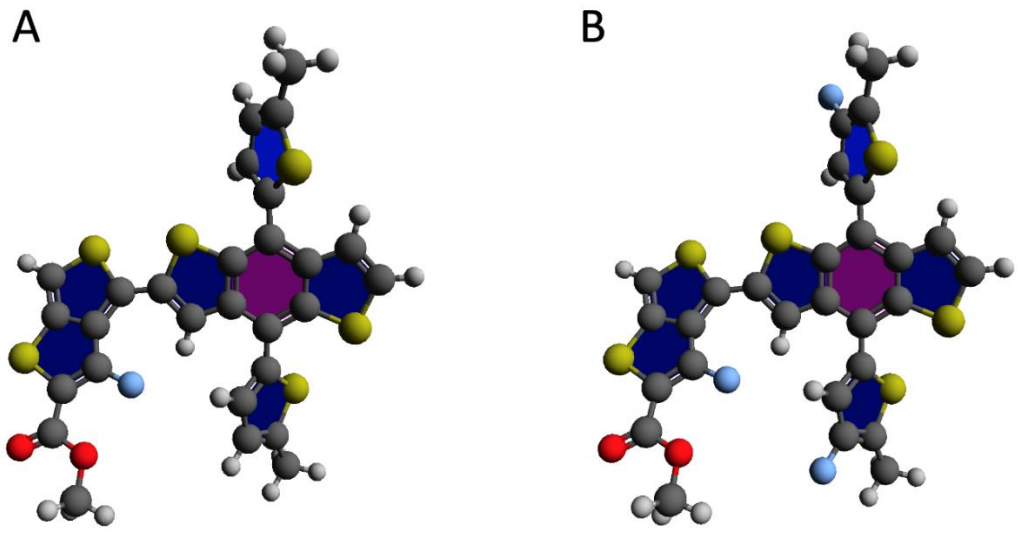

Figure 4.25. Monomer optimized geometries for (A) **PBDTT-FTTE** and (B) **PBDTTF-FTTE**.

Table 4.9. Dimer (N = 2) Dipole Moments.

Isomer	PBDTT-FTTE	PBDTTF-FTTE
	x y z	x y z
$\mathbf{p}_g$ (Debye)	-4.2335, 1.4371, 0.5754	-3.6246, 2.3597, 0.6438
$\mathbf{p}_e$ (Debye)	-3.1618, 1.0306, 0.4329	-2.4051, 2.0454, 0.5757
$\mathbf{p}_{tr}$ (Debye)	5.6308, 0.6682, -0.1726	5.4662, 0.3642, -0.2763
	Total	Total
$\lvert\mathbf{p}_g\rvert$ (Debye)	4.50765	4.37269
$\lvert\mathbf{p}_e\rvert$ (Debye)	3.35358	3.2093
$\lvert\mathbf{p}_{tr}\rvert$ (Debye)	5.67293	5.48528
Δp_{eg} (Debye)	1.15503	1.26119
θ_{eg} (°)	0.695883	7.45322
Gap (eV)	2.8904	2.8881

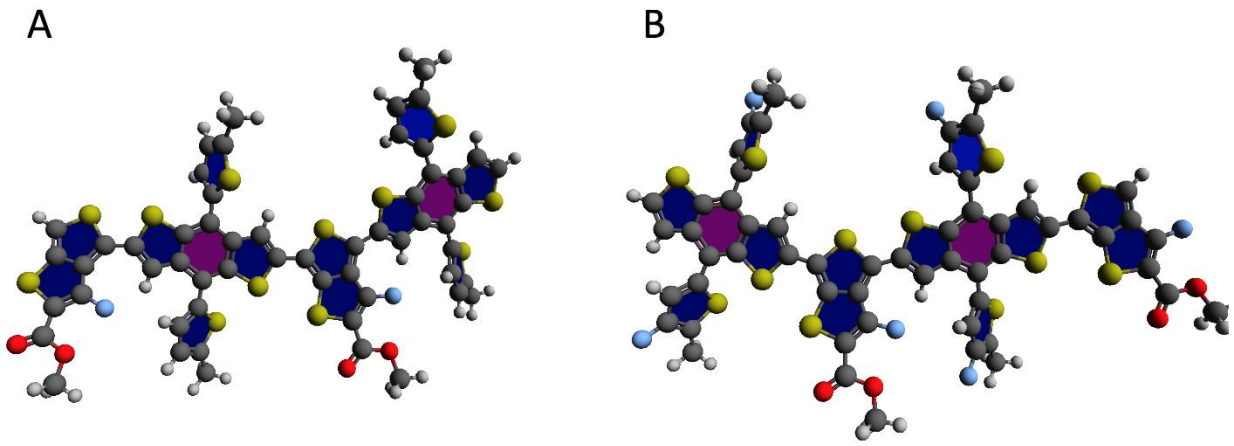

Figure 4.26. Dimer optimized geometries for (A) **PBDTT-FTTE** and (B) **PBDTTF-FTTE**.

Table 4.10. Trimer (N = 3) Dipole Moments.

Isomer	PBDTT-FTTE	PBDTTF-FTTE
	x y z	x y z
$\mathbf{p}_g$ (Debye)	-3.1365 , 3.7425, 0.0280	-6.1296, 2.9579, -0.0332
$\mathbf{p}_e$ (Debye)	2.2060, 3.2532, 0.2942	5.1465, 2.1926, 0.2987
$\mathbf{p}_{tr}$ (Debye)	6.9961, -0.6773, -0.1272	7.0377, -0.6863, -0.1099
	Total	Total
$\lvert\mathbf{p}_g\rvert$ (Debye)	4.88311	6.80605
$\lvert\mathbf{p}_e\rvert$(Debye)	3.94161	5.60207
$\lvert\mathbf{p}_{tr}\rvert$(Debye)	7.02996	7.07194
Δp_{eg} (Debye)	5.37146	11.3069
θ_{eg} (°)	74.1271	131.112
Gap (eV)	2.6816	2.6734

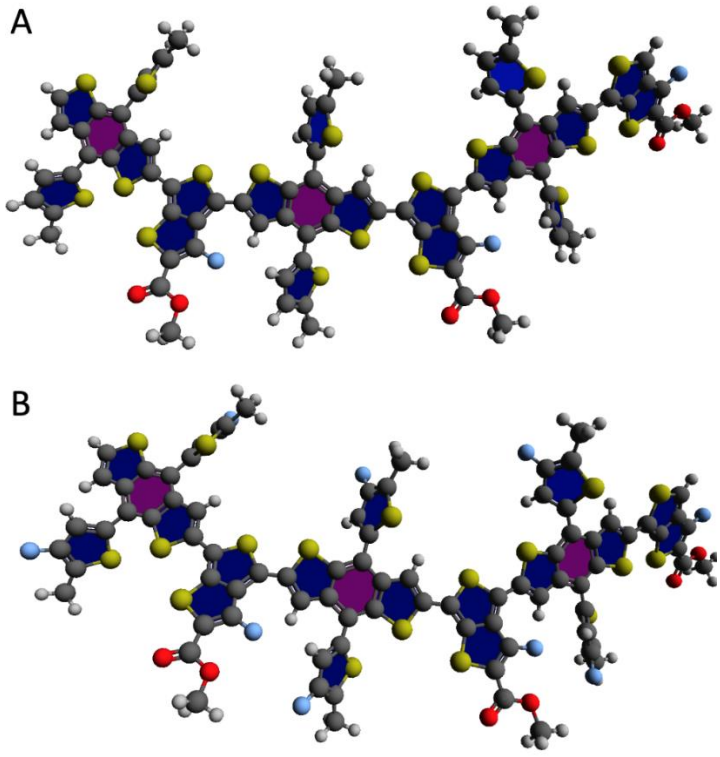

Figure 4.27. Trimer optimized geometries for (A) **PBDTT-FTTE** and (B) **PBDTTF-FTTE**.

Table 4.11. Tetramer (N = 4) Dipole Moments.

Isomer	PBDTT-FTTE	PBDTTF-FTTE
	x y z	x y z
$\mathbf{p}_g$ (Debye)	-4.4177, 4.4856, 0.1778	-7.7753, 3.7247, 0.6688
$\mathbf{p}_e$ (Debye)	3.5432, 3.7314, 0.5427	7.0670, 2.7658, 0.1068
$\mathbf{p}_{tr}$ (Debye)	7.9932, -0.6706, -0.2283	8.0372, -0.5663, -0.3739
	Total	Total
$\lvert\mathbf{p}_g\rvert$ (Debye)	6.29828	8.64731
$\lvert\mathbf{p}_e\rvert$(Debye)	5.17418	7.5897
$\lvert\mathbf{p}_{tr}\rvert$(Debye)	8.02453	8.0658
Δp_{eg} (Debye)	8.00487	14.8839
θ_{eg} (°)	87.9227	132.78
Gap (eV)	2.5939	2.6125

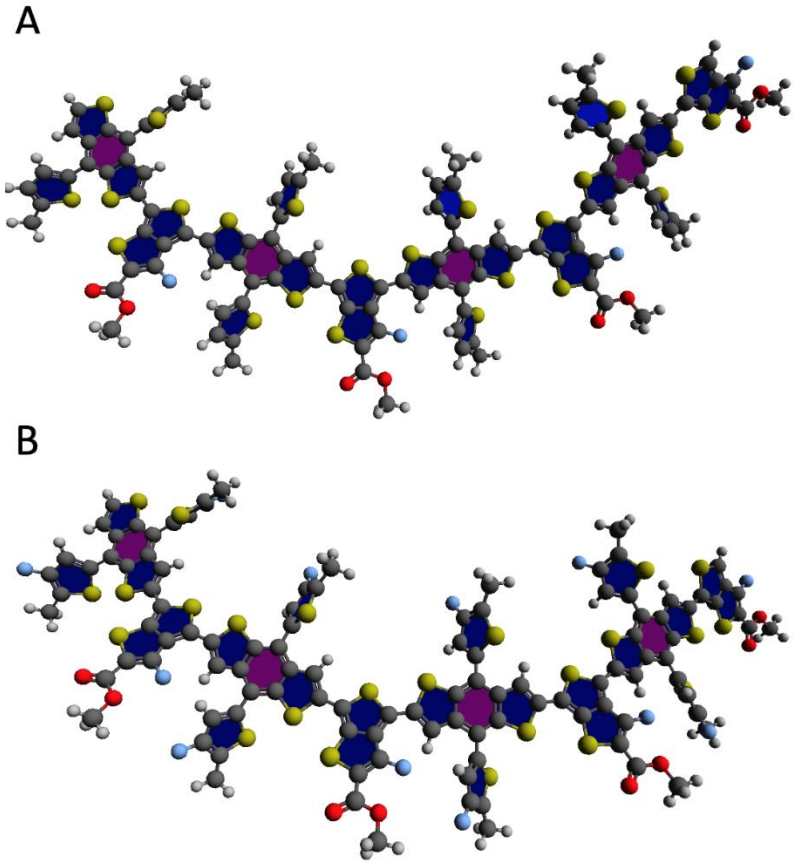

Figure 4.28. Tetramer optimized geometries for (A) **PBDTT-FTTE** and (B) **PBDTTF-FTTE**.

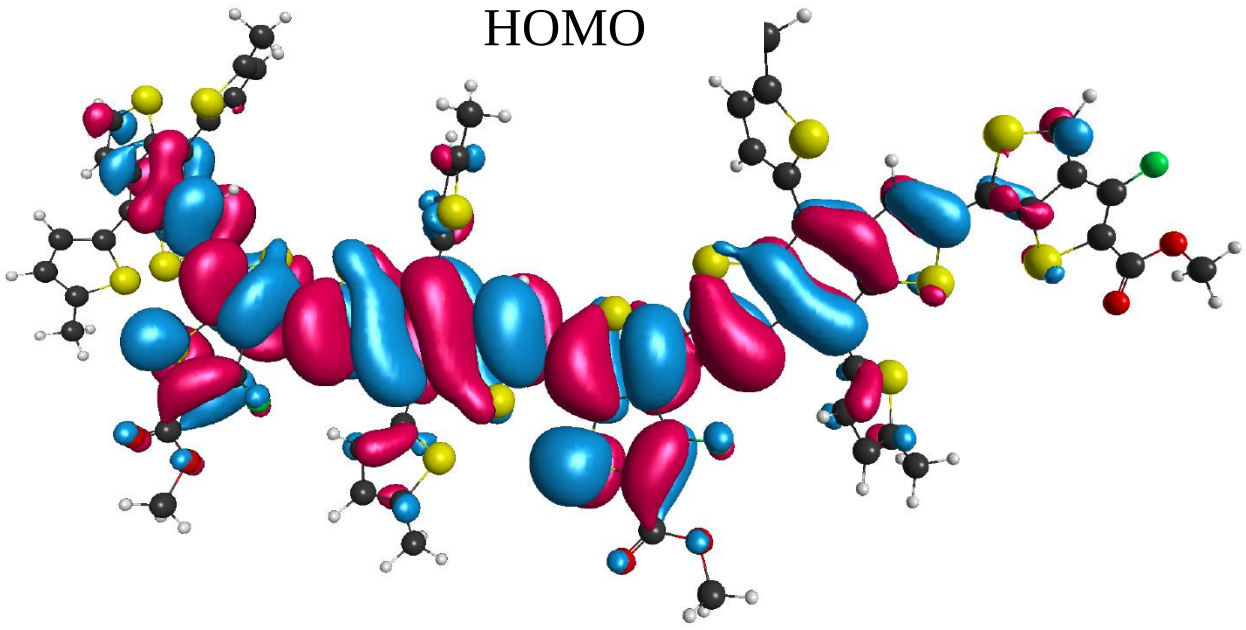

Figure 4.29. HOMO of **PBDTT-FTTE** trimer. Isosurface contour value is +/- 0.01.

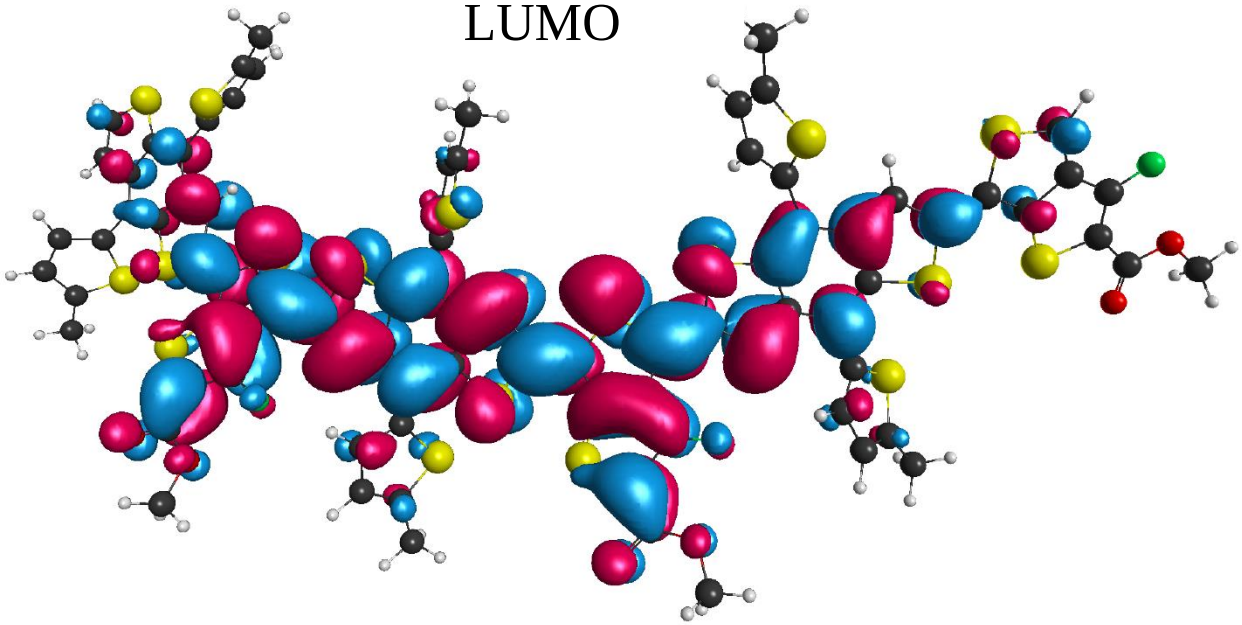

Figure 4.30. LUMO of **PBDTT-FTTE** trimer. Isosurface contour value is +/- 0.01.

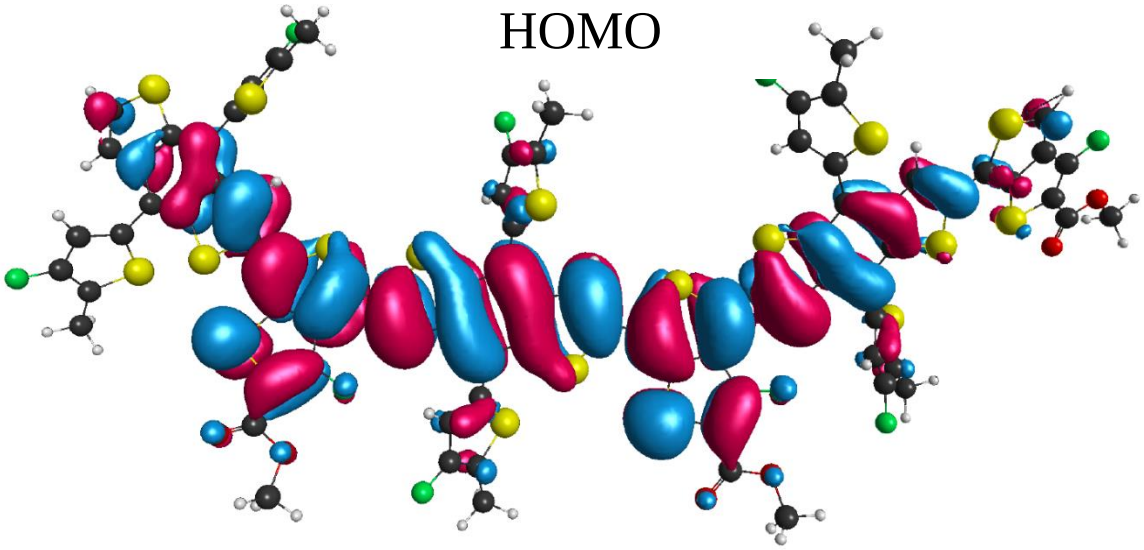

Figure 4.31. HOMO of **PBDTTF-FTTE** trimer. Isosurface contour value is +/- 0.01.

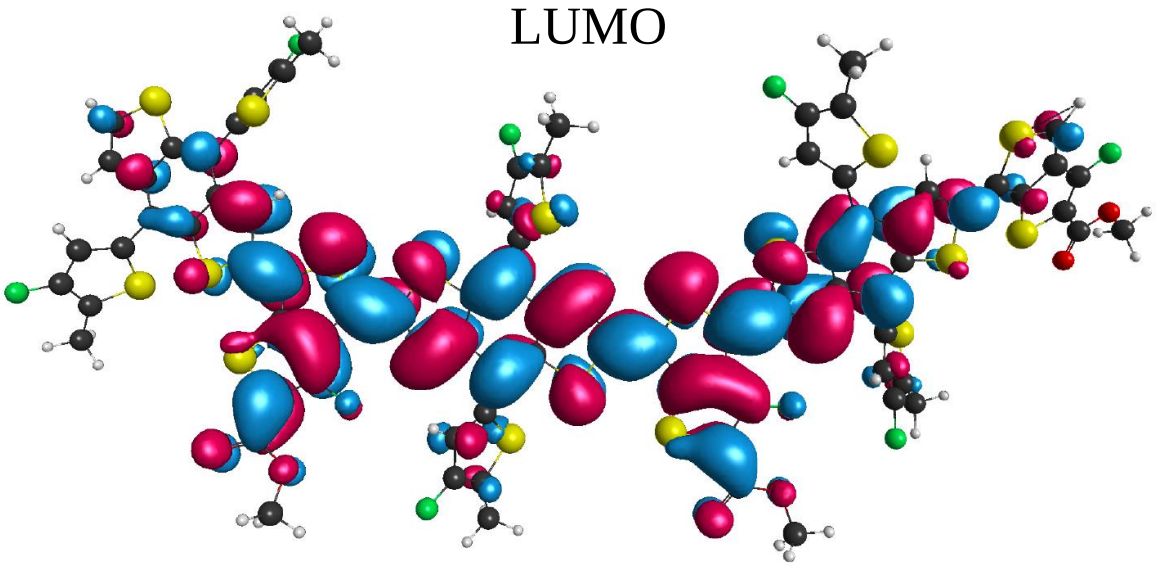

Figure 4.32. LUMO of **PBDTTF-FTTE** trimer. Isosurface contour value is +/- 0.01.

Table 4.12. Exciton Electron-Hole Separation.

	PBDTT-FTTE				PBDTTF-FTTE			
N	1	2	3	4	1	2	3	4
R_{eh} (A)	0.648	0.121	0.171	0.109	0.362	0.280	0.207	0.122

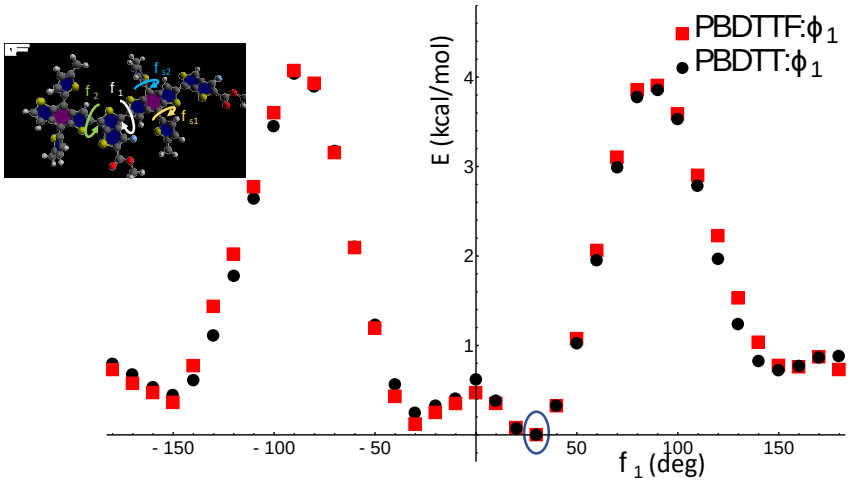

Figure 4.33. The 1D potential energy surface of the during the rotation of the ϕ_1 torsion angle for the **PBDTTF-FTTE** polymer (black circle) and the **PBDTT-FTTE** polymer (red square). The minimum energy angle is circled at 30°.

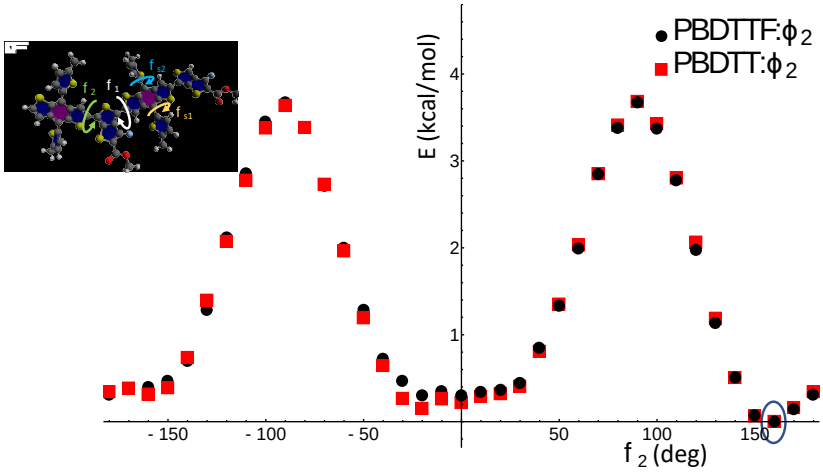

Figure 4.34. The 1D potential energy surface of the during the rotation of the ϕ_2 torsion angle for the **PBDTTF-FTTE** polymer (black circle) and the **PBDTT-FTTE** polymer (red square). The minimum energy angle is circled at 160°.

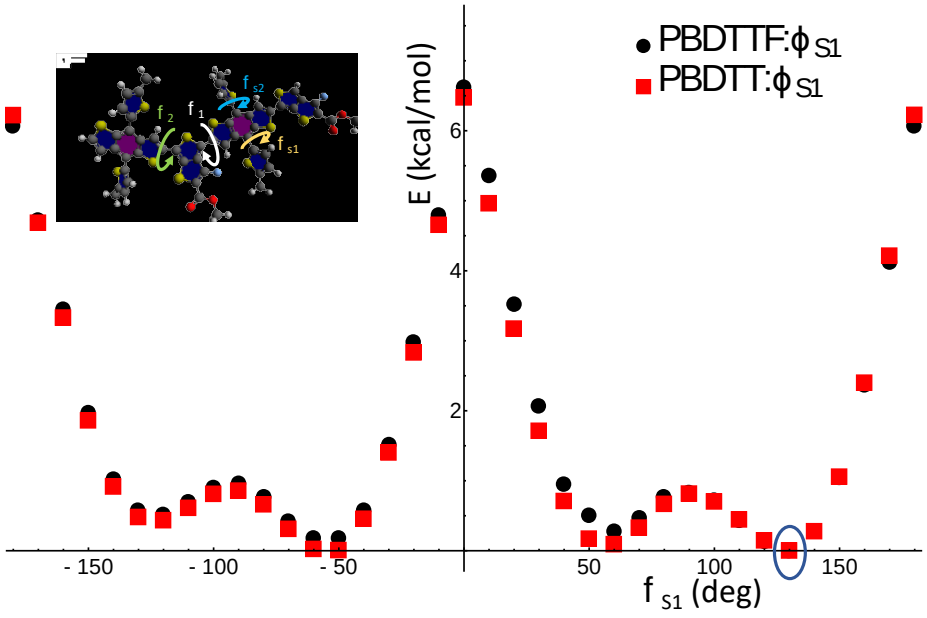

Figure 4.35. The 1D potential energy surface of the during the rotation of the ϕ_{S1} torsion angle for the **PBDTTF-FTTE** polymer (black circle) and the **PBDTT-FTTE** polymer (red square). The minimum energy angle is circled at 130º.

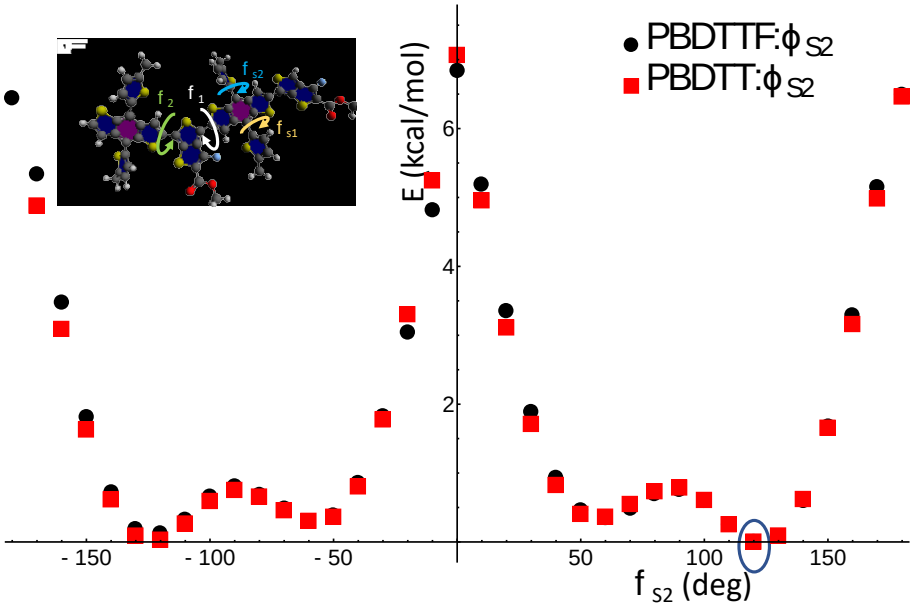

Figure 4.36. The 1D potential energy surface of the during the rotation of the ϕ_{S2} torsion angle for the **PBDTTF-FTTE** polymer (black circle) and the **PBDTT-FTTE** polymer (red square). The minimum energy angle is circled at 120º.

Chapter 5 – Excited-State Dynamics of Fused-Ring Postfullerene Electron Acceptor Bulk Heterojunctions

Selections adapted with permission from *Adv. Energy Mater.* **2020**, 23 (*10*), 2000635, *J. Am. Chem. Soc.* **2020**, 142 (*34*), 14532–14547, and *J. Am. Chem. Soc.* **2021** 143 (*16*), 6123-6139.

5.1. Introduction

Organic solar cells (OSCs), a promising avenue for renewable energy technology, has experienced remarkable growth over the last several years. This technology offers several advantages over traditional solar panels composed of silicon, including lower processing costs, mechanical flexibility, and adaptability to large scale fabrication methods such as inkjet printing.[155, 222] Despite these advantages, organic materials have a much lower dielectric environment than traditional semiconductors, resulting in strongly bound excitons that cannot be easily separated into composite holes and electrons.[223-225] OSCs employ a heterojunction structure, with two different materials acting as the electron donor and electron acceptor with appropriate energetic offsets to facilitate scission of the bound exciton.[27, 108, 155, 226] The most successful version of this technology to date consists of a bulk heterojunction (BHJ) blend composed of a conjugated polymer as an electron donor and a small molecule as the electron acceptor.[227, 228] For decades, the premier electron acceptor materials have been buckminsterfullerene and its derivatives, with power conversion efficiencies (PCEs) of up to 10%, largely outstripping other classes of acceptor materials.[124, 229, 230]

More recently, there has been a renaissance in the development of small molecule acceptors. Early optimization of indacenodithiophene (**ITIC**) as an electron acceptor by Lin *et al.* produced a PCE of 6.8%, one of the highest for a so-called nonfullerene acceptor (**Figure 5.1**).[45] This system was quickly optimized to efficiencies of >10%, exceeding the top PCEs of fullerenes for the first time.[167, 231, 232] This research introduced the molecular design concept of the fused-ring electron acceptor (FREA) as a revolutionary concept in the field of OSCs. FREAs employ an ADA-type structure, consisting of an electron-donating core flanked by multiple strongly electron-

accepting end groups.[112, 233-235] The strongly-electron withdrawing nature of these groups coupled with significant conjugation of π bonds results in these materials demonstrating significantly red-shifted optical absorption properties, ($\lambda_{onset} \geq 850$ nm).[228, 232] By comparison, fullerene derivatives only absorb photons in the ultraviolet range of the electromagnetic spectrum. This greatly expands the range of photon energies available for absorption while the utilization of lower-energy photons mitigates energy losses due to thermalization. Another important feature of these structures is the placement of orthogonal solubilizing groups consisting of either aryl or alkyl substituents, imparting high solubility while allowing the individual molecules to retain π-π stacking and thus electronic communication between the chromophores.[236-239]

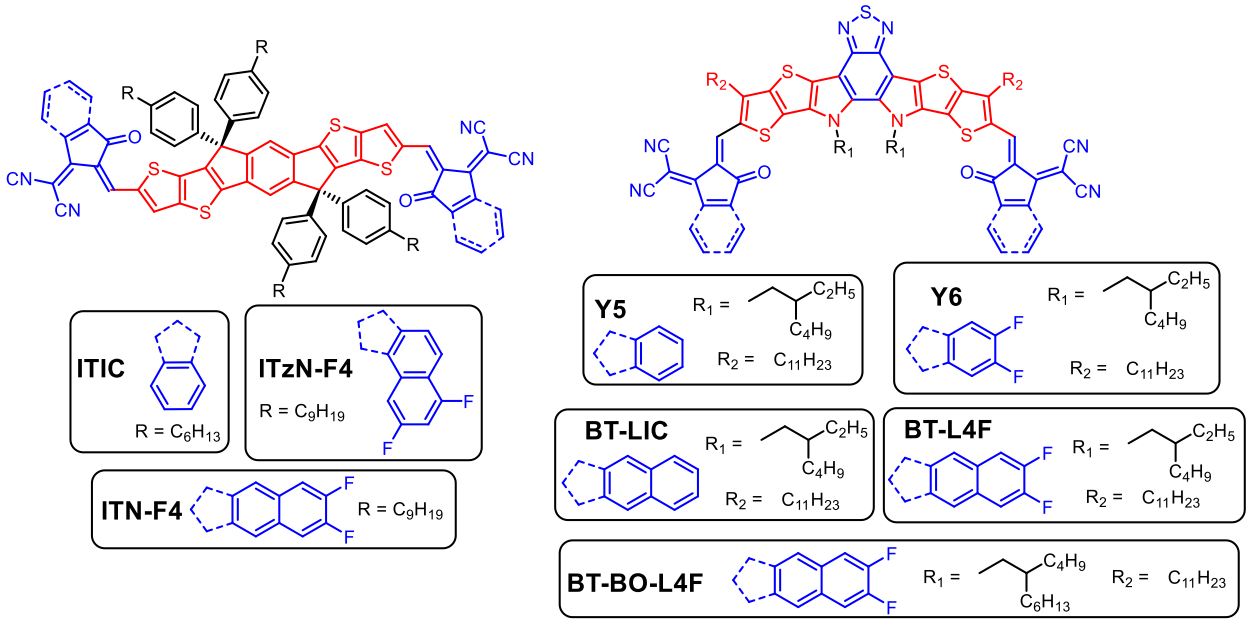

Figure 5.1. Chemical structures of FREA molecules. Blue highlights denote electron accepting units and red highlights denote electron donating units. Dotted lines indicate structural differences in the acceptor end groups.

Several iterations of ADA FREAs with a wide range of optical and electronic properties have been published, demonstrating the versatility of this molecular design. New research by Yuan *et al.* introduced the A-DAD-A design structure **Y5** (**Figure 5.1**) and its derivatives that are

characterized by a curved backbone as opposed to the more linear structure of ITIC by incorporation of an electron-withdrawing unit into their electron-donating core.[240] These FREAs are the current premier electron acceptor materials with efficiencies of over 17%.[13, 241, 242]

Many synthetic strategies have been implemented to modulate the molecular structure of FREAs in search of higher PCEs.[113, 164, 235, 243, 244] Two notable strategies are heteroatom substitution and incorporation of an additional aromatic ring in the structure to extend the conjugation. Fluorine substitution is a powerful synthetic tool in organic semiconductors at lowers the frontier molecular orbital energies of molecules (thus improving J_{sc})[182] and introducing additional electrostatic interactions that improve crystallinity in the microstructure and enhance charge mobilities.[239] Separately, increasing the π-surface of a compound can effectively lower internal reorganization energy and increase overlap between molecules, enhancing electronic coupling and thus charge transport.[208, 244] Applying each of these strategies has resulted in PCE improvements in several FREAs, though the effect on the exciton transfer processes in the heterojunctions has not been thoroughly explored. Here we investigate the excited-state dynamics of several FREAs in BHJ blends using steady-state and time-resolved spectroscopy techniques. We report on the unique photophysics of π-extended and fluorinated derivatives of ITIC known as **ITN-F4** and **ITzN-F4** (**Figure 5.1**) as well as those of **Y5** and similarly derived molecular structures, **BT-LIC** and **BT-L4F**, among others (**Figure 5.1**). All these blends are capable of ultrafast charge transfer to some degree, a key phenomenon among organic photovoltaic blends with efficiencies > 8%.[34, 245] We find that π-extension of ITIC results in a propensity to form an excimer state, though this state does not diminish the PCE of these materials as is observed in other nonfullerene derivatives. The photophysics of **Y5**-type blends are significantly impacted by

thermal annealing, as higher hole mobilities (μ_hs) that result in a PCE increase also accelerate bimolecular recombination in transient absorption experiments (these are performed in the absence of an external bias).

5.2. Experimental Details

5.2.1. Film Preparation

All the films were spin-coated on 25 mm × 25 mm clean glass substrate (VWR) in an Ar-atmosphere glovebox. **ITN-F4**:**PBDB-T-2F** blend films were spin coated from CHCl3 solutions (D/A ratio = 1:0.8, 5 mg/mL polymer concentration, 1000 rpm, 90 s) and **ITzN-F4**:**PBDB-T-2F** blend films were spin-coated from chlorobenzene solutions (D/A ratio = 1:1, 10 mg/mL polymer concentration, 2500 rpm, 60 s). For the control experiments, neat **ITzN-F4** was spin coated from chlorobenzene (15 mg/mL, 2500 rpm, 60 s) and **ITN-F4** films were spin-coated from CHCl3 (7.5 mg/mL, 1000 rpm, 90 s). Neat **PBDB-T-2F**:**Y6** films were spin-coated from 5.5, 11 mg/mL chloroform solution (1000 rpm, 150 s), respectively. **PBDB-T-2F**:**Y6** films were spin-coated as the optimized OPV devices. Neat films of **Y5, BT-LIC, BT-L4F**, and **BT-BO-L4F** were spin coated from chloroform (5 mg/mL, 1000 rpm, 60 s). Blend films were spin-coated from $CHCl_3$ (11 mg/mL, 1000 rpm, 60 s, D:A = 1:1 for the fluorinated acceptors, D:A = 1:1.2 for the non-fluorinated acceptor), and the donor polymers **PBDB-T** and **PBDB-T-2F** were spin coated from chloroform (5 mg/mL, 1000 rpm, 90 s).

5.2.2. Steady-State Optical Characterization

Solution and film UV-vis spectra were recorded on a Varian Cary 100 UV-vis spectrophotometer. The **ITN-F4** and **ITzN-F4** film optical absorption spectra were recorded from films cast from chloroform solutions (5.0 mg/mL, 2500 rpm) onto glass slides. Solutions were

prepared at 0.00500 mg/mL in chloroform and measured at room temperature. The film optical absorption spectra of **BT-LIC**, **BT-BIC**, **BT-L4F**, **BT-BO-L4F**, **Y5** and **Y6** were recorded from films cast from chloroform solutions (5.0 mg/mL, 1000 rpm, 1 rpm = 0.105 rad/s) onto glass slides. Neat **PBDB-T-2F**:**Y6** films were spin-coated from 5.5, 11 mg/mL chloroform solution (1000 rpm, 150 s), respectively. **PBDB-T-2F:Y6** bulk-heterojunction (BHJ) films were spin-coated using the same conditions as organic photovoltaic (OPV) devices. Emission spectra were collected on a Horiba Nanolog fluorimeter with a perpendicular arrangement of the excitation source and detector for solution samples and a front-facing arrangement for film samples. All emission spectra were corrected for monochromator wavelength dependence and CCD-detector spectral response functions.

5.2.3. Time-Resolved Spectroscopy

The high-fluence femtosecond transient absorption (fsTA) and nanosecond transient absorption (nsTA) setups have been previously described.[192] To minimize sample degradation due to air, all films samples were measured under vacuum in a Janis VPF-100 cryostat at room temperature. Kinetic analysis is performed in MATLAB using global analysis according to linear and non-linear kinetic models described previously.[242]

5.3. Results and Discussion

5.3.1. Excited-State Dynamics of π-Extended ADA Small Molecule Acceptors

ITN-F4 and **ITzN-F4** are FREAs derived from the prototypical ITIC using the π-extension and fluorination strategies described above. These compounds function successfully as small molecular acceptors in organic solar cells, reaching high PCEs of 10.3% and 10.0%, respectively.[236] While several studies have observed and commented on the ultrafast charge

generation processes of several ADA FREAs,[33, 148, 246] the effects of these synthetic modifications has not yet been examined. The transient dynamics of **ITN-F4** and **ITzN-F4** in toluene are reported for the first time (**Figures 5.10** and **5.11**). Following photoexcitation of **ITzN-F4** at 695 nm, ground-state bleach (GSB) features are observed from 600-750 nm and excited state absorption (ESA) features present from 830-1010 nm with a local maximum at 980 nm. There is also a weak absorption feature from 1300-1500 nm in the near-infrared region of the spectrum. Global analysis produces a three-state decay model A→B→C→GS. The spectral features of **ITN-F4** mirror those of **ITzN-F4**, albeit with features that are red-shifted in accordance with the lower FMO energies of **ITN-F4** and **ITzN-F4**. The negative feature at 760 nm is no longer present in state B in both **ITN-F4** and **ITzN-F4**, thus it is assigned as a stimulated emission (SE) feature. Contrary to chromophores such as PDI, the excited-state behavior of FREAs consists of multiple decay components, likely originating from the push-pull nature of the ADA structure.[192] There are no significant spectral shifts in any of the three components and all spectral features are present at the same relative intensity in each state, ruling out the possibility of other photophysical processes competing with decay of the excited state. The excited-state lifetimes of these compounds range from 100-200 ps, much shorter than that of other acceptor molecules employed in organic photovoltaic cells.[247, 248]

We then probed the charge separation dynamics of **ITN-F4** and **ITzN-F4** blend films of the same composition used for solar cells. The donor polymer **PBDB-T-2F** employed in these blends (**Figure 5.5**) does not absorb at 740 nm, therefore photoexcitation at 740 nm in **ITN-F4** and **ITzN-F4** blends permitted selective monitoring of hole transfer dynamics.[249] Global fits of each film at selected wavelengths according to a nonlinear kinetic model that accounts for singlet-

singlet annihilation and long-lived bimolecular recombination of free carriers in the blends are provided in the supporting information (**Figures 5.5-5.9**). Notably, both **ITN-F4** and **ITzN-F4** conduct ultrafast hole transfer to **PBDB-T-2F** within the instrument response time (<300 fs), demonstrated by the appearance of **PBDB-T-2F** ground-state bleach (GSB) features just after excitation. These are accompanied by excited-state absorption of the acceptor (^{1*}A) centered near 990 nm and a broad absorption centered at ~1200 nm (**Figure 5.2A** and **5.2B**). This broad feature also appears in neat films of **ITN-F4** and **ITzN-F4** (**Figures 5.8** and **5.9**) with similar decay time constants and is attributed to an excimer state. The excimer state observed is likely due to the high degree of overlap between the extended π-surfaces of the end groups of **ITN-F4** and **ITzN-F4** which is retained in the blend films. Steady-state fluorescence spectra of films of **ITN-F4** and **ITzN-F4** (**Figure 5.1**) demonstrate broad, featureless emission profiles that are red-shifted from the solution emission profiles (166 nm for **ITN-F4** and 112 nm for **ITzN-F4**), all of which are known characteristics of excimer emission.[77, 250] The presence of these features in the blends is suggestive of a highly crystalline acceptor morphology that is retained even in the presence of **PBDB-T-2F**, which is consistent with GIWAXS measurements of blend films.

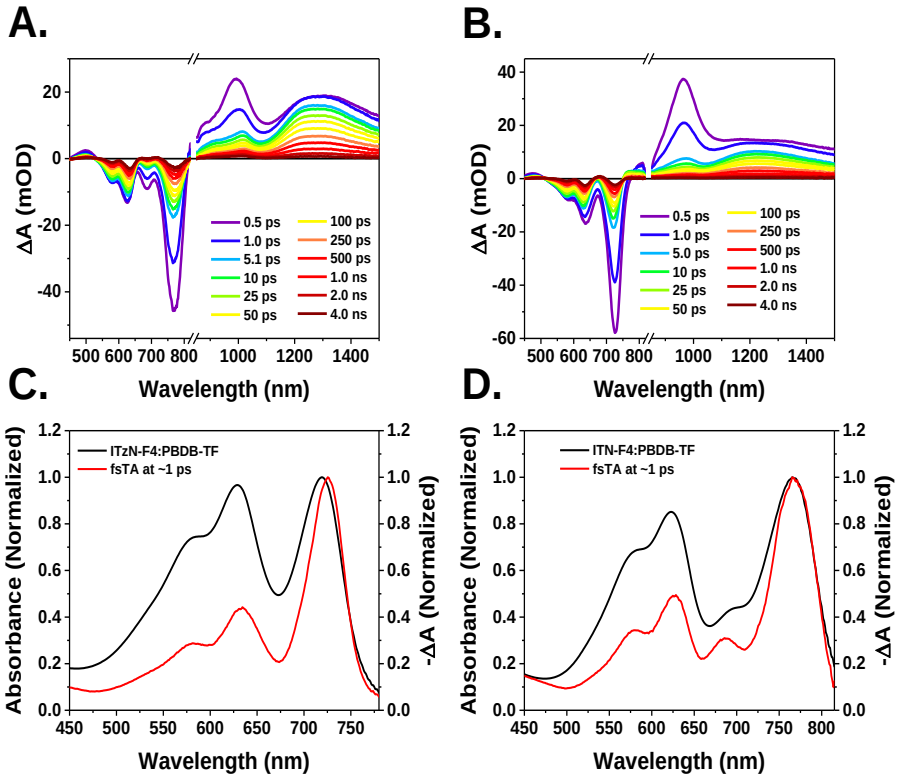

Figure 5.2. Time-resolved spectra at selected time points of A. **ITN-F4**:**PBDB-T-2F** and B. **ITzN-F4**:**PBDB-T-2F**. Single wavelength fitting of the kinetics of C. neat **ITzN-F4** versus the blend at 970 nm and D. neat **ITN-F4** versus the blend at 990 nm. A and B, the signal at 580 nm was chosen to determine the degree of hole transfer as it contains minimal absorption signals from **ITN-F4** and **ITzN-F4**, and at ~1 ps singlet-singlet annihilation is no longer contributing to changes in the absorption of the fsTA spectra.

Excimer states have been observed in other NFAs[67, 77, 128] and are known to act as low-energy trap states that inhibit charge separation of the bound electron-hole pair at the interface and contribute to reduced charge mobilities and PCEs.[23, 24, 61, 251, 252]. Comparing the normalized steady-state absorption of the blends to the transient spectra at ~1 ps at 580 nm demonstrates a significant (~40% and ~50%) yield of free carriers from ultrafast hole transfer in **ITzN-F4** and **ITN-F4**, respectively (**Figure 5.2C**, **D**). Monitoring the kinetics of ^{1*}A reveals that ~80% of ^{1*}A decays within ~500 fs in both the blends and neat acceptors (**Figure 5.12**). Note this also includes the loss of signal due to singlet-singlet annihilation. It is likely that the excimer species formed in these blends represents the portion of ^{1*}A that is unable to participate in charge separation and merely

behaves as a lower energy relaxation pathway of ^{1*}A, likely originating from isolated crystalline domains. The presence of donor and acceptor GSB at long times suggests the presence of long-lived charge carriers[249] (**Figures 5.5** and **5.7**), further evidence that blends of **ITN-F4** and **ITzN-F4** retain the ability to efficiently generate charges despite the presence of excimer states. The ~2 ps and ~60 ps components in the blends are assigned to a combination of diffusion-limited charge separation occurring in domains of **ITN-F4** and **ITzN-F4** near the interface and slow excimer relaxation processes, and in the neat films (~2 ps and ~30 ps) are solely due to excimer relaxation. Multiple decay components are largely a result of different populations arising from disorder in the solid state. The > 1 ns decay component in the blends is assigned to bimolecular recombination of the charge-separated hole and electron. From these data, the extensive π-conjugation and molecular ordering of **ITN-F4** and **ITzN-F4** enable access to an excimer state that accounts for the acceptor excitations that do not participate in charge separation, in contrast to multiexponential decay of ^{1*}A in other fused-ring acceptors. Overall, the high PCEs and electron mobilities of **ITN-F4** and **ITzN-F4** are promoted by ultrafast hole transfer and the ability to generate free carriers despite the formation of an excimer state.

5.3.2. Photoinduced Charge Generation Processes of PBDB-T-2F:Y5 Blend Films

While FREAs of the ADA-type design structure have been optimized to PCES of as high as 14%, other molecular designs have yielded even higher efficiencies. The A-DAD-A-type molecular structure **Y6** developed by Yuan *et al*. demonstrated an initial PCE of 15.7%, outperforming **ITIC** and its derivatives.[240] A number of initial studies found that thermal annealing had pronounced effects on the performance of solar cells based on **Y6**.[242, 253, 254] Owing to the more recent development of FREAs of this type, the charge transfer dynamics of these molecules are

less well-understood. Thus, femtosecond/nanosecond transient absorption (fs/ns TA) spectroscopies were employed to examine photoinduced charge generation processes in these materials. The excited state dynamics of **Y6** were first examined in solution. Time-resolved spectral analysis of **Y6** in toluene excited at 670 nm is reported (**Figure 5.17**). The excited-state dynamics of this molecule are similar to those of the aforementioned ADA-type molecules, with several decay components that likely result from the electronic push-pull character of the chromophore. The overall excited state lifetime is somewhat longer in **Y6** than in ITIC and the derivatives explored above, persisting for ~500 ps compared to 100-200 ps in the ADA case. There is also an additional decay component that persists past the ~7 ns time window of the experiment, which may be some small contribution from an intersystem crossing event to the lowest triplet excited state. The yield of this process is typically low in organic molecules, which appears to hold in this case given the low absorptive intensity of this feature.

Next, the thermal annealing effects on charge photogeneration and recombination dynamics in **PBDB-T-2F:Y6** films were investigated. Excitation of **Y6** at λ = 740 nm permits selective monitoring of charge dynamics by hole transfer (**Figure 5.3A** and **5.3B**).[192] Each **PBDB-T-2F:Y6** film was globally fit at selected wavelengths to a higher order kinetic model consisting of multiple first-order decays, a singlet-singlet annihilation (SSA) component, and a bimolecular mechanism that accounts for recombination of unbound electrons and holes (**Figures 5.14** and **5.15**). The appearance of ground-state bleach (GSB) features of **PBDB-T-2F** at 630 nm in both the as cast and annealed **PBDB-T-2F:Y6** films within the instrument response function (w < 300 fs) is indicative of ultrafast hole transfer, a known occurrence in high-efficiency BHJs.[28, 40]

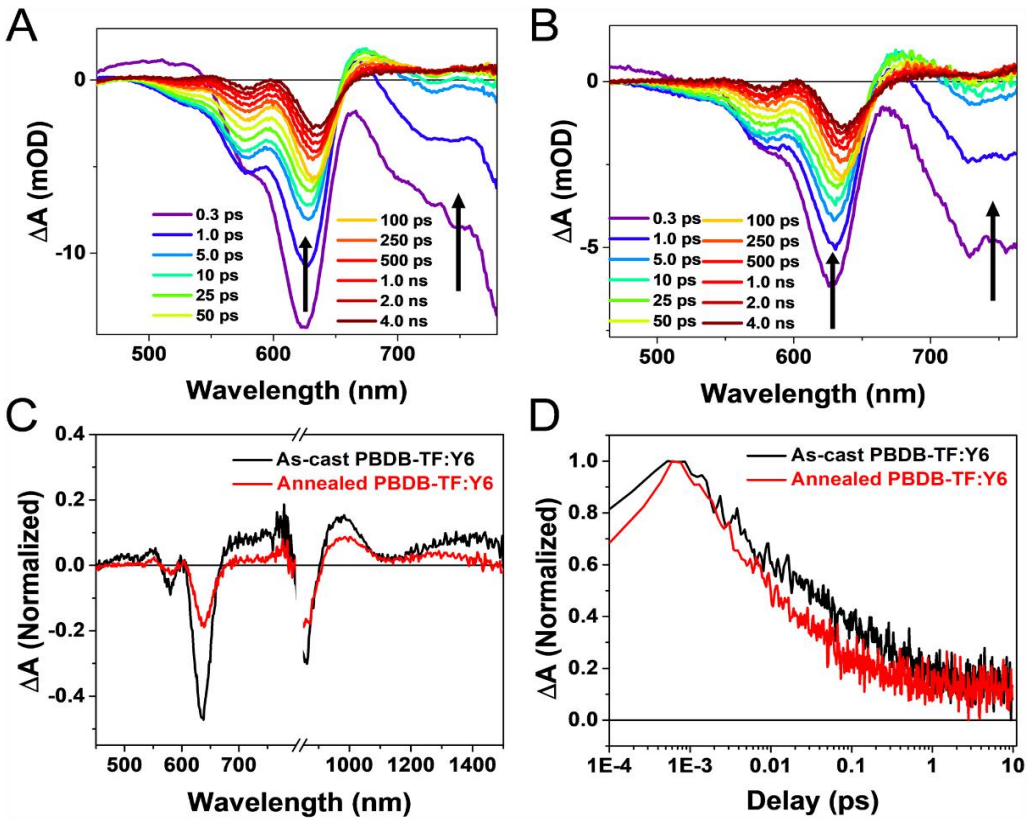

Figure 5.3. Selected time points of the fsTA spectrum (λ_{ex} = 740 nm) of (A) the as cast **PBDB-T-2F**:**Y5** BHJ and (B) the annealed **PBDB-T-2F**:**Y5** BHJ zoomed into the visible region demonstrating ultrafast hole transfer. (C) Transient absorption spectra at 6 ns for blends excited at 740 nm in fsTA experiments, normalized to the **Y5** bleach at 865 nm immediately after excitation. (D) FC decay dynamics monitored at the polymer GSB (630 nm) in the nsTA experiments.

In these blends, the bleach features maximize with the instrument response function and therefore, only the decay of the polymer GSB is observed (**Figure 5.3A, B**). Unexpectedly, the fits for the annealed **PBDB-T-2F:Y6** film (**Figure 5.15**) indicates that the kinetics are accelerated when compared to the as cast **PBDB-T-2F:Y5** film (**Figure 5.14**). Importantly, annealed **PBDB-T-2F:Y6** undergoes BR more rapidly (k_{BR} = 1.7 ± 0.1 ×10^{10} ΔA^{-1} s^{-1}) than does as cast **PBDB-T-2F:Y6** (k_{BR} = 5.2 ± 0.4 × 10^{8} ΔA^{-1} s^{-1}). Normalized spectra at long times (~ 6 ns) suggest the as cast **PBDB-T-2F:Y5** produces a larger quantity of FCs (**Figure 5.3C**), contrary to expectations based on PCEs. Additionally, though both blend films display long-lived **PBDB-T-2F** and **Y6** GSB features that suggest persistence of FCs, FC recombination monitored at these features in the

nsTA experiment occurs more rapidly in annealed **PBDB-T-2F**:**Y6** by an order of magnitude (**Figures 5.18** and **5.19**), consistent with the observations from the fsTA data. As a result, as cast **PBDB-T-2F**:**Y6** produces an overall higher yield of FCs at times > 1 μs (**Figure 5.3D**). The differences in the charge carrier dynamics of the **PBDB-T-2F**:**Y6** films are better understood in conjunction with the BHJ morphological observations from the AFM, XPS, and NEXAFS measurements. More extensive individual component mixing in the annealed **PBDB-T-2F**:**Y6** film implies an increase in interfacial contact points between the donor **PBDB-T-2F** domains and acceptor **Y6** domains, which increases the possibility for FCs to recombine.

Thus, the accelerated FC recombination and lower overall yield in the annealed **PBDB-T-2F**:**Y5** film is likely due to (1) the altered vertical phase segregation and increased **PBDB-T-2F**:**Y6** contact interface, and (2) the significantly enhanced μ_h (> 10^{-3} cm^2 V^{-1} s^{-1}), both of which allow the photogenerated FCs move easily and encounter more interface to suffer faster and more BR. Note the TA experiments are conducted in the absence of an external electrical bias, which is known to impact the FC dynamics as well. These observations are similar to those recorded for other high-performance BHJs, in which slower/less FC recombination, longer FC lifetime, and higher FC yield was observed in the blends demonstrating clear donor/acceptor phase segregation.[223, 225, 255-257] Overall, these results suggest that the primary factors that determine the increased PCE in annealed **PBDB-T-2F:Y6** are morphological in nature, and the ultrafast photogenerated charge carrier dynamics is not the only factor that decides the final PCE, since other parameters such as photon absorption, charge transport and collection also affect photoconversion in completed devices.[258-260] Ultimately, the insights derived from time-resolved

absorption spectroscopy are not decisive in isolating the differences in **PBDB-T-2F:Y6** solar cell performance and other related electronic measurements are needed.

5.3.3. Excited-State Dynamics of Fluorinated and π-Extended Y6 Derivatives

Following the establishment of **Y6** as the premier FREA material, many studies have sought to synthetically tune the molecular structure in hopes of improving PCE. The success of fluorination and π-extension in ADA-type FREAs made them ideal strategies for optimizing the molecular structure of **Y6**. As part of a comprehensive study on the effects of these molecular modifications, transient absorption spectroscopy (fsTA) and nanosecond transient absorption spectroscopy (nsTA) were utilized to investigate charge photogeneration and recombination to further understand differences in device performance in systematically π-extended and fluorinated A-DAD-A acceptor materials. The excited-state dynamics of **Y5 Y6**, **BT-LIC**, **BT-L4F**, and **BT-BT-L4F** were characterized in toluene solution (**Figures 5.30-5.34**). All five compounds exhibit similar photophysical behavior, undergoing three successive first-order decays followed by relaxation to a fourth species that lives past the time window of the experiment (7 ns). Both fluorination and π-extension appear to individually extend the excited state lifetime. The non-fluorinated **Y5** decays in 279 ± 0.8 ps while **Y6** decays in 475 ± 1.6 ps and the non-fluorinated π-extended **BT-LIC** decays in 419 ± 1.4 ps. The incpororation of both strategies extends the lifetime even further, as **BT-L4F** and **BT-BO-L4F** decay in 616 ± 3.3 ps and, 600 ± 4.0 ps, respectively. Spin-coated films of the BHJ blends were selectively photoexcited at 760 nm, minimizing electron transfer processes due to negligible absorption of the polymer donor materials, and thus permitting kinetic analysis exclusively involving hole transfer. A global analysis was applied to each dataset according to a sequential kinetic model accounting for singlet-singlet-annihilation and bimolecular

recombination (BR) of free carriers (FCs) as described in the Supplementary Information. While fluorination does not appear to significantly impact the transient dynamics in the neat films, π-extension produces significant spectra differences. The time-resolved spectra of neat films of **BT-L4F** and **BT-BO-L4F** have a particularly pronounced absorptive feature beginning at 1200 nm and extending past the spectra window of the experiment. This is likely attributable to an excimer relation process as was previously observed for **ITN-F4** and **ITzN-F4** previously (**Figures 5.25** and **5.28**). However, in the blend films, this feature is of much weaker intensity relative to the pure excited-state peak at 980 nm, unlike in **ITzN-F4** and **ITN-F4**. This implies that the presence of the donor polymer, whether through competing charge generation or morphological changes, inhibits the formation of this lower energy state. This may partially account for the observed PCEs exceeding 16% compared to **ITN-F4** and **ITzN-F4** that have maximum PCEs of about 10%. Further examination of the blend films reveals ultrafast hole transfer from the acceptor material to the donor polymer within 300 fs (the instrument limit) for each blend (**Figures 5.14, 5.20-5.29**) following the established trend in many recently reported high-efficiency OSC materials,[31] and reaffirming the ability of BHJ blends incorporating A-DAD-A type NFAs to efficiently generate bound excitons following light absorption (**Figure 5.4**).

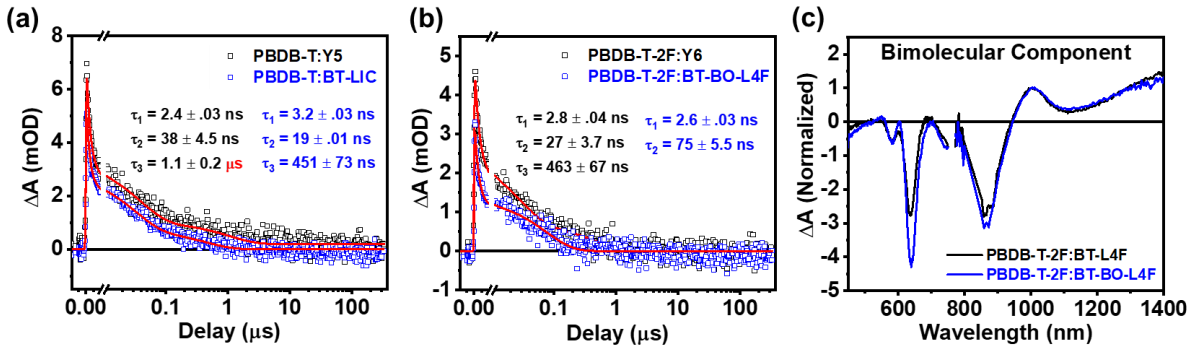

Figure 5.4. FC decay dynamics and single wavelength fits monitored at the polymer GSB (630 nm) in the nsTA experiments for (a). **PBDB-T**:**Y5** and **PBDB-T**:**BT-LIC** and (b). **PBDB-T-2F**:**Y5** and **PBDB-T-2F**:**BT-BO-L4F**. Data are inverted for clarity. (c). Bimolecular component from the evolution-associated spectra of the fsTA of **PBDB-T-2F**:**BT-L4F** and **PBDB-T-2F**:**BT-BO-L4F**.

Power dependence studies confirm that ultrafast hole transfer occurs to some degree independent of the laser fluence (**Figure 5.35**). At a low laser fluence, the kinetics at the polymer GSB (630 nm) experience a slower growth, with the GSB maximizing between 10-100 ps (**Figure 5.35**), consistent with other reports of high-performing NFAs.[261, 262] Slower hole transfer dynamics are apparent in **Y5** when compared to the newly synthesized acceptors (**Figure 5.35**), indicating some favorability for hole transfer in these blends, likely owing to the lower hole reorganization energies induced by extended conjugation in the end groups. Furthermore, nsTA experiments demonstrate long-lived bleach features past ~100 ns, indicating the presence of free carriers even at long times (**Figure 5.37**). The polymer ground-state bleach is accompanied by excited state absorption near 980 nm that is likely associated with the acceptor anion, which indicates the presence of free carriers (**Figures 5.14**, **5.23**, **5.25**, **5.27**, **5.29**). Recombination of the free carriers is reflected in the polymer GSB in nsTA experiments, in which the decay of the polymer GSB is complete by ~70 ns in blends of **BT-BO-L4F**, while there is a third, slow decay component of ~400 ns for **PBDB-T-2F:Y6** blends (**Figure 5.4B**).

Impedance photocurrent device analysis performed on **Y6** cells vs. **BT-BO-L4F** cells indicates that the superior performance of **BT-BO-L4F** is the result of improved μ_{eff} despite an apparent larger k_{BR} based on the scaling of the θ parameter. These results are consistent with those on previously studied **Y6** cells in which higher FF and PCE result from increases in μ_{eff} although fsTA experiments indicate an increase in BR (we note that the measured BR rate is at open circuit conditions).[8] The difference in performance between **BT-L4F** and **BT-BO-L4F** can be attributed to **BT-BO-L4F** maintaining more FCs at long times, as indicated by the polymer GSB (**Figure 5.4C**). This would suggest that while all acceptors can generate FCs with lifetimes sufficiently long enough to be collected as charges, **BT-L4F** and **BT-BO-L4F** experience accelerated recombination times owing to their increased mobilities in these experiments, which under device operating conditions translates into increased charge collection and higher PCE. Similarly, the polymer GSB is ~90% depleted by 30-40 ns in both **PBDB-T**-centric blends, though **PBDB-T:Y5** demonstrates a slower third decay component of 1.1 μs (**Figure 5.4A**). In contrast to the **PBDB-T-2F** donor systems, the measured μ_h and μ_e values are generally similar in the case of **PBDB-T:Y5** versus **PBDB-T:BT-LIC**. Here the differences in measured BR rates are likely attributable to a slight increase in domain size in **PBDB-T**:**Y5** that may diminish charge transport and facilitate trapping of free charge carriers. Thus, the differences in μ_h/μ_e and morphology are consistent with the superior performance of **PBDB-T-2F:BT-BO-L4F** devices and reinforce the synergy of π-extension and fluorination as effective tools for OSC device improvements.

5.4. Conclusions

Here we have examined the photophysics of several FREA molecules and rationalized observed spectral trends in relation to their photovoltaic performance. **ITN-F4** and **ITzN-F4**

demonstrate ultrafast charge generation in the solid state as well as formation of an excimer state in pure acceptor domains, which decays rapidly and does not inhibit the photovoltaic response of these materials. Blends of **PBDB-T-2F:Y6** exhibit increased recombination of free carriers in the transient experiments despite their increased PCE, which reinforce the importance of the increased μ_h and the propagation of free carriers under operating device conditions. Similar behavior is observed for the π-extended and fluorinated molecular series **Y5**, **Y6**, **BT-LIC**, **BT-L4F** and **BT-BO-L4F**, in which increases in the charge mobility μ_{eff} outweigh the bimolecular recombination factor k_{BR} in fabricated devices.

5.5. Supplementary Information

5.5.1. Structure of Polymer Donors.

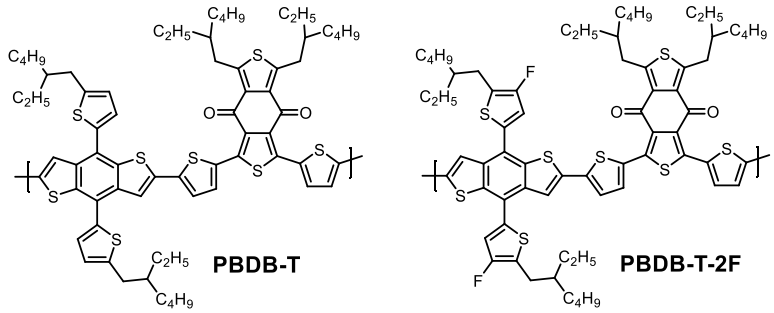

Figure 5.5. Chemical structures of donor polymers used in the blend films.

5.5.2. Global Analysis of ITzN-F4 and ITN F4.

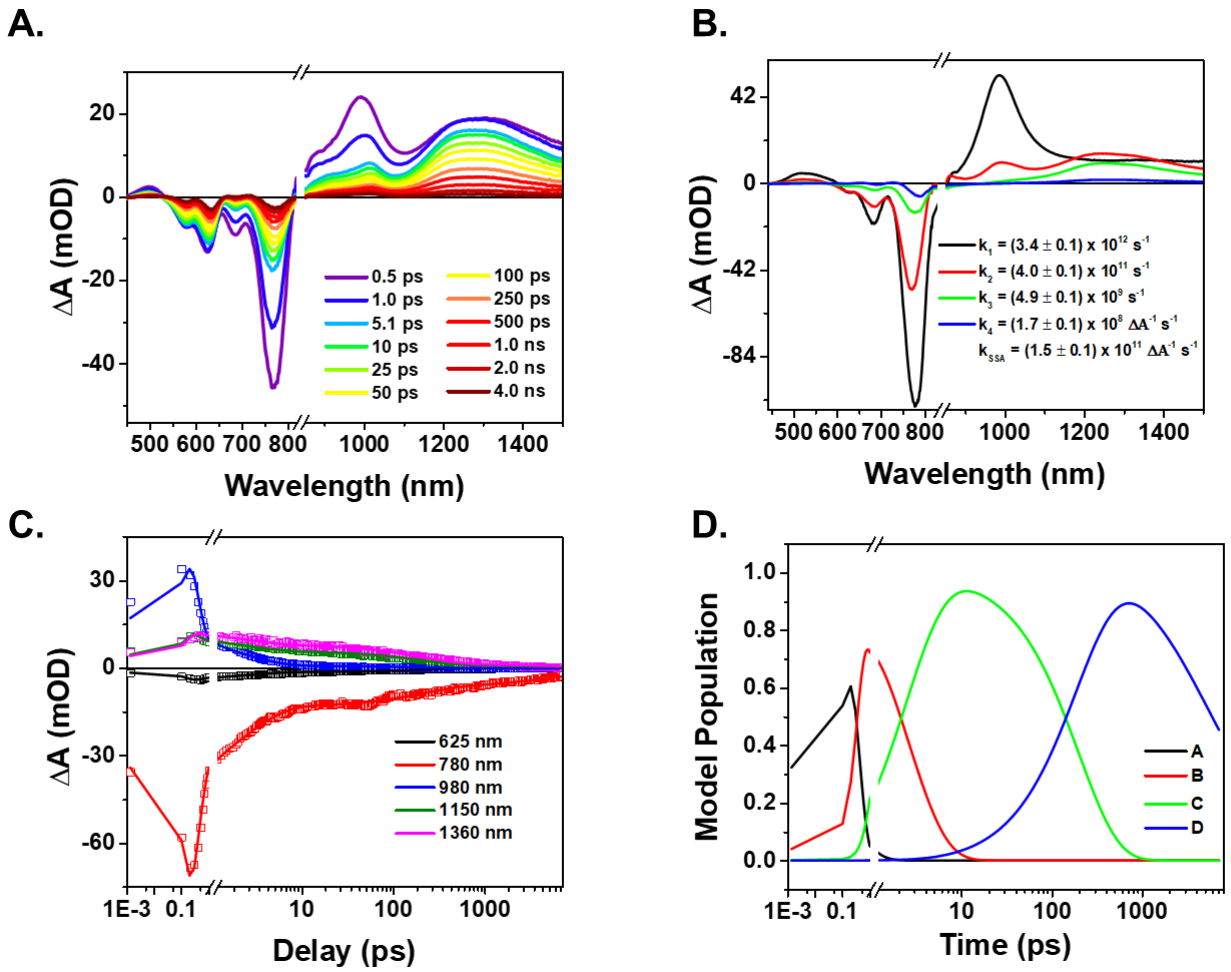

Figure 5.6. Global fits of the **ITN-F4:PBDB-TF** blend excited at 740 nm as described in the text. **A.** Time-resolved spectra at selected time points of **ITN-F4:PBDB-TF**; **B.** Evolution-associated spectra, k_1 is the decay of species A to species B, etc.; **C.** Kinetic fits to the raw data at the indicated wavelengths with the kinetic model described by **Eqn. S4**[236].; **D.** Model population kinetics, distribution of species in time.

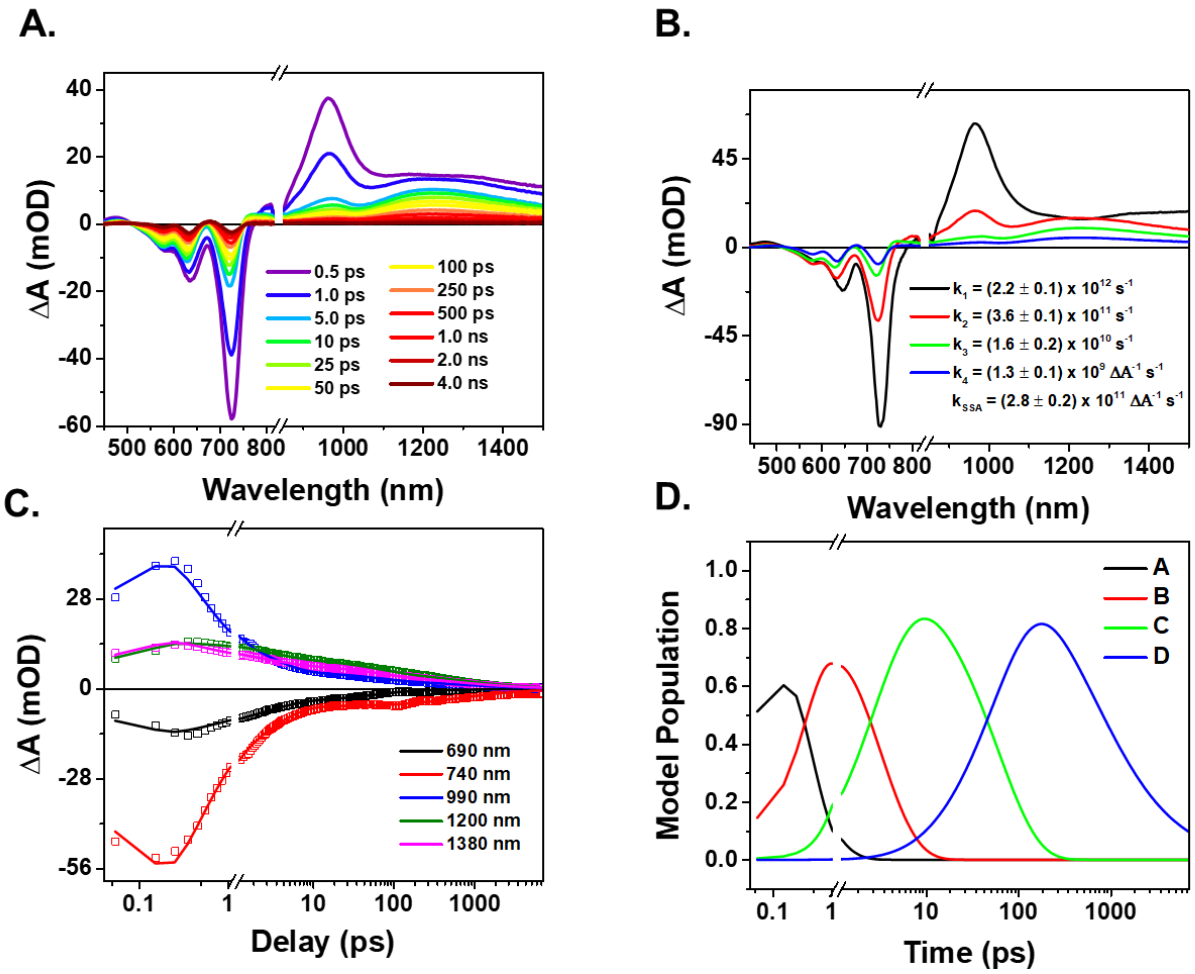

Figure 5.7. Global fits of the **ITzN-F4:PBDB-TF** blend excited at 740 nm as described in the text. **A.** Time-resolved spectra at selected time points of **ITzN-F4:PBDB-TF B.** Evolution-associated spectra, k_1 is the decay of species A to species B, etc.; **C.** Kinetic fits to the raw data at the indicated wavelengths with the kinetic model described by **Eqn. S4**[236]; **D.** Model population kinetics, distribution of species in time.

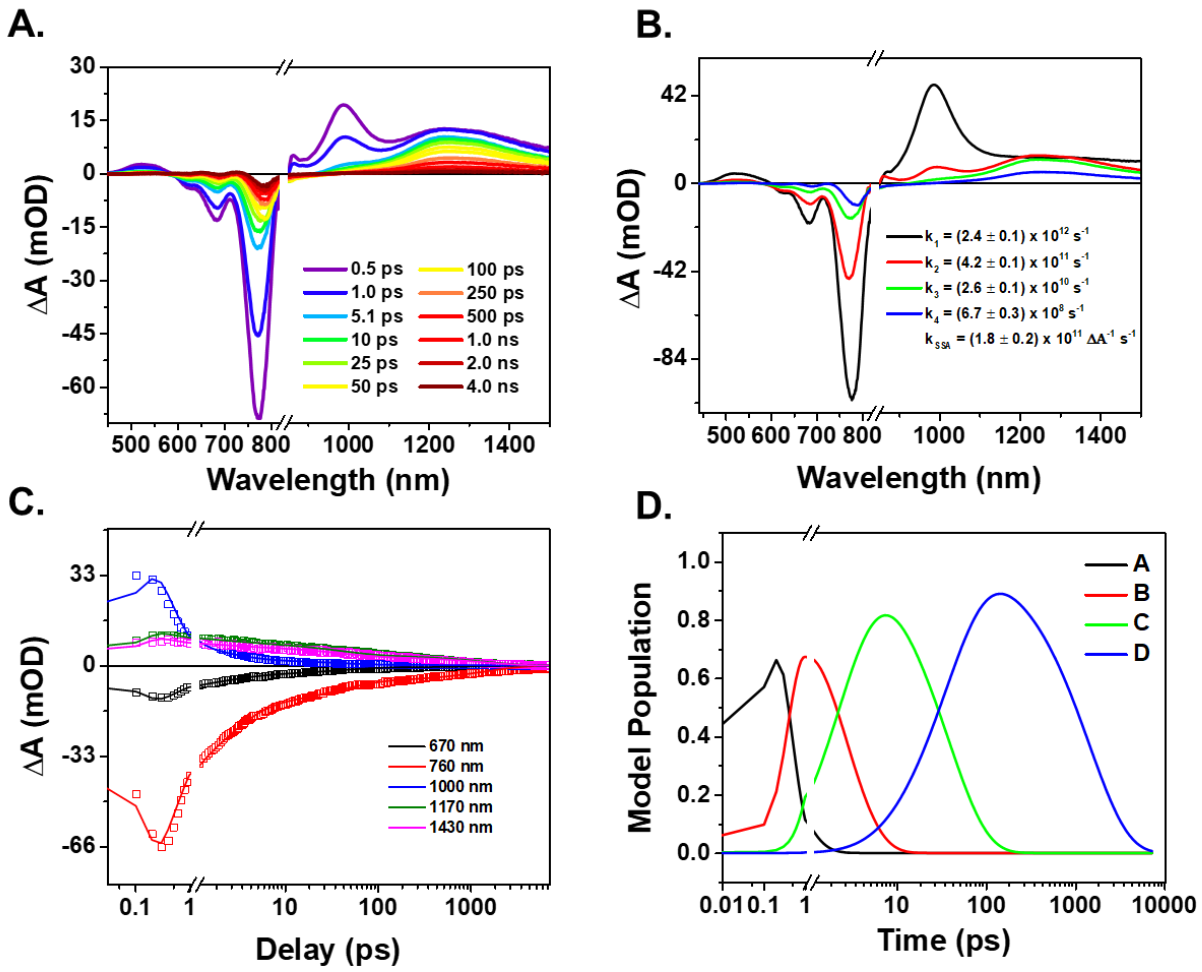

Figure 5.8. Global fits of the **ITN-F4** neat film excited at 740 nm as described in the text. **A.** Time-resolved spectra at selected time points of **ITN-F4; B.** Evolution-associated spectra, k_1 is the decay of species A to species B, etc.; **C.** Kinetic fits to the raw data at the indicated wavelengths with the kinetic model described by **Eqn. S3**[236].; **D.** Model population kinetics, distribution of species in time.

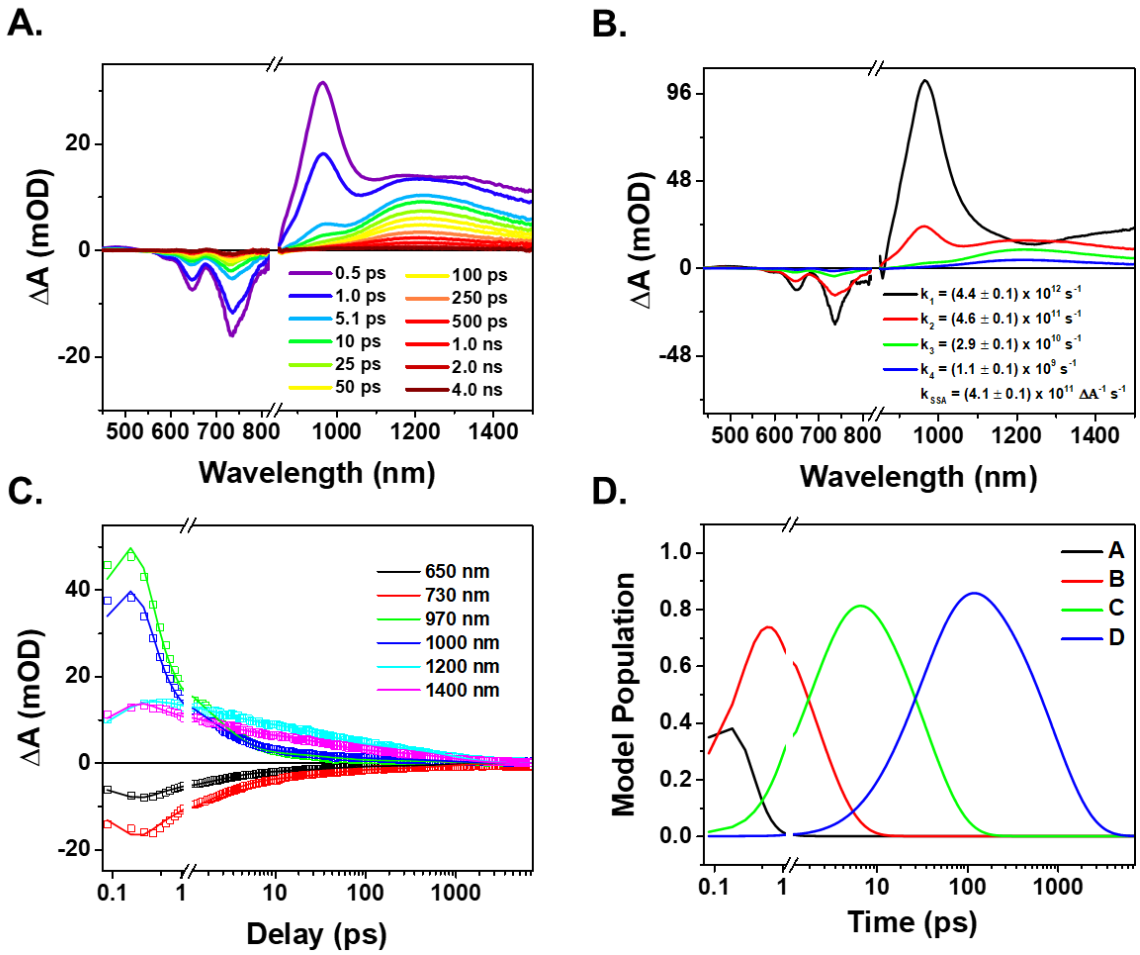

Figure 5.9. Global fits of the **ITzN-F4** neat film excited at 740 nm as described in the text. **A.** Time-resolved spectra at selected time points of **ITzN-F4; B.** Evolution-associated spectra, k_1 is the decay of species A to species B, etc.; **C.** Kinetic fits to the raw data at the indicated wavelengths with the kinetic model described by **Eqn. S3**[236].; **D.** Model population kinetics, distribution of species in time.

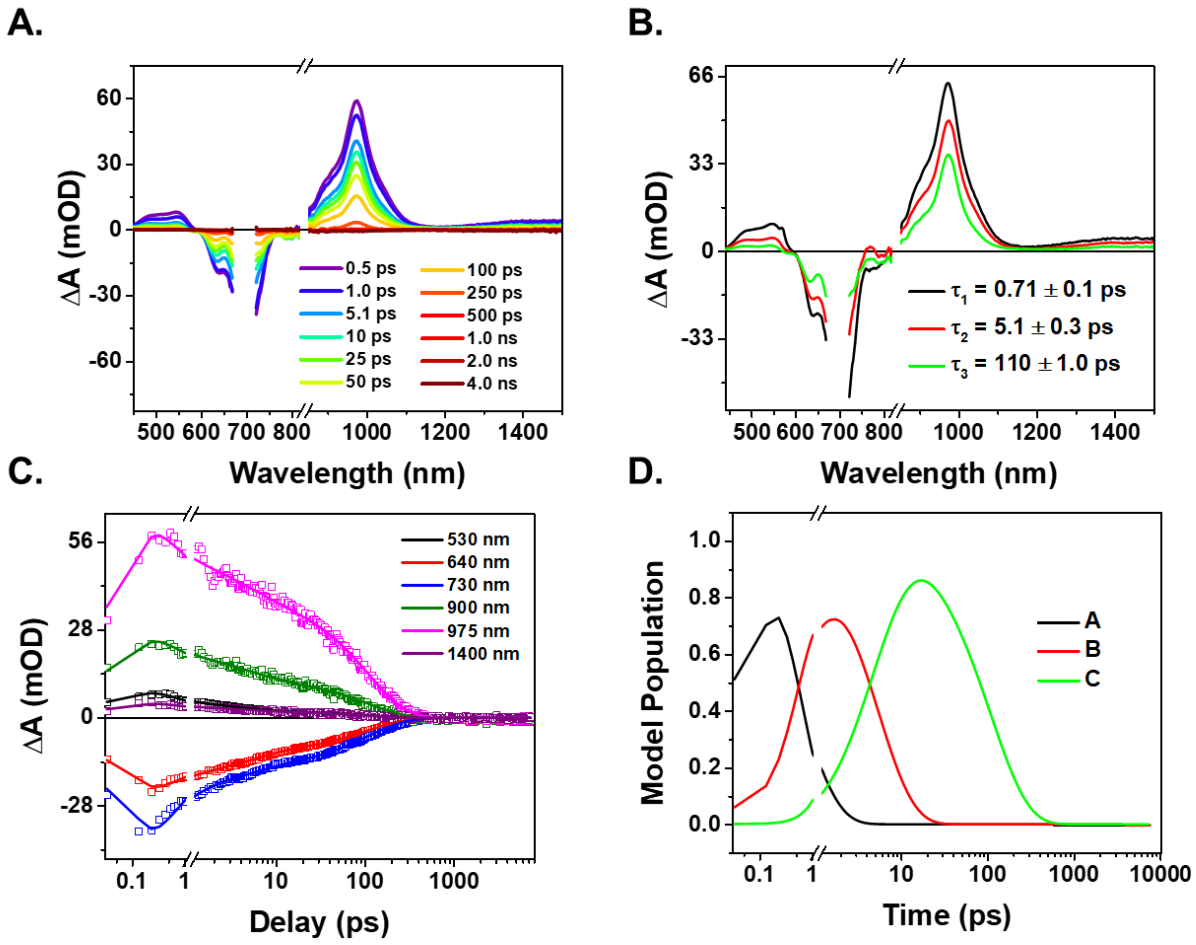

Figure 5.10. Global fits of the **ITN-F4** toluene solution excited at 695 nm. **A.** Time resolved spectrum of solution ITN-F4. Data from 680-720 nm are removed via masking due to pump scatter. **B.** Kinetics fits to the raw data at the indicated wavelengths with the kinetic model as described by **Eqn. S1**[236]. **C.** Evolution-associated spectra with time constants $\tau = 1/k$. **D.** Model population kinetics, distribution of species in time.

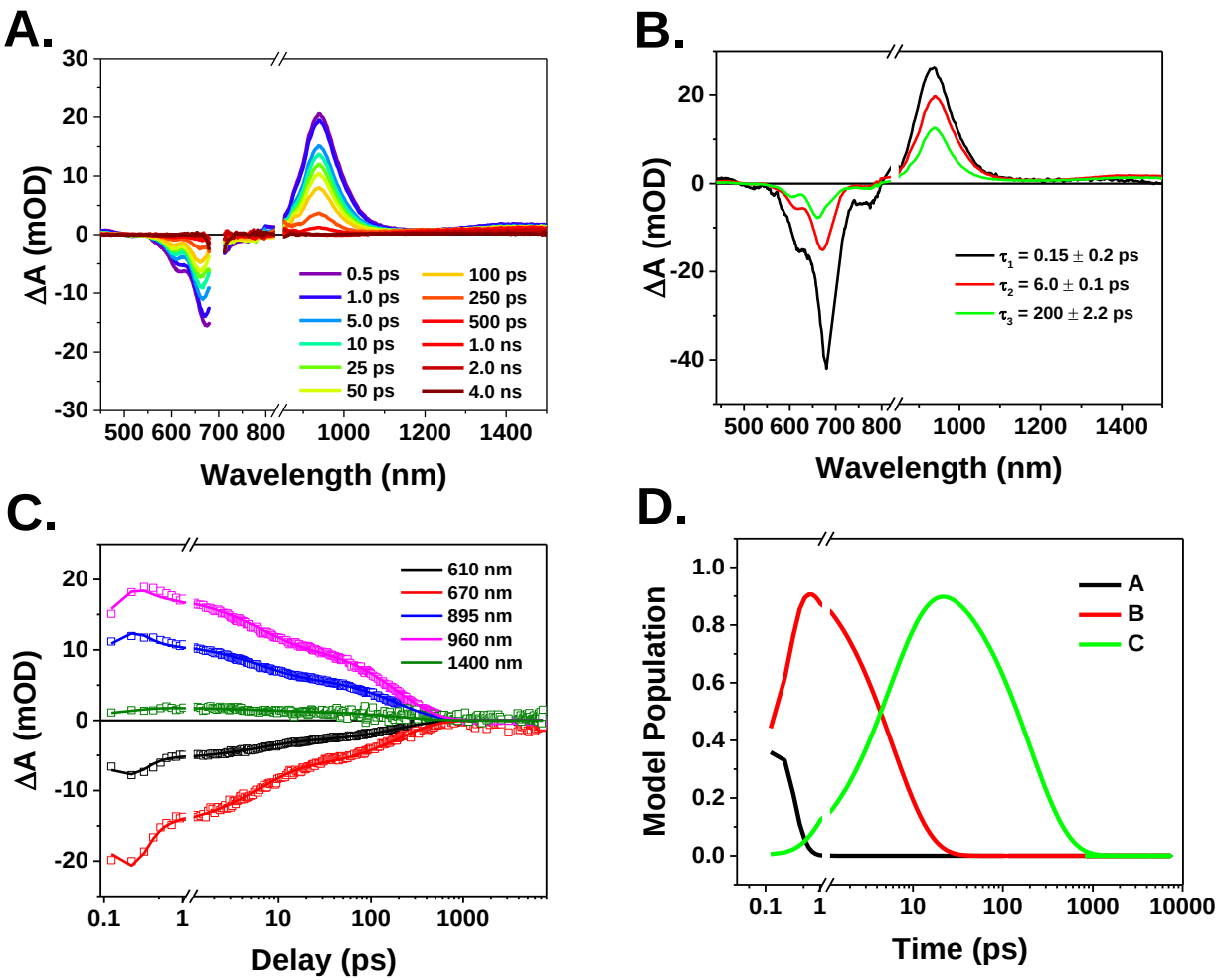

Figure 5.11. Global fits of the **ITzN-F4** toluene solution excited at 695 nm. **A.** Time resolved spectrum of solution ITzN-F4. Data from 680-720 nm are removed via masking due to pump scatter. **B.** Kinetics fits to the raw data at the indicated wavelengths with the kinetic model as described by **Eqn. S1**[236]. **C.** Evolution-associated spectra with time constants $\tau = 1/k$. **D.** Model population kinetics, distribution of species in time.

5.5.4. Single-Wavelength Analysis of ITzN-F4 and ITN-F4.

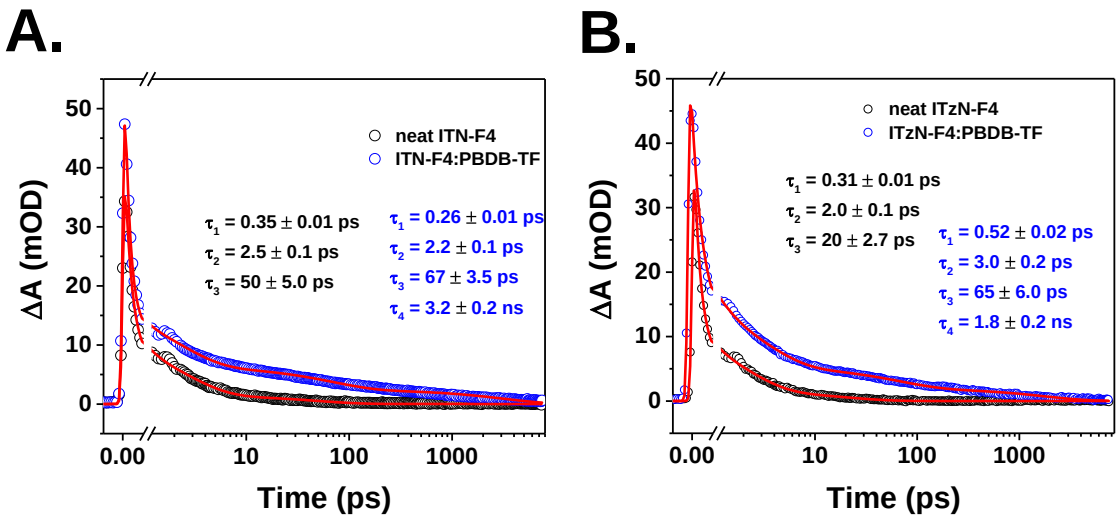

Figure 5.12. Single wavelength fitting of the kinetics of **A.** neat **ITN-F4** versus the blend at 990 nm and **B.** neat **ITzN-F4** versus the blend at 970 nm. **A** and **B**, the signal at 580 nm was chosen to determine the degree of hole transfer as it contains minimal absorption signals from **ITN-F4** and **ITzN-F4**, and at ~1 ps singlet-singlet annihilation is no longer contributing to changes in the absorption of the fsTA spectra.

5.5.5. Emission Spectra of ITzN-F4 and ITN-F4.

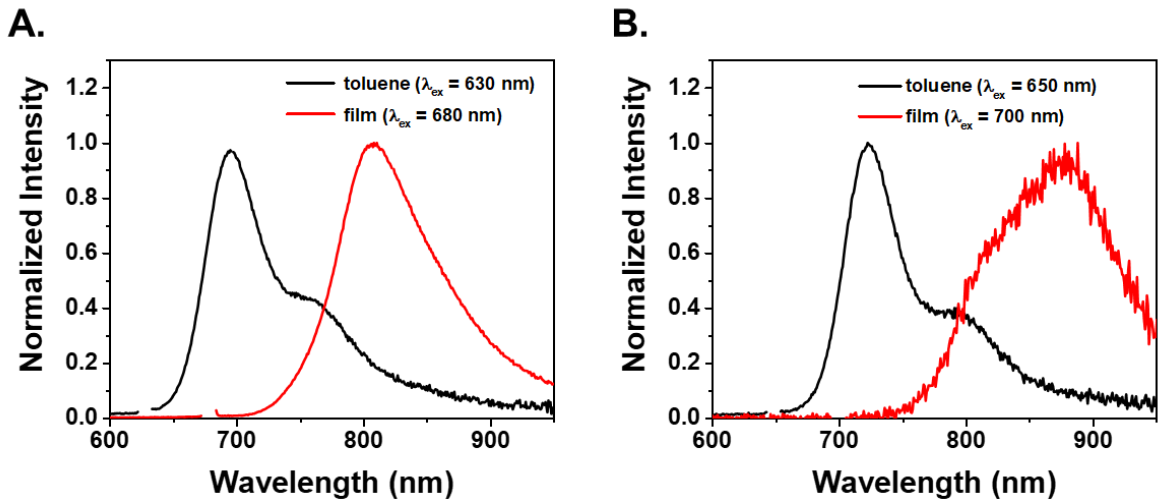

Figure 5.13. Steady-state fluorescence spectra of **A. ITzN-F4**, and **B. ITN-F4**. Scattering from the excitation beam is removed by masking.

5.5.6. Global Analysis of PBDB-T-2F:Y6.

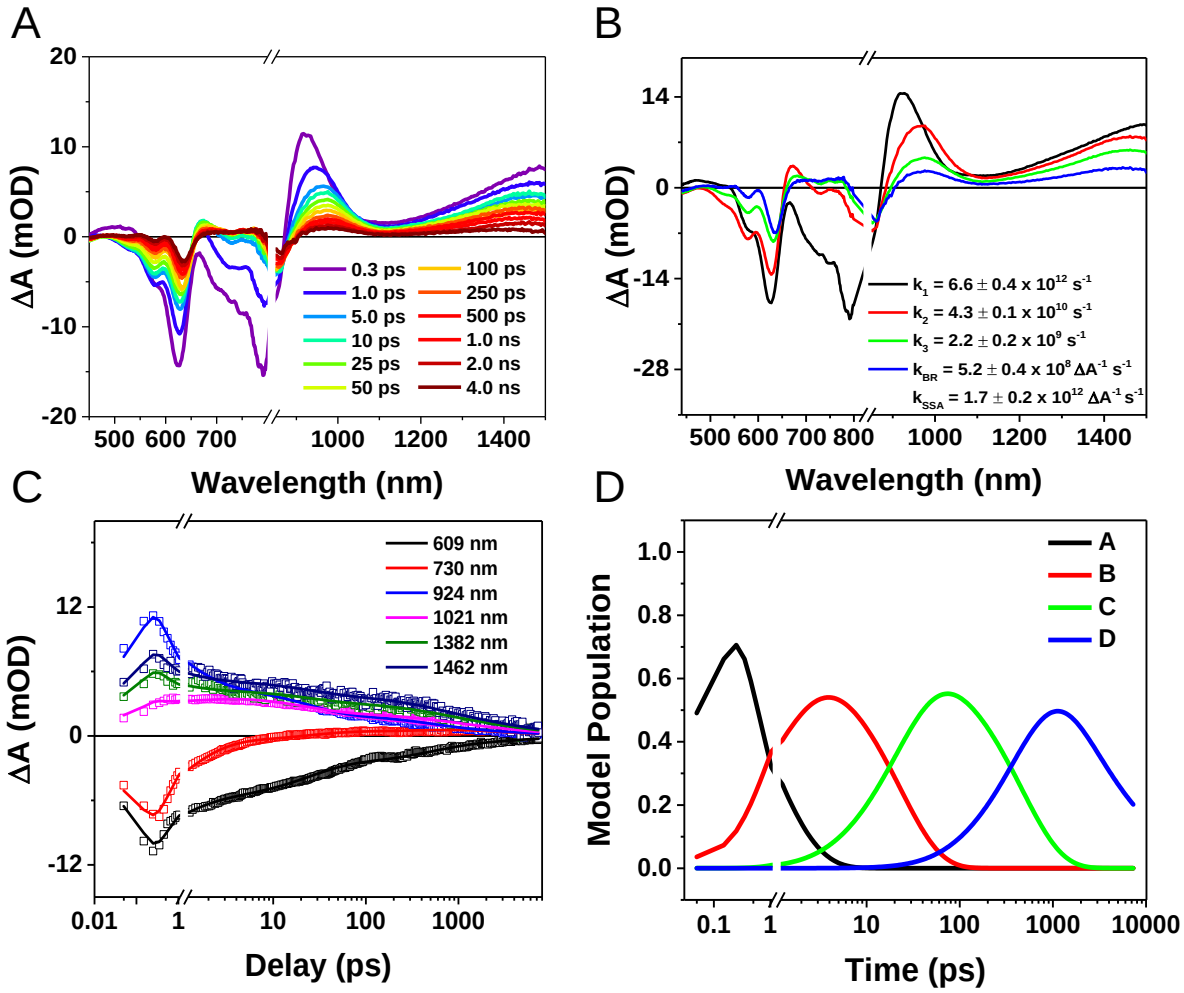

Figure 5.14. Global fits of the as cast **PBDB-T-2F:Y6** film excited at 740 nm as described in the text. (a) Time-resolved spectra at selected time points of as cast **PBDB-T-2F:Y6**, (b) Evolution-associated spectra, k_1 is the decay of species A to species B, etc. (c) Kinetic fits to the raw data at the indicated wavelengths with the kinetic model described by **Eqn. S4**[242]. (d) Model population kinetics, distribution of species in time.

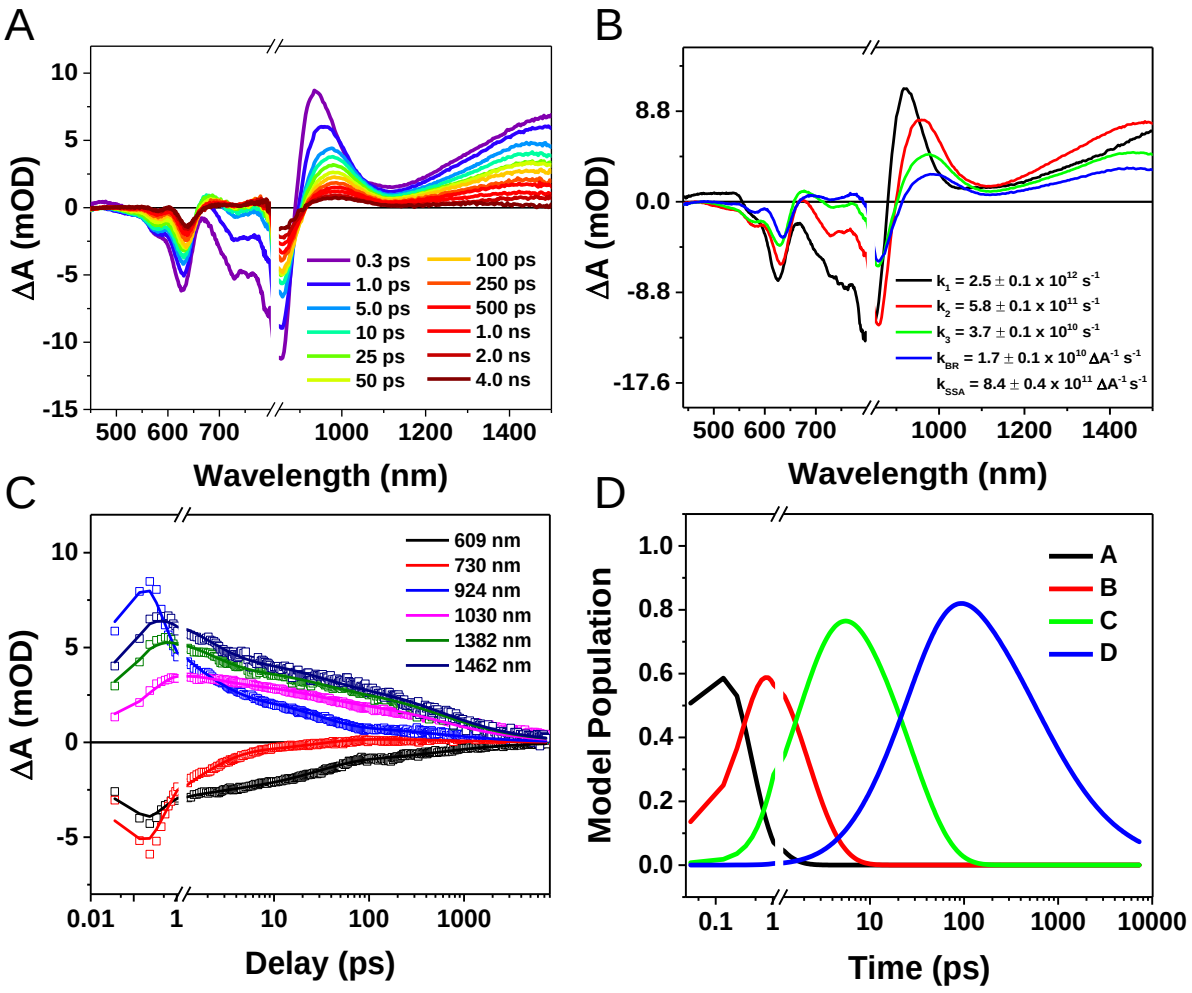

Figure 5.15. Global fits of the annealed **PBDB-T-2F:Y6** film (110 °C for 3 mins) excited at 740 nm as described in the text. (a) Time-resolved spectra at selected time points of annealed **PBDB-T-2F:Y6**, (b) Evolution-associated spectra, k_1 is the decay of species A to species B, etc. (c) Kinetic fits to the raw data at the indicated wavelengths with the kinetic model described by **Eqn. S4**[242]. (d) Model population kinetics, distribution of species in time.

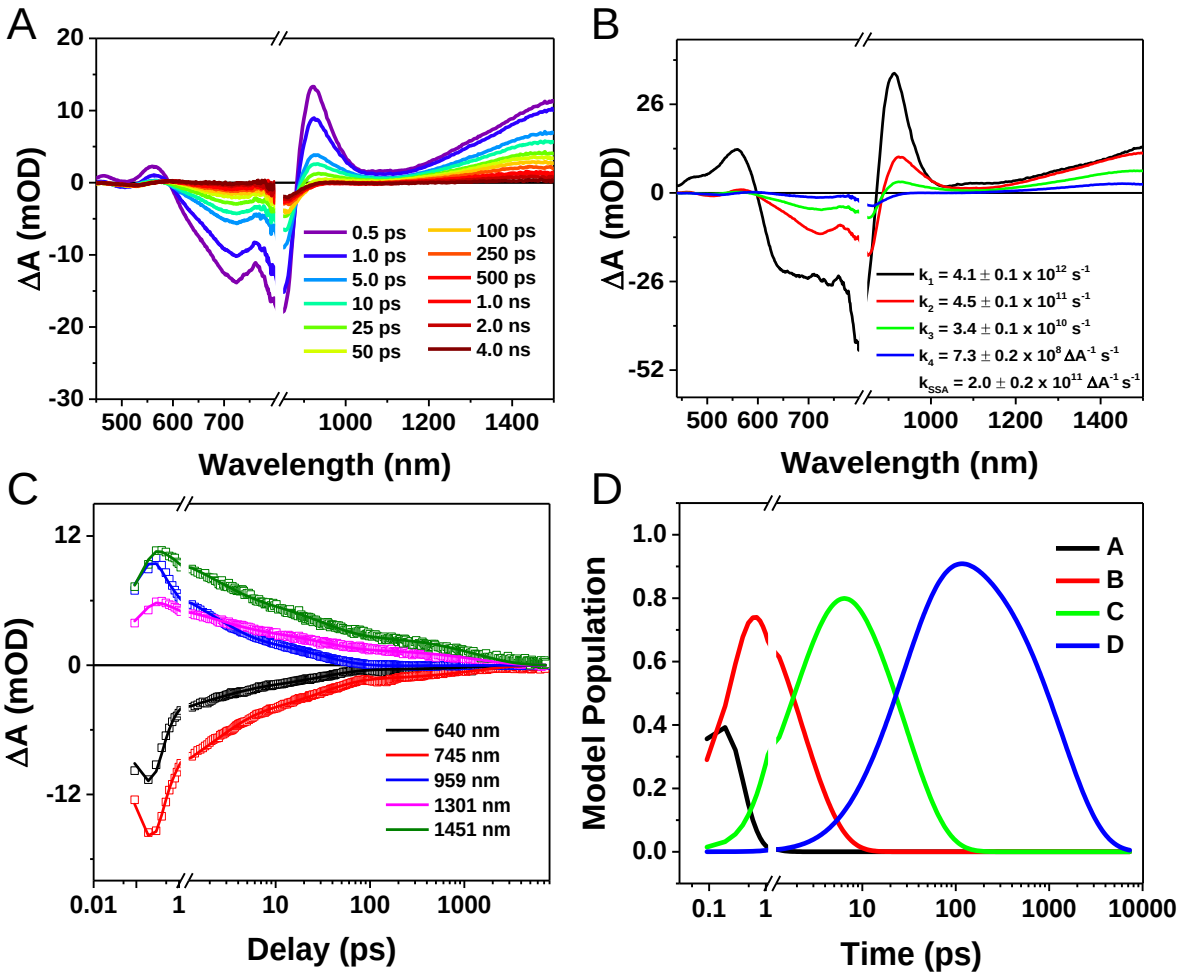

Figure 5.16. Global fits of the neat **Y6** film excited at 740 nm as described in the text. (a) Time-resolved spectra at selected time points of neat **Y6**, (b) Evolution-associated spectra, k_1 is the decay of species A to species B, etc. (c) Kinetic fits to the raw data at the indicated wavelengths with the kinetic model described by **Eqn. S2**[242]. (d) Model population kinetics, distribution of species in time.

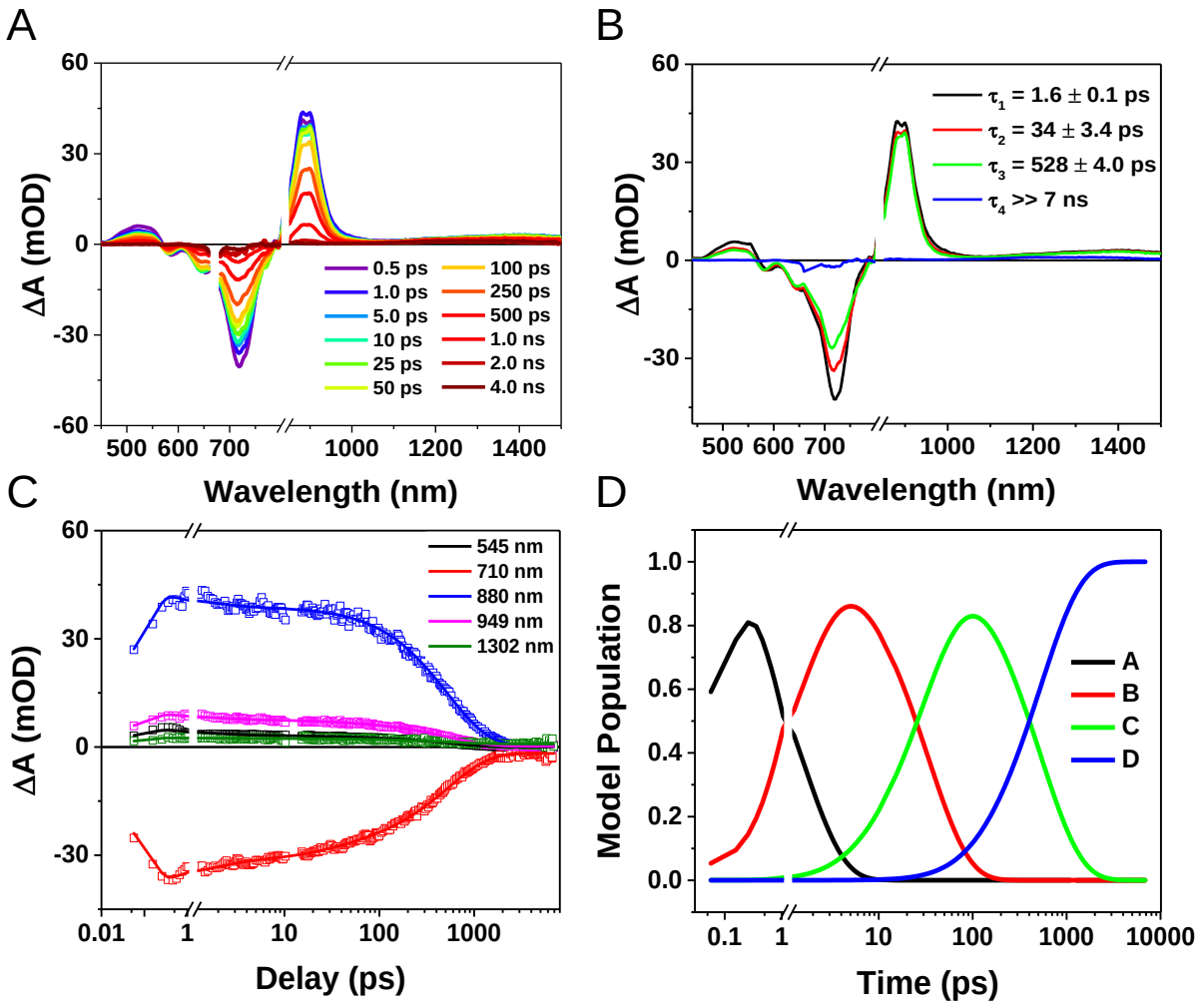

Figure 5.17. fsTA of **Y6** in toluene solution excited at 670 nm at the absorption maxima. (a) Time resolved spectrum of **Y6** in solution. (b) Evolution-associated spectra. (c) Kinetics fits to the raw data at the indicated wavelengths with the kinetic model as described by **Eqn. S1**[242]. $\tau = 1/k$. (d) Model population kinetics, distribution of species in time.

5.5.7. Nanosecond Time-Resolved Spectra of PBDB-T-2F:Y6.

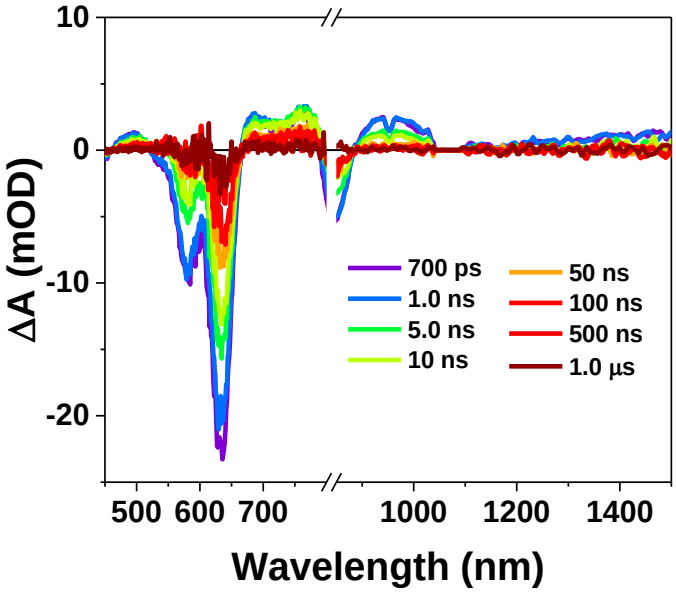

Figure 5.18. nsTA spectrum of as cast **PBDB-T-2F:Y5** film with λ_{ex} = 740 nm at selected time points.

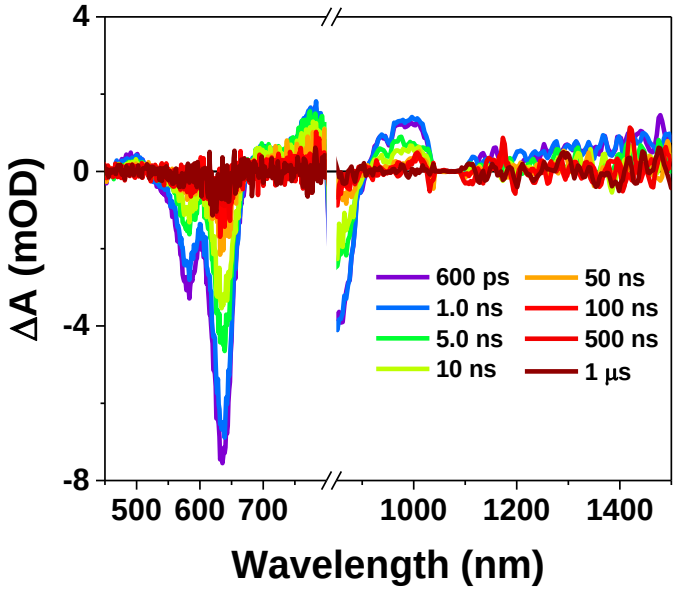

Figure 5.19. nsTA spectrum of annealed **PBDB-T-2F:Y6** film (110 °C for 3 mins) with λ_{ex} = 740 nm at selected time points.

5.5.8. Global Analysis of Fluorinated and π-Extended A-DAD-A FREAs.

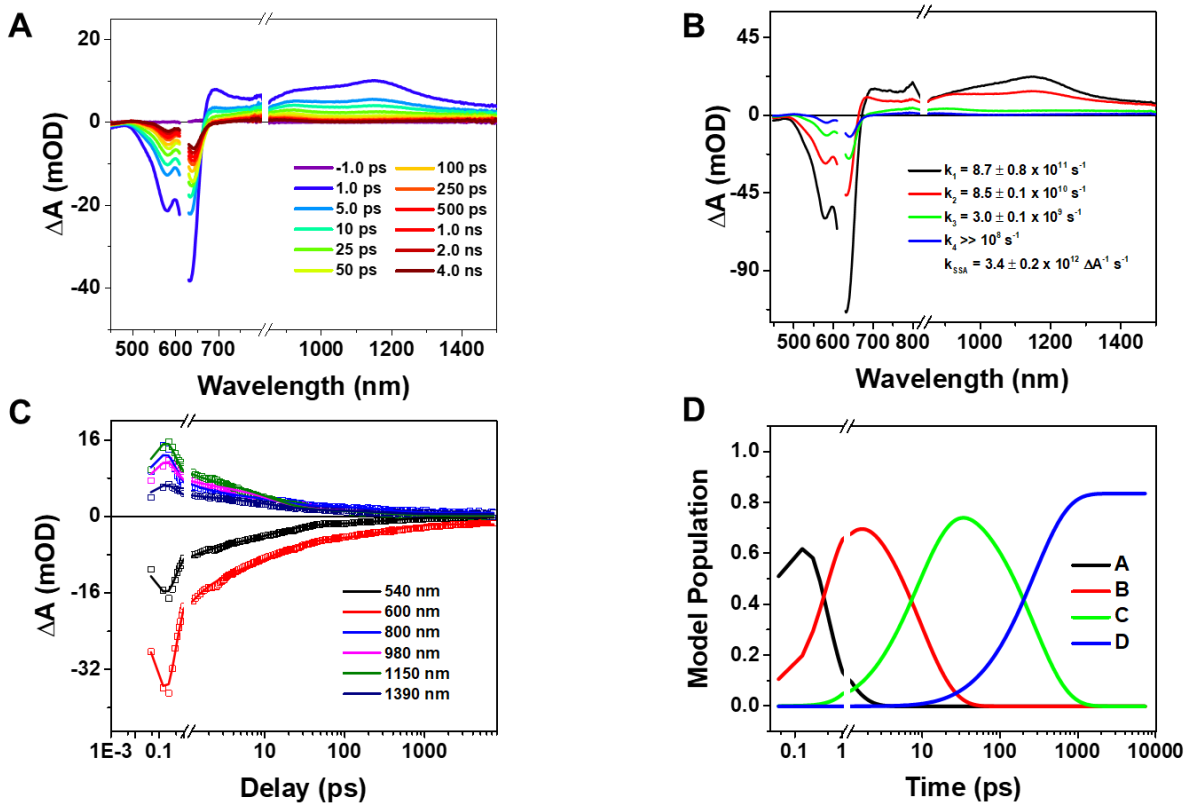

Figure 5.20. Global fits of the neat **PBDB-T** film excited at **520 nm** as described in the text. (a) Time-resolved spectra at selected time points of neat **PBDB-T**, (b) Evolution-associated spectra, k_1 is the decay of species A to species B, etc. (c) Kinetic fits to the raw data at the indicated wavelengths with the kinetic model described by **Eqn. S1**[243]. (d) Model population kinetics, distribution of species in time.

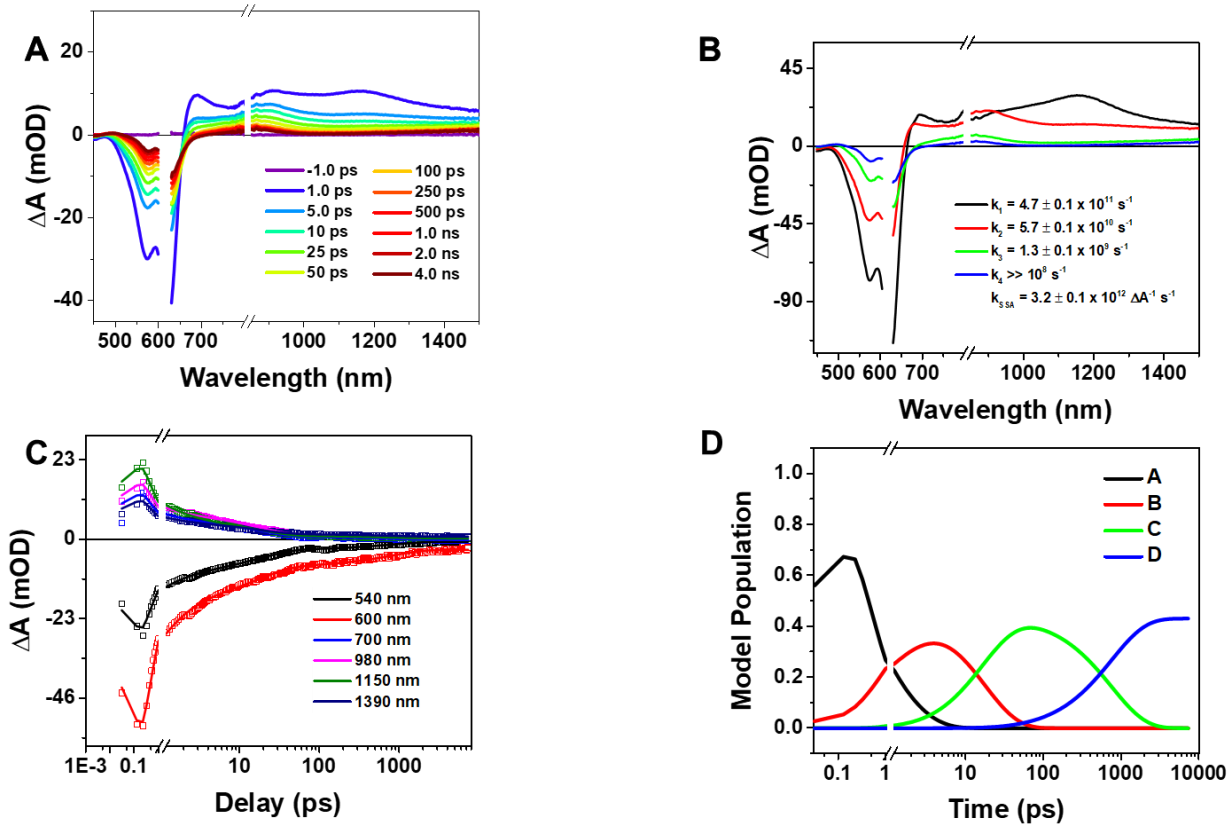

Figure 5.21. Global fits of the neat **PBDB-T-2F** film excited at 620 nm as described in the text. (a) Time-resolved spectra at selected time points of neat **PBDB-T-2F**, (b) Evolution-associated spectra, k_1 is the decay of species A to species B, etc. (c) Kinetic fits to the raw data at the indicated wavelengths with the kinetic model described by **Eqn. S1**[243]**.** (d) Model population kinetics, distribution of species in time.

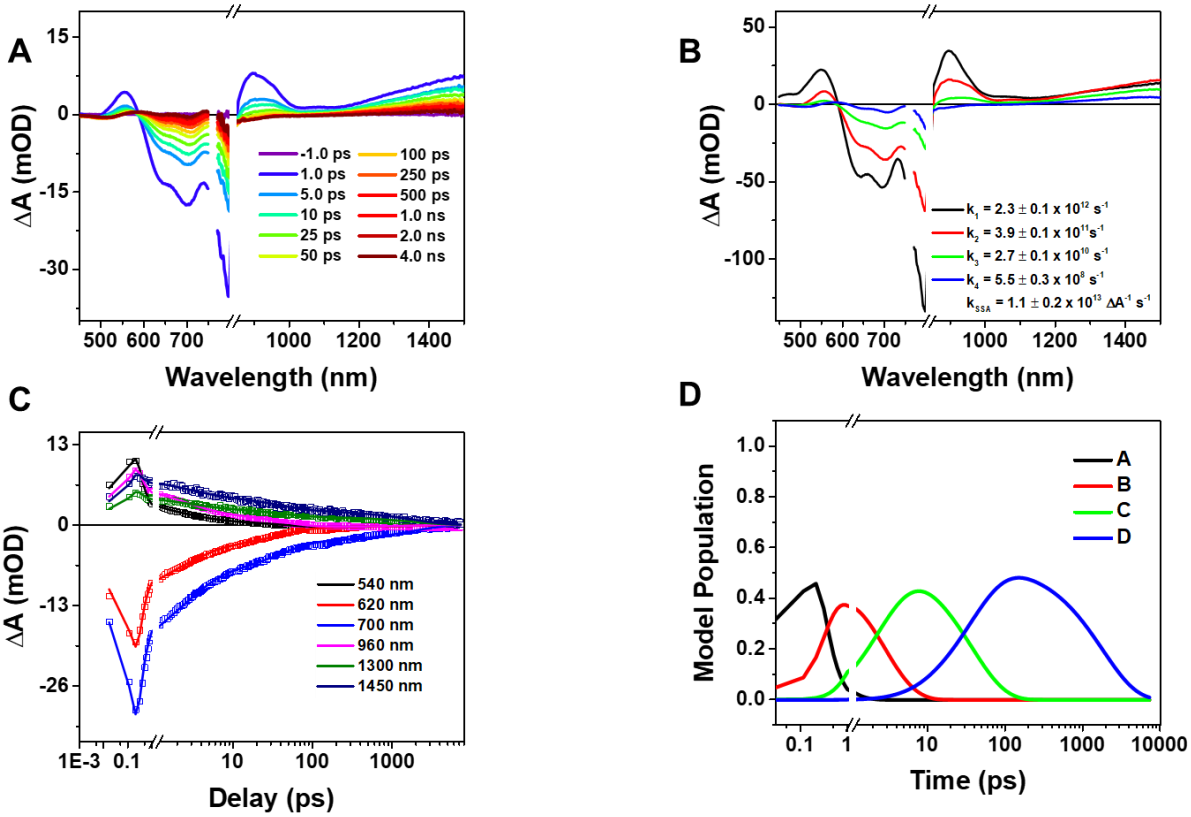

Figure 5.22. Global fits of the neat **Y5** film excited at 760 nm as described in the text. (a) Time-resolved spectra at selected time points of **Y5**, (b) Evolution-associated spectra, k_1 is the decay of species A to species B, etc. (c) Kinetic fits to the raw data at the indicated wavelengths with the kinetic model described by **Eqn. S1**[243]. (d) Model population kinetics, distribution of species in time.

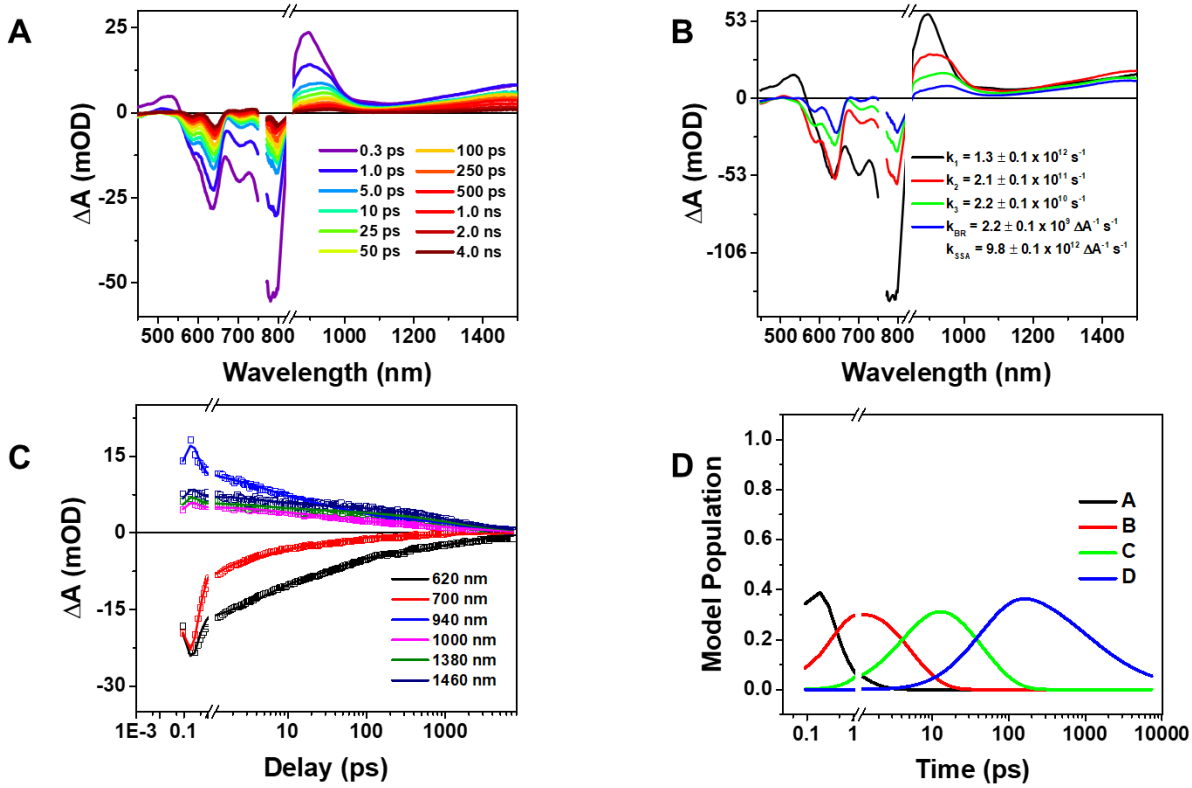

Figure 5.23. Global fits of the **PBDB-T:Y5** blend film excited at 760 nm as described in the text. (a) Time-resolved spectra at selected time points of **PBDB-T:Y5** (b) Evolution-associated spectra, k_1 is the decay of species A to species B, etc. (c) Kinetic fits to the raw data at the indicated wavelengths with the kinetic model described by **Eqn. S1**[243]. (d) Model population kinetics, distribution of species in time.

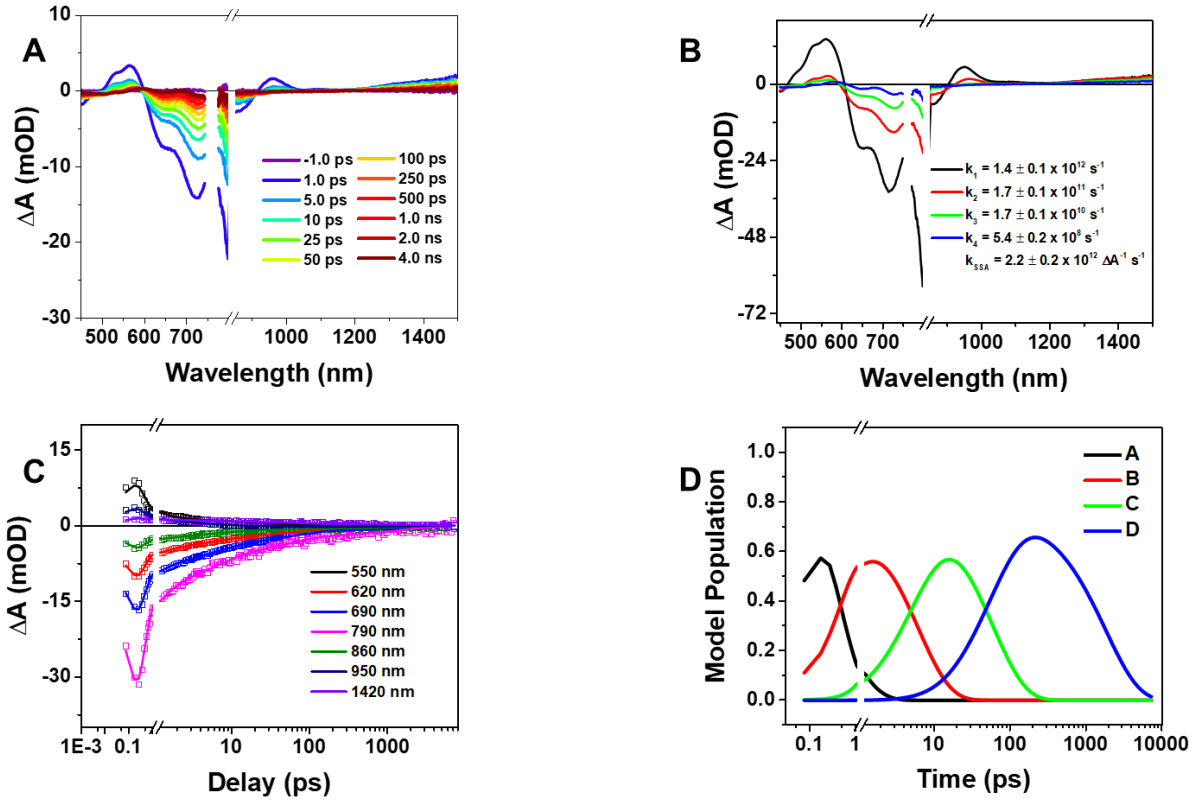

Figure 5.24. Global fits of the neat **BT-LIC** film excited at 760 nm as described in the text. (a) Time-resolved spectra at selected time points of **BT-LIC**, (b) Evolution-associated spectra, k_1 is the decay of species A to species B, etc. (c) Kinetic fits to the raw data at the indicated wavelengths with the kinetic model described by **Eqn. S1**[243]. (d) Model population kinetics, distribution of species in time.

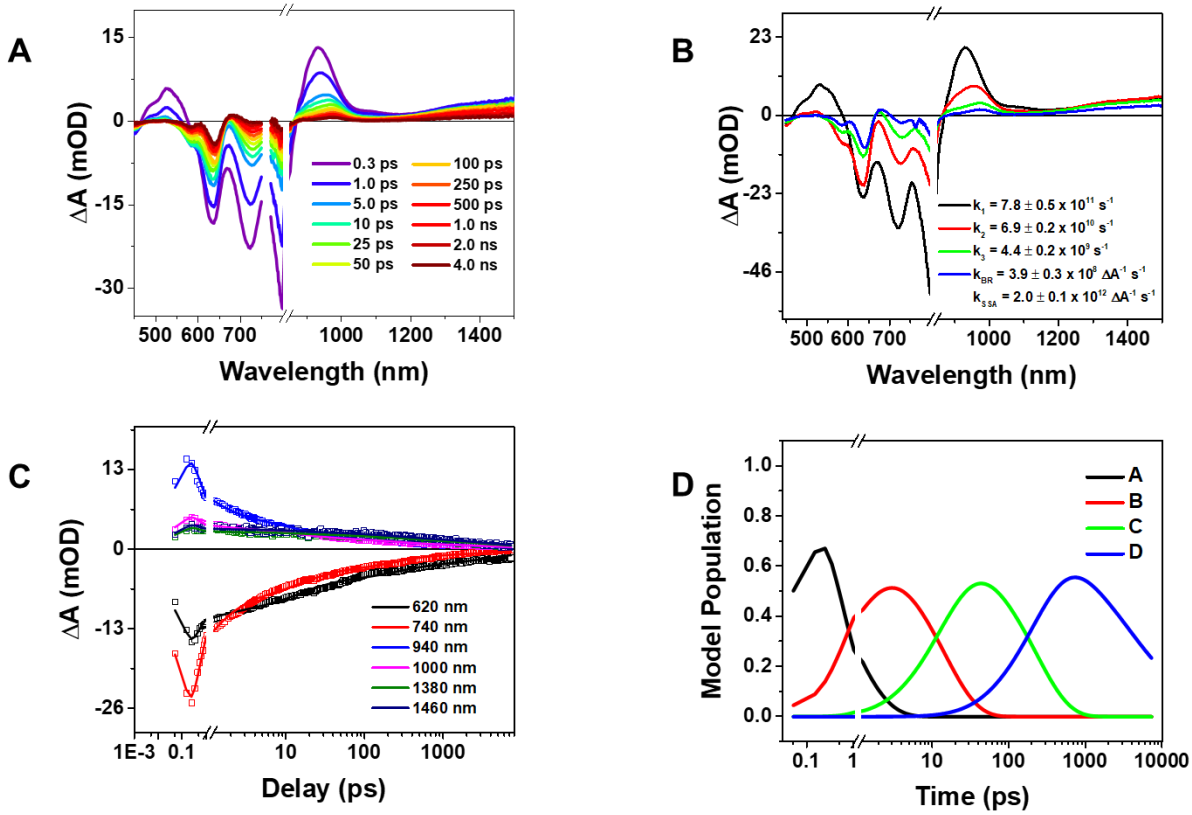

Figure 5.25. Global fits of the **PBDB-T:BT-LIC** blend film excited at 760 nm as described in the text. (a) Time-resolved spectra at selected time points of **PBDB-T:BT-LIC**, (b) Evolution-associated spectra, k_1 is the decay of species A to species B, etc. (c) Kinetic fits to the raw data at the indicated wavelengths with the kinetic model described by **Eqn. S1**[243]. (d) Model population kinetics, distribution of species in time.

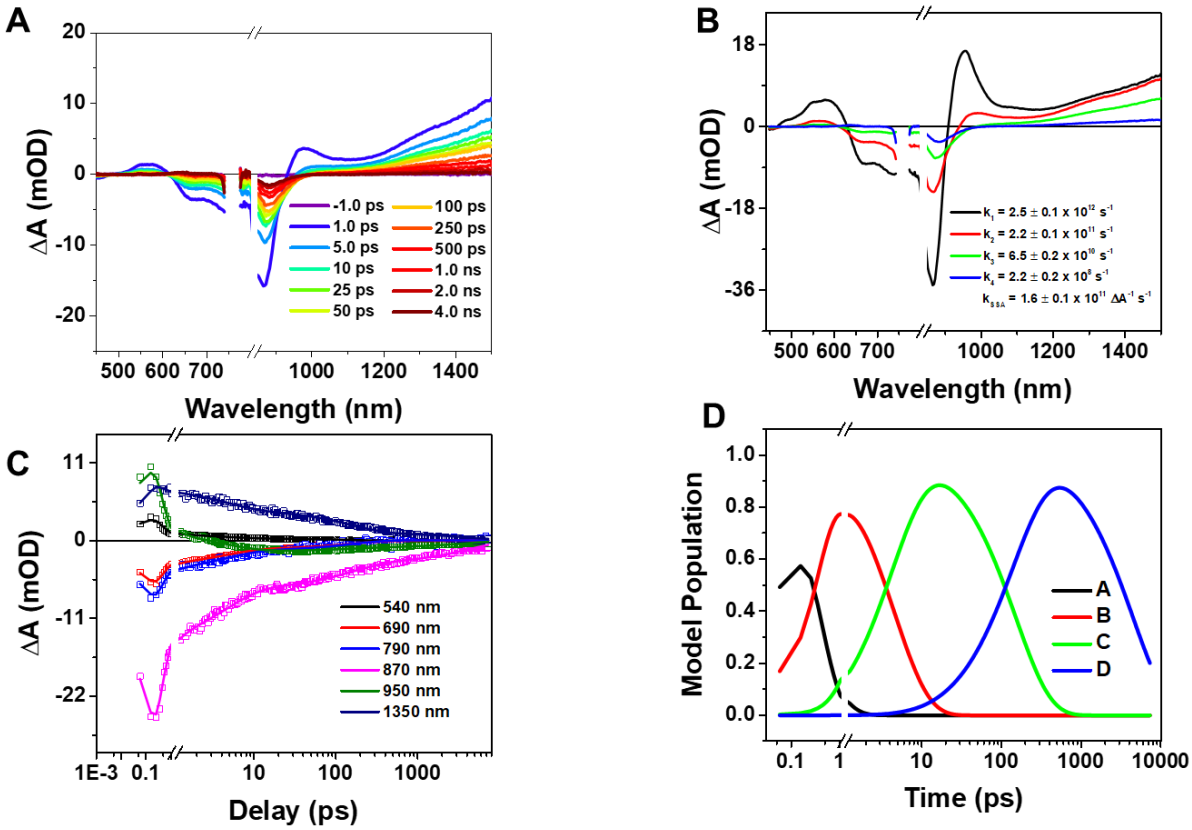

Figure 5.26. Global fits of the neat **BT-L4F** film excited at 760 nm as described in the text. (a) Time-resolved spectra at selected time points of **BT-L4F**, (b) Evolution-associated spectra, k_1 is the decay of species A to species B, etc. (c) Kinetic fits to the raw data at the indicated wavelengths with the kinetic model described by **Eqn. S1**[243]. (d) Model population kinetics, distribution of species in time.

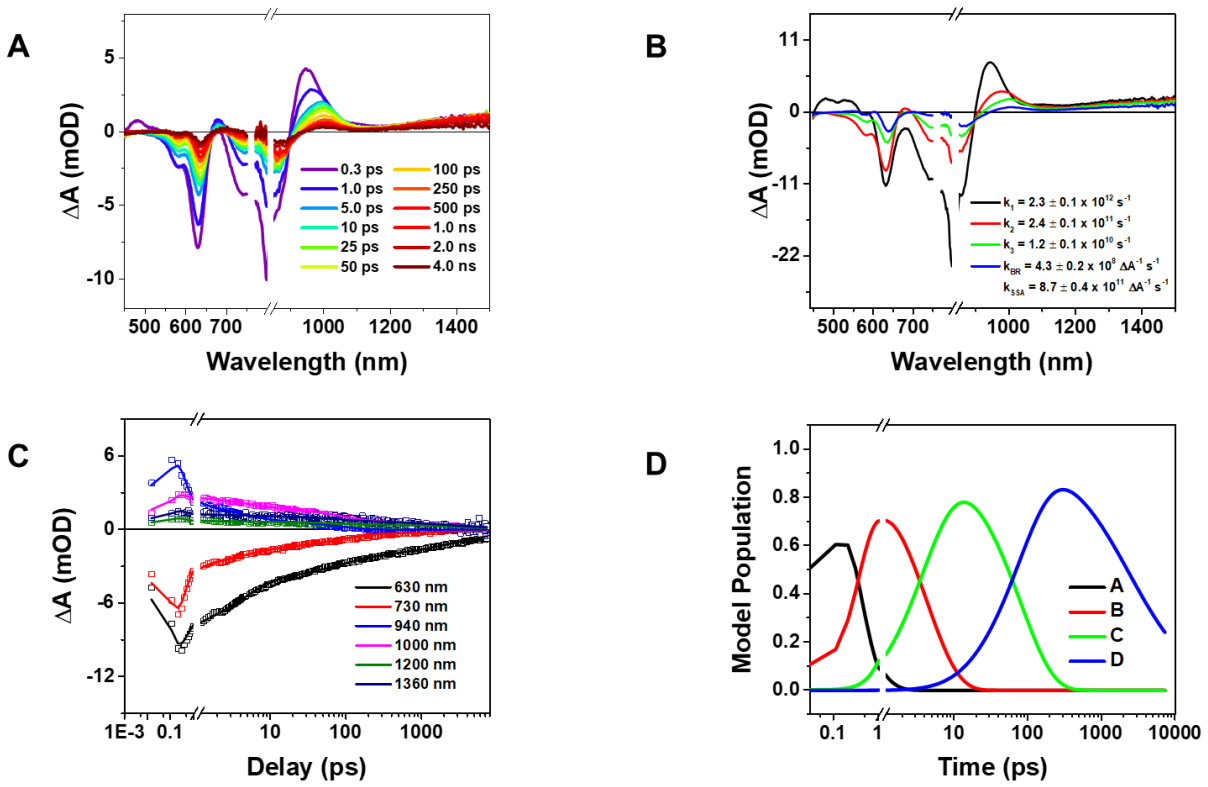

Figure 5.27. Global fits of the **PBDB-T-2F:BT-L4F** blend film excited at 760 nm as described in the text. (a) Time-resolved spectra at selected time points of **PBDB-T-2F:BT-L4F**, (b) Evolution-associated spectra, k_1 is the decay of species A to species B, etc. (c) Kinetic fits to the raw data at the indicated wavelengths with the kinetic model described by **Eqn. S1**[243]. (d) Model population kinetics, distribution of species in time.

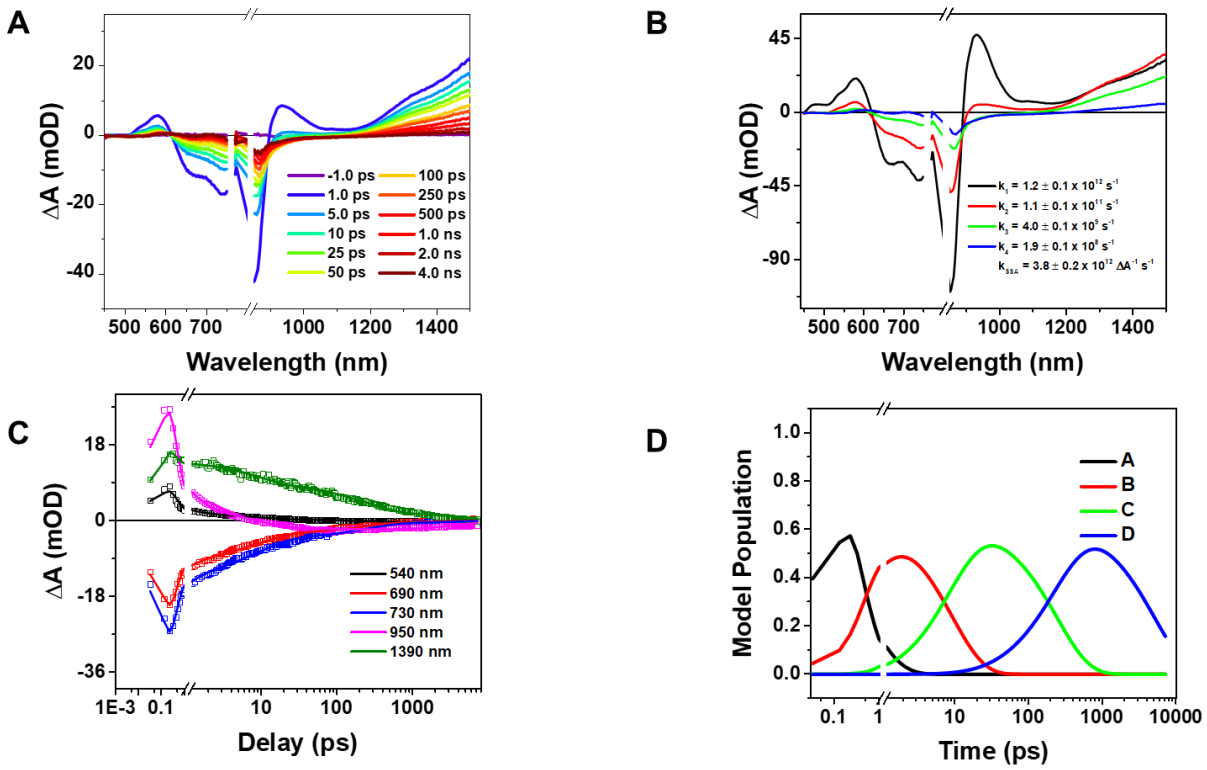

Figure 5.28. Global fits of the neat **BT-BO-L4F** film excited at 760 nm as described in the text. (a) Time-resolved spectra at selected time points of **BT-BO-L4F**, (b) Evolution-associated spectra, k_1 is the decay of species A to species B, etc. (c) Kinetic fits to the raw data at the indicated wavelengths with the kinetic model described by **Eqn. S1**[243]. (d) Model population kinetics, distribution of species in time.

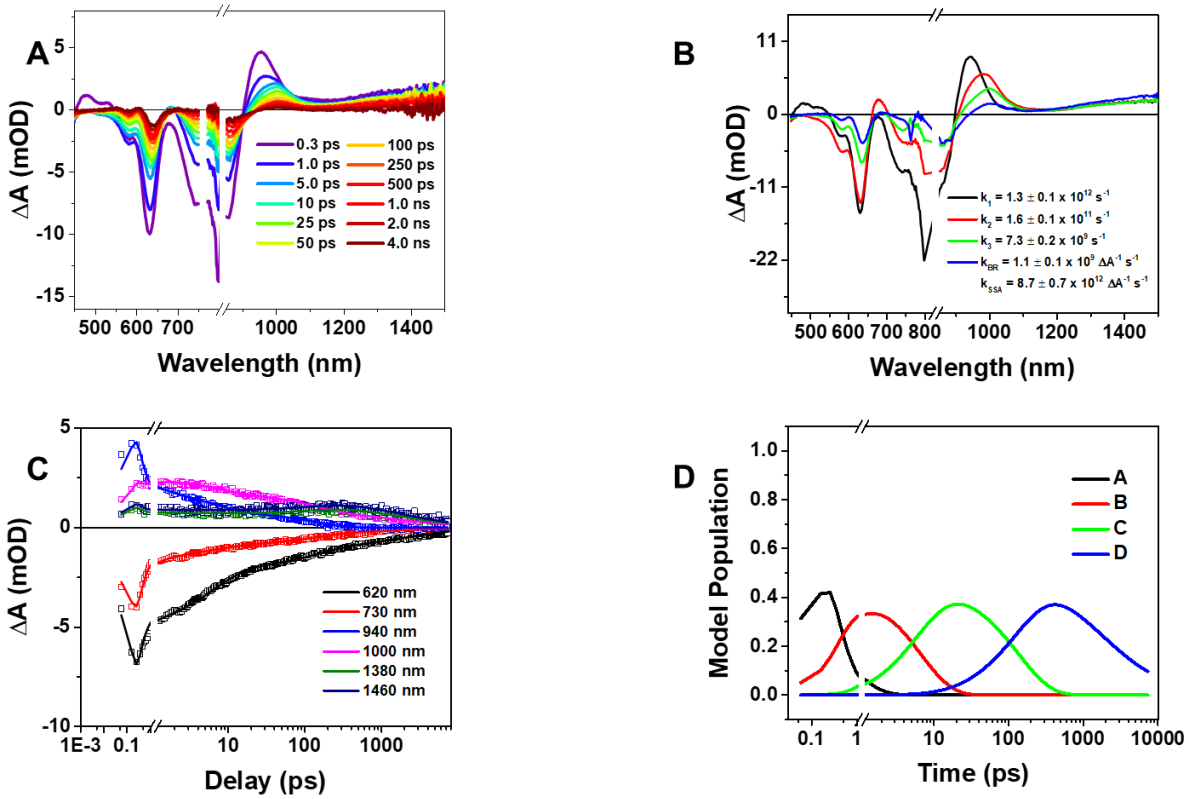

Figure 5.29. Global fits of the **PBDB-T-2F:BT-BO-L4F** blend film excited at 760 nm as described in the text. (a) Time-resolved spectra at selected time points of **PBDB-T-2F:BT-BO-L4F**, (b) Evolution-associated spectra, k_1 is the decay of species A to species B, etc. (c) Kinetic fits to the raw data at the indicated wavelengths with the kinetic model described by **Eqn. S1**[243]. (d) Model population kinetics, distribution of species in time.

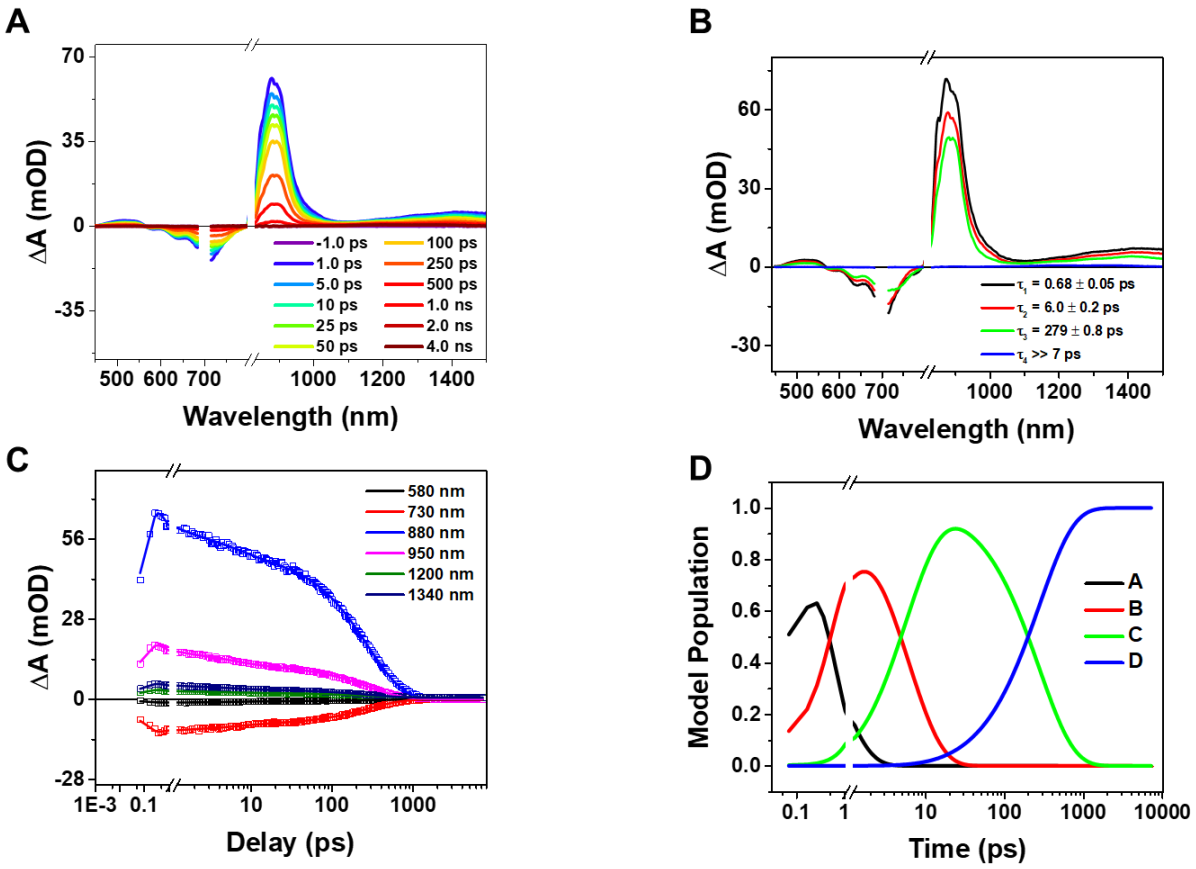

Figure 5.30. fsTA of **Y5** in toluene solution excited at 700 nm at the absorption maxima. (a) Time resolved spectrum of **Y5** in solution. (b) Evolution-associated spectra. (c) Kinetics fits to the raw data at the indicated wavelengths with the kinetic model as described by **Eqn. S1**[243]. $\tau = 1/k$. (d) Model population kinetics, distribution of species in time.

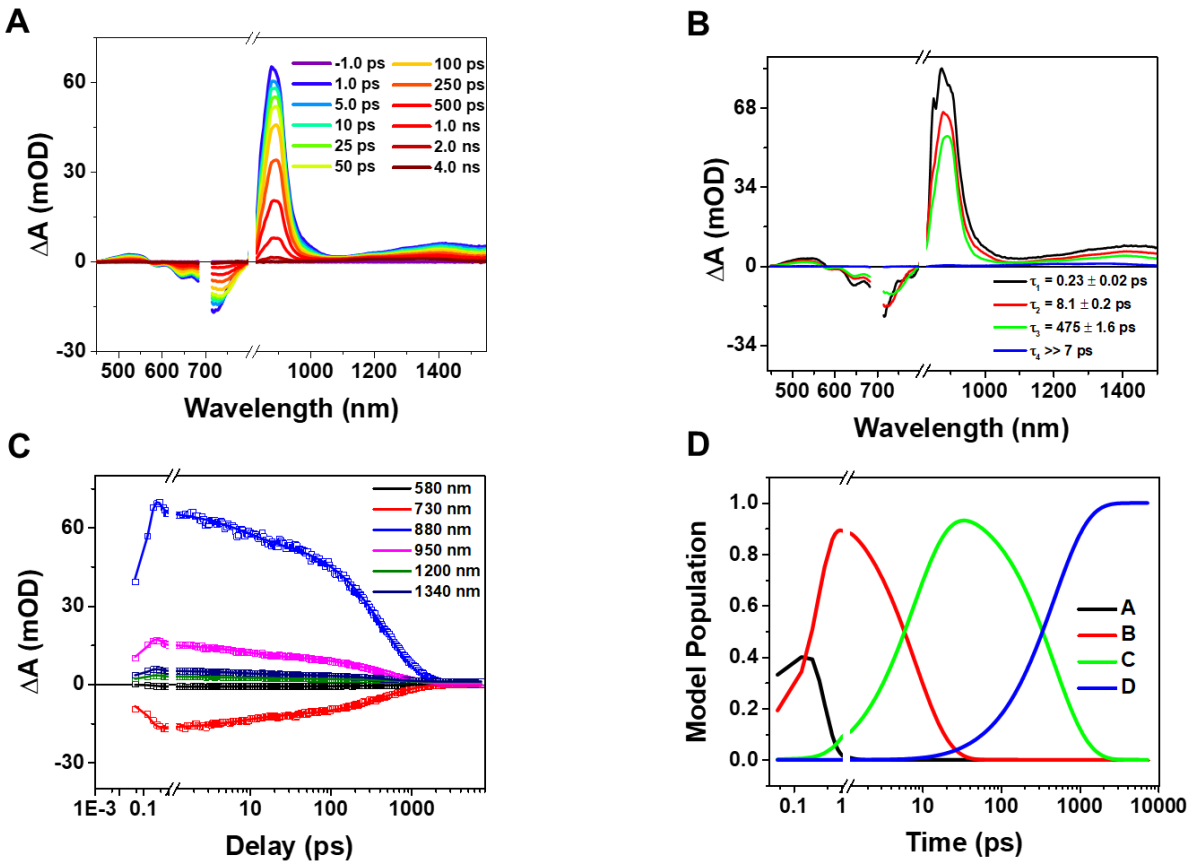

Figure 5.31. fsTA of **Y6** in toluene solution excited at 700 nm at the absorption maxima. (a) Time resolved spectrum of **Y6** in solution. (b) Evolution-associated spectra. (c) Kinetics fits to the raw data at the indicated wavelengths with the kinetic model as described by **Eqn. S1**[243]. $\tau = 1/k$. (d) Model population kinetics, distribution of species in time.

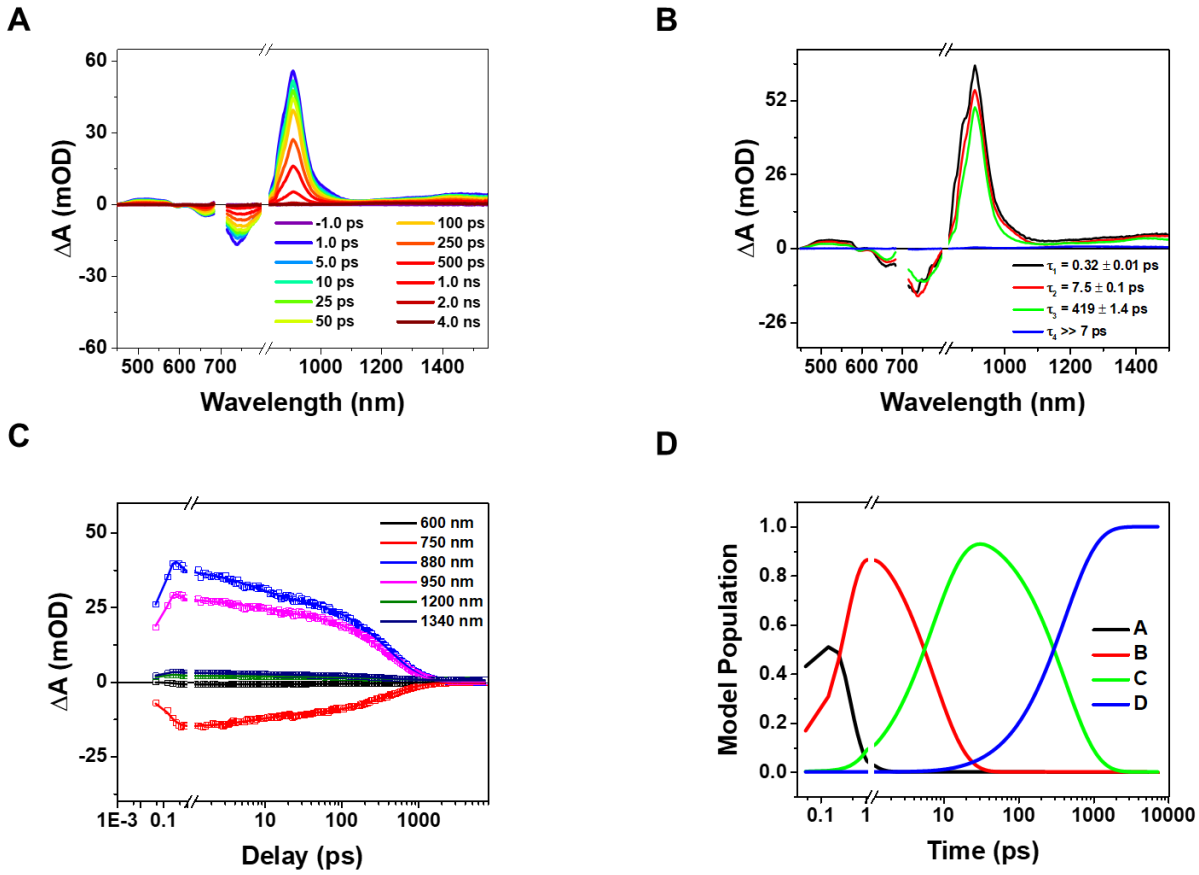

Figure 5.32. fsTA of **BT-LIC** in toluene solution excited at 700 nm at the absorption maxima. (a) Time resolved spectrum of **BT-LIC** in solution. (b) Evolution-associated spectra. (c) Kinetics fits to the raw data at the indicated wavelengths with the kinetic model as described by **Eqn. S1**[243]. $\tau = 1/k$. (d) Model population kinetics, distribution of species in time.

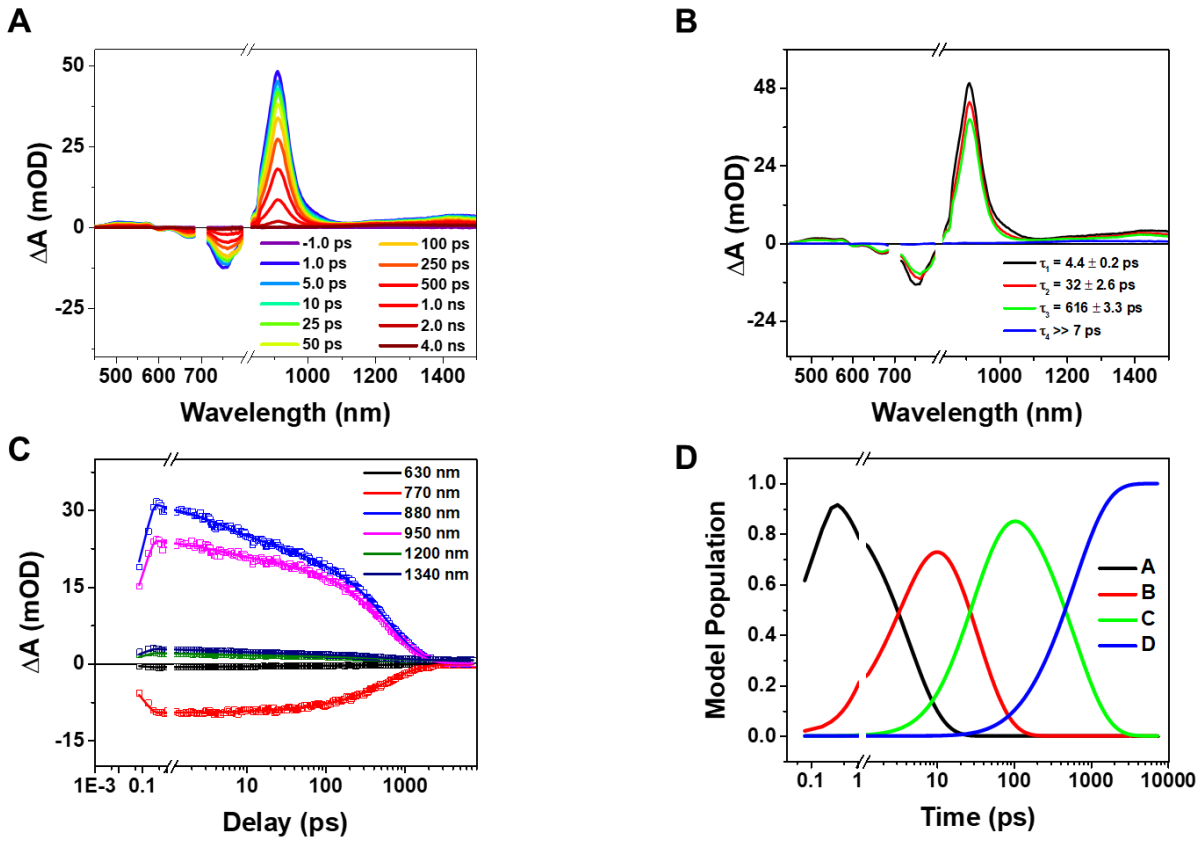

Figure 5.33. fsTA of **BT-L4F** in toluene solution excited at 700 nm at the absorption maxima. (a) Time resolved spectrum of **BT-L4F** in solution. (b) Evolution-associated spectra. (c) Kinetics fits to the raw data at the indicated wavelengths with the kinetic model as described by **Eqn. S1**[243]. $\tau = 1/k$. (d) Model population kinetics, distribution of species in time.

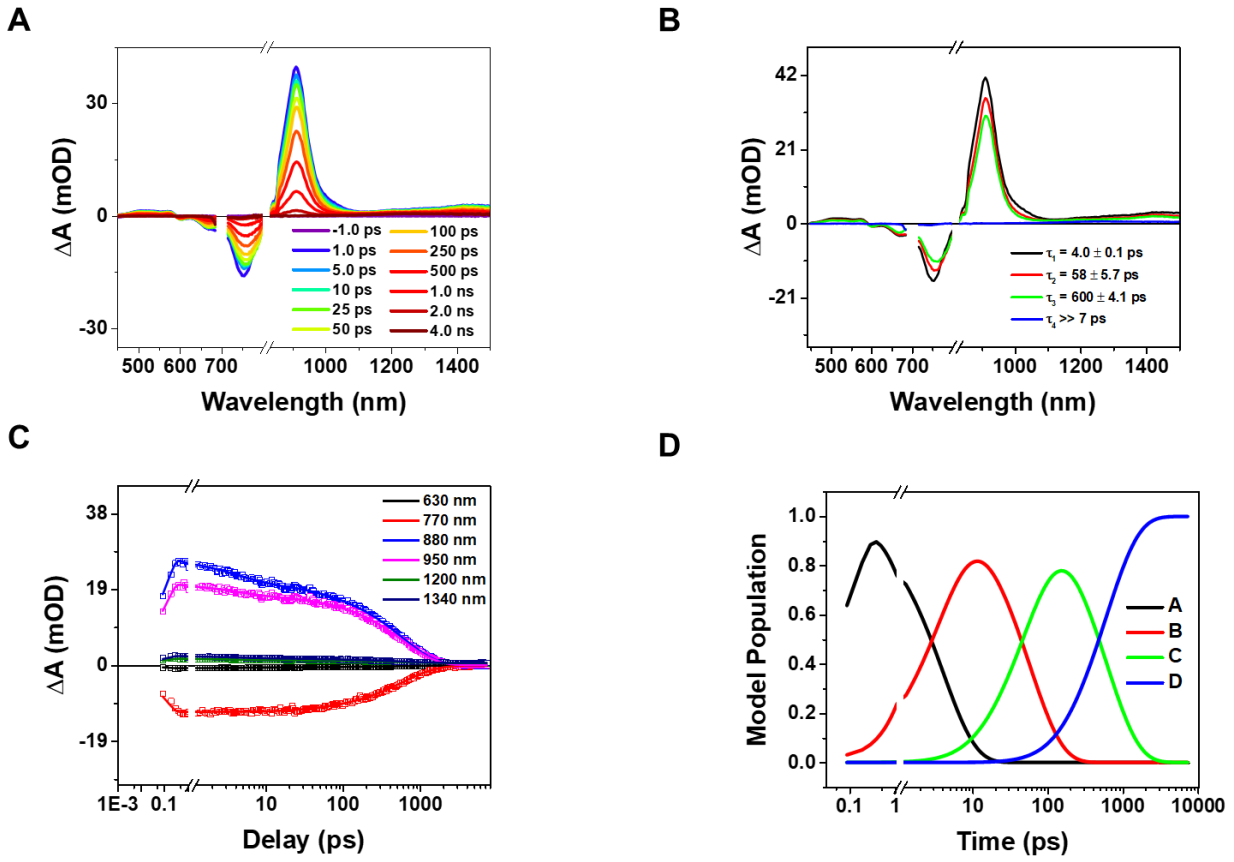

Figure 5.34. fsTA of **BT-BO-L4F** in toluene solution excited at 700 nm at the absorption maxima. (a) Time resolved spectrum of **BT-BO-L4F** in solution. (b) Evolution-associated spectra. (c) Kinetics fits to the raw data at the indicated wavelengths with the kinetic model as described by **Eqn. S1**[243]. $\tau = 1/k$. (d) Model population kinetics, distribution of species in time.

5.5.9. Laser Fluence-Dependent fsTA Spectra of FREA Blend Films.

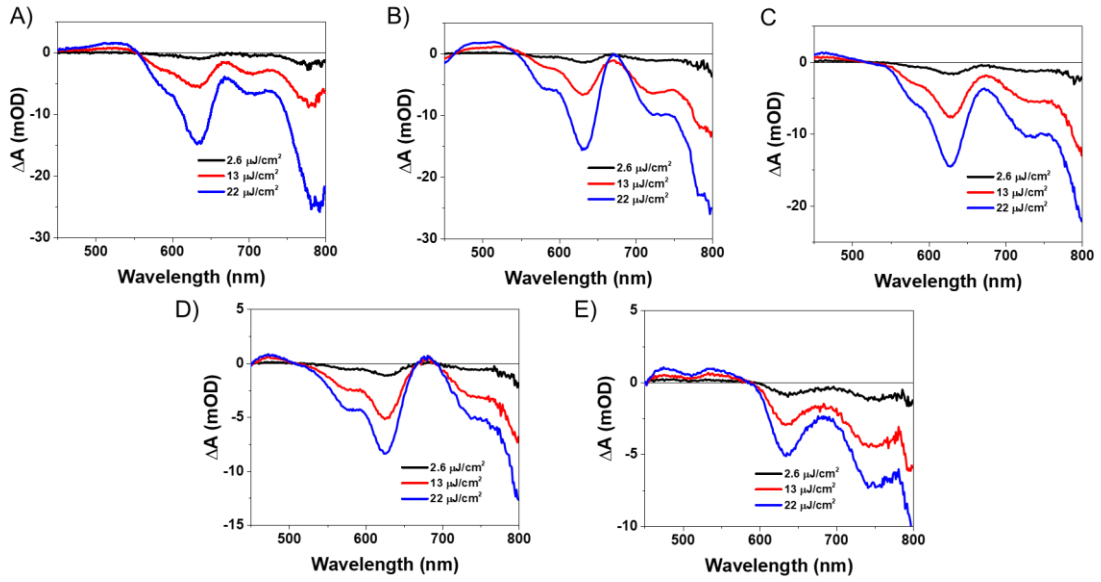

Figure 5.35. fsTA spectra excited at λ = 760 nm at a time delay τ = 0.3 ps using several different laser fluences for A) **PBDB-T**:**Y5** B) **PBDB-T**:**BT-LIC** C) **PBDB-T-2F**:**Y6** D) **PBDB-T-2F**:**BT-L4F** E) **PBDB-T-2F**:**BT-BO-L4F**.

5.5.10. Single-Wavelength Analysis of FREA Blend Films.

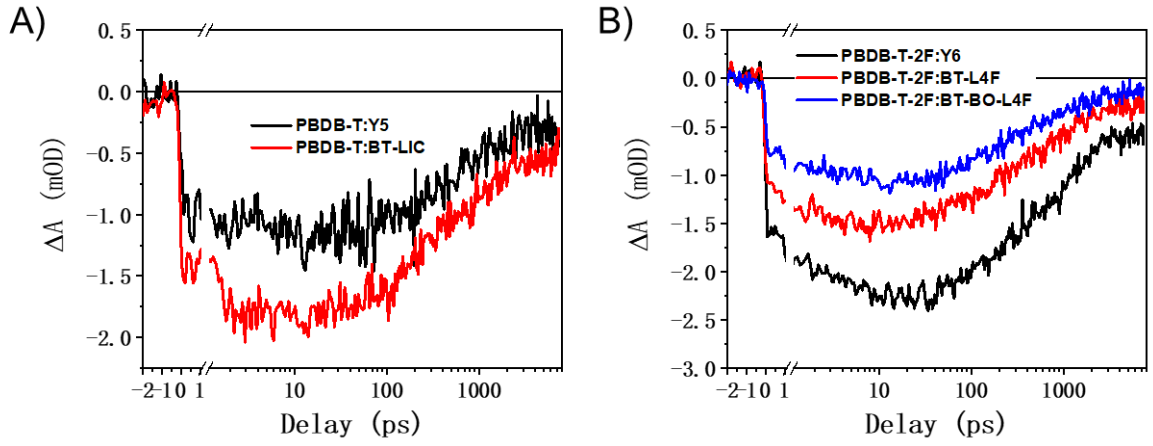

Figure 5.36. Kinetics at 630 nm from the fsTA experiments with laser fluence 2.6 μJ/cm^2 A) **PBDB-T**:**Y5** and **PBDB-T**:**BT-LIC** B) **PBDB-T-2F**:**Y6**, **PBDB-T-2F**:**BT-L4F** and **PBDB-T-2F**:**BT-BO-L4F**.

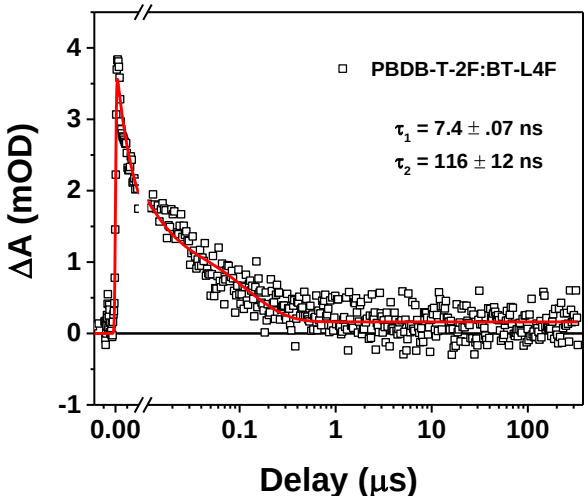

Figure 5.37. FC decay dynamics and single wavelength fits monitored at the polymer GSB (630 nm) in the nsTA experiments for **PBDB-T-2F**:**BT-L4F**. Data are inverted for clarity.

5.5.11. nsTA Spectra of FREA Blend Films.

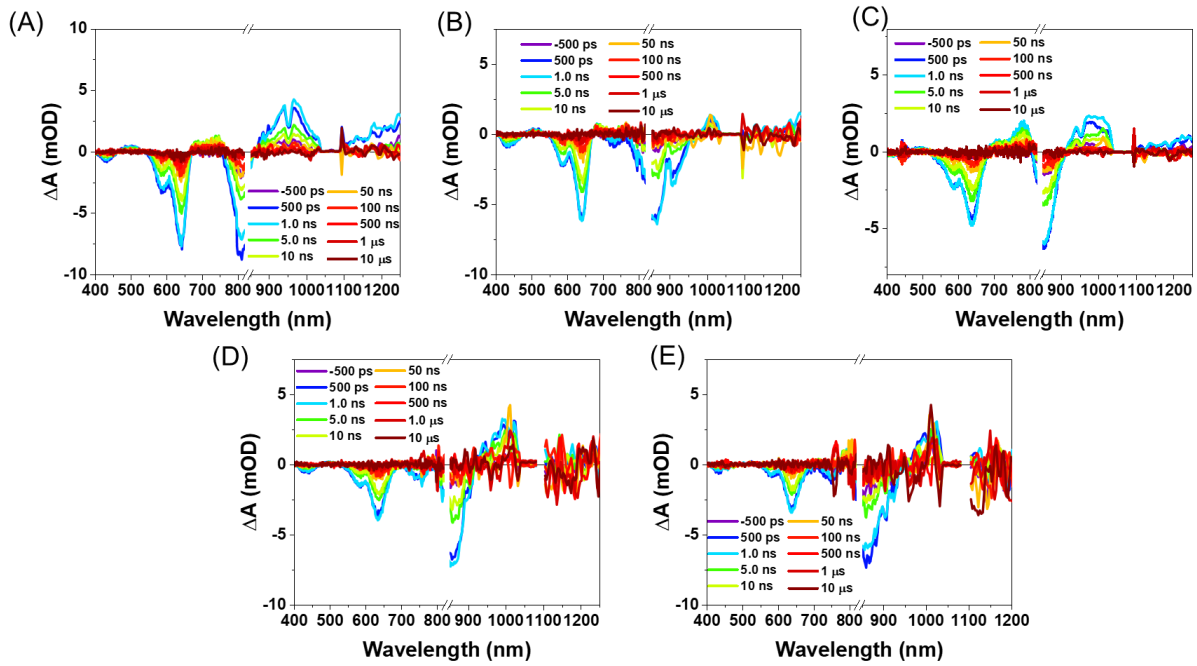

Figure 5.38. nsTA spectra excited at λ = 760 nm at selected time points for A) **PBDB-T**:**Y5** B) **PBDB-T**:**BT-LIC** C) **PBDB-T-2F**:**Y6** D) **PBDB-T-2F**:**BT-L4F** E) **PBDB-T-2F**:**BT-BO-L4F**.

References

1. van Ruijven, B. J.; De Cian, E.; Sue Wing, I., Amplification of future energy demand growth due to climate change. *Nature Communications* **2019,** *10* (1), 2762.
2. Ghasemian, S.; Faridzad, A.; Abbaszadeh, P.; Taklif, A.; Ghasemi, A.; Hafezi, R., An overview of global energy scenarios by 2040: identifying the driving forces using cross-impact analysis method. *International Journal of Environmental Science and Technology* **2020**.
3. Haegel, N. M.; Atwater, H.; Barnes, T.; Breyer, C.; Burrell, A.; Chiang, Y.-M.; De Wolf, S.; Dimmler, B.; Feldman, D.; Glunz, S.; Goldschmidt, J. C.; Hochschild, D.; Inzunza, R.; Kaizuka, I.; Kroposki, B.; Kurtz, S.; Leu, S.; Margolis, R.; Matsubara, K.; Metz, A.; Metzger, W. K.; Morjaria, M.; Niki, S.; Nowak, S.; Peters, I. M.; Philipps, S.; Reindl, T.; Richter, A.; Rose, D.; Sakurai, K.; Schlatmann, R.; Shikano, M.; Sinke, W.; Sinton, R.; Stanbery, B. J.; Topic, M.; Tumas, W.; Ueda, Y.; van de Lagemaat, J.; Verlinden, P.; Vetter, M.; Warren, E.; Werner, M.; Yamaguchi, M.; Bett, A. W., Terawatt-scale photovoltaics: Transform global energy. *Science* **2019,** *364* (6443), 836.
4. Eicke, R. W. In *Photovoltaics moving into the terawatt age*, Proc.SPIE, 2017.
5. Gul, M.; Kotak, Y.; Muneer, T., Review on recent trend of solar photovoltaic technology. *Energy Exploration & Exploitation* **2016,** *34* (4), 485-526.
6. Green, M. A., How Did Solar Cells Get So Cheap? *Joule* **2019,** *3* (3), 631-633.
7. Gorjian, S.; Sharon, H.; Ebadi, H.; Kant, K.; Scavo, F. B.; Tina, G. M., Recent technical advancements, economics and environmental impacts of floating photovoltaic solar energy conversion systems. *Journal of Cleaner Production* **2021,** *278*, 124285.
8. Sofia, S. E.; Mailoa, J. P.; Weiss, D. N.; Stanbery, B. J.; Buonassisi, T.; Peters, I. M., Economic viability of thin-film tandem solar modules in the United States. *Nat. Energy* **2018,** *3* (5), 387-394.
9. Armin, A.; Stoltzfus, D. M.; Donaghey, J. E.; Clulow, A. J.; Nagiri, R. C. R.; Burn, P. L.; Gentle, I. R.; Meredith, P., Engineering dielectric constants in organic semiconductors. *J. Mat. Chem. C* **2017,** *5* (15), 3736-3747.
10. Knupfer, M., Exciton binding energies in organic semiconductors. *Appl. Phys. A* **2003,** *77* (5), 623-626.
11. Firdaus, Y.; Le Corre, V. M.; Karuthedath, S.; Liu, W.; Markina, A.; Huang, W.; Chattopadhyay, S.; Nahid, M. M.; Nugraha, M. I.; Lin, Y.; Seitkhan, A.; Basu, A.; Zhang, W.; McCulloch, I.; Ade, H.; Labram, J.; Laquai, F.; Andrienko, D.; Koster, L. J. A.; Anthopoulos, T. D., Long-range exciton diffusion in molecular non-fullerene acceptors. *Nature Communications* **2020,** *11* (1), 5220.
12. Sajjad, M. T.; Blaszczyk, O.; Jagadamma, L. K.; Roland, T. J.; Chowdhury, M.; Ruseckas, A.; Samuel, I. D. W., Engineered exciton diffusion length enhances device efficiency in small molecule photovoltaics. *J. Mat. Chem. A* **2018,** *6* (20), 9445-9450.
13. Cui, Y.; Yao, H.; Hong, L.; Zhang, T.; Tang, Y.; Lin, B.; Xian, K.; Gao, B.; An, C.; Bi, P.; Ma, W.; Hou, J., Organic photovoltaic cell with 17% efficiency and superior processability. *National Science Review* **2019,** *7* (7), 1239-1246.
14. Tang, C. W., 2-Layer Organic Photovoltaic Cell. *Appl. Phys. Lett.* **1986,** *48* (2), 183-185.
15. Singh, R.; Aluicio-Sarduy, E.; Kan, Z.; Ye, T.; MacKenzie, R. C. I.; Keivanidis, P. E., Fullerene-free organic solar cells with an efficiency of 3.7% based on a low-cost geometrically planar perylene diimide monomer. *J. Mat. Chem. A* **2014,** *2* (35), 14348-14353.

16. Lin, Y.; Wang, Y.; Wang, J.; Hou, J.; Li, Y.; Zhu, D.; Zhan, X., A Star-Shaped Perylene Diimide Electron Acceptor for High-Performance Organic Solar Cells. *Adv. Mater.* **2014,** *26* (30), 5137-5142.
17. Lu, Z.; Jiang, B.; Zhang, X.; Tang, A.; Chen, L.; Zhan, C.; Yao, J., Perylene–Diimide Based Non-Fullerene Solar Cells with 4.34% Efficiency through Engineering Surface Donor/Acceptor Compositions. *Chem. Mater.* **2014,** *26* (9), 2907-2914.
18. Reese, M. O.; Nardes, A. M.; Rupert, B. L.; Larsen, R. E.; Olson, D. C.; Lloyd, M. T.; Shaheen, S. E.; Ginley, D. S.; Rumbles, G.; Kopidakis, N., Photoinduced Degradation of Polymer and Polymer-Fullerene Active Layers: experiment and Theory. *Adv. Funct. Mater.* **2010,** *20* (20), 3476-3483.
19. Lin, Y.; Zhan, X., Non-fullerene acceptors for organic photovoltaics: an emerging horizon. *Mat. Horiz.* **2014,** *1* (5), 470-488.
20. Savoie, B. M.; Rao, A.; Bakulin, A. A.; Gelinas, S.; Movaghar, B.; Friend, R. H.; Marks, T. J.; Ratner, M. A., Unequal Partnership: Asymmetric Roles of Polymeric Donor and Fullerene Acceptor in Generating Free Charge. *Journal of the American Chemical Society* **2014,** *136* (7), 2876-2884.
21. Zhang, J.; Li, Y.; Huang, J.; Hu, H.; Zhang, G.; Ma, T.; Chow, P. C. Y.; Ade, H.; Pan, D.; Yan, H., Ring-Fusion of Perylene Diimide Acceptor Enabling Efficient Nonfullerene Organic Solar Cells with a Small Voltage Loss. *Journal of the American Chemical Society* **2017,** *139* (45), 16092-16095.
22. Zhang, G.; Feng, J.; Xu, X.; Ma, W.; Li, Y.; Peng, Q., Perylene Diimide-Based Nonfullerene Polymer Solar Cells with over 11% Efficiency Fabricated by Smart Molecular Design and Supramolecular Morphology Optimization. *Adv. Funct. Mater.* **2019,** *29* (50), 1906587.
23. Hartnett, P. E.; Timalsina, A.; Matte, H. S. S. R.; Zhou, N.; Guo, X.; Zhao, W.; Facchetti, A.; Chang, R. P. H.; Hersam, M. C.; Wasielewski, M. R.; Marks, T. J., Slip-Stacked Perylenediimides as an Alternative Strategy for High Efficiency Nonfullerene Acceptors in Organic Photovoltaics. *J. Am. Chem. Soc.* **2014,** *136* (46), 16345-16356.
24. Hartnett, P. E.; Matte, H. S. S. R.; Eastham, N. D.; Jackson, N. E.; Wu, Y.; Chen, L. X.; Ratner, M. A.; Chang, R. P. H.; Hersam, M. C.; Wasielewski, M. R.; Marks, T. J., Ring-fusion as a perylenediimide dimer design concept for high-performance non-fullerene organic photovoltaic acceptors. *Chem. Sci.* **2016,** *7* (6), 3543-3555.
25. Hu, H.; Li, Y.; Zhang, J.; Peng, Z.; Ma, L.-k.; Xin, J.; Huang, J.; Ma, T.; Jiang, K.; Zhang, G.; Ma, W.; Ade, H.; Yan, H., Effect of Ring-Fusion on Miscibility and Domain Purity: Key Factors Determining the Performance of PDI-Based Nonfullerene Organic Solar Cells. *Advanced Energy Materials* **2018,** *8* (26), 1800234.
26. Bakulin, A. A.; Rao, A.; Pavelyev, V. G.; van Loosdrecht, P. H. M.; Pshenichnikov, M. S.; Niedzialek, D.; Cornil, J.; Beljonne, D.; Friend, R. H., The Role of Driving Energy and Delocalized States for Charge Separation in Organic Semiconductors. *Science* **2012,** *335* (6074), 1340.
27. Gélinas, S.; Rao, A.; Kumar, A.; Smith, S. L.; Chin, A. W.; Clark, J.; van der Poll, T. S.; Bazan, G. C.; Friend, R. H., Ultrafast Long-Range Charge Separation in Organic Semiconductor Photovoltaic Diodes. *Science* **2014,** *343* (6170), 512.

28. Tamai, Y.; Fan, Y.; Kim, V. O.; Ziabrev, K.; Rao, A.; Barlow, S.; Marder, S. R.; Friend, R. H.; Menke, S. M., Ultrafast Long-Range Charge Separation in Nonfullerene Organic Solar Cells. *ACS Nano* **2017,** *11* (12), 12473-12481.
29. Timalsina, A.; Hartnett, P. E.; Melkonyan, F. S.; Strzalka, J.; Reddy, V. S.; Facchetti, A.; Wasielewski, M. R.; Marks, T. J., New donor polymer with tetrafluorinated blocks for enhanced performance in perylenediimide-based solar cells. *J. Mat. Chem. A* **2017,** *5* (11), 5351-5361.
30. Jakowetz, A. C.; Böhm, M. L.; Zhang, J.; Sadhanala, A.; Huettner, S.; Bakulin, A. A.; Rao, A.; Friend, R. H., What Controls the Rate of Ultrafast Charge Transfer and Charge Separation Efficiency in Organic Photovoltaic Blends. *Journal of the American Chemical Society* **2016,** *138* (36), 11672-11679.
31. Isakova, A.; Karuthedath, S.; Arnold, T.; Howse, J. R.; Topham, P. D.; Toolan, D. T. W.; Laquai, F.; Lüer, L., Efficient long-range electron transfer processes in polyfluorene–perylene diimide blends. *Nanoscale* **2018,** *10* (23), 10934-10944.
32. Eastham, N. D.; Logsdon, J. L.; Manley, E. F.; Aldrich, T. J.; Leonardi, M. J.; Wang, G.; Powers-Riggs, N. E.; Young, R. M.; Chen, L. X.; Wasielewski, M. R.; Melkonyan, F. S.; Chang, R. P. H.; Marks, T. J., Hole-Transfer Dependence on Blend Morphology and Energy Level Alignment in Polymer: ITIC Photovoltaic Materials. *Adv. Mater.* **2018,** *30* (3), 1704263.
33. Cha, H.; Wheeler, S.; Holliday, S.; Dimitrov, S. D.; Wadsworth, A.; Lee, H. H.; Baran, D.; McCulloch, I.; Durrant, J. R., Influence of Blend Morphology and Energetics on Charge Separation and Recombination Dynamics in Organic Solar Cells Incorporating a Nonfullerene Acceptor. *Adv. Funct. Mater.* **2018,** *28* (3), 1704389.
34. Liu, J.; Chen, S.; Qian, D.; Gautam, B.; Yang, G.; Zhao, J.; Bergqvist, J.; Zhang, F.; Ma, W.; Ade, H.; Inganäs, O.; Gundogdu, K.; Gao, F.; Yan, H., Fast charge separation in a non-fullerene organic solar cell with a small driving force. *Nat. Energy* **2016,** *1* (7), 16089.
35. Hartnett, P. E.; Dyar, S. M.; Margulies, E. A.; Shoer, L. E.; Cook, A. W.; Eaton, S. W.; Marks, T. J.; Wasielewski, M. R., Long-lived charge carrier generation in ordered films of a covalent perylenediimide-diketopyrrolopyrrole-perylenediimide molecule. *Chem. Sci.* **2015,** *6* (1), 402-411.
36. Logsdon, J. L.; Hartnett, P. E.; Nelson, J. N.; Harris, M. A.; Marks, T. J.; Wasielewski, M. R., Charge Separation Mechanisms in Ordered Films of Self-Assembled Donor–Acceptor Dyad Ribbons. *ACS Appl. Mater. Interfaces* **2017,** *9* (39), 33493-33503.
37. Nowak-Król, A.; Shoyama, K.; Stolte, M.; Würthner, F., Naphthalene and perylene diimides – better alternatives to fullerenes for organic electronics? *Chem. Commun.* **2018,** *54* (98), 13763-13772.
38. Zhan, X.; Facchetti, A.; Barlow, S.; Marks, T. J.; Ratner, M. A.; Wasielewski, M. R.; Marder, S. R., Rylene and Related Diimides for Organic Electronics. *Adv. Mater.* **2011,** *23* (2), 268-284.
39. Wang, J.; Zhan, X., Rylene Diimide Electron Acceptors for Organic Solar Cells. *Trends in Chemistry* **2019,** *1* (9), 869-881.
40. Zhu, W.; Alzola, J. M.; Aldrich, T. J.; Kohlstedt, K. L.; Zheng, D.; Hartnett, P. E.; Eastham, N. D.; Huang, W.; Wang, G.; Young, R. M.; Schatz, G. C.; Wasielewski, M. R.; Facchetti, A.; Melkonyan, F. S.; Marks, T. J., Fluorine Tuning of Morphology, Energy Loss, and

Carrier Dynamics in Perylenediimide Polymer Solar Cells. *ACS Energy Letters* **2019,** *4* (11), 2695-2702.
41. Meng, D.; Fu, H.; Xiao, C.; Meng, X.; Winands, T.; Ma, W.; Wei, W.; Fan, B.; Huo, L.; Doltsinis, N. L.; Li, Y.; Sun, Y.; Wang, Z., Three-Bladed Rylene Propellers with Three-Dimensional Network Assembly for Organic Electronics. *Journal of the American Chemical Society* **2016,** *138* (32), 10184-10190.
42. Fan, Y.; Ziabrev, K.; Zhang, S.; Lin, B.; Barlow, S.; Marder, S. R., Comparison of the Optical and Electrochemical Properties of Bi(perylene diimide)s Linked through Ortho and Bay Positions. *ACS Omega* **2017,** *2* (2), 377-385.
43. Wu, Q.; Zhao, D.; Schneider, A. M.; Chen, W.; Yu, L., Covalently Bound Clusters of Alpha-Substituted PDI—Rival Electron Acceptors to Fullerene for Organic Solar Cells. *Journal of the American Chemical Society* **2016,** *138* (23), 7248-7251.
44. Hartnett, P. E.; Mauck, C. M.; Harris, M. A.; Young, R. M.; Wu, Y.-L.; Marks, T. J.; Wasielewski, M. R., Influence of Anion Delocalization on Electron Transfer in a Covalent Porphyrin Donor–Perylenediimide Dimer Acceptor System. *Journal of the American Chemical Society* **2017,** *139* (2), 749-756.
45. Lin, Y.; Wang, J.; Zhang, Z.-G.; Bai, H.; Li, Y.; Zhu, D.; Zhan, X., An Electron Acceptor Challenging Fullerenes for Efficient Polymer Solar Cells. *Adv. Mater.* **2015,** *27* (7), 1170-1174.
46. Yuan, J.; Zhang, Y.; Zhou, L.; Zhang, G.; Yip, H.-L.; Lau, T.-K.; Lu, X.; Zhu, C.; Peng, H.; Johnson, P. A.; Leclerc, M.; Cao, Y.; Ulanski, J.; Li, Y.; Zou, Y., Single-Junction Organic Solar Cell with over 15% Efficiency Using Fused-Ring Acceptor with Electron-Deficient Core. *Joule* **2019,** *3* (4), 1140-1151.
47. Cheng, M.; Li, Y.; Liu, P.; Zhang, F.; Hajian, A.; Wang, H.; Li, J.; Wang, L.; Kloo, L.; Yang, X.; Sun, L., A Perylenediimide Tetramer-Based 3D Electron Transport Material for Efficient Planar Perovskite Solar Cell. *Solar RRL* **2017,** *1* (5), 1700046.
48. Yao, J.; Qiu, B.; Zhang, Z.-G.; Xue, L.; Wang, R.; Zhang, C.; Chen, S.; Zhou, Q.; Sun, C.; Yang, C.; Xiao, M.; Meng, L.; Li, Y., Cathode engineering with perylene-diimide interlayer enabling over 17% efficiency single-junction organic solar cells. *Nature Communications* **2020,** *11* (1), 2726.
49. Wang, Y.; Zhong, H.; Hong, Y.; Shan, T.; Ding, K.; Zhu, L.; Liu, F.; Wei, H.; Yu, C.; Zhong, H., Tailoring the molecular geometry of polyfluoride perylene diimide acceptors towards efficient organic solar cells. *J. Mat. Chem. C* **2020,** *8* (24), 8224-8233.
50. Wang, H.; Chen, L.; Xiao, Y., A simple molecular structure of ortho-derived perylene diimide diploid for non-fullerene organic solar cells with efficiency over 8%. *J. Mat. Chem. A* **2017,** *5* (42), 22288-22296.
51. Eaton, S. W.; Shoer, L. E.; Karlen, S. D.; Dyar, S. M.; Margulies, E. A.; Veldkamp, B. S.; Ramanan, C.; Hartzler, D. A.; Savikhin, S.; Marks, T. J.; Wasielewski, M. R., Singlet Exciton Fission in Polycrystalline Thin Films of a Slip-Stacked Perylenediimide. *J. Am. Chem. Soc.* **2013,** *135* (39), 14701-14712.
52. Muthike, A. K.; Carlotti, B.; Madu, I. K.; Jiang, H.; Kim, H.; Wu, Q.; Yu, L.; Zimmerman, P. M.; Goodson, T., The Role of the Core Attachment Positioning in Triggering Intramolecular Singlet Exciton Fission in Perylene Diimide Tetramers. *J. Phys. Chem. B* **2021**.

53. Young, R. M.; Wasielewski, M. R., Mixed Electronic States in Molecular Dimers: Connecting Singlet Fission, Excimer Formation, and Symmetry-Breaking Charge Transfer. *Acc. Chem. Res.* **2020,** *53* (9), 1957-1968.
54. Wu, Y.; Young, R. M.; Frasconi, M.; Schneebeli, S. T.; Spenst, P.; Gardner, D. M.; Brown, K. E.; Würthner, F.; Stoddart, J. F.; Wasielewski, M. R., Ultrafast Photoinduced Symmetry-Breaking Charge Separation and Electron Sharing in Perylenediimide Molecular Triangles. *Journal of the American Chemical Society* **2015,** *137* (41), 13236-13239.
55. Bartynski, A. N.; Gruber, M.; Das, S.; Rangan, S.; Mollinger, S.; Trinh, C.; Bradforth, S. E.; Vandewal, K.; Salleo, A.; Bartynski, R. A.; Bruetting, W.; Thompson, M. E., Symmetry-Breaking Charge Transfer in a Zinc Chlorodipyrrin Acceptor for High Open Circuit Voltage Organic Photovoltaics. *Journal of the American Chemical Society* **2015,** *137* (16), 5397-5405.
56. Kong, J.; Zhang, W.; Li, G.; Huo, D.; Guo, Y.; Niu, X.; Wan, Y.; Tang, B.; Xia, A., Excited-State Symmetry-Breaking Charge Separation Dynamics in Multibranched Perylene Diimide Molecules. *The Journal of Physical Chemistry Letters* **2020,** *11* (24), 10329-10339.
57. Coleman, A. F.; Chen, M.; Zhou, J.; Shin, J. Y.; Wu, Y.; Young, R. M.; Wasielewski, M. R., Reversible Symmetry-Breaking Charge Separation in a Series of Perylenediimide Cyclophanes. *J. Phys. Chem. C* **2020,** *124* (19), 10408-10419.
58. Giaimo, J. M.; Gusev, A. V.; Wasielewski, M. R., Excited-State Symmetry Breaking in Cofacial and Linear Dimers of a Green Perylenediimide Chlorophyll Analogue Leading to Ultrafast Charge Separation. *Journal of the American Chemical Society* **2002,** *124* (29), 8530-8531.
59. Cook, R. E.; Phelan, B. T.; Kamire, R. J.; Majewski, M. B.; Young, R. M.; Wasielewski, M. R., Excimer Formation and Symmetry-Breaking Charge Transfer in Cofacial Perylene Dimers. *J. Phys. Chem. A* **2017,** *121* (8), 1607-1615.
60. Ramirez, C. E.; Chen, S.; Powers-Riggs, N. E.; Schlesinger, I.; Young, R. M.; Wasielewski, M. R., Symmetry-Breaking Charge Separation in the Solid State: Tetra(phenoxy)perylenediimide Polycrystalline Films. *Journal of the American Chemical Society* **2020,** *142* (42), 18243-18250.
61. Nowak-Król, A.; Fimmel, B.; Son, M.; Kim, D.; Würthner, F., Photoinduced electron transfer (PET) versus excimer formation in supramolecular p/n-heterojunctions of perylene bisimide dyes and implications for organic photovoltaics. *Faraday Discuss.* **2015,** *185* (0), 507-527.
62. Fang, S.; Zhou, J.; Zhou, X.; Wang, C.; Jiang, N.; Liu, L.; Xie, Z., Interchromophore Rotation-Related Ultrafast Charge Separation at Excited States in Head-to-Tail Linked Perylene Diimide Dyads. *J. Phys. Chem. C* **2019,** *123* (38), 23306-23311.
63. Shao, Y.; Gan, Z.; Epifanovsky, E.; Gilbert, A. T. B.; Wormit, M.; Kussmann, J.; Lange, A. W.; Behn, A.; Deng, J.; Feng, X.; Ghosh, D.; Goldey, M.; Horn, P. R.; Jacobson, L. D.; Kaliman, I.; Khaliullin, R. Z.; Kuś, T.; Landau, A.; Liu, J.; Proynov, E. I.; Rhee, Y. M.; Richard, R. M.; Rohrdanz, M. A.; Steele, R. P.; Sundstrom, E. J.; Woodcock, H. L.; Zimmerman, P. M.; Zuev, D.; Albrecht, B.; Alguire, E.; Austin, B.; Beran, G. J. O.; Bernard, Y. A.; Berquist, E.; Brandhorst, K.; Bravaya, K. B.; Brown, S. T.; Casanova, D.; Chang, C.-M.; Chen, Y.; Chien, S. H.; Closser, K. D.; Crittenden, D. L.; Diedenhofen, M.; DiStasio, R. A.; Do, H.; Dutoi, A. D.; Edgar, R. G.; Fatehi, S.; Fusti-Molnar, L.; Ghysels, A.; Golubeva-

Zadorozhnaya, A.; Gomes, J.; Hanson-Heine, M. W. D.; Harbach, P. H. P.; Hauser, A. W.; Hohenstein, E. G.; Holden, Z. C.; Jagau, T.-C.; Ji, H.; Kaduk, B.; Khistyaev, K.; Kim, J.; Kim, J.; King, R. A.; Klunzinger, P.; Kosenkov, D.; Kowalczyk, T.; Krauter, C. M.; Lao, K. U.; Laurent, A. D.; Lawler, K. V.; Levchenko, S. V.; Lin, C. Y.; Liu, F.; Livshits, E.; Lochan, R. C.; Luenser, A.; Manohar, P.; Manzer, S. F.; Mao, S.-P.; Mardirossian, N.; Marenich, A. V.; Maurer, S. A.; Mayhall, N. J.; Neuscamman, E.; Oana, C. M.; Olivares-Amaya, R.; O'Neill, D. P.; Parkhill, J. A.; Perrine, T. M.; Peverati, R.; Prociuk, A.; Rehn, D. R.; Rosta, E.; Russ, N. J.; Sharada, S. M.; Sharma, S.; Small, D. W.; Sodt, A.; Stein, T.; Stück, D.; Su, Y.-C.; Thom, A. J. W.; Tsuchimochi, T.; Vanovschi, V.; Vogt, L.; Vydrov, O.; Wang, T.; Watson, M. A.; Wenzel, J.; White, A.; Williams, C. F.; Yang, J.; Yeganeh, S.; Yost, S. R.; You, Z.-Q.; Zhang, I. Y.; Zhang, X.; Zhao, Y.; Brooks, B. R.; Chan, G. K. L.; Chipman, D. M.; Cramer, C. J.; Goddard, W. A.; Gordon, M. S.; Hehre, W. J.; Klamt, A.; Schaefer, H. F.; Schmidt, M. W.; Sherrill, C. D.; Truhlar, D. G.; Warshel, A.; Xu, X.; Aspuru-Guzik, A.; Baer, R.; Bell, A. T.; Besley, N. A.; Chai, J.-D.; Dreuw, A.; Dunietz, B. D.; Furlani, T. R.; Gwaltney, S. R.; Hsu, C.-P.; Jung, Y.; Kong, J.; Lambrecht, D. S.; Liang, W.; Ochsenfeld, C.; Rassolov, V. A.; Slipchenko, L. V.; Subotnik, J. E.; Van Voorhis, T.; Herbert, J. M.; Krylov, A. I.; Gill, P. M. W.; Head-Gordon, M., Advances in molecular quantum chemistry contained in the Q-Chem 4 program package. *Mol. Phys.* **2015,** *113* (2), 184-215.

64. Becke, A. D., A new mixing of Hartree–Fock and local density-functional theories. *J. Chem. Phys.* **1993,** *98* (2), 1372-1377.

65. Lee, C.; Yang, W.; Parr, R. G., Development of the Colle-Salvetti correlation-energy formula into a functional of the electron density. *Phys. Rev. B* **1988,** *37* (2), 785-789.

66. Young, R. M.; Dyar, S. M.; Barnes, J. C.; Juricek, M.; Stoddart, J. F.; Co, D. T.; Wasielewski, M. R., Ultrafast Conformational Dynamics of Electron Transfer in ExBox4+⊂Perylene. *J. Phys. Chem. A* **2013,** *117* (47), 12438-12448.

67. Hartnett, P. E.; Margulies, E. A.; Matte, H. S. S. R.; Hersam, M. C.; Marks, T. J.; Wasielewski, M. R., Effects of Crystalline Perylenediimide Acceptor Morphology on Optoelectronic Properties and Device Performance. *Chem. Mater.* **2016,** *28* (11), 3928-3936.

68. Mauck, C. M.; Young, R. M.; Wasielewski, M. R., Characterization of Excimer Relaxation via Femtosecond Shortwave- and Mid-Infrared Spectroscopy. *J. Phys. Chem. A* **2017,** *121* (4), 784-792.

69. Chen, M.; Bae, Y. J.; Mauck, C. M.; Mandal, A.; Young, R. M.; Wasielewski, M. R., Singlet Fission in Covalent Terrylenediimide Dimers: Probing the Nature of the Multiexciton State Using Femtosecond Mid-Infrared Spectroscopy. *Journal of the American Chemical Society* **2018,** *140* (29), 9184-9192.

70. Rubio, M.; Merchán, M.; Ortí, E., The internal rotational barrier of biphenyl studied with multiconfigurational second-order perturbation theory (CASPT2). *Theoretica chimica acta* **1995,** *91* (1), 17-29.

71. Jia, J.; Wu, H.-S.; Chen, Z.; Mo, Y., Elucidation of the Forces Governing the Stereochemistry of Biphenyl. *Eur. J. Org. Chem.* **2013,** *2013* (3), 611-616.

72. Thompson, A. L.; Ahn, T.-S.; Thomas, K. R. J.; Thayumanavan, S.; Martínez, T. J.; Bardeen, C. J., Using Meta Conjugation To Enhance Charge Separation versus Charge

Recombination in Phenylacetylene Donor−Bridge−Acceptor Complexes. *Journal of the American Chemical Society* **2005,** *127* (47), 16348-16349.
73. Türkmen, G.; Erten-Ela, S.; Icli, S., Highly soluble perylene dyes: Synthesis, photophysical and electrochemical characterizations. *Dyes and Pigments* **2009,** *83* (3), 297-303.
74. Yan, Q.; Zhou, Y.; Zheng, Y.-Q.; Pei, J.; Zhao, D., Towards rational design of organic electron acceptors for photovoltaics: a study based on perylenediimide derivatives. *Chem. Sci.* **2013,** *4* (12), 4389-4394.
75. Kasha, M.; Rawls, H. R.; El-Bayoumi, M. A., THE EXCITON MODEL IN MOLECULAR

SPECTROSCOPY. *Pure Appl. Chem.* **1965,** *11* (4), 371-392.
76. Li, X.; Wang, H.; Schneider, J. A.; Wei, Z.; Lai, W.-Y.; Huang, W.; Wudl, F.; Zheng, Y., Catalyst-free one-step synthesis of ortho-tetraaryl perylene diimides for efficient OPV non-fullerene acceptors. *J. Mater. Chem. C* **2017,** *5* (11), 2781-2785.
77. Brown, K. E.; Salamant, W. A.; Shoer, L. E.; Young, R. M.; Wasielewski, M. R., Direct Observation of Ultrafast Excimer Formation in Covalent Perylenediimide Dimers Using Near-Infrared Transient Absorption Spectroscopy. *J Phys Chem Lett* **2014,** *5* (15), 2588-93.
78. Schill, J.; van Dun, S.; Pouderoijen, M. J.; Janssen, H. M.; Milroy, L.-G.; Schenning, A. P. H. J.; Brunsveld, L., Synthesis and Self-Assembly of Bay-Substituted Perylene Diimide Gemini-Type Surfactants as Off-On Fluorescent Probes for Lipid Bilayers. *Che. Eur. J* **2018,** *24* (30), 7734-7741.
79. Bukauskytė, A.; Karpicz, R.; Striela, R.; Labanauskas, L.; Gruodis, A.; Peckus, D.; Augulis, R.; Gulbinas, V., The influence of substituents of perylenediimides on their spectroscopic properties. *J. Lumin.* **2018,** *195*, 252-258.
80. Alzola, J. M.; Powers-Riggs, N. E.; La Porte, N. T.; Young, R. M.; Marks, T. J.; Wasielewski, M. R., Photoinduced electron transfer from zinc meso-tetraphenylporphyrin to a one-dimensional perylenediimide aggregate: Probing anion delocalization effects. *J. Porphyrins Phthalocyanines* **2019,** *24*, 143-152.
81. Bae, Y. J.; Shimizu, D.; Schultz, J. D.; Kang, G.; Zhou, J.; Schatz, G. C.; Osuka, A.; Wasielewski, M. R., Balancing Charge Transfer and Frenkel Exciton Coupling Leads to Excimer Formation in Molecular Dimers: Implications for Singlet Fission. *J. Phys. Chem. A* **2020,** *124* (41), 8478-8487.
82. Hestand, N. J.; Spano, F. C., Expanded Theory of H- and J-Molecular Aggregates: The Effects of Vibronic Coupling and Intermolecular Charge Transfer. *Chem. Rev.* **2018,** *118* (15), 7069-7163.
83. Brown, K. E.; Salamant, W. A.; Shoer, L. E.; Young, R. M.; Wasielewski, M. R., Direct Observation of Ultrafast Excimer Formation in Covalent Perylenediimide Dimers Using Near-Infrared Transient Absorption Spectroscopy. *The Journal of Physical Chemistry Letters* **2014,** *5* (15), 2588-2593.
84. Lefler, K. M.; Brown, K. E.; Salamant, W. A.; Dyar, S. M.; Knowles, K. E.; Wasielewski, M. R., Triplet State Formation in Photoexcited Slip-Stacked Perylene-3,4:9,10-bis(dicarboximide) Dimers on a Xanthene Scaffold. *J. Phys. Chem. A* **2013,** *117* (40), 10333-10345.

85. Hong, Y.; Kim, J.; Kim, W.; Kaufmann, C.; Kim, H.; Würthner, F.; Kim, D., Efficient Multiexciton State Generation in Charge-Transfer-Coupled Perylene Bisimide Dimers via Structural Control. *Journal of the American Chemical Society* **2020,** *142* (17), 7845-7857.
86. Lang, E.; Hildner, R.; Engelke, H.; Osswald, P.; Würthner, F.; Köhler, J., Comparison of the Photophysical Parameters for Three Perylene Bisimide Derivatives by Single-Molecule Spectroscopy. *ChemPhysChem* **2007,** *8* (10), 1487-1496.
87. Fron, E.; Schweitzer, G.; Osswald, P.; Würthner, F.; Marsal, P.; Beljonne, D.; Müllen, K.; De Schryver, F. C.; Van der Auweraer, M., Photophysical study of bay substituted perylenediimides. *Photochemical & Photobiological Sciences* **2008,** *7* (12), 1509-1521.
88. Dance, Z. E. X.; Mickley, S. M.; Wilson, T. M.; Ricks, A. B.; Scott, A. M.; Ratner, M. A.; Wasielewski, M. R., Intersystem Crossing Mediated by Photoinduced Intramolecular Charge Transfer: Julolidine−Anthracene Molecules with Perpendicular π Systems. *J. Phys. Chem. A* **2008,** *112* (18), 4194-4201.
89. Powers-Riggs, N. E.; Zuo, X.; Young, R. M.; Wasielewski, M. R., Symmetry-Breaking Charge Separation in a Nanoscale Terrylenediimide Guanine-Quadruplex Assembly. *Journal of the American Chemical Society* **2019,** *141* (44), 17512-17516.
90. Weller, A., Photoinduced Electron Transfer in Solution: Exciplex and Radical Ion Pair Formation Free Enthalpies and their Solvent Dependence. *Z. Phys. Chem.* **1982,** *133* (1), 93-98.
91. Kellogg, M.; Akil, A.; Muthiah Ravinson, D. S.; Estergreen, L.; Bradforth, S. E.; Thompson, M. E., Symmetry breaking charge transfer as a means to study electron transfer with no driving force. *Faraday Discuss.* **2019,** *216* (0), 379-394.
92. Marcus, R. A., On the Theory of Oxidation-Reduction Reactions Involving Electron Transfer. I. *J. Chem. Phys.* **1956,** *24* (5), 966-978.
93. Marcus, R. A., On the Theory of Electron-Transfer Reactions. VI. Unified Treatment for Homogeneous and Electrode Reactions. *J. Chem. Phys.* **1965,** *43* (2), 679-701.
94. Wu, Y.; Zhou, J.; Phelan, B. T.; Mauck, C. M.; Stoddart, J. F.; Young, R. M.; Wasielewski, M. R., Probing Distance Dependent Charge-Transfer Character in Excimers of Extended Viologen Cyclophanes Using Femtosecond Vibrational Spectroscopy. *Journal of the American Chemical Society* **2017,** *139* (40), 14265-14276.
95. Yu, Z.; Wu, Y.; Peng, Q.; Sun, C.; Chen, J.; Yao, J.; Fu, H., Accessing the Triplet State in Heavy-Atom-Free Perylene Diimides. *Che. Eur. J* **2016,** *22* (14), 4717-4722.
96. Veldman, D.; Chopin, S. M. A.; Meskers, S. C. J.; Groeneveld, M. M.; Williams, R. M.; Janssen, R. A. J., Triplet Formation Involving a Polar Transition State in a Well-Defined Intramolecular Perylenediimide Dimeric Aggregate. *J. Phys. Chem. A* **2008,** *112* (26), 5846-5857.
97. Mohan, A.; Sebastian, E.; Gudem, M.; Hariharan, M., Near-Quantitative Triplet State Population via Ultrafast Intersystem Crossing in Perbromoperylenediimide. *J. Phys. Chem. B* **2020,** *124* (31), 6867-6874.
98. Bolton, O.; Lee, K.; Kim, H.-J.; Lin, K. Y.; Kim, J., Activating efficient phosphorescence from purely organic materials by crystal design. *Nat. Chem.* **2011,** *3* (3), 205-210.
99. Nagarajan, K.; Mallia, A. R.; Muraleedharan, K.; Hariharan, M., Enhanced intersystem crossing in core-twisted aromatics. *Chem. Sci.* **2017,** *8* (3), 1776-1782.

100. Ito, S.; Hiroto, S.; Shinokubo, H., Synthesis of Pyridine-Fused Perylene Imides with an Amidine Moiety for Hydrogen Bonding. *Org. Lett.* **2013,** *15* (12), 3110-3113.
101. Leo, K., Organic photovoltaics. *Nat. Rev. Mater.* **2016,** *1* (8), 16056.
102. Pivrikas, A.; Sariciftci, N. S.; Juska, G.; Osterbacka, R., A review of charge transport and recombination in polymer/fullerene organic solar cells. *Prog. Photovoltaics* **2007,** *15* (8), 677-696.
103. Nelson, J., Polymer:fullerene bulk heterojunction solar cells. *Materials Today* **2011,** *14* (10), 462-470.
104. Brabec, C. J.; Gowrisanker, S.; Halls, J. J.; Laird, D.; Jia, S.; Williams, S. P., Polymer-fullerene bulk-heterojunction solar cells. *Adv. Mater.* **2010,** *22* (34), 3839-56.
105. Park, S. H.; Roy, A.; Beaupré, S.; Cho, S.; Coates, N.; Moon, J. S.; Moses, D.; Leclerc, M.; Lee, K.; Heeger, A. J., Bulk heterojunction solar cells with internal quantum efficiency approaching 100%. *Nat. Photonics* **2009,** *3*, 297.
106. Facchetti, A., π-Conjugated Polymers for Organic Electronics and Photovoltaic Cell Applications. *Chem. Mater.* **2011,** *23* (3), 733-758.
107. Dou, L.; Liu, Y.; Hong, Z.; Li, G.; Yang, Y., Low-Bandgap Near-IR Conjugated Polymers/Molecules for Organic Electronics. *Chem. Rev.* **2015,** *115* (23), 12633-12665.
108. Ganesamoorthy, R.; Sathiyan, G.; Sakthivel, P., Review: Fullerene based acceptors for efficient bulk heterojunction organic solar cell applications. *Sol. Energy Mater. Sol. Cells* **2017,** *161*, 102-148.
109. Zhu, D.; Bao, X.; Ouyang, D.; Wang, J.; Yuan, X.; Wang, Q.; Zhou, D.; Wen, S.; Yang, R., Single-junction fullerene solar cells with 10% efficiency and high open-circuit voltage approaching 1V. *Nano Energy* **2017,** *40*, 495-503.
110. Matsuo, Y.; Ozu, A.; Obata, N.; Fukuda, N.; Tanaka, H.; Nakamura, E., Deterioration of bulk heterojunction organic photovoltaic devices by a minute amount of oxidized fullerene. *Chem. Commun.* **2012,** *48* (32), 3878-3880.
111. Nielsen, C. B.; Holliday, S.; Chen, H.-Y.; Cryer, S. J.; McCulloch, I., Non-Fullerene Electron Acceptors for Use in Organic Solar Cells. *Acc. Chem. Res.* **2015,** *48* (11), 2803-2812.
112. Yan, C.; Barlow, S.; Wang, Z.; Yan, H.; Jen, A. K. Y.; Marder, S. R.; Zhan, X., Non-fullerene acceptors for organic solar cells. *Nature Reviews Materials* **2018,** *3*, 18003.
113. Chen, W.; Zhang, Q., Recent progress in non-fullerene small molecule acceptors in organic solar cells (OSCs). *J. Mat. Chem. C* **2017,** *5* (6), 1275-1302.
114. Li, C.; Wonneberger, H., Perylene Imides for Organic Photovoltaics: Yesterday, Today, and Tomorrow. *Adv. Mater.* **2012,** *24* (5), 613-636.
115. Nowak-Krol, A.; Wuerthner, F., Progress in the synthesis of perylene bisimide dyes. *Org. Chem. Front.* **2019,** *6* (8), 1272-1318.
116. Liu, Z.; Wu, Y.; Zhang, Q.; Gao, X., Non-fullerene small molecule acceptors based on perylene diimides. *J. Mat. Chem. A* **2016,** *4* (45), 17604-17622.
117. Gehrig, D. W.; Howard, I. A.; Sweetnam, S.; Burke, T. M.; McGehee, M. D.; Laquai, F., The Impact of Donor–Acceptor Phase Separation on the Charge Carrier Dynamics in pBTTT:PCBM Photovoltaic Blends. *Macromol. Rapid Commun.* **2015,** *36* (11), 1054-1060.
118. Deibel, C.; Strobel, T.; Dyakonov, V., Role of the Charge Transfer State in Organic Donor–Acceptor Solar Cells. *Adv. Mater.* **2010,** *22* (37), 4097-4111.
119. Onsager, L., Initial Recombination of Ions. *Phys. Rev.* **1938,** *54* (8), 554-557.

120. Braun, C. L., Electric field assisted dissociation of charge transfer states as a mechanism of photocarrier production. *J. Chem. Phys.* **1984,** *80* (9), 4157-4161.
121. Thompson, B. C.; Frechet, J. M., Polymer-fullerene composite solar cells. *Angew. Chem. Int. Ed. Engl.* **2008,** *47* (1), 58-77.
122. Street, R. A.; Cowan, S.; Heeger, A. J., Experimental test for geminate recombination applied to organic solar cells. *Phys. Rev. B* **2010,** *82* (12), 121301.
123. Clarke, T. M.; Durrant, J. R., Charge Photogeneration in Organic Solar Cells. *Chem. Rev.* **2010,** *110* (11), 6736-6767.
124. Liu, T.; Troisi, A., What Makes Fullerene Acceptors Special as Electron Acceptors in Organic Solar Cells and How to Replace Them. *Adv. Mater.* **2012,** *25* (7), 1038-1041.
125. Liu, J.; Chen, S.; Qian, D.; Gautam, B.; Yang, G.; Zhao, J.; Bergqvist, J.; Zhang, F.; Ma, W.; Ade, H.; Inganäs, O.; Gundogdu, K.; Gao, F.; Yan, H., Fast charge separation in a non-fullerene organic solar cell with a small driving force. *Nat. Energy* **2016,** *1*, 16089.
126. Natali, M.; Campagna, S.; Scandola, F., Photoinduced electron transfer across molecular bridges: electron- and hole-transfer superexchange pathways. *Chem. Soc. Rev.* **2014,** *43* (12), 4005-4018.
127. Greenfield, S. R.; Wasielewski, M. R., Near-transform-limited visible and near-IR femtosecond pulses from optical parametric amplification using type II β-barium borate. *Opt. Lett.* **1995,** *20* (12), 1394-6.
128. Mauck, C. M.; Young, R. M.; Wasielewski, M. R., Characterization of Excimer Relaxation via Femtosecond Shortwave- and Mid-Infrared Spectroscopy. *J. Phys. Chem. A* **2017,** *121* (4), 784-792.
129. Akimoto, S.; Yamazaki, T.; Yamazaki, I.; Osuka, A., Excitation relaxation of zinc and free-base porphyrin probed by femtosecond fluorescence spectroscopy. *Chem. Phys. Lett.* **1999,** *309* (3), 177-182.
130. Kirstein, S.; Bourbon, S.; Gao, M.; De Rossi, U., Layer-by-layer deposition of J-aggregates and polyelectrolytes for electroluminescence applications: A spectroscopic study. *Isr. J. Chem.* **2010,** *40* (2), 129-138.
131. Sarbu, A.; Biniek, L.; Guenet, J.-M.; Mesini, P. J.; Brinkmann, M., Reversible J- to H-aggregate transformation in thin films of a perylenebisimide organogelator. *J. Mat. Chem. C* **2015,** *3* (6), 1235-1242.
132. Moravec, D. B.; Lovaasen, B. M.; Hopkins, M. D., Near-infrared transient-absorption spectroscopy of zinc tetraphenylporphyrin and related compounds. Observation of bands that selectively probe the S1 excited state. *Journal of Photochemistry and Photobiology A: Chemistry* **2013,** *254*, 20-24.
133. Gosztola, D.; Niemczyk, M. P.; Svec, W.; Lukas, A. S.; Wasielewski, M. R., Excited Doublet States of Electrochemically Generated Aromatic Imide and Diimide Radical Anions. *J. Phys. Chem. A* **2000,** *104* (28), 6545-6551.
134. Fajer, J.; Borg, D. C.; Forman, A.; Dolphin, D.; Felton, R. H., . pi.-Cation radicals and dications of metalloporphyrins. *Journal of the American Chemical Society* **1970,** *92* (11), 3451-3459.
135. Song, O.-K.; Yoon, M.-J.; Chang, J.-R.; Kim, D., Comparative Vibrational Spectroscopic Studies between Nickel, Zinc, Tetraphenylporphyrins and Tetraphenylchlorins. *Bull. Korean. Chem. Soc.* **1989,** *10*, 39-47.

136. Gross, Z.; Barzilay, C., Spectroscopic Characterization of Two Types of Tetraarylporphyrin Cation Radicals. *Angew. Chem. Int. Ed.* **1992,** *31* (12), 1615-1617.
137. Andersson, L. A.; Loehr, T. M.; Stershic, M. T.; Stolzenberg, A. M., Spectral properties of cis- and trans-metallooctaethylchlorins: effects of pyrroline ring stereochemistry and macrocyclic conformation. *Inorg. Chem.* **1990,** *29* (12), 2278-2285.
138. Clayton, A. H. A.; Scholes, G. D.; Ghiggino, K. P.; Paddon-Row, M. N., Through-Bond and Through-Space Coupling in Photoinduced Electron and Energy Transfer: An ab Initio and Semiempirical Study. *J. Phys. Chem.* **1996,** *100* (26), 10912-10918.
139. Shao, C.; Grüne, M.; Stolte, M.; Würthner, F., Perylene Bisimide Dimer Aggregates: Fundamental Insights into Self-Assembly by NMR and UV/Vis Spectroscopy. *Che. Eur. J* **2012,** *18* (43), 13665-13677.
140. Kaufmann, C.; Kim, W.; Nowak-Król, A.; Hong, Y.; Kim, D.; Würthner, F., Ultrafast Exciton Delocalization, Localization, and Excimer Formation Dynamics in a Highly Defined Perylene Bisimide Quadruple π-Stack. *Journal of the American Chemical Society* **2018,** *140* (12), 4253-4258.
141. Mani, T.; Grills, D. C.; Newton, M. D.; Miller, J. R., Electron Localization of Anions Probed by Nitrile Vibrations. *J. Am. Chem. Soc.* **2015,** *137* (34), 10979-10991.
142. Koch, M.; Letrun, R.; Vauthey, E., Exciplex Formation in Bimolecular Photoinduced Electron-Transfer Investigated by Ultrafast Time-Resolved Infrared Spectroscopy. *J. Am. Chem. Soc.* **2014,** *136* (10), 4066-4074.
143. Margulies, E. A.; Kerisit, N.; Gawel, P.; Mauck, C. M.; Ma, L.; Miller, C. E.; Young, R. M.; Trapp, N.; Wu, Y.-L.; Diederich, F.; Wasielewski, M. R., Substituent Effects on Singlet Exciton Fission in Polycrystalline Thin Films of Cyano-Substituted Diaryltetracenes. *J. Phys. Chem. C* **2017,** *121* (39), 21262-21271.
144. Mauck, C. M. Effects of Intermolecular Coupling on Excimer Formation and Singlet Fission. Northwestern University, Evanston, IL, 2017.
145. Tauber, M. J.; Kelley, R. F.; Giaimo, J. M.; Rybtchinski, B.; Wasielewski, M. R., Electron Hopping in π-Stacked Covalent and Self-Assembled Perylene Diimides Observed by ENDOR Spectroscopy. *J. Am. Chem. Soc.* **2006,** *128* (6), 1782-1783.
146. Pan, Q.-Q.; Li, S.-B.; Duan, Y.-C.; Wu, Y.; Zhang, J.; Geng, Y.; Zhao, L.; Su, Z.-M., Exploring what prompts ITIC to become a superior acceptor in organic solar cell by combining molecular dynamics simulation with quantum chemistry calculation. *Phys. Chem. Chem. Phys.* **2017,** *19* (46), 31227-31235.
147. Walwark, D. J.; Datko, B. D.; Wu, Q.; Neshchadin, A.; Berrens, M. L.; Yu, L.; Grey, J. K., Conformational Flexibility Determines Electronic Coupling and Charge Transfer Character in Single Propeller-Shaped Perylene Diimide Tetramer Arrays. *J. Phys. Chem. C* **2018,** *122* (41), 23261-23270.
148. Carlotti, B.; Cai, Z.; Kim, H.; Sharapov, V.; Madu, I. K.; Zhao, D.; Chen, W.; Zimmerman, P. M.; Yu, L.; Goodson, T., Charge Transfer and Aggregation Effects on the Performance of Planar vs. Twisted Nonfullerene Acceptor Isomers for Organic Solar Cells. *Chem. Mater.* **2018,** *30* (13), 4263-4276.
149. Shimizu, K. D.; Dewey, T. M.; Rebek, J., Jr., Convergent Functional Groups. 15. Synthetic and Structural Studies of Large and Rigid Molecular Clefts. *Journal of the American Chemical Society* **1994,** *116* (12), 5145-5149.

150. Wang, R.; Shi, Z.; Zhang, C.; Zhang, A.; Chen, J.; Guo, W.; Sun, Z., Facile synthesis and controllable bromination of asymmetrical intermediates of perylene monoanhydride/monoimide diester. *Dyes and Pigments* **2013,** *98* (3), 450-458.
151. Mickley Conron, S. M.; Shoer, L. E.; Smeigh, A. L.; Ricks, A. B.; Wasielewski, M. R., Photoinitiated Electron Transfer in Zinc Porphyrin–Perylenediimide Cruciforms and Their Self-Assembled Oligomers. *J. Phys. Chem. B* **2013,** *117* (7), 2195-2204.
152. Hayes, R. T.; Walsh, C. J.; Wasielewski, M. R., Competitive Electron Transfer from the S2 and S1 Excited States of Zinc meso-Tetraphenylporphyrin to a Covalently Bound Pyromellitimide: Dependence on Donor−Acceptor Structure and Solvent. *J. Phys. Chem. A* **2004,** *108* (13), 2375-2381.
153. Piotrowiak, P., Photoinduced electron transfer in molecular systems: recent developments. *Chem. Soc. Rev.* **1999,** *28* (2), 143-150.
154. Ørnsø, K. B.; Jónsson, E. Ö.; Jacobsen, K. W.; Thygesen, K. S., Importance of the Reorganization Energy Barrier in Computational Design of Porphyrin-Based Solar Cells with Cobalt-Based Redox Mediators. *J. Phys. Chem. C* **2015,** *119* (23), 12792-12800.
155. Lu, L.; Zheng, T.; Wu, Q.; Schneider, A. M.; Zhao, D.; Yu, L., Recent Advances in Bulk Heterojunction Polymer Solar Cells. *Chem. Rev.* **2015,** *115* (23), 12666-12731.
156. He, Y.; Li, Y., Fullerene derivative acceptors for high performance polymer solar cells. *Phys. Chem. Chem. Phys.* **2011,** *13*, 1970.
157. Yu, G.; Gao, J.; Hummelen, J. C.; Wudl, F.; Heeger, A. J., Polymer Photovoltaic Cells: Enhanced Efficiencies via a Network of Internal Donor-Acceptor Heterojunctions. *Science* **1995,** *270* (5243 %U http://www.sciencemag.org/content/270/5243/1789.abstract), 1789-1791.
158. Hou, J.; Inganäs, O.; Friend, R. H.; Gao, F., Organic solar cells based on non-fullerene acceptors. *Nat. Mater.* **2018,** *17*, 119.
159. Li, S.; Zhan, L.; Sun, C.; Zhu, H.; Zhou, G.; Yang, W.; Shi, M.; Li, C. Z.; Hou, J.; Li, Y.; Chen, H., Highly Efficient Fullerene-Free Organic Solar Cells Operate at Near Zero Highest Occupied Molecular Orbital Offsets. *J. Am. Chem. Soc.* **2019,** *141*, 3073.
160. Ziffer, M. E.; Jo, S. B.; Zhong, H.; Ye, L.; Liu, H.; Lin, F.; Zhang, J.; Li, X.; Ade, H. W.; Jen, A. K.; Ginger, D. S., Long-Lived, Non-Geminate, Radiative Recombination of Photogenerated Charges in a Polymer/Small-Molecule Acceptor Photovoltaic Blend. *J. Am. Chem. Soc.* **2018,** *140*, 9996.
161. Meng, L.; Zhang, Y.; Wan, X.; Li, C.; Zhang, X.; Wang, Y.; Ke, X.; Xiao, Z.; Ding, L.; Xia, R.; Yip, H.-L.; Cao, Y.; Chen, Y., Organic and solution-processed tandem solar cells with 17.3% efficiency. *Science* **2018,** *361* (6407), 1094.
162. Vandewal, K.; Albrecht, S.; Hoke, E. T.; Graham, K. R.; Widmer, J.; Douglas, J. D.; Schubert, M.; Mateker, W. R.; Bloking, J. T.; Burkhard, G. F.; Sellinger, A.; Fréchet, J. M. J.; Amassian, A.; Riede, M. K.; McGehee, M. D.; Neher, D.; Salleo, A., Efficient charge generation by relaxed charge-transfer states at organic interfaces. *Nat. Mater.* **2014,** *13*, 63.
163. Aldrich, T. J.; Matta, M.; Zhu, W.; Swick, S. M.; Stern, C. L.; Schatz, G. C.; Facchetti, A.; Melkonyan, F. S.; Marks, T. J., Fluorination Effects on Indacenodithienothiophene Acceptor Packing and Electronic Structure, End-Group Redistribution, and Solar Cell Photovoltaic Response. *J. Am. Chem. Soc.* **2019,** *141*, 3274.

164. Zhang, G.; Zhao, J.; Chow, P. C. Y.; Jiang, K.; Zhang, J.; Zhu, Z.; Zhang, J.; Huang, F.; Yan, H., Nonfullerene Acceptor Molecules for Bulk Heterojunction Organic Solar Cells. *Chem. Rev.* **2018,** *118* (7), 3447-3507.
165. Swick, S. M.; Gebraad, T.; Jones, L.; Fu, B.; Aldrich, T. J.; Kohlstedt, K. L.; Schatz, G. C.; Facchetti, A.; Marks, T. J., Building Blocks for High-Efficiency Organic Photovoltaics. Interplay of Molecular, Crystal, and Electronic Properties of Post-Fullerene ITIC Ensembles. *ChemPhysChem* **2019**.
166. Sisto, T. J.; Zhong, Y.; Zhang, B.; Trinh, M. T.; Miyata, K.; Zhong, X.; Zhu, X. Y.; Steigerwald, M. L.; Ng, F.; Nuckolls, C., Long, Atomically Precise Donor–Acceptor Cove-Edge Nanoribbons as Electron Acceptors. *J. Am. Chem. Soc.* **2017,** *139*, 5648.
167. Zhang, G.; Zhao, J.; Chow, P. C. Y.; Jiang, K.; Zhang, J.; Zhu, Z.; Zhang, J.; Huang, F.; Yan, H., Nonfullerene Acceptor Molecules for Bulk Heterojunction Organic Solar Cells. *Chem. Rev.* **2018,** *118*, 3447.
168. Dai, S.; Zhao, F.; Zhang, Q.; Lau, T. K.; Li, T.; Liu, K.; Ling, Q.; Wang, C.; Lu, X.; You, W.; Zhan, X., Fused Nonacyclic Electron Acceptors for Efficient Polymer Solar Cells. *J. Am. Chem. Soc.* **2017,** *139*, 1336.
169. Gao, W.; An, Q.; Ming, R.; Xie, D.; Wu, K.; Luo, Z.; Zou, Y.; Zhang, F.; Yang, C., Side Group Engineering of Small Molecular Acceptors for High-Performance Fullerene-Free Polymer Solar Cells: Thiophene Being Superior to Selenophene. *Adv. Funct. Mater.* **2017,** *27*, 1702194.
170. Lv, A.; Puniredd, S. R.; Zhang, J.; Li, Z.; Zhu, H.; Jiang, W.; Dong, H.; He, Y.; Jiang, L.; Li, Y.; Pisula, W.; Meng, Q.; Hu, W.; Wang, Z., High Mobility, Air Stable, Organic Single Crystal Transistors of an n-Type Diperylene Bisimide. *Adv. Mater.* **2012,** *24*, 2626.
171. Gsanger, M.; Oh, J. H.; Konemann, M.; Hoffken, H. W.; Krause, A. M.; Bao, Z.; Wurthner, F., A crystal-engineered hydrogen-bonded octachloroperylene diimide with a twisted core: an n-channel organic semiconductor. *Angew. Chem., Int. Ed.* **2010,** *49*, 740.
172. Margulies, E. A.; Miller, C. E.; Wu, Y.; Ma, L.; Schatz, G. C.; Young, R. M.; Wasielewski, M. R., Enabling singlet fission by controlling intramolecular charge transfer in π-stacked covalent terrylenediimide dimers. *Nat. Chem.* **2016,** *8* (12), 1120-1125.
173. Weiss, E. A.; Ahrens, M. J.; Sinks, L. E.; Gusev, A. V.; Ratner, M. A.; Wasielewski, M. R., Making a Molecular Wire: Charge and Spin Transport through para-Phenylene Oligomers. *J. Am. Chem. Soc.* **2004,** *126*, 5577.
174. Duan, Y.; Xu, X.; Yan, H.; Wu, W.; Li, Z.; Peng, Q., Pronounced Effects of a Triazine Core on Photovoltaic Performance-Efficient Organic Solar Cells Enabled by a PDI Trimer-Based Small Molecular Acceptor. *Adv. Mater.* **2017,** *29*, 1605115.
175. Liang, N. N.; Zhu, X. X.; Zheng, Z.; Meng, D.; Liu, G. G.; Zhang, J. Q.; Li, S. S.; Li, Y.; Hou, J. H.; Hu, B.; Wang, Z. H., Tuning Charge Generation Process of Rylene Imide-Based Solar Cells via Chalcogen-Atom-Annulation. *Chem. Mater.* **2019,** *31*, 3636.
176. Luo, Z.; Liu, T.; Chen, Z.; Xiao, Y.; Zhang, G.; Huo, L.; Zhong, C.; Lu, X.; Yan, H.; Sun, Y.; Yang, C., Isomerization of Perylene Diimide Based Acceptors Enabling High-Performance Nonfullerene Organic Solar Cells with Excellent Fill Factor. *Adv. Sci. (Weinh)* **2019,** *6*, 1802065.
177. Eastham, N. D.; Dudnik, A. S.; Aldrich, T. J.; Manley, E. F.; Fauvell, T. J.; Hartnett, P. E.; Wasielewski, M. R.; Chen, L. X.; Melkonyan, F. S.; Facchetti, A.; Chang, R. P. H.;

Marks, T. J., Small Molecule Acceptor and Polymer Donor Crystallinity and Aggregation Effects on Microstructure Templating: Understanding Photovoltaic Response in Fullerene-Free Solar Cells. *Chem. Mater.* **2017,** *29*, 4432.
178. Hartnett, P. E.; Margulies, E. A.; Matte, H. S. S. R.; Hersam, M. C.; Marks, T. J.; Wasielewski, M. R., Effects of Crystalline Perylenediimide Acceptor Morphology on Optoelectronic Properties and Device Performance. *Chem. Mater.* **2016,** *28*, 3928.
179. Zhang, Q.; Kelly, M. A.; Bauer, N.; You, W., The Curious Case of Fluorination of Conjugated Polymers for Solar Cells. *Acc. Chem. Res.* **2017,** *50*, 2401.
180. Yoon, M. H.; Facchetti, A.; Stern, C. E.; Marks, T. J., Fluorocarbon-Modified Organic Semiconductors: Molecular Architecture, Electronic, and Crystal Structure Tuning of Arene- versus Fluoroarene-Thiophene Oligomer Thin-Film Properties. *J. Am. Chem. Soc.* **2006,** *128*, 5792.
181. Leclerc, N.; Chavez, P.; Ibraikulov, O. A.; Heiser, T.; Leveque, P., Impact of Backbone Fluorination on pi-Conjugated Polymers in Organic Photovoltaic Devices: A Review. *Polymers (Basel, Switz.)* **2016,** *8*, 11.
182. Benatto, L.; Koehler, M., Effects of Fluorination on Exciton Binding Energy and Charge Transport of π-Conjugated Donor Polymers and the ITIC Molecular Acceptor: A Theoretical Study. *J. Phys. Chem. C* **2019,** *123*, 6395.
183. Stuart, A. C.; Tumbleston, J. R.; Zhou, H.; Li, W.; Liu, S.; Ade, H.; You, W., Fluorine Substituents Reduce Charge Recombination and Drive Structure and Morphology Development in Polymer Solar Cells. *J. Am. Chem. Soc.* **2013,** *135*, 1806.
184. Carsten, B.; Szarko, J. M.; Lu, L.; Son, H. J.; He, F.; Botros, Y. Y.; Chen, L. X.; Yu, L., Mediating Solar Cell Performance by Controlling the Internal Dipole Change in Organic Photovoltaic Polymers. *Macromolecules* **2012,** *45*, 6390.
185. Valeev, E. F.; Coropceanu, V.; da Silva Filho, D. A.; Salman, S.; Brédas, J. L., Effect of Electronic Polarization on Charge-Transport Parameters in Molecular Organic Semiconductors. *J. Am. Chem. Soc.* **2006,** *128*, 9882.
186. Aldrich, T. J.; Zhu, W.; Mukherjee, S.; Richter, L. J.; Gann, E.; DeLongchamp, D. M.; Facchetti, A.; Melkonyan, F. S.; Marks, T. J., Stable Postfullerene Solar Cells via Direct C-H Arylation Polymerization. Morphology-Performance Relationships. *Chem. Mater.* **2019,** *31* (11), 4313-4321.
187. Dudnik, A. S.; Aldrich, T. J.; Eastham, N. D.; Chang, R. P. H.; Facchetti, A.; Marks, T. J., Tin-Free Direct C–H Arylation Polymerization for High Photovoltaic Efficiency Conjugated Copolymers. *J. Am. Chem. Soc.* **2016,** *138*, 15699.
188. Seo, J. H.; Nguyen, T.-Q., Electronic Properties of Conjugated Polyelectrolyte Thin Films. *Journal of the American Chemical Society* **2008,** *130* (31), 10042-10043.
189. Henson, Z. B.; Welch, G. C.; van der Poll, T.; Bazan, G. C., Pyridalthiadiazole-Based Narrow Band Gap Chromophores. *J Am Chem Soc* **2012,** *134* (8), 3766-3779.
190. Jiang, Z.; Li, X.; Strzalka, J.; Sprung, M.; Sun, T.; Sandy, A. R.; Narayanan, S.; Lee, D. R.; Wang, J., The dedicated high-resolution grazing-incidence X-ray scattering beamline 8-ID-E at the Advanced Photon Source. *Journal of Synchrotron Radiation* **2012,** *19* (4), 627-636.
191. Jiang, Z., GIXSGUI is available for download: http://www.aps.anl.gov/Sectors/

Sector8/Operations/GIXSGUI.html.

192. Eastham, N. D.; Logsdon, J. L.; Manley, E. F.; Aldrich, T. J.; Leonardi, M. J.; Wang, G.; Powers-Riggs, N. E.; Young, R. M.; Chen, L. X.; Wasielewski, M. R.; Melkonyan, F. S.; Chang, R. P. H.; Marks, T. J., Hole-Transfer Dependence on Blend Morphology and Energy Level Alignment in Polymer: ITIC Photovoltaic Materials. *Adv. Mater.* **2018,** *30*, 1704263.
193. Plasser, F.; Lischka, H., Analysis of Excitonic and Charge Transfer Interactions from Quantum Chemical Calculations. *Journal of Chemical Theory and Computation* **2012,** *8* (8), 2777-2789.
194. Surján, P. R., Natural orbitals in CIS and singular-value decomposition. *Chem. Phys. Lett.* **2007,** *439* (4), 393-394.
195. Richard, R. M.; Herbert, J. M., Time-Dependent Density-Functional Description of the 1La State in Polycyclic Aromatic Hydrocarbons: Charge-Transfer Character in Disguise? *Journal of Chemical Theory and Computation* **2011,** *7* (5), 1296-1306.
196. He, Z.; Xiao, B.; Liu, F.; Wu, H.; Yang, Y.; Xiao, S.; Wang, C.; Russell, T. P.; Cao, Y., Single-junction polymer solar cells with high efficiency and photovoltage. *Nat. Photonics* **2015,** *9*, 174.
197. Liao, S. H.; Jhuo, H. J.; Cheng, Y. S.; Chen, S. A., Fullerene Derivative-Doped Zinc Oxide Nanofilm as the Cathode of Inverted Polymer Solar Cells with Low-Bandgap Polymer (PTB7-Th) for High Performance. *Adv. Mater.* **2013,** *25*, 4766.
198. Dudnik, A. S.; Aldrich, T. J.; Eastham, N. D.; Chang, R. P. H.; Facchetti, A.; Marks, T. J., Tin-Free Direct C-H Arylation Polymerization for High Photovoltaic Efficiency Conjugated Copolymers. *J. Am. Chem. Soc.* **2016,** *138* (48), 15699-15709.
199. Lu, L.; Chen, W.; Xu, T.; Yu, L., High-performance ternary blend polymer solar cells involving both energy transfer and hole relay processes. *Nat. Commun.* **2015,** *6*, 7327.
200. Kawashima, K.; Tamai, Y.; Ohkita, H.; Osaka, I.; Takimiya, K., High-efficiency polymer solar cells with small photon energy loss. *Nat. Commun.* **2015,** *6*, 10085.
201. Yao, J.; Kirchartz, T.; Vezie, M. S.; Faist, M. A.; Gong, W.; He, Z.; Wu, H.; Troughton, J.; Watson, T.; Bryant, D.; Nelson, J., Quantifying Losses in Open-Circuit Voltage in Solution-Processable Solar Cells. *Phys. Rev. Appl.* **2015,** *4*, 014020.
202. Xu, X.; Yu, T.; Bi, Z.; Ma, W.; Li, Y.; Peng, Q., Realizing Over 13% Efficiency in Green-Solvent-Processed Nonfullerene Organic Solar Cells Enabled by 1,3,4-Thiadiazole-Based Wide-Bandgap Copolymers. *Adv. Mater.* **2018,** *30*, 1703973.
203. Yao, Z.; Liao, X.; Gao, K.; Lin, F.; Xu, X.; Shi, X.; Zuo, L.; Liu, F.; Chen, Y.; Jen, A. K., Dithienopicenocarbazole-Based Acceptors for Efficient Organic Solar Cells with Optoelectronic Response Over 1000 nm and an Extremely Low Energy Loss. *J. Am. Chem. Soc.* **2018,** *140*, 2054.
204. Chen, S.; Liu, Y.; Zhang, L.; Chow, P. C. Y.; Wang, Z.; Zhang, G.; Ma, W.; Yan, H., A Wide-Bandgap Donor Polymer for Highly Efficient Non-fullerene Organic Solar Cells with a Small Voltage Loss. *J. Am. Chem. Soc.* **2017,** *139*, 6298.
205. Eisner, F. D.; Azzouzi, M.; Fei, Z.; Hou, X.; Anthopoulos, T. D.; Dennis, T. J. S.; Heeney, M.; Nelson, J., Hybridization of Local Exciton and Charge-Transfer States Reduces Nonradiative Voltage Losses in Organic Solar Cells. *Journal of the American Chemical Society* **2019,** *141* (15), 6362-6374.
206. Ullbrich, S.; Benduhn, J.; Jia, X.; Nikolis, V. C.; Tvingstedt, K.; Piersimoni, F.; Roland, S.; Liu, Y.; Wu, J.; Fischer, A.; Neher, D.; Reineke, S.; Spoltore, D.; Vandewal, K.,

Emissive and charge-generating donor-acceptor interfaces for organic optoelectronics with low voltage losses. *Nat. Mater.* **2019,** *18*, 459.
207. Murgatroyd, P. N., Theory of space-charge-limited current enhanced by Frenkel effect. *J. Phys. D: Appl. Phys.* **1970,** *3*, 151.
208. Swick, S. M.; Zhu, W.; Matta, M.; Aldrich, T. J.; Harbuzaru, A.; Lopez Navarrete, J. T.; Ponce Ortiz, R.; Kohlstedt, K. L.; Schatz, G. C.; Facchetti, A.; Melkonyan, F. S.; Marks, T. J., Closely packed, low reorganization energy π-extended postfullerene acceptors for efficient polymer solar cells. *Proceedings of the National Academy of Sciences* **2018,** *115* (36), E8341.
209. Mukherjee, S.; Herzing, A. A.; Zhao, D.; Wu, Q.; Yu, L.; Ade, H.; DeLongchamp, D. M.; Richter, L. J., Morphological characterization of fullerene and fullerene-free organic photovoltaics by combined real and reciprocal space techniques. *J. Mater. Res.* **2017,** *32*, 1921.
210. DeLongchamp, D. M.; Kline, R. J.; Herzing, A., Nanoscale structure measurements for polymer-fullerene photovoltaics. *Energy Environ. Sci.* **2012,** *5*, 5980.
211. Huang, Y.; Kramer, E. J.; Heeger, A. J.; Bazan, G. C., Bulk Heterojunction Solar Cells: Morphology and Performance Relationships. *Chem. Rev.* **2014,** *114*, 7006.
212. Gélinas, S.; Rao, A.; Kumar, A.; Smith, S. L.; Chin, A. W.; Clark, J.; van der Poll, T. S.; Bazan, G. C.; Friend, R. H., Ultrafast Long-Range Charge Separation in Organic Semiconductor Photovoltaic Diodes. *Science* **2014,** *343*, 512.
213. Kan, B.; Zhang, J.; Liu, F.; Wan, X.; Li, C.; Ke, X.; Wang, Y.; Feng, H.; Zhang, Y.; Long, G.; Friend, R. H.; Bakulin, A. A.; Chen, Y., Fine-Tuning the Energy Levels of a Nonfullerene Small-Molecule Acceptor to Achieve a High Short-Circuit Current and a Power Conversion Efficiency over 12% in Organic Solar Cells. *Adv. Mater.* **2018,** *30*, 1704904.
214. Cowan, S. R.; Roy, A.; Heeger, A. J., Recombination in polymer-fullerene bulk heterojunction solar cells. *Phys. Rev. B: Condens. Matter Mater. Phys.* **2010,** *82*, 245207.
215. Rolczynski, B. S.; Szarko, J. M.; Son, H. J.; Liang, Y.; Yu, L.; Chen, L. X., Ultrafast Intramolecular Exciton Splitting Dynamics in Isolated Low-Band-Gap Polymers and Their Implications in Photovoltaic Materials Design. *Journal of the American Chemical Society* **2012,** *134* (9), 4142-4152.
216. Carsten, B.; Szarko, J. M.; Son, H. J.; Wang, W.; Lu, L.; He, F.; Rolczynski, B. S.; Lou, S. J.; Chen, L. X.; Yu, L., Examining the Effect of the Dipole Moment on Charge Separation in Donor–Acceptor Polymers for Organic Photovoltaic Applications. *J. Am. Chem. Soc.* **2011,** *133*, 20468.
217. Rieger, R.; Beckmann, D.; Mavrinskiy, A.; Kastler, M.; Müllen, K., Backbone Curvature in Polythiophenes. *Chem. Mater.* **2010,** *22*, 5314.
218. Lee, W.; Kim, G. H.; Ko, S. J.; Yum, S.; Hwang, S.; Cho, S.; Shin, Y. H.; Kim, J. Y.; Woo, H. Y., Semicrystalline D–A Copolymers with Different Chain Curvature for Applications in Polymer Optoelectronic Devices. *Macromolecules* **2014,** *47*, 1604.
219. Jackson, N. E.; Savoie, B. M.; Kohlstedt, K. L.; Marks, T. J.; Chen, L. X.; Ratner, M. A., Structural and Conformational Dispersion in the Rational Design of Conjugated Polymers. *Macromolecules* **2014,** *47*, 987.
220. Barford, W.; Marcus, M., Theory of optical transitions in conjugated polymers. *J. Chem. Phys.* **2014,** *141*, 164101.
221. Scholes, G. D.; Smyth, C., Perspective: Detecting and measuring exciton delocalization in photosynthetic light harvesting. *J. Chem. Phys.* **2014,** *140*, 110901.

222. Mazzio, K. A.; Luscombe, C. K., The future of organic photovoltaics. *Chem. Soc. Rev.* **2015,** *44* (1), 78-90.
223. Ferron, T.; Waldrip, M.; Pope, M.; Collins, B. A., Increased charge transfer state separation via reduced mixed phase interface in polymer solar cells. *Journal of Materials Chemistry A* **2019,** *7* (9), 4536-4548.
224. Hughes, M. P.; Rosenthal, K. D.; Ran, N. A.; Seifrid, M.; Bazan, G. C.; Nguyen, T.-Q., Determining the Dielectric Constants of Organic Photovoltaic Materials Using Impedance Spectroscopy. *Adv. Funct. Mater.* **2018,** *28* (32), 1801542.
225. Gao, W.; Liu, T.; Luo, Z.; Zhang, L.; Ming, R.; Zhong, C.; Ma, W.; Yan, H.; Yang, C., Regulating exciton bonding energy and bulk heterojunction morphology in organic solar cells via methyl-functionalized non-fullerene acceptors. *Journal of Materials Chemistry A* **2019,** *7* (12), 6809-6817.
226. Bakulin, A. A.; Rao, A.; Pavelyev, V. G.; van Loosdrecht, P. H. M.; Pshenichnikov, M. S.; Niedzialek, D.; Cornil, J.; Beljonne, D.; Friend, R. H., The Role of Driving Energy and Delocalized States for Charge Separation in Organic Semiconductors. *Science* **2012,** *335* (6074), 1340-1344.
227. Chen, J.; Chen, Y.; Feng, L. W.; Gu, C.; Li, G.; Su, N.; Wang, G.; Swick, S. M.; Huang, W.; Guo, X.; Facchetti, A.; Marks, T. J., Hole (donor) and electron (acceptor) transporting organic semiconductors for bulk-heterojunction solar cells. *EnergyChem.* **2020,** *2* (5), 100042.
228. Lin, Y.; Zhao, F.; Prasad, S. K. K.; Chen, J.-D.; Cai, W.; Zhang, Q.; Chen, K.; Wu, Y.; Ma, W.; Gao, F.; Tang, J.-X.; Wang, C.; You, W.; Hodgkiss, J. M.; Zhan, X., Balanced Partnership between Donor and Acceptor Components in Nonfullerene Organic Solar Cells with >12% Efficiency. *Adv. Mater.* **2018,** *30* (16), 1706363.
229. Li, H.; Earmme, T.; Ren, G.; Saeki, A.; Yoshikawa, S.; Murari, N. M.; Subramaniyan, S.; Crane, M. J.; Seki, S.; Jenekhe, S. A., Beyond Fullerenes: Design of Nonfullerene Acceptors for Efficient Organic Photovoltaics. *Journal of the American Chemical Society* **2014,** *136* (41), 14589-14597.
230. Dutton, G. J.; Robey, S. W., Non-fullerene acceptors: exciton dissociation with PTCDA versus C60. *Physical Chemistry Chemical Physics* **2015,** *17* (24), 15953-15962.
231. Li, S.; Liu, W.; Li, C.-Z.; Shi, M.; Chen, H., Efficient Organic Solar Cells with Non-Fullerene Acceptors. *Small* **2017,** *13* (37), 1701120.
232. Li, Y.; Zhong, L.; Gautam, B.; Bin, H.-J.; Lin, J.-D.; Wu, F.-P.; Zhang, Z.; Jiang, Z.-Q.; Zhang, Z.-G.; Gundogdu, K.; Li, Y.; Liao, L.-S., A near-infrared non-fullerene electron acceptor for high performance polymer solar cells. *Energy & Environmental Science* **2017,** *10* (7), 1610-1620.
233. Zhang, J. Q.; Tan, H. S.; Guo, X. G.; Facchetti, A.; Yan, H., Material insights and challenges for non-fullerene organic solar cells based on small molecular acceptors. *Nat. Energy* **2018,** *3* (9), 720.
234. Sun, H.; Chen, F.; Chen, Z. K., Recent progress on non-fullerene acceptors for organic photovoltaics. *Mater. Today* **2019,** *24*, 94.
235. Wadsworth, A.; Moser, M.; Marks, A.; Little, M. S.; Gasparini, N.; Brabec, C. J.; Baran, D.; McCulloch, I., Critical review of the molecular design progress in non-fullerene

electron acceptors towards commercially viable organic solar cells. *Chem. Soc. Rev.* **2019,** *48* (6), 1596.
236. Swick, S. M.; Alzola, J. M.; Sangwan, V. K.; Amsterdam, S. H.; Zhu, W.; Jones, L. O.; Powers-Riggs, N.; Facchetti, A.; Kohlstedt, K. L.; Schatz, G. C.; Hersam, M. C.; Wasielewski, M. R.; Marks, T. J., Fluorinating π-Extended Molecular Acceptors Yields Highly Connected Crystal Structures and Low Reorganization Energies for Efficient Solar Cells. *Adv. Energy Mater.* **2020,** *10* (23), 2000635.
237. Swick, S. M.; Gebraad, T.; Jones, L.; Fu, B.; Aldrich, T. J.; Kohlstedt, K. L.; Schatz, G. C.; Facchetti, A.; Marks, T. J., Building Blocks for High-Efficiency Organic Photovoltaics: Interplay of Molecular, Crystal, and Electronic Properties in Post-Fullerene ITIC Ensembles. *ChemPhysChem* **2019,** *20* (20), 2608.
238. Swick, S. M.; Zhu, W.; Matta, M.; Aldrich, T. J.; Harbuzaru, A.; Lopez Navarrete, J. T.; Ponce Ortiz, R.; Kohlstedt, K. L.; Schatz, G. C.; Facchetti, A.; Melkonyan, F. S.; Marks, T. J., Closely packed, low reorganization energy pi-extended postfullerene acceptors for efficient polymer solar cells. *Proc. Natl. Acad. Sci. U. S. A.* **2018,** *115*, E8341.
239. Aldrich, T. J.; Matta, M.; Zhu, W. G.; Swick, S. M.; Stern, C. L.; Schatz, G. C.; Facchetti, A.; Melkonyan, F. S.; Marks, T. J., Fluorination Effects on Indacenodithienothiophene Acceptor Packing and Electronic Structure, End-Group Redistribution, and Solar Cell Photovoltaic Response. *J. Am. Chem. Soc.* **2019,** *141* (7), 3274.
240. Yuan, J.; Zhang, Y. Q.; Zhou, L. Y.; Zhang, G. C.; Yip, H. L.; Lau, T. K.; Lu, X. H.; Zhu, C.; Peng, H. J.; Johnson, P. A.; Leclerc, M.; Cao, Y.; Ulanski, J.; Li, Y. F.; Zou, Y. P., Single-Junction Organic Solar Cell with over 15% Efficiency Using Fused-Ring Acceptor with Electron-Deficient Core. *Joule* **2019,** *3*, 1140.
241. Wang, R.; Zhang, C.; Li, Q.; Zhang, Z.; Wang, X.; Xiao, M., Charge Separation from an Intra-Moiety Intermediate State in the High-Performance PM6:Y6 Organic Photovoltaic Blend. *J. Am. Chem. Soc.* **2020,** *142* (29), 12751.
242. Zhu, W. G.; Spencer, A. P.; Mukherjee, S.; Alzola, J. M.; Sangwan, V. K.; Amsterdam, S. H.; Swick, S. M.; Jones, L. O.; Heiber, M. C.; Herzing, A. A.; Li, G. P.; Stern, C. L.; DeLongchamp, D. M.; Kohlstedt, K. L.; Hersam, M. C.; Schatz, G. C.; Wasielewski, M. R.; Chen, L. X.; Facchetti, A.; Marks, T. J., Crystallography, Morphology, Electronic Structure, and Transport in Non-Fullerene/Non-Indacenodithienothiophene Polymer:Y6 Solar Cells. *J. Am. Chem. Soc.* **2020,** *142* (34), 14532.
243. Li, G.; Zhang, X.; Jones, L. O.; Alzola, J. M.; Mukherjee, S.; Feng, L.-w.; Zhu, W.; Stern, C. L.; Huang, W.; Yu, J.; Sangwan, V. K.; DeLongchamp, D. M.; Kohlstedt, K. L.; Wasielewski, M. R.; Hersam, M. C.; Schatz, G. C.; Facchetti, A.; Marks, T. J., Systematic Merging of Nonfullerene Acceptor π-Extension and Tetrafluorination Strategies Affords Polymer Solar Cells with >16% Efficiency. *Journal of the American Chemical Society* **2021,** *143* (16), 6123-6139.
244. Yang, K.; Liao, Q. G.; Koh, C. W.; Chen, J. H.; Su, M. Y.; Zhou, X.; Tang, Y. M.; Wang, Y.; Zhang, Y. M.; Woo, H. Y.; Guo, X. G., Improved photovoltaic performance of a nonfullerene acceptor based on a benzo[b]thiophene fused end group with extended pi-conjugation. *J. Mater. Chem. A* **2019,** *7* (16), 9822.
245. Chen, S.; Lee, S. M.; Xu, J.; Lee, J.; Lee, K. C.; Hou, T.; Yang, Y.; Jeong, M.; Lee, B.; Cho, Y.; Jung, S.; Oh, J.; Zhang, Z.-G.; Zhang, C.; Xiao, M.; Li, Y.; Yang, C., Ultrafast

Channel II process induced by a 3-D texture with enhanced acceptor order ranges for high-performance non-fullerene polymer solar cells. *Energy & Environmental Science* **2018,** *11* (9), 2569-2580.
246. Cha, H.; Wu, J.; Wadsworth, A.; Nagitta, J.; Limbu, S.; Pont, S.; Li, Z.; Searle, J.; Wyatt, M. F.; Baran, D.; Kim, J.-S.; McCulloch, I.; Durrant, J. R., An Efficient, "Burn in" Free Organic Solar Cell Employing a Nonfullerene Electron Acceptor. *Adv. Mater.* **2017,** *29* (33), 1701156.
247. Hartnett, P. E.; Matte, H. S. S. R.; Eastham, N. D.; Jackson, N. E.; Wu, Y.; Chen, L. X.; Ratner, M. A.; Chang, R. P. H.; Hersam, M. C.; Wasielewski, M. R.; Marks, T. J., Ring-fusion as a perylenediimide dimer design concept for high-performance non-fullerene organic photovoltaic acceptors. *Chem. Sci.* **2016,** *7*, 3543.
248. Kaunisto, K. M.; Vivo, P.; Dubey, R. K.; Chukharev, V. I.; Efimov, A.; Tkachenko, N. V.; Lemmetyinen, H. J., Charge-Transfer Dynamics in Poly(3-hexylthiophene):Perylenediimide-C60 Blend Films Studied by Ultrafast Transient Absorption. *J. Phys. Chem. C* **2014,** *118* (20), 10625-10630.
249. Eastham, N. D.; Logsdon, J. L.; Manley, E. F.; Aldrich, T. J.; Leonardi, M. J.; Wang, G.; Powers-Riggs, N. E.; Young, R. M.; Chen, L. X.; Wasielewski, M. R.; Melkonyan, F. S.; Chang, R. P. H.; Marks, T. J., Hole-Transfer Dependence on Blend Morphology and Energy Level Alignment in Polymer:ITIC Photovoltaic Materials. *Adv. Mater. (Weinheim, Ger.)* **2018,** *30* (3), n/a.
250. Samanta, S.; Chaudhuri, D., Suppressing Excimers in H-Aggregates of Perylene Bisimide Folda-Dimer: Role of Dimer Conformation and Competing Assembly Pathways. *J Phys Chem Lett* **2017,** *8* (14), 3427-3432.
251. Aluicio-Sarduy, E.; Singh, R.; Kan, Z.; Ye, T.; Baidak, A.; Calloni, A.; Berti, G.; Duò, L.; Iosifidis, A.; Beaupré, S.; Leclerc, M.; Butt, H.-J.; Floudas, G.; Keivanidis, P. E., Elucidating the Impact of Molecular Packing and Device Architecture on the Performance of Nanostructured Perylene Diimide Solar Cells. *ACS Appl. Mater. Interfaces* **2015,** *7* (16), 8687-8698.
252. Liu, Z.; Zhang, L.; Shao, M.; Wu, Y.; Zeng, D.; Cai, X.; Duan, J.; Zhang, X.; Gao, X., Fine-Tuning the Quasi-3D Geometry: Enabling Efficient Nonfullerene Organic Solar Cells Based on Perylene Diimides. *ACS Appl. Mater. Interfaces* **2018,** *10* (1), 762-768.
253. Qiu, B.; Chen, Z.; Qin, S.; Yao, J.; Huang, W.; Meng, L.; Zhu, H.; Yang, Y.; Zhang, Z.-G.; Li, Y., Highly Efficient All-Small-Molecule Organic Solar Cells with Appropriate Active Layer Morphology by Side Chain Engineering of Donor Molecules and Thermal Annealing. *Adv. Mater.* **2020,** *32* (21), 1908373.
254. Zhu, L.; Zhang, M.; Zhou, G.; Hao, T.; Xu, J.; Wang, J.; Qiu, C.; Prine, N.; Ali, J.; Feng, W.; Gu, X.; Ma, Z.; Tang, Z.; Zhu, H.; Ying, L.; Zhang, Y.; Liu, F., Efficient Organic Solar Cell with 16.88% Efficiency Enabled by Refined Acceptor Crystallization and Morphology with Improved Charge Transfer and Transport Properties. *Advanced Energy Materials* **2020,** *10* (18), 1904234.
255. Liu, T.; Huo, L.; Chandrabose, S.; Chen, K.; Han, G.; Qi, F.; Meng, X.; Xie, D.; Ma, W.; Yi, Y.; Hodgkiss, J. M.; Liu, F.; Wang, J.; Yang, C.; Sun, Y., Optimized Fibril Network Morphology by Precise Side-Chain Engineering to Achieve High-Performance Bulk-Heterojunction Organic Solar Cells. *Advanced Materials* **2018,** *30* (26), 1707353.

256. Tang, Z.; Wang, J.; Melianas, A.; Wu, Y.; Kroon, R.; Li, W.; Ma, W.; Andersson, M. R.; Ma, Z.; Cai, W.; Tress, W.; Inganäs, O., Relating open-circuit voltage losses to the active layer morphology and contact selectivity in organic solar cells. *Journal of Materials Chemistry A* **2018,** *6* (26), 12574-12581.
257. Zhang, J.; Li, Y.; Hu, H.; Zhang, G.; Ade, H.; Yan, H., Chlorinated Thiophene End Groups for Highly Crystalline Alkylated Non-Fullerene Acceptors toward Efficient Organic Solar Cells. *Chemistry of Materials* **2019,** *31* (17), 6672-6676.
258. Song, X.; Gasparini, N.; Ye, L.; Yao, H.; Hou, J.; Ade, H.; Baran, D., Controlling Blend Morphology for Ultrahigh Current Density in Nonfullerene Acceptor-Based Organic Solar Cells. *ACS Energy Lett.* **2018,** *3* (3), 669-676.
259. Izawa, S.; Shintaku, N.; Hiramoto, M., Effect of Band Bending and Energy Level Alignment at the Donor/Acceptor Interface on Open-Circuit Voltage in Organic Solar Cells. *The Journal of Physical Chemistry Letters* **2018,** *9* (11), 2914-2918.
260. Yuan, J.; Huang, T.; Cheng, P.; Zou, Y.; Zhang, H.; Yang, J. L.; Chang, S. Y.; Zhang, Z.; Huang, W.; Wang, R.; Meng, D.; Gao, F.; Yang, Y., Enabling low voltage losses and high photocurrent in fullerene-free organic photovoltaics. *Nat Commun* **2019,** *10* (1), 570.
261. Karki, A.; Vollbrecht, J.; Gillett, A. J.; Xiao, S. S.; Yang, Y. L.; Peng, Z. X.; Schopp, N.; Dixon, A. L.; Yoon, S.; Schrock, M.; Ade, H.; Reddy, G. N. M.; Friend, R. H.; Nguyen, T. Q., The role of bulk and interfacial morphology in charge generation, recombination, and extraction in non-fullerene acceptor organic solar cells. *Energy & Environmental Science* **2020,** *13* (10), 3679-3692.
262. Wu, J. Y.; Lee, J.; Chin, Y. C.; Yao, H. F.; Cha, H.; Luke, J.; Hou, J. H.; Kim, J. S.; Durrant, J. R., Exceptionally low charge trapping enables highly efficient organic bulk heterojunction solar cells. *Energy & Environmental Science* **2020,** *13* (8), 2422-2430.